Angus, Fraser (2026) *Extracting meaning from ion migration in perovskite solar cells.* PhD thesis.

Extracting Meaning from Ion Migration in Perovskite Solar Cells

Fraser Angus
University of Glasgow
College of Science and Engineering
School of Chemistry

A thesis presented for the degree of
Doctor of Philosophy

June 2026

Declaration

I hereby certify that the thesis submitted for examination for the PhD degree at the University of Glasgow represents my original work. Where I have included contributions from others, I have clearly indicated these instances and specified the extent of any collaborative efforts. Additionally, I confirm that the thesis has not been edited by any third party beyond the allowances outlined in the University's PGR Code of Practice.

Fraser Angus, June 2026

Abstract

Perovskite solar cells (PSCs) have rapidly emerged as one of the most promising next-generation photovoltaic technologies, with certified power conversion efficiencies now exceeding 27%. Unlike conventional photovoltaic materials, metal-halide perovskites contain mobile ionic defects that fundamentally alter the underlying device physics. As a consequence, PSCs conduct both electronic and ionic charge. Ion migration has been widely linked to current–voltage hysteresis, performance variability, and long-term degradation. While considerable effort has focused on mitigating these effects, far less attention has been paid to the information that can be extracted from the presence and redistribution of mobile ions within operating devices.

In this thesis, ion migration is used as a diagnostic of internal device energetics and recombination dynamics. Central to this work is the Stabilise and Pulse (SaP) technique, which enables controlled manipulation of ionic redistribution within an operating solar cell. By altering the distribution of mobile ions within the device, SaP modulates the internal electric field and enables access to the flat-band condition, which, as shown here, is equivalent to the built-in potential in PSCs. Controlling ionic redistribution, therefore, provides a means to probe interfacial charge accumulation, recombination behaviour, and energetic alignment within the device.

Using this approach, we experimentally show, for the first time, that mobile ions can systematically enhance the open-circuit voltage of perovskite solar cells, relative to an equivalent ion-free device. This is achieved through ionic redistribution, which reduces minority-carrier accumulation at transport-layer interfaces and suppresses interfacial recombination. The magnitude of this enhancement depends on the surface recombination strength and the energetic alignment of the transport layers.

Applying the SaP methodology to devices incorporating self-assembled molecules reveals that the molecular dipole strength directly shifts the built-in potential in PSCs, confirming that the Fermi-level difference across the transport layers governs the internal potential drop. At the same time, excessively large dipole moments introduce interfacial barriers that lead to charge accumulation and limit current extraction via increased recombination at the interface.

Extending the Stabilise and Pulse analysis to Spiro-based systems further demonstrates that the spatial localisation of the highest occupied molecular orbital plays a decisive role in recombination dynamics and charge extraction. Contrary to conventional design assumptions, promoting direct charge injection does not necessarily improve performance, as it can limit the quasi-Fermi level splitting in perovskite solar cells and reduce the achievable open-circuit voltage. This highlights that control of interfacial recombination can be more important than maximising energetic overlap.

Taken together, these findings show that mobile ionic charge should not be regarded solely as a source of instability, but rather as a feature that reshapes the internal electrostatics of PSCs in a measurable, design-relevant way.

Acknowledgements

To begin, I would like to thank my supervisor, Professor Pablo Docampo. You provided me with the opportunity to join your research group and offered your unwavering support throughout my research; for this, I am truly grateful. I will never forget the long days and nights spent working on the SaP rig code, or the incredibly inspiring Post-it notes stuck to my monitor. I will always appreciate the numerous discussions we had that helped shape the ideas presented in this thesis.

I would also like to thank Professor Graeme Cooke for his continued support and encouragement. I am grateful for the time you took to discuss my progress and the positive encouragement you offered along the way.

To all members, past and present, of the Docampo group, this journey wouldn't have been the same without you all. I want to extend my heartfelt thanks for making the past few years so enjoyable: Dr Namrata Pant, Dr Ivan Shmarov, Dr Benjamin Vella, Dr Marcin Giza, Dr Wai Kin Yiu, Madeleine McRoberts, and Aneirin Rodrigo. Thank you for all the scientific and hypothetical discussions we've had, the conference trips, and all the celebrations over the years. These are memories I will always cherish.

Furthermore, my sincere thanks go to all members (past and present) of the Cooke group for the shared group events and support over the years. I would also like to thank my friends around the School of Chemistry, particularly Dr Joy Farnaby and all the Farnaby group members, for the many great times we've enjoyed.

I also sincerely thank the Engineering and Physical Sciences Research Council and the University of Glasgow, through the School of Chemistry Scholarship, for supporting this research. I would also like to thank the staff at the University of Glasgow for their efforts in fostering a positive research environment and ensuring everything runs smoothly.

It has been a pleasure to work with all the collaborators involved in this research, particularly Dr Piers R. F. Barnes, Dr Lucy J. F. Hart, Professor Aleksandra B. Djurišić, and Dr Wenhui Li. I deeply appreciate the many meetings and engaging discussions we shared, as well as the significant effort involved in bringing our work to publication. I have learned a great deal from collaborating with you, and I am truly thankful for the experience.

To all my friends outside academia, for the many wonderful times and laughs we've shared, I will forever be grateful. You have always been there for me, and I'm lucky to have such great friends. I look forward to creating many more memories. A special thanks to Lewis, Cooper, Donald, Ciaran, and Rebecca for always being there and for making life that little bit easier along the way.

To my family, I love you all very much. Mum, Dad, Stewart, Irene, and Granny Elsie, thank you for being so supportive throughout this journey. I am especially grateful to my parents, Liz and Ian. Without you both, none of this would have been possible. You have always believed in me and supported me in whatever I chose to do in life, and I feel very lucky to have you as my parents. I will forever appreciate the opportunities you have given me. The biggest thanks go to Daisy, who sat by my side every day while I was writing this thesis. I'm sure you all understand.

Finally, to my incredible fiancée, Monica. You are my rock. You have stood by me through every step of this journey with unwavering patience, love, and support. I truly could not have done this without you. I am also very thankful to your family for all the kindness and support they have shown me over the years. I will forever appreciate having shared this experience with you and look forward to our next adventure. I love you.

In loving memory of Robert Duncan.

Publications

Peer-reviewed journal articles

1. Hart, L. J. F.; **Angus, F. J.**; Li, Y.; Khaleed, A.; Calado, P.; Durrant, J. R.; Djurišić, A. B.; Docampo, P.; Barnes, P. R. F. More Is Different: Mobile Ions Improve the Design Tolerances of Perovskite Solar Cells. *Energy Environ. Sci.* 2024. DOI: 10.1039/D4EE02669A.

2. **Angus, F. J.**; Yiu, W. K.; Mo, H.; Leung, T. L.; Ali, M. U.; Li, Y.; Wang, J.; Ho-Baillie, A. W. Y.; Cooke, G.; Djurišić, A. B.; Docampo, P. Understanding the Impact of SAM Fermi Levels on High Efficiency p–i–n Perovskite Solar Cells. *J. Phys. Chem. Lett.* 2024, **15** (42), 10686–10695. DOI: 10.1021/acs.jpclett.4c02345.

3. **Angus, F. J.**; Mackenzie, L.; Giza, M.; Wilkinson, D.; Arca, E.; Palomares, E.; Li, W.; Docampo, P.; Cooke, G. The Case Against Hole Injection Through SAMs in Perovskite Solar Cells. *J. Mater. Chem. A* 2025. DOI: 10.1039/D5TA06749A.

4. Ginesi, R. E.; **Angus, F. J.**; Giza, M.; Macleod, G. N. M.; Doutch, J.; Docampo, P.; Draper, E. R. Using Heat-Cool Processing to Change the Assembly and Photoconductive Properties of Perylene Bisimides. *Adv. Mater. Interfaces* 2025. DOI: 10.1002/admi.202500151.

5. Giza, M.; **Angus, F. J.**; Yiu, W. K.; McRoberts, M.; Vella, B.; Wang, J.; Djurišić, A. B.; Cooke, G.; Arca, E.; Docampo, P. The Case of the Vanishing Perovskite Layer. *Cell Rep. Phys. Sci.* 2025. DOI: 10.1016/j.xcrp.2025.102890.

6. Mo, H.; Li, D.; Sergeev, A.; Yiu, W. K.; Wang, J.; Zhang, G.; Yuan, Z.; Li, Y.; He, Y.; Zhu, T.; Yu Lam, M.; **Angus, F. J.**; Li, W.-D.; Tang, J.; Wong, K. S.; Cooke, G.; Docampo, P.; Popović, J.; Li, G.; Djurišić, A. B. Fullerene Derivative Layer as a Charge Transfer Bridge for Efficient and Stable Perovskite Solar Cells. *Adv. Funct. Mater.* 2026. DOI: 10.1002/adfm.202517140.

7. Serrano-Nieto, R.; Yiu, W. K.; Giza, M.; **Angus, F. J.**; Cooke, G.; Horcajada, P.; Pérez, Y.; Docampo, P. Controlling Band-Bending for Perovskite Optoelectronic Devices Using Bismuth-Based Interlayers. *ACS Omega* 2025, **10** (43), 52067–52075. DOI: 10.1021/acsomega.5c09745.

8. Vella, B.; Fsadni, M. H.; Pope, T.; Giza, M.; **Angus, F. J.**; Shmarov, I.; Lalaguna, P. L.; Cariello, M.; Wilson, C.; Kadodwala, M.; Penfold, T. J.; Docampo, P.; Cooke, G. Overcoming the Mobility Penalty Introduced by Dipole Disorder in Small-Molecule HTM Films. *J. Mater. Chem. A* 2024. DOI: 10.1039/D4TA00956H.

9. Tao, R.; Wang, G.; Li, Z.; Sun, N.; Bing, J.; Leung, T. L.; **Angus, F. J.**; Tang, J.; Liao, C.; Yi, J.; Bailey, C.; Liu, L.; Wang, Y.; Huang, G.; Lambertz, A.; Yin, S.; Gong, B.; Cavallaro, A.-A.; Evans, D.; Griffith, M.; Kalantar-Zadeh, K.; Zheng, J.; Docampo, P.; McKenzie, D. R.; Mahmud, M. A.; Ding, K.; Ho-Baillie, A. W. Y. pH Modulation for Self-Assembly-Monolayer-Type Hole Transport Layer for Efficient and Stable Perovskite–Silicon Double-Junction Solar Cells. *Joule* 2026. DOI: 10.1016/j.joule.2025.102314.

Manuscripts in preparation

1. **Angus, F. J.**; Worsley, C.; Garcia Rodriguez, R.; Steed, A.; Watson, T.; Docampo, P. Shining a Light on Fermi-Level Shifts and Ionic Contributions in Triple Mesoscopic Perovskite Solar Cells. *Manuscript in preparation.*

2. Yiu, W. K.; **Angus, F. J.**; Wilkinson, D.; Mo, H.; Wang, J.; Cooke, G.; Djurišić, A. B.; Docampo, P. Fine-Tuning Fermi-Level Position by Utilising Mixed Self-Assembled Monolayers in Perovskite Solar Cells. *Manuscript in preparation.*

Conference Contributions

Oral Presentations

1. **Angus, F. J.**; Hart, L. J. F.; Li, Y.; Khaleed, A.; Calado, P.; Durrant, J. R.; Djurišić, A. B.; Docampo, P.; Barnes, P. R. F. More Is Different: Mobile Ions Improve the Design Tolerances of Perovskite Solar Cells. *International Conference on Hybrid and Organic Photovoltaics (HOPV25)*, Rome, Italy, May 12–14, 2025. Oral Presentation.

Poster Presentations

1. **Angus, F. J.**; Hart, L. J. F.; Barnes, P. R. F.; Docampo, P. Understanding the Impact of Ions on Open-Circuit Voltage in Perovskite Solar Cells. *2023 MRS Fall Meeting & Exhibit*, Boston, MA, USA, November 26–December 1, 2023. Poster.

2. **Angus, F. J.**; Docampo, P. Exploring the Correlation Between the Built-In Potential of Perovskite Solar Cells and the Thickness of Passivating Layered Perovskites. *2023 MRS Fall Meeting & Exhibit*, Boston, MA, USA, November 26–December 1, 2023. Poster.

Contents

List of Figures

List of Tables

Nomenclature

Abbreviations

AFM	Atomic force microscopy
AM1.5G	Air mass 1.5 global spectrum
CV	Cyclic voltammetry
DC	Double-cation perovskite
ETL	Electron transport layer
FF	Fill factor
FTO	Fluorine-doped tin oxide
HOMO	Highest occupied molecular orbital
HTL	Hole transport layer
ITO	Indium-doped tin oxide
J–V	Current density–voltage
KPFM	Kelvin probe force microscopy
LUMO	Lowest unoccupied molecular orbital
MAPI	Methylammonium lead iodide
MPP	Maximum power point
PCE	Power conversion efficiency
PSC	Perovskite solar cell
PV	Photovoltaic
QFLS	Quasi-Fermi level splitting

QSS	Quasi-steady-state
SAM	Self-assembled molecule
SaP	Stabilise and Pulse
SEM	Scanning electron microscopy
SRH	Shockley–Read–Hall
TRPL	Time-resolved photoluminescence
UPS	Ultraviolet photoelectron spectroscopy
UV–Vis	Ultraviolet–visible absorption spectroscopy
XPS	X-ray photoelectron spectroscopy
XRD	X-ray diffraction

Symbols

$\Delta\phi_{\mathrm{psk}}$	Electrostatic potential across the perovskite layer (V)
ΔE_{TL}	Energetic offset between the perovskite and transport layer (eV)
μ_n	Electron mobility ($\mathrm{cm^2\,V^{-1}\,s^{-1}}$)
μ_p	Hole mobility ($\mathrm{cm^2\,V^{-1}\,s^{-1}}$)
ρ	Electrical resistivity ($\Omega\,\mathrm{m}$)
σ	Electrical conductivity ($\mathrm{S\,m^{-1}}$)
ε	Permittivity ($\mathrm{F\,m^{-1}}$)
D_n	Electron diffusion coefficient ($\mathrm{cm^2\,s^{-1}}$)
D_p	Hole diffusion coefficient ($\mathrm{cm^2\,s^{-1}}$)
E	Local electric field ($\mathrm{V\,m^{-1}}$)
G	Local photogeneration rate ($\mathrm{cm^{-3}\,s^{-1}}$)
J_n	Electron current density ($\mathrm{A\,cm^{-2}}$)
J_p	Hole current density ($\mathrm{A\,cm^{-2}}$)
J_{MP}	Current density at the maximum power point ($\mathrm{mA\,cm^{-2}}$)

n	Electron carrier density ($\mathrm{cm^{-3}}$)
N_{dop}	Fixed dopant charge density in the transport layers ($\mathrm{cm^{-3}}$)
N_{ion}	Net ionic charge density within the perovskite ($\mathrm{cm^{-3}}$)
p	Hole carrier density ($\mathrm{cm^{-3}}$)
q	Elementary charge (C)
R	Total charge-carrier recombination rate ($\mathrm{cm^{-3}\,s^{-1}}$)
R_{rad}	Radiative recombination rate ($\mathrm{cm^{-3}\,s^{-1}}$)
R_{SRH}	Shockley–Read–Hall recombination rate ($\mathrm{cm^{-3}\,s^{-1}}$)
V_{MP}	Voltage at the maximum power point (V)
d	Interplanar spacing (Å)
$\frac{\mathrm{d}J}{\mathrm{d}V}$	Differential current density with respect to voltage ($\mathrm{mA\,cm^{-2}\,V^{-1}}$)
E_C	Conduction band edge (eV)
E_F	Fermi level (eV)
$E_{F,n}$	Electron quasi-Fermi level (eV)
$E_{F,p}$	Hole quasi-Fermi level (eV)
E_g	Band gap (eV)
η	Power conversion efficiency
E_V	Valence band edge (eV)
E_{vac}	Vacuum level (eV)
I	Current (A)
I_{SC}	Short-circuit current (A)
J	Current density ($\mathrm{mA\,cm^{-2}}$)
J_{SC}	Short-circuit current density ($\mathrm{mA\,cm^{-2}}$)
k_1	Monomolecular recombination rate constant ($\mathrm{s^{-1}}$)
k_2	Bimolecular recombination coefficient ($\mathrm{cm^3/s}$)

P_{in}	Incident optical power density ($\mathrm{mW\,cm^{-2}}$)
Φ_{PL}	Photoluminescence intensity (arb. units)
λ	Wavelength (nm)
τ	Carrier lifetime (s)
θ	Bragg angle (°)
t	Time (s)
V	Voltage (V)
V_{bi}	Built-in potential (V)
V_{bias}	Applied bias voltage (V)
V_{flat}	Flat-band potential (V)
V_{OC}	Open-circuit voltage (V)
ϕ	Work function (eV)
SRV	Surface recombination velocity ($\mathrm{cm\,s^{-1}}$)

Units

D	Debye
eV	Electron volt
$\mathrm{mA\,cm^{-2}}$	Current density unit
$\mathrm{mW\,cm^{-2}}$	Irradiance unit
A	Ampere
Å	Ångström
°C	Degree Celsius
nm	Nanometre
V	Volt
TWh	Terawatt-hour

Chapter 1

Introduction

1.1 Thesis Overview

The rapid adoption of renewable energy sources is essential to addressing the global climate crisis and meeting rising energy demands.[1] To slow global warming, protect ecosystems, and transition to cleaner, more secure energy systems, we must reduce carbon emissions, increase the use of renewable energy, phase out fossil fuels, and accelerate the deployment of clean energy technologies.[1, 2] These goals are key topics at the Conference of the Parties (COP) summits, where global commitments are made to drive meaningful change.[3] As a result of these commitments, we have already seen significant progress.[1, 4] In 2024, carbon dioxide emissions from the energy sector increased at a slower rate than in 2023, while global clean power deployment reached record highs, indicating that crucial shifts in the energy system are already taking place.[5]

The rapid deployment of renewable energy came at just the right time, as the world's appetite for energy is growing steadily, and in 2024, it grew faster than in recent years.[5–7] Global energy demand increased by 2.2%, which is considerably faster than the 1.3% average growth between 2013 and 2023. This was driven by an acceleration in global electricity demand, with a surge of 4.3%, nearly double the annual average over the past decade. This sharp increase was driven by record global temperatures, which boosted demand for cooling, and by the rapid adoption of energy-intensive technologies.[5] The rapid expansion of large-scale computing, artificial intelligence (AI), and data centres is a major contributor to global energy consumption, and there is no sign of slowing.[8] This surge in demand highlights a simple reality: future growth must be powered by clean, reliable energy, underscoring the need for rapid expansion of renewable energy.

Encouragingly, the world is moving in the right direction. According to Ember's Global Electricity Review 2025 and the International Energy Agency (IEA), clean electricity surpassed 40% of global generation for the first time in the modern era (reaching 40.9% in 2024).[5, 6] This milestone was driven by a record 858 TWh increase in renewable generation.[5, 6] Among the available renewable technologies, solar power played the dominant role. Solar alone added 474 TWh of new generation in 2024, making it the fastest-growing electricity source globally for the twentieth consecutive year.[5–7] Solar generation has now doubled in just three years, surpassing 2,000 TWh worldwide and continuing its long-standing trajectory.[5, 6] This momentum is changing expectations about the future electricity system. As the world electrifies transport, heating, industry, and digital infrastructure, the ability to generate large amounts of clean electricity is becoming central to economic development and meeting the rising demand. Solar energy, being modular, increasingly affordable, and rapidly deployable, is exceptionally well-positioned to meet this growing demand.

To sustain this momentum, solar energy must continue to develop. Devices must become more efficient at converting sunlight into electricity, while also becoming cheaper and easier to manufacture at scale. Achieving these improvements will likely require advances beyond traditional single-junction silicon-based photovoltaics (PVs). Against this backdrop, perovskite solar cells (PSCs) have emerged as one of the most promising next-generation PV technologies, particularly as a complementary material that can be integrated with silicon in tandem architectures to surpass the efficiency limits of single-junction devices. Since their introduction in 2009, perovskite solar cells have seen meteoric gains in efficiency, now rivalling the efficiency of the widely adopted silicon technology.[9, 10] Yet the behaviour of perovskite materials is distinctly different from traditional solar technologies. They do not simply generate and conduct electrical charge; they also allow particular ionic species within the material to migrate under working conditions.[11] This feature is highly unusual for a photovoltaic material, and as a result, this technology is governed by different physical principles compared with traditional technologies. It is these physical principles that need to be studied before the widespread adoption of perovskite solar cells can occur. Understanding how this ionic movement interacts with a device's electronic processes is crucial.

This thesis seeks to build on our understanding of the perovskite solar cell system and demonstrate how meaningful physical information can be extracted from the presence of mobile ions. The following chapters bring together advanced characterisation measurements and interfacial energetics to build a coherent picture of how ion migration influences performance. This work aims to deepen our understanding of perovskite solar cells and support their continued development as a leading technology in the transition to clean, scalable, and affordable renewable electricity.

1.2 Perovskite Solar Cells

Perovskite solar cells were first introduced by Miyasaka *et al.* in 2009, achieving a modest 3.8% conversion efficiency.[9] For reference, at this time, single-crystal silicon technology held a record efficiency of 25%[1]. As of late 2025, perovskite technologies have reached 27%[2] efficiency, with record silicon at 27.8%.[10] This meteoric rise in efficiency is what has made perovskite solar cells one of the most revolutionary technologies in the solar world, so what actually are they?

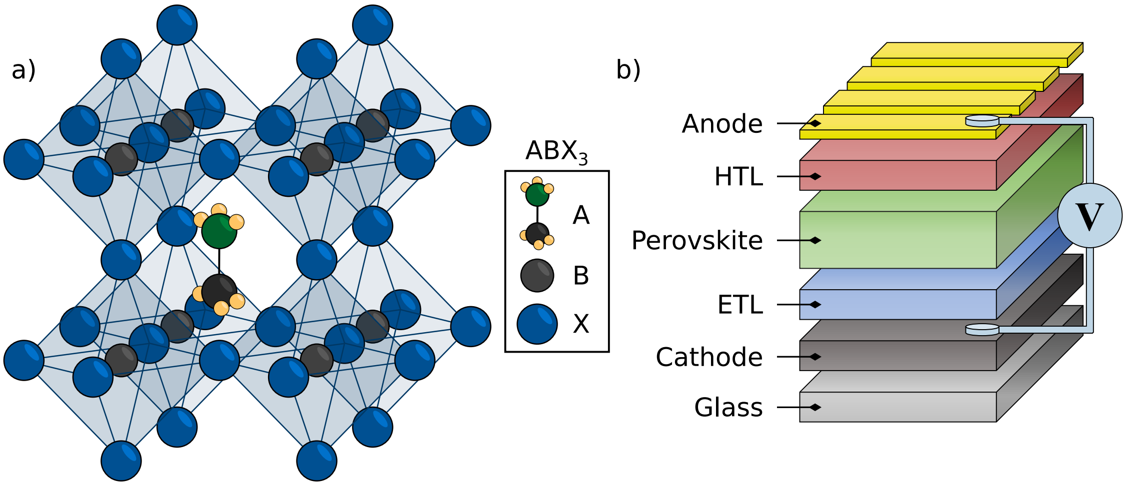

Figure 1.1: a) Crystal structure of an ABX$_3$ metal-halide perovskite, illustrating the corner-sharing BX$_6$ octahedra and A-site cation. Here, the A-site cation is shown as a cartoon representation of methylammonium. b) Cartoon schematic of a perovskite solar cell.

The term perovskite describes a wide family of materials sharing the same general ABX$_3$ crystal structure, as shown in Figure 1.1a.[12] In this structure, the A and B positions are occupied by cations, while anions, usually halides, fill the X sites. One of the most extensively studied examples is methylammonium lead iodide (MAPI),

---

[1] The record for this class of material was set in 1999 and not beaten again until 2014 by Panasonic, where they achieved an efficiency of 25.6%

[2] Perovskite solar cells are only outperformed by Silicon heterostructures and, as of 2025, outperform all other types of single junction silicon technology.

although many related compounds exist.[13] Various compounds can occupy the different sites in the perovskite structure. However, the class of materials that can achieve the highest power conversion efficiencies are organic-inorganic lead halide perovskites. The versatility of the perovskite structure is one of the many incredible properties that have enabled this class of materials to improve efficiency so quickly. Other benefits of perovskites include: low costs for both raw materials and fabrication methods; and the ability to absorb sunlight extremely well, enabling the production of ultra-thin films.[14] They also work incredibly well with traditional silicon technology, allowing tandem devices to achieve efficiencies of almost 35%.[15]

The structure of a PSC consists of a thin layer of perovskite which is sandwiched between two charge-selective contacts, as illustrated in Figure 1.1b. The perovskite layer absorbs light, and the photogenerated charge is then passed through the selective layers towards the respective contact, where it is extracted. This simple configuration has demonstrated remarkable photovoltaic performance, although several barriers have prevented full-scale commercialisation.[16] Poor stability of the perovskite material in the presence of water vapour, light and oxygen has hindered the widespread deployment. The dual nature of perovskites, which conduct both ionic and electronic charge, has generated extensive research.[11] However, these challenges in stability and a better fundamental understanding of the physical properties must be overcome before commercially competitive devices can be widely adopted.

1.3 Aims of the Present Thesis

Although perovskite solar cells have been studied for almost two decades, there is still much to uncover. One of the most critical features encompassing much of the research in this topic is the presence of mobile ions. Utilising novel measurement techniques and extracting the information these ions contain is essential to understanding this system entirely, and this constitutes the main aim of this thesis.

We begin with Chapter 2, where we review a significant body of literature and discuss the relevant theories of photovoltaics, starting from the working principles, before exploring the influence that mobile ionic charge has on electric fields and device interfaces in perovskite solar cells. This chapter provides general context, while more specific background sections are included at the beginning of each results chapter to facilitate faster access to the relevant concepts. Chapter 3 gives technical details of all experimental measurement techniques used throughout the results chapters.

The results section begins with Chapter 4, where the impact of mobile ions on device performance is evaluated. Conducted in collaboration with Dr Lucy Hart and Dr Piers R F Barnes of Imperial College London, we successfully show that mobile ions can reduce surface recombination rates by redistributing electronic charge. In this work, I utilise the Stabilise and Pulse technique to decouple ionic and electronic effects within a working perovskite solar cell. By doing so, we extract the performance of an equivalent device with no mobile ionic charge and compare it with that of a device with ions at a steady-state distribution. We demonstrate that the presence of mobile ions enables a higher achievable open-circuit voltage and then evaluate the overall impact of ions on device performance.

In Chapter 5, I investigate the role the Fermi level of commonly employed self-assembled molecules plays in device performance. I identify a correlation between the dipole moment and the Fermi level, which is measured directly by the Stabilise and Pulse technique. Furthermore, I identify that molecules with too large a dipole can create an unintentional interfacial energy barrier, leading to reduced charge-collection efficiency and, consequently, reduced overall device efficiency. This work was completed in collaboration with Professor Aleksandra B. Djurišić and Dr Wai Kin Yiu.

Finally, in Chapter 6, I propose that direct charge injection through a Spiro moiety's highest occupied molecular orbital is not beneficial in perovskite solar cells. In collaboration with Dr Lewis Mackenzie and Dr Wenhui Li, I show that a molecule specifically designed to promote charge injection performs worse than a novel material intentionally designed to separate this charge-injection pathway. The Stabilise and Pulse technique reveals that the material that blocks the injection pathway contains a reduced built-in potential, yet can achieve a higher open-circuit voltage. This seemingly contradictory result is explained by increased charge accumulation in the perovskite. Through time-resolved photoluminescence and SaP measurements, an increase in surface recombination is identified, consistent with the hypothesis of charge accumulation at the interface. As a result, the quasi-Fermi level splitting widens, ultimately enhancing the open-circuit voltage and, consequently, the power conversion efficiency.

References

(1) Intergovernmental Panel on Climate Change, Climate Change 2023: Synthesis Report, 2023, `https://www.ipcc.ch/report/ar6/syr/`.

(2) International Energy Agency, World Energy Outlook 2025, 2025, `https://www.iea.org/reports/world-energy-outlook-2025`.

(3) United Nations Framework Convention on Climate Change, COP30 Action Agenda: Outcomes Report, 2025, `https://unfccc.int`.

(4) United Nations Framework Convention on Climate Change, Paris Agreement, 2015, `https://unfccc.int/process-and-meetings/the-paris-agreement/the-paris-agreement`.

(5) International Energy Agency, Global Energy Review 2025, 2025, `https://www.iea.org/reports/global-energy-review-2025`.

(6) Ember, Global Electricity Review 2025, 2025, `https://ember-energy.org/latest-insights/global-electricity-review-2025/`.

(7) International Energy Agency, Renewables 2025, 2025, `https://www.iea.org/reports/renewables-2025`.

(8) International Energy Agency, Energy and AI, 2025, `https://www.iea.org/reports/energy-and-ai`.

(9) Kojima, A.; Teshima, K.; Shirai, Y.; Miyasaka, T. *Journal of the American Chemical Society* **2009**, *131*, 6050–6051.

(10) NREL, Best Research-Cell Efficiency Chart, `https://www.nrel.gov/pv/cell-efficiency`.

(11) Calado, P.; Telford, A. M.; Bryant, D.; Li, X.; Nelson, J.; O'Regan, B. C.; Barnes, P. R. *Nature Communications* **2016**, *7*, 13831.

(12) Green, M. A.; Ho-Baillie, A.; Snaith, H. J. *Nature Photonics* **2014**, *8*, 506–514.

(13) Tao, S.; Schmidt, I.; Brocks, G.; Jiang, J.; Tranca, I.; Meerholz, K.; Olthof, S. *Nature Communications* **2019**, *10*, 2560.

(14) Snaith, H. J. *The Journal of Physical Chemistry Letters* **2013**, *4*, 3623–3630.

(15) Al-Ashouri, A. et al. *Science* **2020**, *370*, 1300–1309.

(16) Rong, Y.; Hu, Y.; Mei, A.; Tan, H.; Saidaminov, M. I.; Seok, S. I.; McGehee, M. D.; Sargent, E. H.; Han, H. *Science* **2018**, *361*, eaat8235.

Chapter 2

Theory

2.1 The Working Principles of Photovoltaics

As its name implies, a photovoltaic device converts light (photo) to electricity (-voltaic). This chapter establishes the theoretical framework for understanding the operation of photovoltaic devices and, in particular, how it must be adapted for metal-halide perovskite solar cells. This discussion is selective; rather than providing a comprehensive study of semiconductor theory, it focuses on the physical concepts directly relevant to interpreting the experimental results presented in later chapters.

The first part of this section introduces the working principles of photovoltaics. Key concepts, including band structure, charge carriers, the Fermi level, and equilibrium behaviour, are introduced to provide a foundation for understanding how light absorption gives rise to a photocurrent and photovoltage. The role of interfaces, band bending, and built-in electric fields is then discussed, followed by the fundamental recombination pathways that limit device performance. These concepts are then brought together through a minimal photovoltaic device model, which gives a reference point for understanding current-voltage characteristics.

The second part of this chapter extends this model to metal-halide perovskite solar cells. While perovskite devices share many similarities with conventional semiconductor devices, their soft ionic lattice and mixed ionic-electronic conduction provide a fascinating behaviour that traditional models cannot capture. The structure and defect chemistry of perovskites are discussed, with an emphasis on the formation and transport of mobile ionic defects.

Finally, the consequences of ionic motion for device operation are discussed. The redistribution of mobile ions under applied bias or illumination alters internal electric fields and band bending, thereby screening the electric field. This redistribution provides the physical basis for current-voltage hysteresis and motivates the measurements used in this thesis. Together, the concepts introduced in this chapter provide a foundation for demonstrating how meaning can be extracted from ion migration in perovskite solar cells.

2.1.1 Semiconductors and the Fermi level

In photovoltaic devices, electrical power generation ultimately depends on the ability of photo-generated charge carriers to move through the semiconductor and be extracted at the device contacts. Understanding how charge carriers are transported within a material is therefore central to explaining the behaviour and performance of solar cells. A material's ability to support electrical transport depends on its electronic structure, which determines whether mobile charge carriers are present.

Under standard conditions, most solid-state materials can be classified as insulators, conductors, or semiconductors according to how readily they allow electric current to flow.[1] Insulators exhibit very low conductivity, conductors exhibit high conductivity, and semiconductors lie between these two extremes. This distinction arises from the electronic band structure of the material, which governs the availability of states that can support charge transport.[2]

In crystalline inorganic semiconductors, atoms are arranged in a periodic lattice that produces a periodic electrostatic potential throughout the material. Electrons moving within this periodic potential are therefore not confined to individual atoms or molecules. Instead, their quantum-mechanical wavefunctions extend throughout the crystal and are described by Bloch states that reflect the lattice's translational symmetry.[2] Physically, this means that electronic states are delocalised throughout the crystal lattice rather than being associated with a single atom or bond. A full quantum-mechanical derivation of Bloch states is beyond the scope of this thesis; however, the key consequence is that the periodic symmetry of a crystal lattice leads to delocalised electronic states that form energy bands.[2]

The periodic nature of the crystal lattice imposes restrictions on the energies that these delocalised states may occupy. As a result, the allowed electron energies form continuous energy bands that depend on the electron crystal momentum, commonly described by dispersion relations $E(\mathbf{k})$. Between these allowed bands, there may exist ranges of energy in which no electronic states are permitted. The two bands most relevant for electronic transport are the valence band (E_V), which contains the highest-energy electrons occupied at equilibrium, and the conduction band (E_C), which is the lowest-energy band that is largely unoccupied.[2] These bands are separated by an energy range in which no electronic states exist, known as the band gap (E_g). Electrical conduction occurs when charge carriers occupy states within these bands and move through the crystal under the influence of an electric field.

The band gap magnitude, therefore, plays a central role in determining the material's electronic properties. Materials with large band gaps behave as insulators, whereas semiconductors possess intermediate band gaps that allow charge carriers to be generated thermally or optically. To describe the occupation of electronic states within these bands, the Fermi level, E_F, must be introduced. In thermal equilibrium, the E_F corresponds to the chemical potential of the electronic system and represents the energy that determines the probability that an electronic state is occupied.[1]

In metals, the Fermi level lies within a partially filled energy band. As a result, electronic states exist at energies arbitrarily close to the equilibrium occupation, and an applied electric field can redistribute electrons among these nearby states to produce a net current without requiring excitation across an energy gap.

In insulators, the valence band is almost completely filled and is separated from the conduction band by a large band gap, as illustrated in Figure 2.1a. At equilibrium, the Fermi level lies within this gap, meaning that electronic states below it are essentially occupied while those above it are essentially empty. Because the valence band is nearly filled, an applied electric field cannot produce a net current: any attempted redistribution of electron momentum is cancelled by the symmetry of the occupied states. The absence of electrical conduction, therefore, arises from band filling and the Pauli exclusion principle.

Semiconductors lie between metals and insulators in terms of their electronic properties. In the absence of external excitation, they behave similarly to insulators, exhibiting very low electrical conductivity. However, their band gaps are sufficiently small (typically 0.5–3 eV) that thermal energy or illumination can generate mobile charge carriers.[1] When an electron is excited into the conduction band, it becomes free to move through the crystal and contribute to electrical conduction, while the empty state left behind in the valence band behaves as a positively charged carrier known as a hole. This process therefore generates an electron–hole pair, and electrical conduction in semiconductors involves the motion of both electrons and holes.[3]

Semiconductors can be further classified as either intrinsic or extrinsic.[1] Intrinsic semiconductors are materials in which the concentration of charge carriers is determined by thermal excitation across the band gap rather than by intentional doping. At finite temperatures, a small fraction of electrons are thermally excited across the band gap into the conduction band, leaving behind an equal number of holes in the valence band. In this case, the electron and hole concentrations are equal,

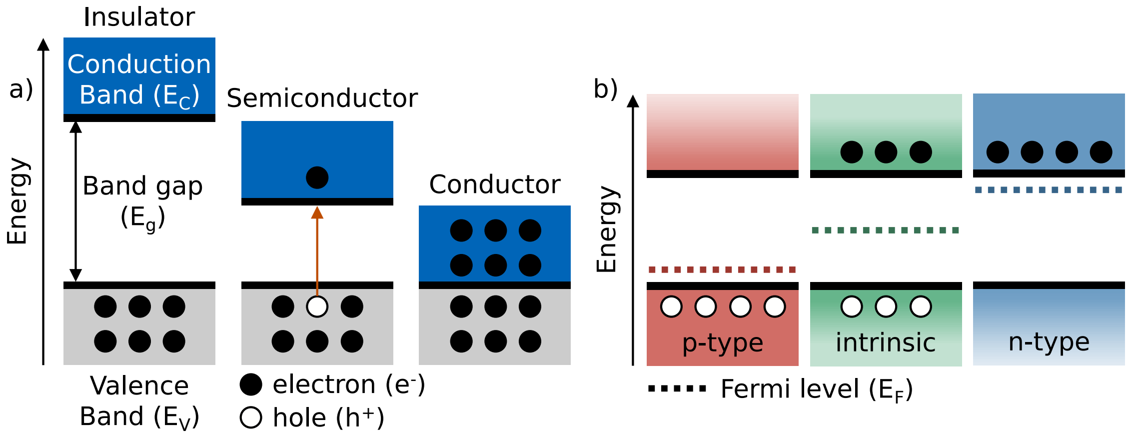

Figure 2.1: a) Simplified electronic band diagrams for an insulator, semiconductor, and conductor, illustrating the relationship between band filling and the presence of a band gap. In conductors, the Fermi level lies within a partially filled band, enabling electrical conduction without excitation across an energy gap. In semiconductors and insulators, the valence and conduction bands are separated by a band gap (E_g). b) Schematic illustration of how doping modifies carrier populations in semiconductors. Donor impurities increase the electron density and shift the equilibrium Fermi level towards the conduction band (n-type). In contrast, acceptor impurities increase the hole density and shift the Fermi level towards the valence band (p-type). For clarity, only the majority carrier is shown in each case.

$$n = p = n_i \tag{2.1}$$

where n is the electron concentration in the conduction band, p is the hole concentration in the valence band, and n_i is the intrinsic carrier concentration. Under these conditions, the Fermi level, E_F, lies close to the midpoint of the band gap and acts as a reference energy that determines the probability that an electronic state is occupied.[1] The position of E_F therefore reflects the equilibrium balance between electrons and holes within the material. This situation is illustrated in Figure 2.1b.

When controlled amounts of impurities are introduced into a semiconductor, it becomes an extrinsic semiconductor; this process is known as doping.[2] These impurities introduce additional electronic energy levels within the band gap, thereby modifying the distribution of electronic states available for occupation. Donor-like impurities introduce energy levels near the conduction band and increase the electron density relative to the hole density, thereby shifting the Fermi level upward. Materials doped in this way are referred to as n-type semiconductors. Conversely, acceptor-like impurities introduce energy levels close to the valence band and increase the density of holes relative to electrons, shifting the Fermi level downward; these materials are referred to as p-type semiconductors.[1] This concept is illustrated in Figure 2.1b.

Such doping strategies are widely used in semiconductor device engineering. For example, silicon solar cells are fabricated by introducing dopants such as boron or phosphorus to create p- and n-type regions within the device.[4] The position of the Fermi level is therefore central to semiconductor physics, providing a unified description of carrier populations under equilibrium conditions.

The following section builds on this foundation by considering how illumination alters carrier populations and drives the system out of equilibrium, leading to photocurrent generation and the emergence of separate quasi-Fermi levels for electrons and holes.

2.1.2 Photocurrent Generation and Quasi-Fermi Level Splitting

Photocurrent generation in a solar cell begins with light absorption in a semiconductor. When incident photons have energies greater than or equal to the material's band gap, they can excite electrons from the valence band into the conduction band, generating electron–hole pairs.[3] These photo-generated carriers provide the mobile charges required for electrical power generation. For efficient solar energy conversion, semiconductors with band gaps of approximately 1–2 eV are typically employed.[3] This range is well matched to the visible portion of the solar spectrum, which spans photon energies from around 1.6 to 3.3 eV.[5] Materials with band gaps in this window can therefore absorb a significant portion of incident sunlight and generate mobile charge carriers.

Upon illumination, the populations of electrons in the conduction band and holes in the valence band increase beyond their equilibrium values. As a result, the system is no longer described by a single Fermi level. Instead, separate quasi-Fermi levels are introduced for electrons ($E_{F,n}$) and holes ($E_{F,p}$), which describe non-equilibrium carrier populations under illumination.[3] This concept is schematically illustrated in Figure 2.2. The energy separation between these two quasi-Fermi levels, referred to as quasi-Fermi level splitting (QFLS), provides a direct measure of the internal potential generated by photogenerated charge within a semiconductor.[6]

In an ideal photovoltaic device, the QFLS corresponds to the maximum voltage that can be achieved under illumination.[6] This relationship can be expressed as:

$$QFLS(qV) = E_{F,n} - E_{F,p} \tag{2.2}$$

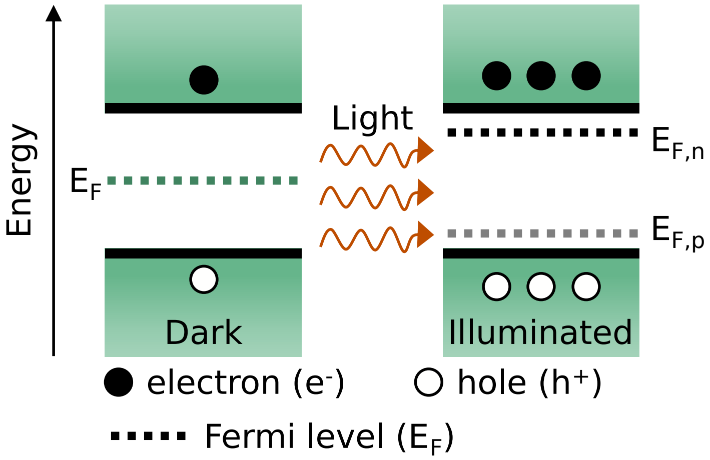

Figure 2.2: Schematic illustration of quasi-Fermi level splitting in an intrinsic semiconductor in the dark and under illumination. In thermal equilibrium (dark), a single Fermi level describes the electron and hole populations. Under illumination, separate quasi-Fermi levels for electrons ($E_{F,n}$) and holes ($E_{F,p}$) are established, reflecting non-equilibrium carrier populations. The energy separation between these quasi-Fermi levels defines quasi-Fermi level splitting.

Where q is the elementary charge, and V is the photovoltage.[6] The QFLS therefore provides a direct measure of non-equilibrium carrier populations under illumination and sets an upper limit to the voltage that may be obtained under open-circuit conditions, commonly referred to as the open-circuit voltage (V_{OC}).[6]

Photocurrent generation, however, arises from the generation of electron-hole pairs and their subsequent transport to device contacts.[3] When an illuminated semiconductor is connected to an external circuit, photogenerated carriers can be extracted through this circuit, giving rise to a measurable current known as the photocurrent. Photocurrent extraction, therefore, relies on the presence of interfaces between the semiconducting layer and the external circuit that allow electrons and holes to be collected separately.[3] The nature of these interfaces and their role in establishing internal electric fields and energy-band alignment are now considered.

2.1.3 Semiconductor Interfaces and Band Bending

Efficient operation of solar cells requires that photogenerated charge carriers be separated and extracted at the device contacts. This process occurs at interfaces between the semiconducting absorber and the surrounding transport layers or electrodes. When materials with different electronic energy levels come into contact, charge redistribution occurs until electrochemical equilibrium is established. This redistribution generates internal electric fields and bends the electronic energy bands near the interface. Understanding how these effects arise is essential for describing charge separation and extraction in semiconductor devices.[3]

When a metal and a semiconductor are brought into contact, an interface forms between them.[7] Before contact, each material is characterised by its own Fermi level, reflecting its equilibrium carrier population. In a metal, the Fermi level is equal to the work function (ϕ), which is defined as the energy required to remove an electron from the Fermi level to the vacuum level (E_{vac}).[3] Upon contact, the difference in the materials' work functions leads to a mismatch in chemical potential.[8] Charge is transferred across the interface until the Fermi levels align, establishing thermal equilibrium.

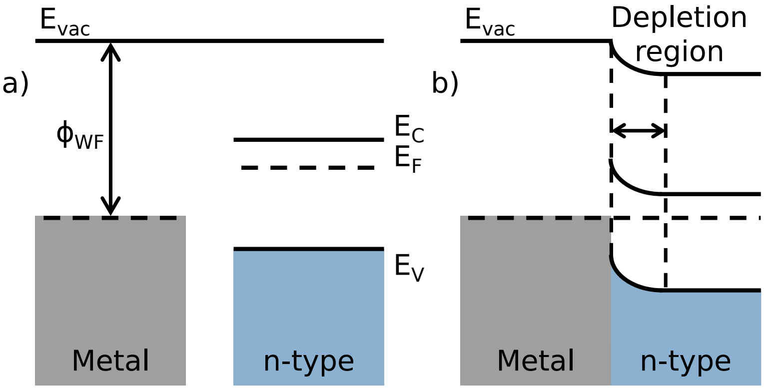

Figure 2.3: Schematic energy band diagrams illustrating the formation of a metal-semiconductor contact. a) Before contact, the metal and n-type semiconductor are characterised by their different Fermi levels, reflecting a mismatch in chemical potential. The metal's work function (ϕ) is also highlighted. b) Upon contact, charge is transferred across the interface until the Fermi levels align and thermal equilibrium is reached. The redistribution of charge results in the formation of a depletion region within the semiconductor and an associated bending of the energy bands near the interface. Adapted from Ref. [7]. Copyright 2012 American Chemical Society.

An illustrative example is shown in Figure 2.3, where an n-type semiconductor is brought into contact with a metal whose chemical potential lies at a lower energy, corresponding to a larger work function. Upon contact, electrons flow from the semiconductor into the metal to equalise the Fermi levels and establish thermal equilibrium. As electrons are removed from the semiconductor near the interface, a region depleted of mobile charge forms.[7] This region, known as the space-charge region or depletion region, contains fixed ionised donor atoms and generates an internal electric field within the semiconductor. The presence of this internal electric field leads to a spatial variation in the electrostatic potential, resulting in an upward bending of the conduction and valence bands near the interface. This band bending reflects the redistribution of charge required to balance the difference in chemical potential between the metal and semiconductor.[7] The resulting band bending and internal electric field determine whether charge carriers can be efficiently extracted across the interface.

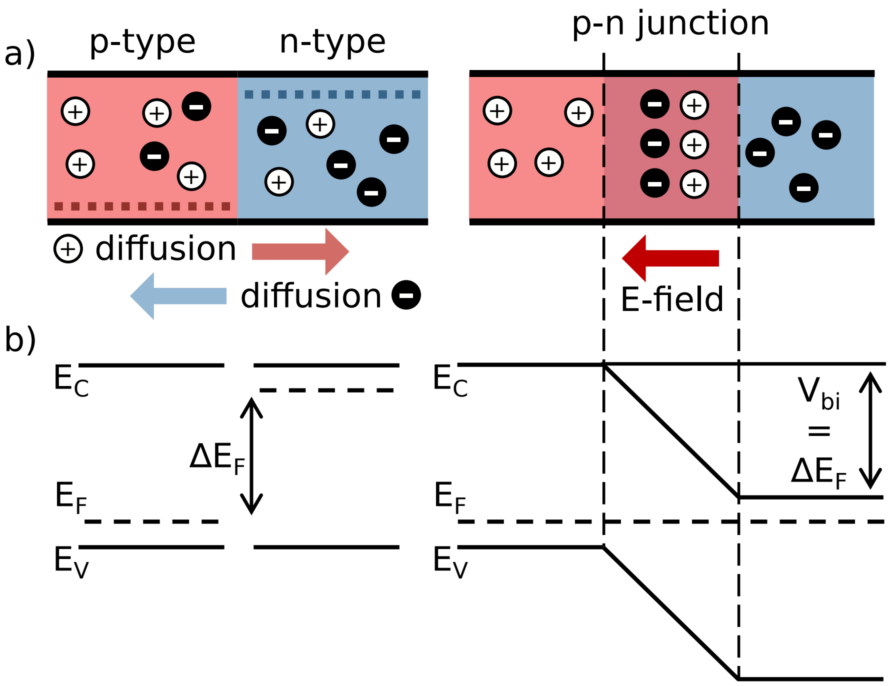

Figure 2.4: Formation of a p-n junction and the associated built-in potential. a) Upon contact, electrons diffuse from the n-type region to the p-type region, and hole diffusion occurs in the opposite direction due to a carrier concentration gradient. This results in charge accumulation near the interface and the formation of an internal electric field that opposes further diffusion. b) Corresponding energy band diagrams before and after contact. Initially, the p-type and n-type materials have different Fermi levels. After contact and carrier diffusion, equilibrium is reached, and the Fermi level becomes uniform across the junction. This gives rise to band bending and a built-in potential (V_{bi}) which is equal to the initial Fermi level difference (ΔE_F).

The same principles apply when two semiconductors with different carrier concentrations are brought into contact, as shown in Figure 2.4. Prior to contact, each semiconductor is characterised by its own Fermi level, determined by its doping type and carrier density. When the two materials meet, charge is transferred across the interface until the Fermi levels align and thermal equilibrium is established.[7] In the case of a junction formed between an n-type and p-type semiconductor, electrons diffuse from the n-type region into the p-type region, while holes diffuse in the opposite direction, as shown in Figure 2.4a.[1] This redistribution of charge again creates a space charge region; however, this time on both sides of the junction. The resulting charge separation generates an internal electric field that opposes further carrier diffusion.[3]

---

[1] This is, of course, with the simple assumption that p-type material has a lower chemical potential and therefore a greater work function than the n-type material. i.e. the Fermi level of the p-type material is lower in energy than that of the n-type material.

As in the metal-semiconductor case, the presence of this internal electric field leads to a spatial variation in the electrostatic potential, which results in band bending near the junction. In a semiconductor-semiconductor junction, however, band bending occurs across both materials, giving rise to a built-in potential (V_{bi}), as shown in Figure 2.4b.[3] In classical photovoltaics, this built-in field plays a central role in separating photogenerated charge carriers and directing them towards their respective contacts. The V_{bi} represents the electrostatic potential difference across the space charge region at equilibrium. This V_{bi} arises from the difference in chemical potential between the two semiconductors prior to contact and can be expressed in terms of their work functions as[8]:

$$V_{\mathrm{bi}} = \Delta\phi = W_p - W_n \tag{2.3}$$

Here, W_p and W_n denote the work functions of the p-type and n-type materials, respectively, and their difference $\Delta\phi$ defines the built-in potential V_{bi}.[8] Physically, this potential reflects the energy difference that must be balanced through charge redistribution when the two materials are brought into contact.

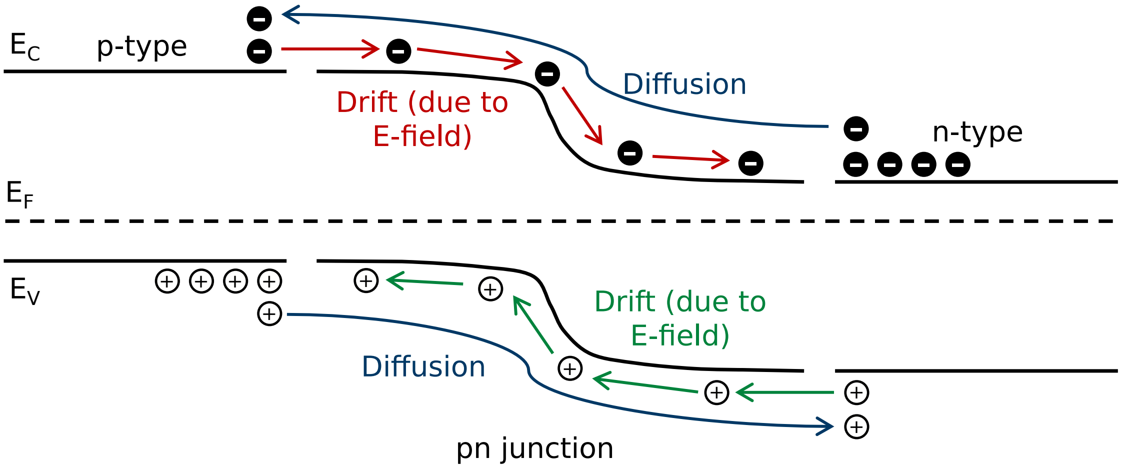

Figure 2.5: Schematic representation of carrier transport mechanisms within a pn junction at thermal equilibrium. The built-in electric field, which points from the n-type side towards the p-type side, drives electrons and holes to drift in opposite directions. This drift current exactly balances the opposing diffusion current arising from carrier concentration gradients, resulting in a net zero current across the junction under equilibrium and in the dark.

Within the space charge region of a semiconductor-semiconductor junction, the built-in electric field associated with band bending provides a driving force for charge separation.[3] The field points from the n-type to the p-type side, with the field originating from the positively charged donors on the n-type side and the negatively charged acceptors on the p-type side. Due to this built-in field, electrons are driven towards the n-type side, while holes are driven towards the p-type side. Carrier motion in this region is therefore governed by two competing processes: diffusion driven by carrier concentration gradients, and drift driven by the internal electric field arising from the built-in potential.[3] At thermal equilibrium, the drift current driven by the built-in electric field exactly balances the diffusion current driven by carrier concentration gradients, resulting in a net current of zero across the junction. This process is schematically illustrated in Figure 2.5.

When an external voltage is applied across a semiconductor junction, such as the pn junction described, the internal potential is modified.[1] Under forward bias, the applied voltage reduces the built-in potential and narrows the space-charge region, lowering the energetic barrier to carrier transport across the junction. This increases carrier injection and increases the net current flowing through the device. In contrast, under reverse bias, the applied voltage increases the built-in potential and widens the space charge region, further hindering carrier transport.[1] These bias-dependent changes in the internal electric field underlie current-voltage measurements and are central to the characterisation of photovoltaic devices.

Although junctions and built-in electric fields promote charge separation and extraction, photogenerated charge carriers may recombine before reaching the contacts, limiting device performance. The mechanisms by which charge can be lost in a photovoltaic device are now considered.

2.1.4 Recombination Pathways

The performance of a photovoltaic device ultimately depends on how efficiently photo-generated charge carriers can be collected at the device contacts. However, not all carriers contribute to useful electrical output. Electrons and holes may recombine before they are extracted, reducing both the photocurrent and the achievable photovoltage. Recombination, therefore, represents a fundamental loss mechanism in semiconductor devices and plays a central role in determining overall device performance.[3]

Recombination refers to the process by which an electron in the conduction band loses energy and returns to an available state in the valence band, by doing so annihilating a hole.[1] Recombination processes are commonly classified into two broad categories: radiative and non-radiative recombination. In radiative recombination, the energy released during electron-hole recombination is emitted as a photon via a direct band-to-band transition. While radiative recombination is a loss mechanism in solar cells, it is also directly related to light emission and underlies optoelectronic devices such as light-emitting diodes. This is an intrinsic process: the same electronic transitions that allow a material to absorb photons also permit it to emit photons. Radiative losses are, therefore, thermodynamically unavoidable in photovoltaic devices.[3] As a result, even an ideal solar cell with no defects must experience some degree of radiative recombination. These unavoidable losses set an upper limit on the maximum efficiency that a solar cell can achieve.[9] Schematic illustrations of the possible recombination pathways in semiconductors are shown in Figure 2.6.

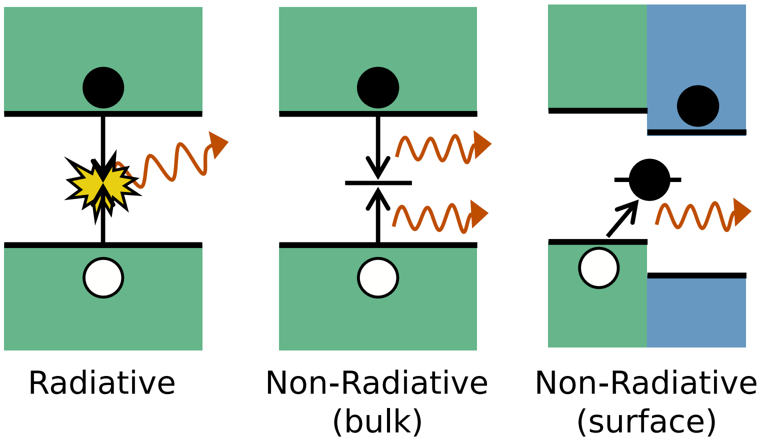

Figure 2.6: Schematic illustration of the dominant recombination pathways in semiconductors and photovoltaics. Radiative recombination occurs via a direct band-to-band transition, resulting in the emission of a photon. In contrast, non-radiative recombination proceeds via defect-mediated pathways, either in the bulk of the material or at surfaces and interfaces, where the energy released is dissipated without photon emission.

In contrast, non-radiative recombination involves the loss of electronic energy without the emission of a photon. Instead, the energy released during electron-hole recombination is transferred to the lattice in the form of vibrations (phonons).[3] Non-radiative recombination is typically mediated by defects or disorder that introduce electronic states within the band gap, enabling recombination to proceed via intermediate trap states rather than directly between the bands.[10]

Non-radiative recombination may occur both within the bulk of the semiconductor and at its surfaces or interfaces. At surfaces and interfaces, the density of recombination-active states is often significantly higher than in the bulk due to broken bonds, chemical mismatch, or incomplete passivation.[3] As a result, interfacial non-radiative recombination frequently represents a dominant loss pathway in photovoltaic devices. As recombination reduces the steady-state populations of photogenerated carriers, it directly limits the achievable quasi-Fermi level splitting and, therefore, the maximum photovoltage of a device.[6]

A widely used framework for describing defect-mediated non-radiative recombination is the Shockley–Read–Hall (SRH) model.[10, 11] In this model, recombination proceeds via trap states located within the band gap, which act as intermediate stepping stones between the conduction and valence bands. Electrons and holes are captured sequentially by these states, enabling recombination without photon emission. Unlike radiative recombination, non-radiative recombination is not an intrinsic consequence of light absorption and can, in principle, be reduced through materials and device engineering.[3] Strategies such as improving crystal quality, reducing defect densities, and passivating surfaces and interfaces are therefore central to suppressing non-radiative losses.

2.1.5 A Minimal Photovoltaic Device

To understand how photogenerated charge carriers produce a measurable electrical output, it is useful to consider a simplified photovoltaic device architecture that captures the essential physics of solar cell operation.

In its simplest form, a photovoltaic device may be represented as a semiconducting absorber layer contacted by two metallic electrodes.[2] In our scenario, we assume the absorber is intrinsic and that the metal contacts are characterised by different work functions, leading to an asymmetrical energy-level alignment at the two interfaces. When materials with different electronic energy levels come into contact, charge redistribution occurs until electrochemical equilibrium is established, resulting in band bending and an internal electric field within the semiconductor. This simplified model is shown in Figure 2.7.

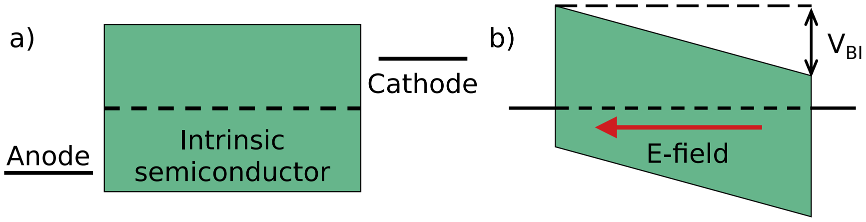

Figure 2.7: Schematic representation of a minimal photovoltaic device consisting of an intrinsic semiconductor absorber contacted by two metallic electrodes with different work functions. a) Before equilibrium, the asymmetric contacts define the energetic alignment at the interfaces. b) Following contact, charge redistribution gives rise to band bending within the absorber and establishes a built- in potential, resulting in an internal electric field.

---

[2] In fact, the first solar cell that adopted this form was in 1883, when Charles Fritts coated selenium with gold on top of a metal plate.[12]

This simplified model provides a valuable framework for understanding how key photovoltaic parameters are extracted under different operating conditions. Prior to contact, the materials are differentiated by their different work functions, as shown in Figure 2.7a. Upon contact, a built-in potential and an electric field are formed (Figure 2.7b) and in the dark and at equilibrium, a single Fermi level is maintained throughout the structure and no net current flows. Upon illumination, the photogenerated electron-hole pairs are driven towards the contacts by the internal electric field (electrons to the cathode and holes to the anode), as shown in Figure 2.8a. This also gives rise to quasi-Fermi levels.[3] When the device is connected to an external circuit under short-circuit conditions, the carriers are extracted as they reach the contacts.[3] This gives rise to a measurable current, known as the short-circuit current, I_{SC}. However, this is more commonly measured in terms of area, and is therefore referred to as the short-circuit current density J_{SC}.

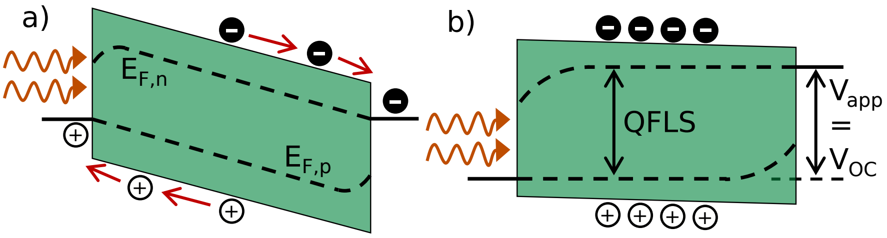

Figure 2.8: Schematic illustration of a photovoltaic device under illumination. a) Photogenerated electron-hole pairs are separated by the internal electric field, giving rise to distinct quasi-Fermi levels for electrons ($E_{F,n}$) and holes ($E_{F,p}$), within the absorber and a photocurrent is extracted. b) Under open-circuit conditions, no net current flows through the external circuit and photogenerated carriers accumulate within the device. The resulting quasi-Fermi level splitting reaches a maximum and therefore corresponds to the open-circuit voltage (V_{OC}).

Applying a positive bias to the anode reduces the electric field across the semiconductor. Here, the net current decreases as recombination increases, offsetting carrier extraction. Under open-circuit conditions, no net photogenerated current flows through the external circuit. In this case, the generated carriers accumulate within the absorber. Thus, the separation between the quasi-Fermi levels of electrons and holes reaches a maximum, giving rise to the V_{OC}. This is described schematically in Figure 2.8b. The V_{OC} lies at the balance between generated carrier lifetimes and recombination rates.[3]

At applied voltages between the short-circuit and open-circuit conditions lies an operating point at which the product of the current and voltage outputs is maximised.[6] This point is known as the maximum power point (MPP) and defines the condition in which the device delivers the greatest electrical power to an external load. By sweeping across a range of voltages, we build the characteristic current density–voltage (J–V) curve, which provides clear insights into device performance. A typical J–V curve of a photovoltaic device is shown in Figure 2.9.

We now know how current and voltage are generated and can be extracted; however, to determine the power conversion efficiency (i.e. how much sunlight is converted into electrical power), the shape of the J–V curve must be considered. We have identified how to extract three key parameters: the V_{OC}, J_{SC}, and MPP. The remaining quantity, fill factor (FF), describes how closely the J–V curve approaches the ideal rectangle that would be obtained for a loss-free device. The FF is defined as the ratio of the power produced at the MPP to the product of the J_{SC} and V_{OC}, as illustrated in Figure 2.9.[6]

Using these quantities, the power conversion efficiency, η, is defined as:

$$\eta = \frac{J_{\mathrm{SC}} V_{\mathrm{OC}} \mathrm{FF}}{P_{\mathrm{in}}} \tag{2.4}$$

Here, P_{in} is the incident optical power density. The PCE, therefore, provides a metric that reflects the balance between charge generation, extraction, and recombination.

To allow for meaningful comparison between different PV devices, performance is measured under standardised conditions. This typically corresponds to the AM1.5G solar spectrum, an approximation of the incident sunlight at Earth's surface. Under these conditions, the incident power density is defined as $P_{\mathrm{in}} = 100\,\mathrm{mW\,cm^{-2}}$, allowing efficiency values reported across different studies to be compared.[13]

In this simplified model, the metal contacts are assumed to be perfectly charge-selective, such that electrons are extracted exclusively at the cathode and holes at the anode. In practice, however, this would not be the case. Instead, charge carriers of both types may reach either contact, increasing interfacial recombination and reducing device performance. To mitigate these losses, practical PV devices employ dedicated charge-selective transport layers.[6]

2.1.6 Charge Selective Contacts

Efficient photovoltaic operation requires that photo-generated electrons and holes are extracted from the absorber and delivered to the external circuit without recombining. To achieve this, modern solar cells employ charge-selective contacts that preferentially extract one type of charge carrier while blocking the other.[3]

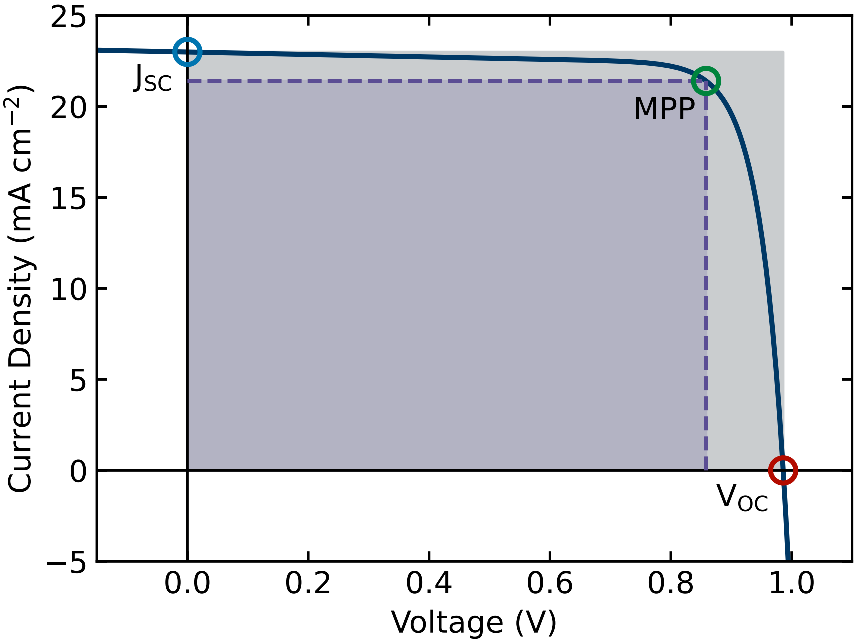

Figure 2.9: Schematic illustration of a current density-voltage J–V curve of a photovoltaic device under illumination, illustrating key performance parameters (Data is fabricated and not from a real device). The short-circuit current density, J_{SC}, is defined at zero applied voltage, while the open-circuit voltage, V_{OC}, corresponds to zero net current. The maximum power point MPP defines the operating condition at which the product of the current density and voltage is maximised. The shaded rectangle highlights the ideal power output J_{SC} x V_{OC}, with the fill factor describing how much the J–V curve approaches the ideal limit.

This selectivity for either electrons or holes is achieved through a combination of favourable energy-level alignment and the formation of energetic barriers that inhibit minority-carrier transport.[6] In conventional semiconductor devices, such selectivity is often realised through controlled doping of transport layers, which shifts the Fermi level and creates regions that preferentially conduct either electrons or holes. In many emerging photovoltaic technologies, including metal-halide perovskite solar cells, selectivity is additionally achieved through the use of dedicated electron- and hole-transport layers that perform a similar function through band alignment and interfacial energetics. In addition to controlling carrier extraction, charge-selective contacts are also used to improve the quality of the semiconductor interface.[3] By engineering interfaces with lower trap-state densities, trap-mediated recombination can be suppressed. Reducing interfacial recombination allows the device to sustain a larger quasi-Fermi-level splitting under illumination and therefore improves the achievable photovoltage.[6]

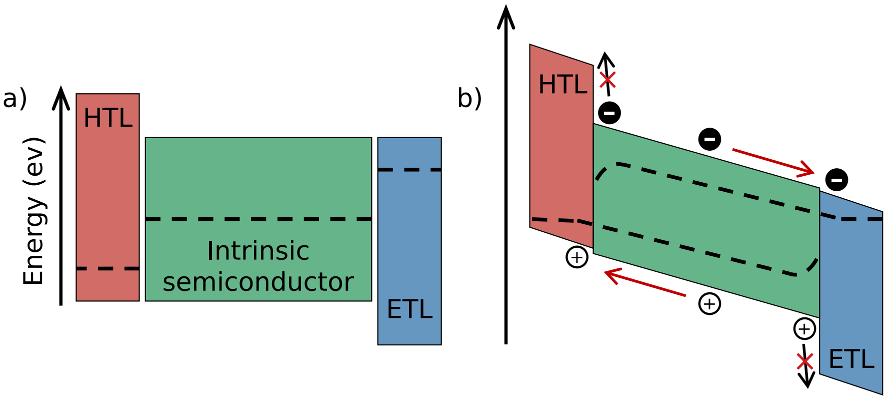

Figure 2.10: Schematic illustration of charge selective contacts in a full p–i–n photovoltaic device. a) Conceptual energy level alignment illustrating the selection of hole- and electron-transport layers with Fermi levels and band-edge positions chosen to promote favourable energetic alignment for selective charge extraction. b) Under operating conditions, the energetic alignment enables electrons to be selectively extracted into the electron transport layer (ETL) and holes into the hole transport layer (HTL). In contrast, energetic barriers suppress minority-carrier transport, thereby reducing surface recombination.

A charge-selective contact must present a low energy barrier to the extraction of the desired carrier type while simultaneously introducing an energy barrier that suppresses transport of the opposite carrier.[6] This promotes directional charge flow and reduces interfacial recombination rates. From an energy-band perspective, this selectivity can be understood in terms of band alignment and band bending at the interface. For an electron-selective contact, also known as an electron transport layer (ETL), the conduction band of the transport layer is favourably aligned with the conduction band of the absorber, allowing efficient electron extraction, as illustrated in Figure 2.10. At the same time, a large energetic offset exists between the valence band of the absorber and the valence band of the ETL, inhibiting hole transport. An analogous situation applies for a hole-selective contact (hole transport layer (HTL)), where favourable alignment with the valence band enables hole extraction while blocking electrons.

When an intrinsic absorber layer is placed between electron- and hole-selective contacts, the device architecture is commonly described as n–i–p (“regular”) or p–i–n (“inverted”), depending on the order of layer deposition.[3] By selectively extracting one carrier type while suppressing minority-carrier transport, charge-selective transport layers improve both photocurrent extraction and the achievable quasi-Fermi-level splitting, thereby enhancing device efficiency.[3] This concept is schematically illustrated in Figure 2.10b.

The principles outlined in this section provide a general framework for understanding photovoltaic device operation. However, metal-halide perovskite solar cells exhibit several material-specific properties that deviate from the conventional picture. These properties and their implications are considered in the following section.

2.2 Fundamental Device Physics of Perovskite Solar Cells

Metal-halide perovskite solar cells have emerged as one of the most promising photovoltaic technologies of recent decades, owing to their rapid improvements in power conversion efficiency and their compatibility with low-temperature, solution-based processing methods.[14, 15] From a device physics perspective, PSCs share many similarities with conventional semiconductor photovoltaics. Charge generation, transport, and recombination all play central roles in determining device performance, and the general framework established in the preceding sections is broadly applicable. However, metal-halide perovskites also exhibit several distinctive material properties that set them apart from classical semiconductors, including soft ionic lattices, mixed ionic-electronic conductivity, and defect-tolerant behaviour.[16–18]

As a result, while PSCs can often be described using established semiconductor concepts, their operational behaviour cannot always be fully captured by traditional models alone. This section, therefore, introduces the fundamental materials properties and device physics specific to metal-halide perovskites, providing the necessary background for understanding how these materials deviate from, and in some cases extend, the conventional photovoltaic framework.

---

[3] Interestingly, this convention is opposite to that used in organic photovoltaics, where p–i–n structures were historically referred to as the “regular” architecture and n–i–p devices as “inverted”. The perovskite community inherited the terminology despite the reversed layer ordering.

2.2.1 Structure and Defect Chemistry of Metal-Halide Perovskites

The electronic properties and defect behaviour of metal-halide perovskites are strongly governed by their underlying crystal structure. Understanding this structure is therefore essential for explaining the unusual optoelectronic properties that make these materials attractive for photovoltaic applications. Metal-halide perovskites used in most solar cells adopt the ABX_3 crystal structure.[19] In this structure, the B-site cation is coordinated by six halide ions, forming a network of corner-sharing BX_6 octahedra, while the A-site cation occupies the space between these octahedra, as illustrated in Figure 2.11a.

This structure provides a flexible framework that allows a wide range of chemical compositions and, therefore, extensive tuning of optical and electronic properties.[20, 21] By varying the species occupying each lattice site, semiconductors with band gaps spanning approximately 1.2–3 eV can be realised, as shown in Figure 2.11b.[22] In this thesis, the focus is placed on hybrid lead-halide perovskites with band gaps of approximately 1.6 eV. These materials comprise a mixture of organic and inorganic ions and have demonstrated exceptionally high power conversion efficiencies in recent years.[14, 23]

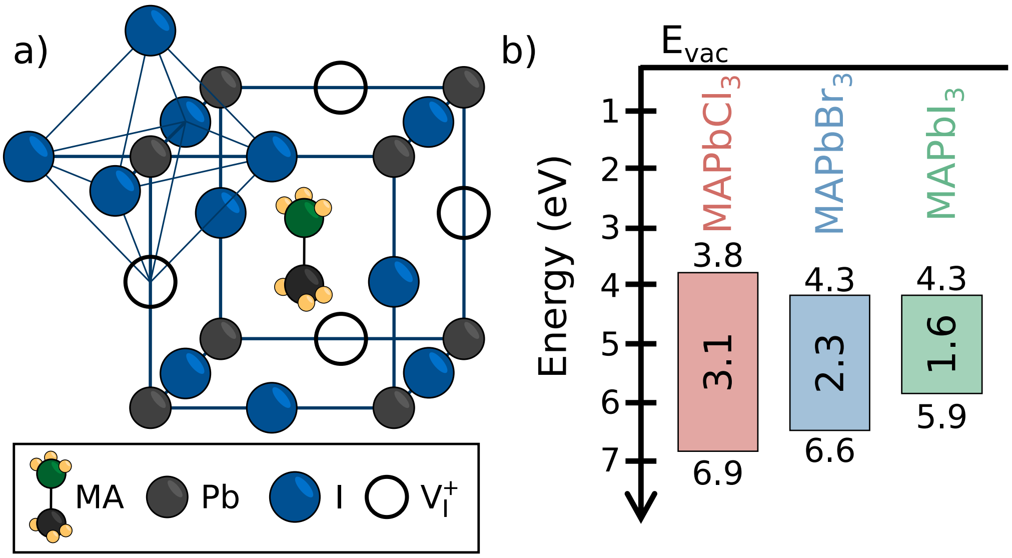

Figure 2.11: a) Schematic illustration of the crystal structure of methylammonium lead iodide (MAPI), illustrating the ABX_3 perovskite structure composed of corner-sharing PbI_6 octahedra and the presence of intrinsic point defects such as halide vacancies (V_I^+). b) Comparison of the band gap energies of methylammonium lead halide perovskites with different halide compositions ($MAPbCl_3$, $MAPbBr_3$, and $MAPbI_3$), highlighting the compositional tunability of the electronic structure in lead-halide perovskites. Adapted from ref. [24] (CC BY).

A defining feature of lead halide perovskites is the relatively soft and polar nature of their ionic lattice[4].[25, 26] In contrast to conventional covalent semiconductors such as silicon, the bonding in perovskites is largely ionic, leading to lower lattice stiffness and greater structural flexibility. An important consequence of this soft lattice is the ease with which point defects can form within the crystal structure.[27–29] The presence of defects is an intrinsic feature of the perovskite crystal. The most common intrinsic defects in lead halide perovskites include vacancies and interstitials that arise during crystallisation.[30, 31] Under typical processing conditions, halide vacancies are often predicted to have particularly low formation energies, making them quite abundant in the lattice, as shown in Figure 2.11a.[27, 32] Despite this high defect density, lead halide perovskites can exhibit long carrier lifetimes and reasonably low non-radiative recombination rates, a behaviour commonly referred to as defect tolerance.[18, 33, 34] This defect tolerance is commonly attributed to the fact that many intrinsic defects introduce shallow states near the band edge rather than deep mid-gap states, thereby limiting their impact on non-radiative recombination.

Importantly, the ionic nature of the defects has significant implications for device operation.[16] The combination of a soft ionic lattice and a high defect density distinguishes perovskites from typical inorganic semiconductors. Of particular interest is the ability of certain defect species to redistribute under applied electric fields or illumination, thereby driving ionic motion within the device.[35] This ionic motion underpins the entire framework of this thesis and is discussed in the following section.

2.2.2 Mobile Ions and Ionic Transport in Perovskites

The operation of metal-halide perovskite solar cells is strongly influenced by the presence of mobile ionic defects within the crystal lattice. Ionic motion can modify internal electric fields, alter band bending at interfaces, and lead to time-dependent device behaviour that is not observed in conventional semiconductors. The presence of mobile ionic species in lead-halide perovskites was recognised early in their development, when observations of unusual device phenomena, including current–voltage hysteresis and slow transient responses, led Snaith *et al.* to suggest that ionic motion plays a critical role in perovskite solar cells.[36]

---

[4] This was once described during a conference as being akin to a jelly-like substance.

This hypothesis has since been supported by a combination of first-principles calculations and device experiments, and ionic transport is now widely accepted as an intrinsic property of hybrid lead-halide perovskites.[37–42] During crystallisation, a variety of point defects can form within the perovskite lattice. In addition to influencing the material's electronic properties, some of these defects are sufficiently mobile to migrate through the crystal under the influence of electric fields or concentration gradients.

During crystallisation, a range of point defects can form within the perovskite lattice, including vacancies on the halide, A-site cation, and B-site cation positions.[16] As shown in Figure 2.12, to move around the lattice, defects, and/or ions need to overcome an energetic barrier and therefore require a certain activation energy.[16, 42] Focusing on activation energies that have been calculated for the most widely studied perovskite composition, methylammonium lead iodide (MAPI), it is found that halides and halide vacancies have the lowest activation energy (~ 0.2–0.4 eV) compared to the other material constituents, as summarised in Table 2.1.[16]

Table 2.1: Representative activation energies for the migration of ionic defects in lead halide perovskites, as reported in the literature. A range of values is provided due to the different migration directions.

Migrating species	Activation energy (eV)	Ref.
V_I^+ (iodide vacancy)	0.2–0.4	[32, 43]
I^- (iodide ion)	0.2–0.3	[32, 43]
V_MA^- (A-site vacancy)	0.5–0.9	[42, 43]
MA^+ (A-site cation)	0.4–0.5	[32]
V_Pb^{2-} (B-site vacancy)	$\gtrsim 2.0$	[16]

Ionic motion in lead halide perovskites is commonly described by a vacancy-mediated hopping mechanism, in which an ion moves between neighbouring lattice sites through the occupation of a vacant site.[16, 44] An example of how this can occur for each constituent atom in MAPI is shown in Figure 2.12. Perovskite materials used in solar cells are typically polycrystalline thin films, and research suggests that ion migration can also occur through grain boundaries and interfaces.[44, 45] The reduced coordination and strain at the grain boundaries may lower the energy required for migration relative to the bulk. Regardless of the exact mechanism, ion migration results in a highly non-uniform distribution of ionic charge in operating devices, with significant implications for device stability and energetics.[44] However, it is important to note the timescales of ionic motion and why they affect traditional measurement techniques.

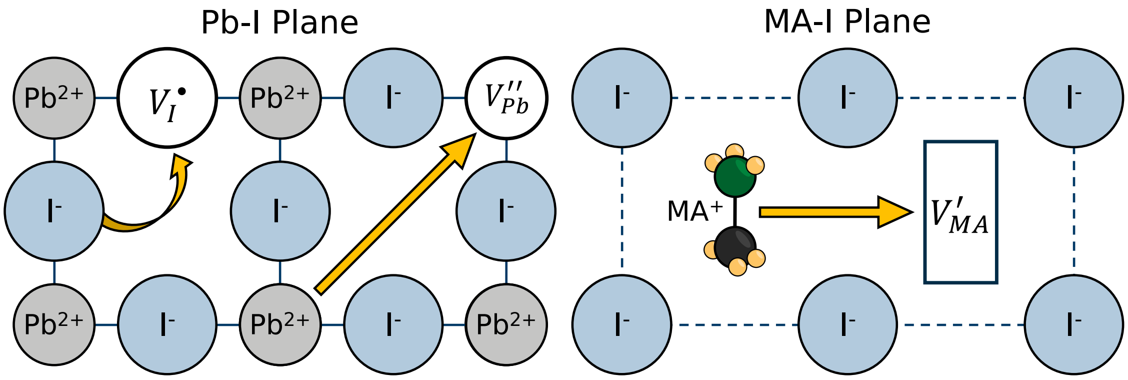

Figure 2.12: Schematic illustration of vacancy-mediated ionic transport in a lead halide perovskite (specifically, MAPI) lattice. In the Pb–I plane, iodide ions migrate through successive hopping into neighbouring halide vacancies ($V_I^\bullet$), which allows for the vacancy to move. The same can occur in this plane for the Pb^{2+} cation, where it moves to occupy a lead vacancy (V''_{Pb}); however, this requires a large activation energy. In the MA-I plane, A-site cations can also migrate via a vacancy-mediated hopping into A-site vacancies (V'_{MA}), but again with typically higher activation energies. Adapted from ref. [16] under a Creative Commons CC BY 4.0 licence.

The large difference in timescales between electronic and ionic processes is a defining feature of lead halide perovskites. While electronic charge carriers respond to changes in illumination or applied bias on nanosecond to microsecond timescales, the redistribution of mobile ions typically occurs over much longer timescales, ranging from milliseconds to seconds or even minutes depending on temperature and composition.[46] As a result, the internal electric field in a perovskite solar cell is not considered static during operation. The difference in response times explains the transient, history-dependent behaviour observed in perovskite solar cells. Although ionic motion occurs at the atomic scale, its consequences are most clearly observed at the device level. As mentioned, the redistribution of mobile ions under bias or illumination modifies internal electric fields and, therefore, band bending. These effects play a central role in electric-field screening and in the current-voltage hysteresis phenomenon.

2.2.3 Consequences of Ionic Motion: Field Screening and J–V Hysteresis

The presence of mobile ions in metal-halide perovskites can significantly alter the internal electric fields within a photovoltaic device. As these ions redistribute under applied bias or illumination, they partially screen the built-in electric field and modify the electrostatic potential across the absorber layer. This dynamic redistribution can lead to time-dependent device behaviour, one manifestation of which is the commonly observed J–V hysteresis in perovskite solar cells.

J–V hysteresis refers to a discrepancy in the measured current density–voltage that depends on the direction and rate of the applied voltage sweep.[40] This behaviour is in stark contrast to conventional photovoltaic devices, where the J–V response is largely independent of measurement history. To understand the origin of this phenomenon, it is first necessary to consider how mobile ionic charge can screen internal electric fields within the device.

Electric-field screening in lead halide perovskites is best explained by extending the simple device model introduced in section 2.1.5. The built-in potential in this model arises from the difference in work functions between the contacts on either side of the absorber. This potential gives rise to an electric field with a fixed direction and magnitude, determined by the energetic alignment of the interfaces. If we now consider the intrinsic absorber to be a lead-halide perovskite containing a mobile ionic species, the picture changes.

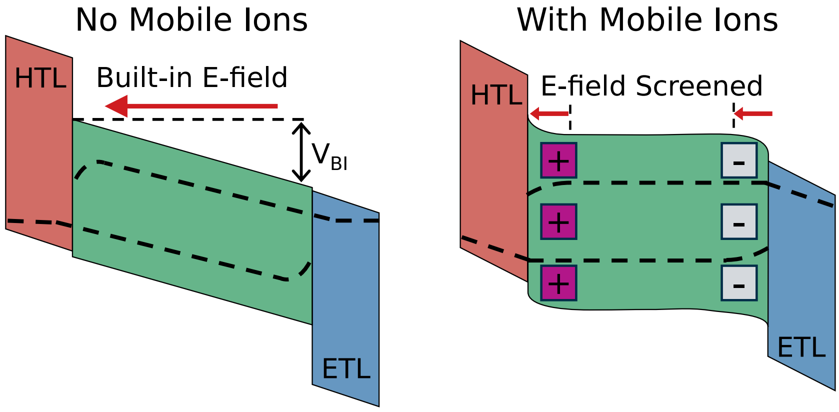

Figure 2.13: Schematic illustration of ionic field screening in a perovskite solar cell. In the absence of mobile ions, an internal electric field arises from the built-in potential gradient due to asymmetric contacts. When mobile ions are present, redistribution occurs, with positive cations (halide vacancies) travelling in the direction of the electric field and negative anions (halide ions) travelling against it. This results in ion-induced electric-field screening, in which the internal electric field is diminished in the bulk and confined to the interfaces. Adapted from ref. [16] under a Creative Commons CC BY 4.0 licence.

In addition to electronic charge carriers, the perovskite contains charged ionic defects that will respond to the established internal electric field.[16, 35] Here, for simplicity, we will consider our mobile ionic charge to consist only of halide vacancies (positively charged) and halide anions (negatively charged). In the device model, the p–i–n device has an electric field pointing from the n-type to the p-type side, as shown in Figure 2.13. Placing a negatively charged mobile halide anion in this region forces the anion to respond to the internal electric field. Here, the anion (negatively charged) will go against the direction of the electric field, and the positively charged vacancy will travel in the direction of the electric field. The response of the ionic charge reduces the strength of the internal electric field, a phenomenon known as electric-field screening.[16] If there is sufficient ionic charge, the internal electric field can be almost entirely screened, thus reducing its effectiveness to occur only at the interfaces. This is schematically described in Figure 2.13b.

It is now necessary to consider why electric-field screening affects J–V sweeps and leads to hysteresis. When a bias is applied to a device, an external electric field is superimposed on the internal field.[16, 35] This will cause the mobile ionic charge to redistribute again to screen the total electric field. As this redistribution is governed by ionic motion, it occurs on timescales much slower than those of electronic charge transport.[37] If the voltage is swept rapidly, the ionic distribution will not reach an 'equilibrium' position, resulting in a different electrostatic profile within the absorber than would be attained at steady-state conditions.[36] The history-dependent redistribution of ionic charge directly affects the electronic charge distribution and extraction.

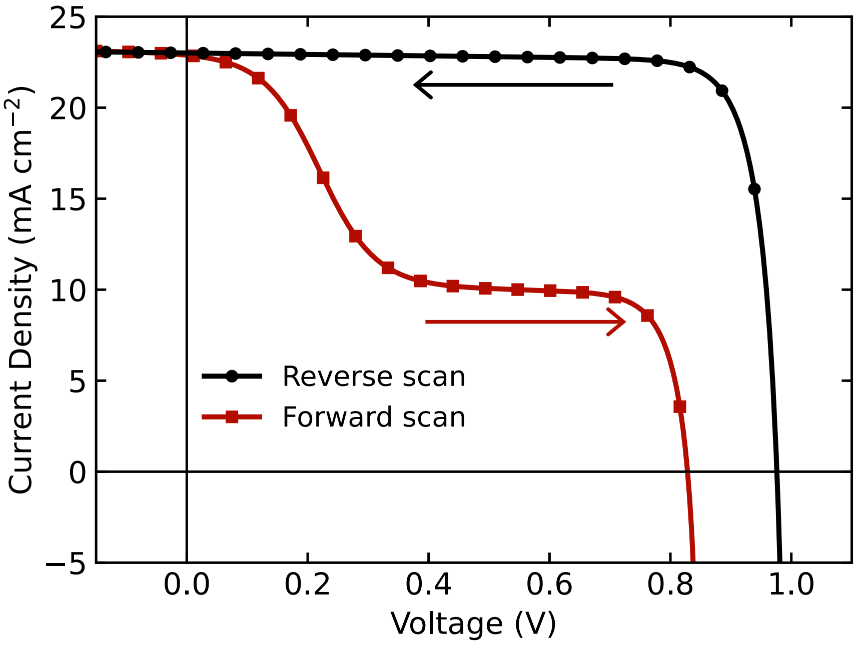

Figure 2.14: Representative current density-voltage (J–V) characteristics of a perovskite solar cell measured under forward and reverse sweeps, illustrating hysteresis in the device response (data fabricated by the author to illustrate hysteresis). The dependence of the measured J–V curve on scan direction reflects the slow redistribution of mobile ions relative to electronic charge, resulting in different internal electric fields at a given applied voltage.

One of the major impacts of electric field screening is the reduction of the internal electric field and potential gradient, which, in the case of no mobile ions, promotes charge extraction.[16, 47] In perovskite solar cells, as this internal driving force is reduced, charge extraction is much more reliant on diffusion rather than drift.[48–50]

This is overcome due to the long carrier lifetimes and diffusion lengths, which far exceed the thickness of most perovskites used in solar cells.[33, 50] However, this increased reliance on diffusion rather than drift can increase recombination losses, particularly near device interfaces, thereby reducing the extracted current.

In a traditional J–V measurement of a perovskite solar cell, these effects result in hysteresis.[36] Forward and reverse voltage sweeps measure the device under different internal electrostatic fields, even for the same applied voltage, due to differences in the ionic distribution.[16] This phenomenon is shown in Figure 2.14. As a result, the measured current density depends on scan direction, scan rate, and any preconditioning bias applied before the measurement.[51] Importantly, hysteresis arises naturally from the interplay between slow ionic motion and fast electronic transport.

Ionic motion in perovskite solar cells is the key theme throughout this thesis. In the chapters to follow, we explore how we can control ionic motion and use it to extract vital information from the devices. Furthermore, the true impact that a mobile ionic species has on device efficiency is unravelled.

References

(1) Neil W. Ashcroft; N. David Mermin, *Solid State Physics*, 1976.

(2) Charles Kittel, *Introduction to Solid State Physics*, 8th ed.; Wiley: 2004.

(3) Jenny Nelson, *The Physics of Solar Cells*, 2003.

(4) Shah, A. V.; Schade, H.; Vanecek, M.; Meier, J.; Vallat-Sauvain, E.; Wyrsch, N.; Kroll, U.; Droz, C.; Bailat, J. *Progress in Photovoltaics: Research and Applications* **2004**, *12*, 113–142.

(5) Rühle, S. *Solar Energy* **2016**, *130*, 139–147.

(6) Peter Würfel, *Physics of solar cells*, 2005.

(7) Zhang, Z.; Yates, J. T. *Chemical Reviews* **2012**, *112*, 5520–5551.

(8) Kwok Kwok Ng; Simon Sze, *Physics of Semiconductor Devices*, 2008.

(9) Shockley, W.; Queisser, H. J. *Journal of Applied Physics* **1961**, *32*, 510–519.

(10) Shockley, W.; Read, W. T. *Physical Review* **1952**, *87*, 835–842.

(11) Hall, R. N. *Physical Review* **1952**, *87*, 387–387.

(12) Marques Lameirinhas, R. A.; Torres, J. P. N.; de Melo Cunha, J. P. *Energies* **2022**, *15*, 1823.

(13) Antonio Luque; Steven Hegedus, *Handbook of Photovoltaic Science and Engineering*, 2002.

(14) NREL, Best Research-Cell Efficiency Chart, `https://www.nrel.gov/pv/cell-efficiency`.

(15) Green, M. A.; Ho-Baillie, A.; Snaith, H. J. *Nature Photonics* **2014**, *8*, 506–514.

(16) Eames, C.; Frost, J. M.; Barnes, P. R. F.; O'Regan, B. C.; Walsh, A.; Islam, M. S. *Nature Communications* **2015**, *6*, 7497.

(17) Guo, Z.; Wang, J.; Yin, W.-J. *Energy & Environmental Science* **2022**, *15*, 660–671.

(18) Steirer, K. X.; Schulz, P.; Teeter, G.; Stevanovic, V.; Yang, M.; Zhu, K.; Berry, J. J. *ACS Energy Letters* **2016**, *1*, 360–366.

(19) Kojima, A.; Teshima, K.; Shirai, Y.; Miyasaka, T. *Journal of the American Chemical Society* **2009**, *131*, 6050–6051.

(20) Brivio, F.; Walker, A. B.; Walsh, A. *APL Materials* **2013**, *1*, 042111.

(21) Gebhardt, J.; Rappe, A. M. *Advanced Materials* **2019**, *31*, 1802697.

(22) Tao, S.; Schmidt, I.; Brocks, G.; Jiang, J.; Tranca, I.; Meerholz, K.; Olthof, S. *Nature Communications* **2019**, *10*, 2560.

(23) Kim, J. Y.; Lee, J.-W.; Jung, H. S.; Shin, H.; Park, N.-G. *Chemical Reviews* **2020**, *120*, 7867–7918.

(24) Tewari, N.; Lam, D.; Li, C. H. A.; Halpert, J. E. *APL Materials* **2022**, *10*, 040905.

(25) Frost, J. M.; Walsh, A. *Accounts of Chemical Research* **2016**, *49*, 528–535.

(26) Brenner, T. M.; Egger, D. A.; Kronik, L.; Hodes, G.; Cahen, D. *Nature Reviews Materials* **2016**, *1*, 15007.

(27) Walsh, A.; Scanlon, D. O.; Chen, S.; Gong, X. G.; Wei, S.-H. *Angewandte Chemie International Edition* **2015**, *54*, 1791–1794.

(28) Yin, W.-J.; Shi, T.; Yan, Y. *Applied Physics Letters* **2014**, *104*, 063903.

(29) Ball, J. M.; Petrozza, A. *Nature Energy* **2016**, *1*, 16149.

(30) Meggiolaro, D.; De Angelis, F. *ACS Energy Letters* **2018**, *3*, 2206–2222.

(31) Meggiolaro, D.; Mosconi, E.; De Angelis, F. *ACS Energy Letters* **2019**, *4*, 779–785.

(32) Yang, D.; Ming, W.; Shi, H.; Zhang, L.; Du, M.-H. *Chemistry of Materials* **2016**, *28*, 4349–4357.

(33) deQuilettes, D. W.; Frohna, K.; Emin, D.; Kirchartz, T.; Bulovic, V.; Ginger, D. S.; Stranks, S. D. *Chemical Reviews* **2019**, *119*, 11007–11019.

(34) Johnston, M. B.; Herz, L. M. *Accounts of Chemical Research* **2016**, *49*, 146–154.

(35) Moia, D.; Gelmetti, I.; Calado, P.; Hu, Y.; Li, X.; Docampo, P.; de Mello, J.; Maier, J.; Nelson, J.; Barnes, P. R. F. *Physical Review Applied* **2022**, *18*, 044056.

(36) Snaith, H. J.; Abate, A.; Ball, J. M.; Eperon, G. E.; Leijtens, T.; Noel, N. K.; Stranks, S. D.; Wang, J. T.-W.; Wojciechowski, K.; Zhang, W. *The Journal of Physical Chemistry Letters* **2014**, *5*, 1511–1515.

(37) Calado, P.; Telford, A. M.; Bryant, D.; Li, X.; Nelson, J.; O'Regan, B. C.; Barnes, P. R. *Nature Communications* **2016**, *7*, 13831.

(38) Richardson, G.; O'Kane, S. E. J.; Niemann, R. G.; Peltola, T. A.; Foster, J. M.; Cameron, P. J.; Walker, A. B. *Energy & Environmental Science* **2016**, *9*, 1476–1485.

(39) Tress, W.; Marinova, N.; Moehl, T.; Zakeeruddin, S. M.; Nazeeruddin, M. K.; Grätzel, M. *Energy & Environmental Science* **2015**, *8*, 995–1004.

(40) Unger, E. L.; Hoke, E. T.; Bailie, C. D.; Nguyen, W. H.; Bowring, A. R.; Heumüller, T.; Christoforo, M. G.; McGehee, M. D. *Energy Environ. Sci.* **2014**, *7*, 3690–3698.

(41) Seol, D.; Jeong, A.; Han, M. H.; Seo, S.; Yoo, T. S.; Choi, W. S.; Jung, H. S.; Shin, H.; Kim, Y. *Advanced Functional Materials* **2017**, *27*, 1701924.

(42) Haruyama, J.; Sodeyama, K.; Han, L.; Tateyama, Y. *Journal of the American Chemical Society* **2015**, *137*, 10048–10051.

(43) Yang, J.-H.; Yin, W.-J.; Park, J.-S.; Wei, S.-H. *Journal of Materials Chemistry A* **2016**, *4*, 13105–13112.

(44) Yuan, Y.; Huang, J. *Accounts of Chemical Research* **2016**, *49*, 286–293.

(45) Xiao, Z.; Yuan, Y.; Shao, Y.; Wang, Q.; Dong, Q.; Bi, C.; Sharma, P.; Gruverman, A.; Huang, J. *Nature Materials* **2015**, *14*, 193–198.

(46) Pockett, A.; Eperon, G. E.; Sakai, N.; Snaith, H. J.; Peter, L. M.; Cameron, P. J. *Physical Chemistry Chemical Physics* **2017**, *19*, 5959–5970.

(47) Ebadi, F.; Aryanpour, M.; Mohammadpour, R.; Taghavinia, N. *Scientific Reports* **2019**, *9*, 11962.

(48) Le Corre, V. M.; Diekmann, J.; Peña-Camargo, F.; Thiesbrummel, J.; Tokmoldin, N.; Gutierrez-Partida, E.; Peters, K. P.; Perdigón-Toro, L.; Futscher, M. H.; Lang, F.; Warby, J.; Snaith, H. J.; Neher, D.; Stolterfoht, M. *Solar RRL* **2022**, *6*, 2100772.

(49) Xu, W.; Hart, L. J. F.; Moss, B.; Caprioglio, P.; Macdonald, T. J.; Furlan, F.; Panidi, J.; Oliver, R. D. J.; Pacalaj, R. A.; Heeney, M.; Gasparini, N.; Snaith, H. J.; Barnes, P. R. F.; Durrant, J. R. *Advanced Energy Materials* **2023**, *13*, 2301102.

(50) Akel, S.; Kulkarni, A.; Rau, U.; Kirchartz, T. *PRX Energy* **2023**, *2*, 013004.

(51) Kim, H.-S.; Park, N.-G. *The Journal of Physical Chemistry Letters* **2014**, *5*, 2927–2934.

Chapter 3

Experimental & Characterisation Methods

This chapter provides a comprehensive description of the experimental procedures, characterisation techniques, and data analysis methods used throughout this thesis. Where collaborators carried out substrate/device fabrication or experimental measurements, this is explicitly stated within the relevant sections.

3.1 Device Fabrication

The regular n–i–p perovskite solar cells used in Chapter 4 were fabricated by me. The following description explains the process in its entirety. Perovskite solar cells made by collaborators, such as those used in Section 4.3.4, Chapter 5, and Chapter 6, are discussed separately. All materials and chemicals were purchased from commercial sources and used as received unless otherwise stated.

3.1.1 Substrate Preparation

All glass substrates with a conducting layer of fluorine-doped tin oxide (FTO) of 8 Ω sq^{-1} sheet resistance were purchased from Yinghou Shangneng Photoelectric Material Co., Ltd. All substrates were washed with a 2 vol% Hellmanex III detergent solution in deionised (DI) water. More deionised water was used to rinse off the detergent, after which successive washings with acetone (VWR), ethanol (VWR), and deionised water were used to remove any trace organic contaminants on the substrates. A nitrogen gun was then used to push the remaining water off the substrate gently.

All cleaned substrates were patterned using a Rofin EasyMark IV F20 laser etcher. A schematic illustration of the etching pattern with a top and side view is shown in Figure 3.1. After removing the FTO from the required areas, the substrate is cleaned again using the same process described above. This step is necessary to remove any conductive residue from the surface and channels created.

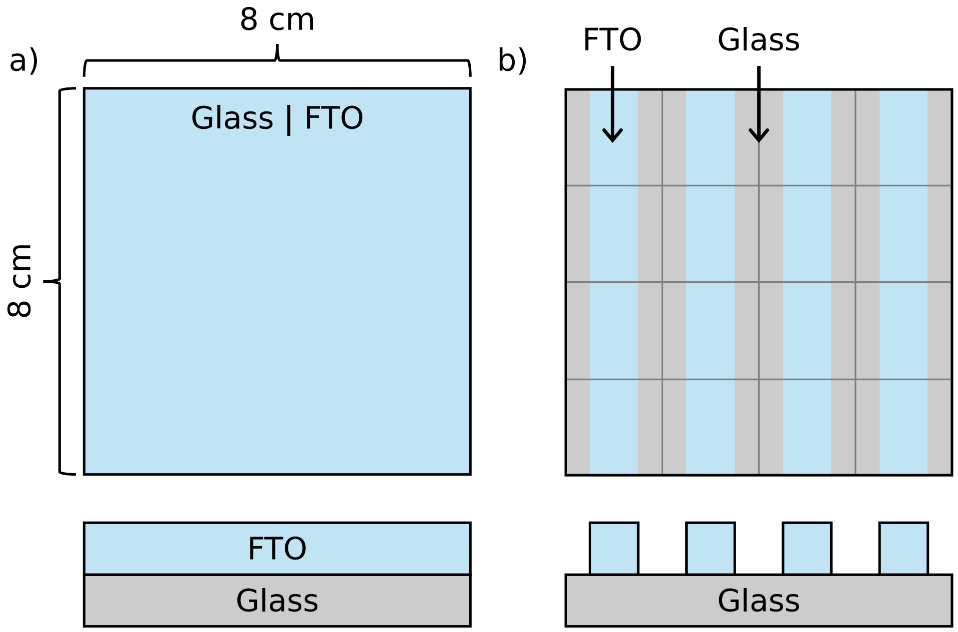

Figure 3.1: Schematic illustration of the laser etching process used to pattern FTO-coated glass substrates. a) Pristine 8 × 8 cm FTO-coated glass substrate before patterning. b) After laser etching, the FTO layer is selectively removed to define electrically isolated stripes, exposing the underlying glass and creating discrete electrode regions for device fabrication.

Each substrate is then cut into individual slides by scribing with a diamond-tipped glass cutter and breaking off the individual slides. Before depositing the first layer onto the slides, the slides were treated with UV/Ozone using an Ossila UV Ozone cleaner for 15 minutes. This step removes any remaining organic contaminants via UV irradiation.[1] Deposition of subsequent layers was started quickly after the UV/Ozone treatment.

3.1.2 Electron Transport Layer

TiO_2 deposition

The compact TiO_2 layer was prepared and deposited via a sol–gel approach. Firstly, 2.5 mL of isopropanol (IPA (99.8%, Thermo Fisher Scientific)) was filtered using a PTFE hydrophilic syringe filter (Thermo Fisher Scientific) with a 0.2 μm pore size. To this, 370 μL of titanium(IV) isopropoxide (Sigma-Aldrich) was slowly added under constant stirring in a glovebox with a nitrogen atmosphere. Additionally, 35

μL of a 2 M hydrochloric acid (HCl (Sigma-Aldrich)) solution in 2.5 mL of IPA was prepared and mixed well. The two solutions were then mixed by adding the contents of the IPA-HCl solution to the IPA-iso solution dropwise while stirring continuously. This solution was prepared fresh each time, approximately 30 minutes before use, to minimise contamination.

The freshly prepared TiO_2 solution was then spin-coated dynamically onto the pre-prepared substrates using a Laurell WS-650-23 B spin coater. 300 μL of the TiO_2 solution was deposited on the sample rotating at 2000 rpm for 45 seconds. Films were then annealed at 150 °C on a hotplate (Heidolph MR Hei-Tec) for at least 10 minutes. After all substrates were coated, they were placed on a lockable hotplate, where the temperature was ramped to 500 °C over 30 minutes. Samples were held at 500 °C for 45 minutes before ramping down to room temperature. Substrates were then immediately transferred to a nitrogen-filled glovebox.

C_{60}-BA SAM deposition

In Chapter 4, samples were treated with a layer of 4-(1′,5′-dihydro-1′-methyl-2′H-[5,6]fullereno-C_{60}-I_h-[1,9-*c*]pyrrol-2′-yl)benzoic acid (C_{60}-BA (>99%, Sigma-Aldrich)). The C_{60}-BA self-assembled molecule (SAM) was prepared by mixing 0.5 mg mL^{-1} in chlorobenzene (CB (99.8% Extra Dry, Thermo Scientific)). This solution was stirred, and 50 μL was dynamically spin-coated at 2000 rpm for 30 s onto the TiO_2 layer, followed by an annealing step at 100 °C for 5 mins. Following the C_{60}-BA layer, a 0.2 wt% IPA solution of aluminium oxide (Al_2O_3) nanoparticles ($<$ 50 nm particle size, 20 wt% in IPA (Sigma-Aldrich)) was deposited on top to improve wetting of the subsequent perovskite layer. The Al_2O_3 was deposited by dynamic spincoating using 50 μL at 2000 rpm for 30 seconds. The samples were then annealed at 100 °C for 5 mins.

3.1.3 Perovskite Precursor Solution and Deposition

The perovskite solution methylammonium lead iodide (MAPI) was synthesised using a 1:1 ratio of methyl ammonium iodide (MAI), which was synthesised by Dr Benjamin Vella at the University of Glasgow, and lead(II) iodide (PbI_2, Tokyo Chemical Industry 99.99%) in a 4:1 dimethylformamide (DMF, 99.8% Extra Dry, Thermo Scientific) to dimethyl sulfoxide (DMSO, 99.7+% Extra Dry, Thermo Scientific) solution, in a nitrogen-filled glovebox. This solution was stirred and left on a hot plate at 100 °C until fully dissolved. The solution was then cooled and passed through a hydrophobic syringe filter (Thermo Fisher).

The MAPI solution was then deposited via dynamic spin coating at 1000 rpm for 10 seconds and then 5000 rpm for 30 seconds. 50 μL of the filtered perovskite solution was deposited at the 5-second mark during the first step, followed by 300 μL of a filtered CB antisolvent at the 23-second mark of the second step. Substrates were then transferred to a dry cloth to air dry for 15 minutes, followed by annealing on a hotplate at 100 °C for 15 minutes.

3.1.4 Hole Transport Layer

The hole transporting layer $2,2',7,7'$-tetrakis[N,N-di(4-methoxyphenyl)amino]-$9,9'$-spirobifluorene (Spiro-OMeTAD) (>99.5%, Luminescence Technology Corp) was dissolved in CB (90 mg/mL). This solution was then doped with 23 μL of a pre-prepared bis(trifluoromethane)sulfonimide lithium salt (LiTFSI (>99.9% anhydrous, Sigma-Aldrich)) stock solution (520 mg in 1 mL acetonitrile (ACN, [>99.9%], Sigma-Aldrich)), 5 μL of FK 209 (Co(III) TFSI, 98%, Sigma-Aldrich) cobalt salt stock solution (180 mg in 1 mL ACN) and 35.5 μL of 4-tert-butylpyridine (tBP, 98%, Sigma-Aldrich) before spincoating. The dopants are added to increase the conductivity of Spiro-OMeTAD, and thus reduce the series resistance when used in a device.[2, 3] The doped Spiro-OMeTAD solution was then deposited dynamically by spin-coating at 4000 rpm for 30 seconds with an acceleration of 2000 rpm. Samples were then placed in a desiccator (Bel-Art) for 24 hours to allow for oxidation of the Spiro-OMeTAD. Without this doping, Spiro-OMeTAD suffers from poor conductivity and hence requires doping to be a viable option for use as a hole transporting layer. This process is achieved by oxidising the material with oxygen in the air, thereby improving hole conductivity. This process, however, can take several hours; therefore, chemical dopants such as LiTFSI and FK209 are used as catalysts to mediate the oxidation of Spiro-OMeTAD.[2, 3]

3.1.5 Metal Contact and Encapsulation

To finish the solar cells, metal contacts were thermally evaporated using a Moorfield NanoPVD thermal evaporator. Gold (Au) pellets (1-3mm, 99.99% Pure, Testbourne Ltd) were placed on a Tungsten Boat (Testbourne Ltd), and samples were loaded into a custom-made evaporation tray with a custom-made non-reflective evaporation shadow mask. An example of the shadow mask pattern is shown in Figure 3.2. The thermal evaporation was conducted under a high vacuum of $\sim 8 \times 10^{-6}$ mbar. Evaporation was continued until a layer of approximately 40 nm of gold was deposited, at a rate of 0.1 nm s^{-1}.

Devices were sealed using an epoxy adhesive mixture (LIQUI MOLY) and a glass slide in a nitrogen-filled glovebox.

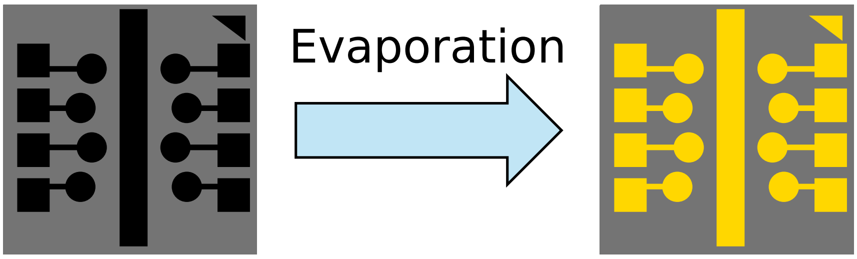

Figure 3.2: Schematic representation of the thermal evaporation process used to deposit metal electrodes. Following perovskite layer deposition, gold is thermally evaporated onto the substrate through a shadow mask, forming patterned top contacts that define the active device areas.

3.1.6 High-Efficiency Inverted Perovskite Solar Cells

Chapter 4 Devices

The high efficiency inverted perovskite solar cell utilised in Section 4.3.4 of Chapter 4 was fabricated by Yin Li and Abdul Khaleed at the University of Hong Kong. A full description of the fabrication protocol can be found in Ref. [4], and is reproduced here for clarity.

N,N-dimethylformamide (DMF), dimethyl sulfoxide (DMSO), isopropanol (IPA), and caesium iodide (CsI) were obtained from Alfa Aesar. Chlorobenzene (CB) and ethylenediamine (EDA) were purchased from Sigma-Aldrich. [2-(9H-carbazol-9-yl)ethyl]phosphonic acid (2PACz), lead iodide (PbI_2), and lead bromide ($PbBr_2$) were sourced from Tokyo Chemical Industry (TCI). Formamidinium iodide (FAI), methylammonium bromide (MABr), and phenethylammonium iodide (PEAI) were supplied by GreatCell Solar. [6,6]-phenyl-C_{61}-butyric acid methyl ester (PCBM) and bathocuproine (BCP) were purchased from Lumtec. Nickel(II) nitrate hexahydrate ($Ni(NO_3)_2{\cdot}6H_2O$) was obtained from International Laboratory, and ethylene glycol (EG) from Dickmann. All reagents were used as received without further purification.

The NiO_x sol–gel precursor was prepared following the approach reported by You *et al.*[5] Briefly, 1.454 g of $Ni(NO_3)_2{\cdot}6H_2O$ was dissolved in 5 mL of ethylene glycol. Subsequently, 335 μL of ethylenediamine was introduced under gentle stirring, and the solution was maintained at room temperature for 4 h to ensure complete complexation.

The perovskite precursor solution was formulated according to the method described by Saliba *et al.*[6] A solvent mixture of DMF (800 μL) and DMSO (200 μL) was added to a vial containing 18.2 mg CsI, 22.4 mg MABr, 172 mg FAI, 73.4 mg $PbBr_2$, and 507.1 mg PbI_2. The mixture was stirred vigorously at 65 °C for 60 min until complete dissolution, then cooled to room temperature. Before use, all precursor solutions were filtered through 0.22 μm PTFE syringe filters.

ITO-coated glass substrates (25 mm × 25 mm) were sequentially cleaned by ultrasonication in detergent solution, deionised water, acetone, and isopropanol (15 min per step). The substrates were then subjected to oxygen plasma treatment (10 V bias, 2 min) to improve surface cleanliness and wettability. The NiO_x layer was deposited by spin-coating the sol–gel precursor at 5000 rpm for 50 s, followed by thermal treatment at 300 °C for 50 min in ambient atmosphere. Once cooled to approximately 80 °C, the substrates were transferred into a nitrogen-filled glovebox. For devices incorporating a 2PACz interlayer, 70 μL of a 0.75 mg mL^{-1} 2PACz solution in IPA was spin-coated at 4000 rpm for 35 s, followed by annealing at 120 °C for 10 min. The substrates were then allowed to cool to room temperature. Perovskite films were formed by depositing 55 μL of precursor solution and spin-coating at 4000 rpm for 35 s. Chlorobenzene (350 μL) was dispensed 10 s after the start of the spin program as an antisolvent. The films were subsequently annealed at 110 °C for 20 min. After a 15 min cooling period, a surface passivation layer was introduced by dynamically spin-coating 70 μL of PEAI solution (2 mg mL^{-1} in IPA) at 5000 rpm for 35 s, followed by annealing at 100 °C for 10 min. PCBM (40 mg mL^{-1} in chlorobenzene) was dynamically spin-coated at 5000 rpm for 35 s. After annealing at 100 °C for 10 min and cooling to room temperature, a saturated BCP solution in IPA (70 μL) was deposited at 4000 rpm for 30 s. Finally, an 80 nm silver electrode was thermally evaporated through a shadow mask. The initial 10 nm was deposited at 0.1 Å s^{-1}, followed by 0.5 Å s^{-1} for the remaining thickness. Finished perovskite solar cells were encapsulated with a microscope glass slide using polyisobutylene (PIB) tape, and the edges were sealed with UV-cured epoxy.

Chapter 5 Devices

The devices utilised in Chapter 5 were fabricated by Dr Wai Kin Yiu at the University of Hong Kong. All chemicals used were obtained from the same sources as in the preceding section, as these devices were fabricated in the same laboratory at the University of Hong Kong. A full description of the fabrication can be found in Ref [7]; it is included here for clarity.

Nickel Oxide Synthesis

This synthesis was conducted by Jingbo Wang at the University of Hong Kong: Six grams of Nickel(II) nitrate hexahydrate were dissolved in 80 mL of DI water under stirring until a clear solution was obtained. 80 mL of sodium hydroxide (NaOH) was added to the nitrate solution at a controlled rate to ensure a continuous stream of droplets. This solution was stirred for 5 minutes. The resulting light-green product was collected by centrifugation at 10,000 rpm after several washes with DI water. The product was then freeze-dried for at least 48 hours and annealed at 270 °C for 2 hours to obtain black nickel oxide (NiO_x) nanoparticles.

Perovskite Solar Cell Fabrication

Patterned ITO substrates were cleaned using a 1% solution of Decon 90 detergent in DI water, followed by sonication in acetone and ethanol for 15 minutes each. The washed substrates were blow-dried with nitrogen and treated with oxygen plasma at 10 V for 10 s. 20 mg/mL in DI water of the NiO_x nanoparticles was spin-coated onto the ITO substrate at 4000 rpm for 30 s, followed by annealing at 110 °C for 10 mins, before being transferred to a nitrogen-filled glovebox. 0.5 mg/mL of the self-assembled molecules (SAMs) ([2-(9H-carbazol-9-yl)ethyl]phosphonic acid (2PACz), [2-(3,6-dimethoxy-9H-carbazol-9-yl)ethyl] phosphonic acid (MeO-2PACz), and [4-(3,6-dimethyl-9H-carbazol-9-yl)butyl]phosphonic acid (Me-4PACz)) was spin-coated at 4000 rpm for 30 s and annealed at 100 °C for 10 mins.

The MAPI perovskite was synthesised using 750 mg of PbI_2 and 240 mg MAI in 1 mL of a DMF/DMSO solution (4:1). The double cation perovskite was synthesised using 433 mg PbI_2, 155 mg formamidinium iodide (FAI), 26 mg caesium iodide (CsI), and 22 mg of lead(II) bromide ($PbBr_2$) in 571 μL of DMF and 143 μL of DMSO. Both perovskite precursor solutions were heated overnight at 60 °C and filtered before use. The MAPI perovskite solution was spin-coated by a two-step process at 1000 rpm for 5 s and 5000 rpm for 25 s. At 5 s after the start of the first step, 50 μL of MAPI perovskite solution was dropped onto the substrate and at 5 s after the start of the second step, 300 μL of a CB antisolvent was dropped onto the film. The DC perovskite solution was deposited using a two-step process: 2000 rpm for 10s, followed by 4000 rpm for 30 s. The DC solution was statically deposited before the start of the process, and during the final 10 seconds, 250 μL of the CB antisolvent was dropped onto the film. Both perovskite films were annealed at 100 °C for 30 mins. To deposit the layered perovskite, a 1 mg/mL solution of the salt phenethylammonium iodide (PEAI) in IPA was prepared and spin-coated onto the perovskite layer at 5000 rpm for 30 s, followed by an annealing step at 100 °C for 3 mins. For the electron-transporting layer, 20 mg/mL in CB of [6,6]-phenyl-C_{61}-butyric acid methyl ester (PCBM) was spin-coated at 1200 rpm for 30 s, followed by annealing at 100 °C for 10 mins. This was followed by a 0.5 mg/mL bathocuproine (BCP) solution in IPA, which was spin-coated at 4000 rpm for 30 s, with no annealing step. Finally, a

100 nm silver (Ag) cathode was thermally evaporated through a shadow mask to obtain a device with an electrode area of 0.09 cm^2. Finished perovskite solar cells were encapsulated with a microscope glass slide using polyisobutylene (PIB) tape, and the edges were sealed with UV-cured epoxy.

Chapter 6 Devices

The devices used in Chapter 5 were fabricated by Dr Wenhui Li at the Institute of Chemical Research of Catalonia (ICIQ-CERCA).

Patterned ITO-coated glass substrates (1.5 cm × 1.5 cm, 15 Ω sq^{-1}) were cleaned by sequential ultrasonication in ethanol and isopropanol (30 min each). The substrates were dried under nitrogen and subsequently treated under UV–ozone for 30 min to improve surface wettability, then transferred directly into a nitrogen-filled glovebox for device fabrication.

Self-assembled molecules (SAMs) of Spiro-A and Spiro-B were prepared as 0.1 mM solutions in DMF. Me-4PACz was dissolved in ethanol at the same concentration (0.1 mM). The SAM solutions were deposited by spin-coating at 3000 rpm for 60 s, followed by thermal annealing at 100 °C for 10 min. The substrates were allowed to cool to room temperature before perovskite deposition.

The perovskite precursor solution (1.5 M) was prepared by dissolving FAI, PbI_2, MABr and $PbBr_2$ in a DMF:DMSO mixed solvent (4:1 v/v). A 1.5 M CsI solution in DMSO was incorporated into the precursor to yield a final composition of $Cs_{0.05}(FA_{0.95}MA_{0.05})_{0.95}Pb(I_{0.95}Br_{0.05})_3$, with 10 mol% MACl additive. The precursor was spin-coated using a two-step process (2000 rpm for 10 s followed by 4500 rpm for 25 s). During the second step, 200 μL of CB was dispensed onto the rotating substrate 12 s before the end of the spin cycle. The films were then annealed at 100 °C for 30 min.

Following perovskite crystallisation, a $PC_{61}BM$ electron transport layer (20 mg mL^{-1} in CB) was deposited at 1000 rpm for 60 s. A BCP interlayer (0.5 mg mL^{-1} in IPA) was subsequently spin-coated at 4000 rpm for 40 s. Finally, a 100 nm silver electrode was thermally evaporated under high vacuum ($< 10^{-6}$ bar), defining an active device area of 0.104 cm^2.

3.2 Electrical Characterisation

This section provides further detail regarding all electrical characterisation techniques utilised in this thesis. Where measurements were conducted by collaborators, this is explicitly stated. A general description of the method is provided, followed by specific details regarding measurements in each chapter.

3.2.1 Current–Voltage Measurements

The performance of solar cells is quantified through their power conversion efficiency (PCE), determined under standardised illumination conditions. The PCE of a photovoltaic device can be characterised by measuring its current density–voltage (J–V) characteristics under simulated AM1.5G irradiation (100 mW cm^{-2}). By sweeping the applied bias across a defined voltage range and recording the current density, a J–V curve is obtained, from which the principal device performance parameters can be determined.

The current density J is defined as the measured current I normalised by the active device area A:

$$J = \frac{I}{A} \tag{3.1}$$

From the illuminated J–V curve, four key parameters are determined:

- Short-circuit current density (J_{SC}): the current density at zero applied bias ($V = 0$),

- Open-circuit voltage (V_{OC}): the applied voltage at which the net current is zero ($J = 0$),

- Fill factor (FF): defined as

  $$\mathrm{FF} = \frac{J_{\mathrm{MP}} V_{\mathrm{MP}}}{J_{\mathrm{SC}} V_{\mathrm{OC}}}, \tag{3.2}$$

  where J_{MP} and V_{MP} correspond to the current density and voltage at the maximum power point,

- Power conversion efficiency (PCE), given by

  $$\mathrm{PCE} = \frac{J_{\mathrm{SC}} V_{\mathrm{OC}} \mathrm{FF}}{P_{\mathrm{in}}}, \tag{3.3}$$

  where P_{in} is the incident optical power density (100 mW cm^{-2} under AM1.5G).

Extraction of photovoltaic parameters

Photovoltaic parameters were extracted using a custom-written Python analysis script. The script processes the measured current density–voltage (J–V) data and determines V_{OC}, J_{SC}, the maximum power point (MPP), the fill factor (FF), and the power conversion efficiency (PCE).

The open-circuit voltage V_{OC} was determined by interpolation of the J–V data in the vicinity of the zero-current crossing. A small window of data points surrounding the first sign change in current density was selected, and the voltage was interpolated as a function of current density using a piecewise cubic Hermite interpolating polynomial (PCHIP). The value of V_{OC} was then obtained by evaluating this interpolant at $J = 0$.

The short-circuit current density J_{SC} was obtained by interpolating the current density as a function of voltage. The full dataset was first sorted in ascending voltage order to ensure monotonicity, after which a PCHIP interpolator was constructed. The value of J_{SC} was evaluated at $V = 0$. If interpolation was not possible (for example, due to insufficient data spanning zero bias), the current density at the voltage closest to zero was used.

The output power density was calculated at each measured bias as

$$P(V) = V \times J(V) \tag{3.4}$$

The maximum power point (MPP) was identified numerically as the bias corresponding to the maximum value of $P(V)$. The fill factor was then calculated as

$$\mathrm{FF} = \frac{P_{\mathrm{max}}}{V_{\mathrm{OC}} \times J_{\mathrm{SC}}} \tag{3.5}$$

The piecewise cubic Hermite interpolating polynomial (PCHIP) method was used to interpolate the J–V data. Unlike standard cubic spline interpolation, PCHIP preserves the local monotonicity and shape of the data and avoids introducing artificial oscillations between points. This is particularly important near V_{OC} and J_{SC}, where small over- or undershoots from conventional spline fitting could introduce systematic errors in parameter extraction.

PCHIP constructs a cubic polynomial between each pair of neighbouring data points, with derivatives chosen to ensure continuity of the first derivative while preserving the dataset's monotonic behaviour. This provides a smooth but physically realistic interpolation of experimental J–V curves.

Chapter 4 Devices

All solar cell characterisation was conducted at room temperature and under ambient conditions.

The regular n–i–p devices J–V curves measured in Chapter 4 were carried out under 1 Sun illumination using a Wavelabs Sinus-70 AAA solar simulator using an Ossila Source Meter Unit. The devices were pre-biased at 1.3 V for 10 s under 1-sun illumination and were then measured in reverse and forward scan directions at 0.2 V s^{-1} steps from 1.3 V to -0.1 V. Non-reflective metal masks with an aperture area of 0.1 cm^2 were used to define the devices' illumination area. The light intensity was calibrated using a certified silicon reference cell.

This measurement was conducted by Yin Li at the University of Hong Kong. The inverted p–i–n device used in Chapter 4 was measured by a Keithley 2400 source-measure unit interfaced and controlled via a custom-built LabVIEW program. Devices were characterised under simulated one-sun illumination (AM1.5G spectrum) provided by an ABET Sun 2000 solar simulator. The incident light intensity was calibrated prior to measurement using an Enli PVM silicon reference cell. A metal shadow mask was used during testing to define the active device area, which was fixed at 0.075 cm^2.

Voltage scans were carried out in both forward and reverse directions. The reverse scan was performed from 1.2 V to -0.2 V, while the forward scan proceeded from -0.2 V to 1.2 V. The effective scan rate was controlled by adjusting the voltage step size and the delay time between successive data acquisition points. Specific scanning parameters used in this work are summarised in Table 3.1.

Table 3.1: Voltage scan parameters used for J–V measurements at different scan speeds.

Scan speed	Scan step (V)	Delay time (ms)
Normal	0.03	10
Fast	0.05	0.1
Slow	0.005	500

Chapter 5 Devices

All J–V measurements on these devices were conducted by Dr Wai Kin Yiu at the University of Hong Kong.

Current density–voltage measurements were carried out using a Keithley 2400 source-measure unit under simulated one-sun illumination (100 mW cm^{-2}, AM1.5G spectrum) generated by an ABET Sun 2000 solar simulator. The illumination intensity was calibrated using an Enli PVM silicon reference cell. All devices were characterised in ambient laboratory conditions (room temperature, relative humidity 60–70%) following encapsulation. An aperture mask defining an active area of 0.04 cm^2 was used during measurement. Voltage scans were conducted with a step size of 0.01 V and a delay time of 10 ms between data points. Reverse scans were performed from 1.2 V to -0.2 V, while forward scans were measured from -0.2 V to 1.2 V.

Chapter 6 Devices

All J–V measurements on these devices were conducted by Dr Wenhui Li at the Institute of Chemical Research of Catalonia.

Current density–voltage characteristics were acquired using an ABET 11000 solar simulator and a Keithley 2400 source-measure unit. Measurements were performed under simulated one-sun illumination (100 mW cm^{-2}, AM1.5G spectrum), with the light intensity calibrated using a certified silicon reference cell.

The applied bias was swept across the selected voltage range using a fixed voltage increment of 0.02 V (20 mV) between consecutive data points. The current response was recorded at each step to construct the full J–V curve.

3.2.2 The Stabilise and Pulse Technique

Theory

The Stabilise and Pulse (SaP) protocol was established by Hill *et al.* to decouple the mixed electronic-ionic nature of perovskite solar cells.[8] Mobile ionic vacancies are able to redistribute under an applied bias on a timescale of seconds to minutes; therefore, conventional J–V measurements probe a coupled response in which both the electronic transport and ionic rearrangement contribute to the measured signal. The SaP method was established to decouple these processes. Additional discussion on this measurement technique is provided in Section 4.2.

This measurement technique consists of long stabilisation periods at an applied voltage, followed by a series of rapid voltage pulses. A schematic of the voltage protocol over time is shown in Figure 3.3. A constant stabilisation voltage (V_{bias}) is applied to the device under continuous illumination for $\sim$120 s to allow the ionic distribution to reach steady state. For more complex perovskite compositions, this stabilisation time was increased to $\geq$240 s to ensure the ions had completely redistributed.

During the stabilisation time, mobile ionic defects redistribute in response to the applied electric field. Following stabilisation, a series of rapid voltage pulses is applied. As ionic vacancies move on long timescales, typically 1–100 s, rapid voltage pulses can extract electronic information from within the material without affecting

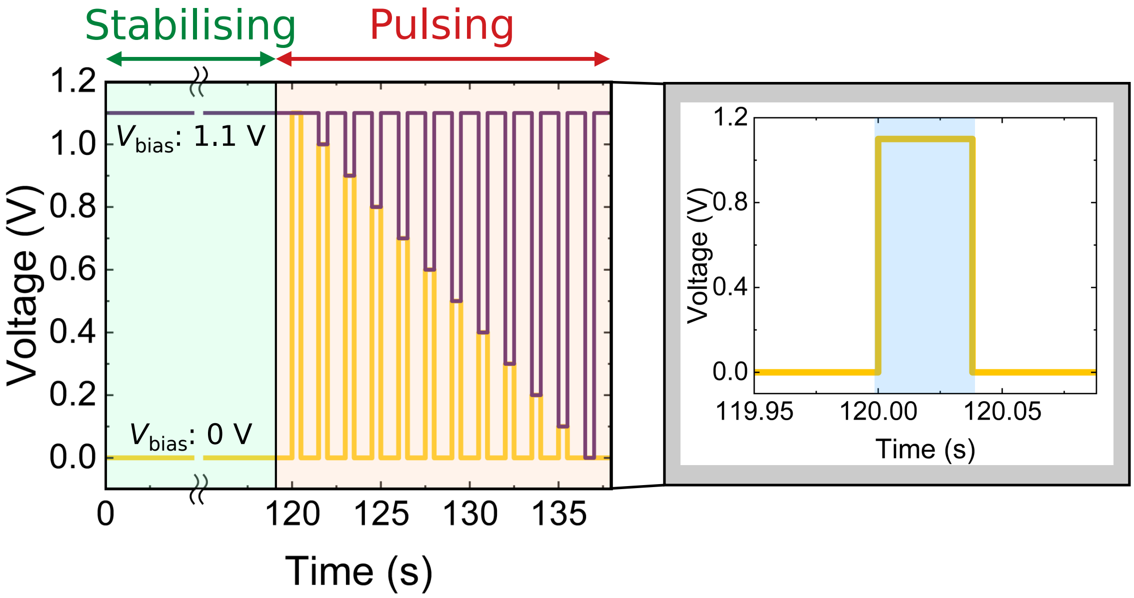

Figure 3.3: Voltage–time protocol used in the Stabilise and Pulse (SaP) measurement technique for two different stabilisation biases. The device is first held at a constant stabilisation bias (green region) to allow ionic redistribution to reach a steady state. The yellow trace corresponds to a stabilisation bias of 0 V, while the purple trace corresponds to a stabilisation bias of 1.1 V. A sequence of square-wave voltage pulses (red region) is then applied to reconstruct the J–V characteristics while maintaining the stabilised ionic configuration. The inset shows a magnified view of a single square-wave pulse highlighted in blue. The current is sampled at the peak of each pulse.

the ionic distribution, provided the pulse is short enough. The pulsing section can be seen on the right-hand side of Figure 3.3, where the zoomed-in section highlights the rapid change in voltage for a short amount of time (approximately 36 ms) before returning to the stabilisation bias for 1 s. During the flat region of the pulse, the current is measured and extracted. By pulsing over a range of voltages, a J–V curve can be reconstructed for a given applied bias, which defines an ionic configuration. In other words, a J–V curve is obtained for a fixed ionic distribution.

Instrument Details

This measurement was performed on a custom-built setup. Here, a Cree high-power white LED was used as the light source, and its intensity was calibrated to match the device's measured short-circuit current density obtained from a calibrated solar simulator measurement. The LED was mounted on a large heat sink, and a fan (Phanteks M25 120mm PWM High-Airflow Chassis Fan) was set to maximum speed to reduce heat buildup and cool the sample. The rapid voltage pulses were provided by an Ossila Source Meter Unit.

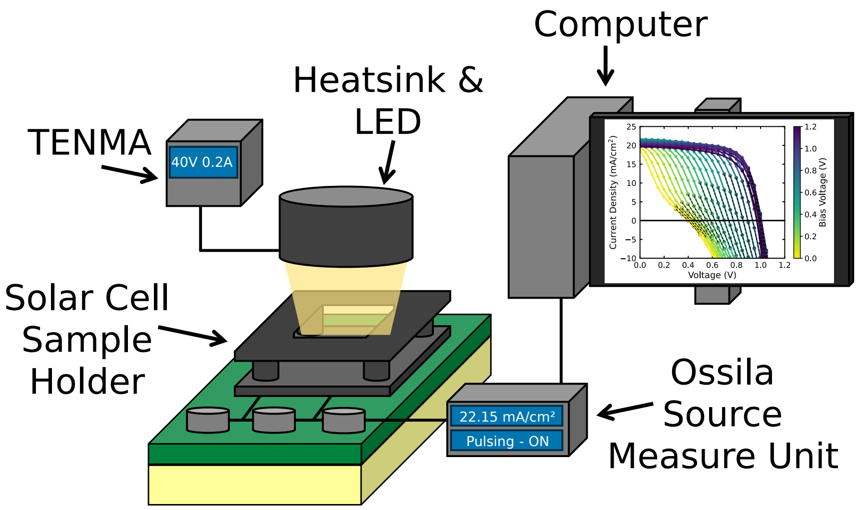

Figure 3.4: Schematic illustration of the custom-built Stabilise and Pulse measurement setup used.

Figure 3.4 shows a schematic illustration of the Stabilise and Pulse measurement setup used throughout this work. The perovskite solar cell was mounted within a custom sample holder positioned beneath the LED illumination source. Illumination intensity was controlled using a TENMA DC power supply, while electrical biasing and current acquisition were performed using the Ossila Source Measure Unit (SMU). During operation, the device was first stabilised at a selected bias before rapid voltage pulses were applied and the resulting current response recorded.

For all measurements, the source delay was set to 1 ms, such that the current acquisition commenced approximately 1 ms after the arrival of the voltage pulse. This delay ensures that the measured current corresponds to the pulse plateau rather than the transient rise time of the voltage signal. The current was sampled 256 times during each pulse, with a sampling interval of 14.2 μs. The recorded signal was therefore averaged over a total acquisition window of 3.62 ms. Given that this timescale is several orders of magnitude shorter than typical ionic migration times, the ionic distribution is assumed to remain effectively unchanged during the pulse measurement.

Each voltage pulse had a duration of approximately 36 ms, and the device was stabilised for 1 s between pulses, resulting in a duty cycle of approximately 3.5%. 50 mV increments were used for the stabilisation voltage to reduce measurement time, with the stabilisation voltage range varying from sample to sample but typically between 0 and 1.3 V.

Electrostatic Interpretation of the Stabilise and Pulse Measurement

The following framework was established by Hill *et al.* [8] using drift–diffusion simulations showing that the reconstructed J–V curve shape is governed by the sign of the residual electric field across the perovskite absorber.[8] The discussion is adapted and provided here to provide greater context for the measurement technique.

To interpret the physical origin of the transition observed in the Stabilise and Pulse (SaP) measurement, it is useful to consider the electrostatic potential profile obtained from drift–diffusion simulations (performed by Dr Lucy J. F. Hart at Imperial College London). Figure 3.5 shows the simulated electrostatic potential $\phi(x)$ across a p–i–n device and the corresponding excess ionic vacancy distributions.[9]

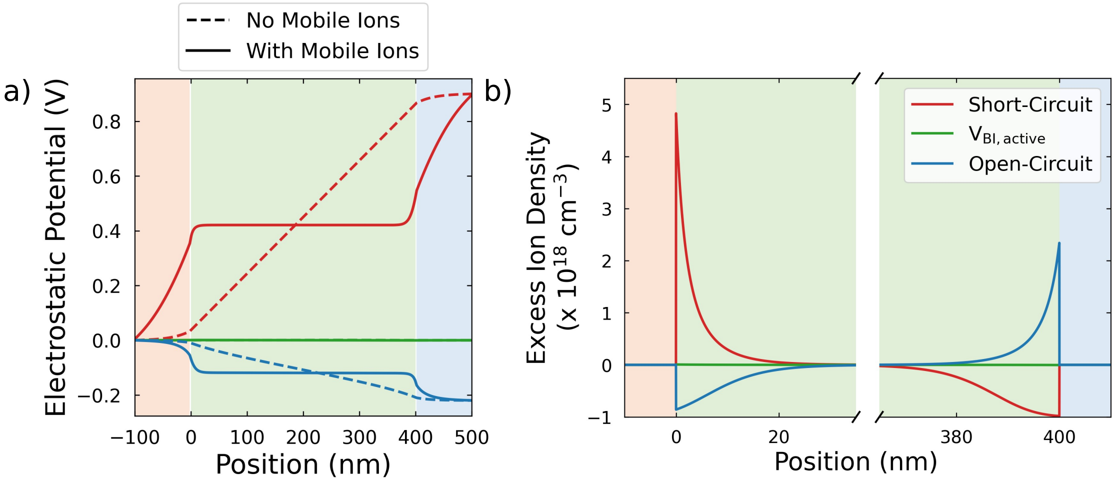

Figure 3.5: Drift–diffusion simulation used to illustrate the electrostatics of the Stabilise and Pulse (SaP) measurement. a) Simulated electrostatic potential profile across a p–i–n device under short-circuit (red), flat-band (V_{flat}, green), and open-circuit (blue) conditions. The dashed curve shows the case without mobile ions, while the solid curves include ionic vacancies, demonstrating redistribution of the internal electric field from the bulk to the interfaces. b) Corresponding excess ionic vacancy density profiles under the same operating conditions, highlighting accumulation at the transport-layer interfaces and its influence on the device electrostatics. Simulations performed by Dr Lucy J. F. Hart (Imperial College London). Adapted from Ref. [9] under a Creative Commons Attribution 3.0 Unported Licence.

In Figure 3.5a, the horizontal axis x is defined to increase from the HTL (left) to the ETL (right). The central green region corresponds to the perovskite absorber layer. The dashed curve represents the case without mobile ions, while the solid curves include mobile ionic vacancies. The green solid line corresponds to the V_{flat} condition (equivalently V_{bi} in the idealised limit), whereas the red and blue lines represent short-circuit and open-circuit conditions, respectively.

To interpret the physical meaning of the slope of these potential profiles, we recall the relationship between electrostatic potential and electric field. The electric field is defined as

$$E(x) = -\frac{d\phi(x)}{dx}. \tag{3.6}$$

The sign of the electric field is therefore determined directly by the spatial slope of the electrostatic potential. Since the coordinate x is defined to increase from the HTL (left) to the ETL (right), a positive slope in $\phi(x)$ across the perovskite corresponds to $d\phi/dx > 0$ and hence a negative electric field, and vice versa.

In practice, the average slope across the perovskite layer can be estimated from the potential difference between the two interfaces as

$$\left\langle \frac{d\phi}{dx} \right\rangle \approx \frac{\phi(x_{\mathrm{ETL}}) - \phi(x_{\mathrm{HTL}})}{x_{\mathrm{ETL}} - x_{\mathrm{HTL}}}. \tag{3.7}$$

This right-minus-left convention follows directly from the chosen coordinate definition and ensures consistency with the relation $E = -d\phi/dx$. Reversing the subtraction order would correspond to redefining the coordinate direction; the underlying physics remains unchanged.

In the absence of mobile ions (dashed curve), the electrostatic potential drops approximately linearly across the perovskite. This corresponds to a uniform built-in electric field in the absorber, as expected for a conventional semiconductor junction. When mobile ions are included (solid curves), ionic vacancies accumulate at the interfaces (Figure 3.5b). This redistribution screens the bulk electric field and reshapes the electrostatic potential profile. The potential within the perovskite bulk becomes nearly flat, while the majority of the potential drop becomes localised at the transport-layer interfaces.[9] Thus, mobile ions do not eliminate the electric field, but redistribute it from a bulk depletion field to an interface-localised field.

The green curve in Figure 3.5a corresponds to the condition where the electrostatic potential across the perovskite is flat, i.e.

$$\frac{d\phi}{dx} = 0 \quad \Rightarrow \quad E = 0 \quad \text{within the perovskite bulk.} \tag{3.8}$$

This condition defines V_{flat} (or equivalently V_{bi}), where the drop in electrostatic potential across the perovskite, $\Delta\phi_{\mathrm{psk}}$, is exactly compensated by the applied stabilisation bias; therefore, there is no ionic accumulation at the interfaces.

At stabilisation biases below V_{flat}, the electrostatic potential across the perovskite increases from HTL to ETL, such that

$$\Delta\phi = \phi(x_{\mathrm{ETL}}) - \phi(x_{\mathrm{HTL}}) > 0. \tag{3.9}$$

This corresponds to

$$\frac{d\phi}{dx} > 0 \quad \Rightarrow \quad E < 0, \tag{3.10}$$

i.e. a negative residual electric field (in the defined coordinate system).

At stabilisation biases above V_{flat}, the slope reverses sign,

$$\frac{d\phi}{dx} < 0 \quad \Rightarrow \quad E > 0, \tag{3.11}$$

corresponding to a positive residual electric field across the perovskite.

Importantly, these fields are small compared to the interface fields and represent the residual bulk slope after ionic screening. The bulk field is largely screened by ionic redistribution, but its sign remains physically significant.

Drift–diffusion simulations, performed by Hill *et al.*, show that the transition from s-shaped to diode-like reconstructed J–V curves occurs when the sign of this residual electric field across the perovskite changes.[8] Rather than directly measuring $\phi(x)$ experimentally (which would require solving Poisson's equation with full knowledge of the charge distribution), the SaP analysis identifies this transition empirically by quantifying the gradient of the reconstructed J–V curve around the open-circuit voltage:

$$g(V_{\text{stab}}) = \left.\frac{dJ}{dV}\right|_{V=V_{\text{OC}}}. \tag{3.12}$$

Small values of g correspond to pronounced s-shaped behaviour (recombination-dominated regime), while larger values correspond to diode-like behaviour (extraction-dominated regime). The stabilisation bias at which g transitions between these regimes provides an experimental estimate of $\Delta\phi_{\text{psk}}$ and hence of the effective interfacial band alignment within the working device.

Experimental extraction of V_{flat} from SaP data

To extract V_{flat}, a custom-built Python script was used to quantify how the reconstructed J–V curve evolves with stabilisation bias and to identify the bias at which the device transitions between its two characteristic regimes. The method follows the empirical procedure introduced by Hill *et al.*, but is implemented here in a fully automated and reproducible manner.

The extraction proceeds in two stages: first, each J–V curve is reduced to a single gradient value evaluated around the open-circuit voltage; second, the stabilisation bias at which this gradient transitions between its limiting low- and high-slope regimes is determined.

For each stabilisation bias $V_{\text{stab},i}$, the corresponding measured trace $J_i(V)$ is analysed to obtain the local slope around the open-circuit voltage,

$$g_i = \left.\frac{dJ}{dV}\right|_{V=V_{\text{OC},i}}. \tag{3.13}$$

The open-circuit voltage $V_{\mathrm{OC},i}$ is estimated by spline interpolation of the measured data and solving $J_i(V) = 0$. To ensure the gradient is evaluated locally and robustly, the five data points closest to $V_{\mathrm{OC},i}$ are selected and fit with a cubic polynomial. The derivative of this cubic, evaluated at $V_{\mathrm{OC},i}$, provides the gradient value g_i.

Repeating this procedure for all stabilisation biases yields a dataset of gradient values $g(V_{\mathrm{stab}})$, which quantifies how strongly s-shaped or diode-like each reconstructed J–V curve is.

The function $g(V_{\mathrm{stab}})$ typically exhibits two plateau regions (low- and high-gradient), separated by a relatively sharp sigmoid-like transition. To locate this transition in an objective and reproducible manner, the numerical derivative of g with respect to stabilisation bias is evaluated:

$$\frac{dg}{dV_{\mathrm{stab}}}.$$

The stabilisation bias at which this derivative reaches its maximum value is taken to define the centre of the transition region. Physically, this corresponds to the point at which the open-circuit gradient changes most rapidly with stabilisation bias, i.e. the steepest part of the $g(V_{\mathrm{stab}})$ curve.

A local fitting window is then defined around this index, consisting of up to 5 neighbouring stabilisation points (2 below and 2 above the identified transition point). The minimum and maximum values of g across the full dataset are identified, and their midpoint is defined as

$$g_{\mathrm{mid}} = \frac{g_{\min} + g_{\max}}{2}. \tag{3.14}$$

All possible three-point combinations within the local transition window are fitted with a linear model. For each accepted fit, the stabilisation bias at which the linear model crosses g_{mid} is calculated. This produces a set of candidate V_{flat} values.

The final V_{flat} is taken as a weighted mean of the accepted candidate values,

$$\overline{V}_{\mathrm{flat}} = \frac{\sum_k w_k V_{\mathrm{flat}}^{(k)}}{\sum_k w_k}, \tag{3.15}$$

where the weights w_k are derived from the goodness-of-fit of each linear regression. The uncertainty is reported as the corresponding weighted standard deviation. The extracted value is therefore quoted as

$$V_{\mathrm{flat}} = \overline{V}_{\mathrm{flat}} \pm \sigma_V. \tag{3.16}$$

This procedure ensures that a single local fit does not determine the reported V_{flat} but instead reflects the consistent behaviour of the transition region in $g(V_{\mathrm{stab}})$.

Uncertainty and Validity of the SaP Method

It is important to distinguish between two different sources of uncertainty in the extraction of V_{flat}: (i) the statistical uncertainty associated with the local fitting procedure applied to the experimental data, and (ii) the intrinsic accuracy of the SaP methodology itself as established through simulation.

The weighted standard deviation reported alongside V_{flat} reflects the sensitivity of the extracted value to the specific local fitting window used in the transition region of $g(V_{\text{stab}})$. This captures the experimental scatter of the linear fits around the midpoint. It does not, however, reflect the fundamental physical accuracy of the SaP method.

Hill *et al.* assessed the intrinsic accuracy of the SaP approach by applying the gradient-based extraction to drift–diffusion simulated datasets in which the electrostatic potential drop across the perovskite, $\Delta\phi_{\text{psk}}$, was explicitly defined.[8] The extracted values were then directly compared with the theoretical input used in the model. Across a range of simulated conditions, including variations in the electron–hole Shockley–Read–Hall lifetime τ_{SRH}, they reported a mean absolute error of approximately 0.09 V in the extracted $\Delta\phi_{\text{psk}}$.[8] The reported mean absolute error, therefore, quantifies the intrinsic accuracy of the SaP extraction under a range of realistic recombination conditions in the simulated device.

Importantly, this uncertainty is substantially smaller than that typically associated with conventional energetic alignment techniques such as UPS and XPS, which measure the work function of individual, isolated layers under vacuum conditions. While highly surface-sensitive, this very sensitivity makes it challenging to directly translate the extracted material properties into a fully assembled device, where buried interfaces and operational conditions differ significantly from those in the measurement environment. In addition, conventional linear fitting of the UPS density-of-states to determine the work function and band offsets can introduce uncertainties of 0.5 eV.[8, 10, 11] Kelvin probe force microscopy (KPFM) can be performed on device cross sections, offering spatially resolved potential information. However, this measurement is strongly influenced by surface adsorbates and contamination, which can reduce accuracy and reproducibility.[12] Electroabsorption (EA) techniques, meanwhile, rely on the assumption of a spatially uniform electric field within the device. In perovskite solar cells, this assumption may not hold due to the presence and redistribution of ionic vacancies.[13] Similarly, Mott–Schottky analysis, commonly used to estimate built-in potentials, must be treated with caution when applied to perovskite solar cells. The conventional Mott–Schottky formalism assumes a depletion region governed by immobile ionised dopants and a well-defined, static space-charge region. In PSCs, however, the presence of mobile ionic vacancies leads to bias-dependent redistribution of charge within the absorber layer. As a result, the reliability of this measurement technique has been challenged for perovskite solar cells.[14–16]

In addition to the recombination-dependent accuracy discussed above, the experimental validity of the SaP method requires that ionic redistribution remains negligible during the voltage pulse used to reconstruct the J–V curve. In practice, this condition is satisfied when the pulse duration is short relative to the characteristic timescale for ionic motion,

$$\tau_{\text{pulse}} \ll \tau_{\text{ion}},$$

such that the ionic distribution can be considered effectively frozen during the electronic measurement. In lead-halide perovskites, ionic motion typically occurs on millisecond-to-second timescales, whereas the electronic response is orders of magnitude faster.[17] Provided that sufficiently short pulses and an appropriate duty cycle are used (i.e., $< 10\%$), the reconstructed J–V curve reflects a fixed electrostatic configuration.[8, 18–20] In the measurements performed in this thesis, the pulse was set to the minimum possible duration of 36.2 ms, with a 1-second stabilisation between pulses; therefore, a duty cycle of $\sim 3.5\%$.

The total experimental uncertainty in V_{flat} therefore comprises both the statistical spread from the local fitting procedure and the intrinsic method-level accuracy of approximately 0.09 V established through simulation. Together, these define the practical limits of precision and validity for the SaP-derived electrostatic potential measurement.

3.2.3 Conductivity Measurements

The Conductivity measurement in Chapter 5 Section 5.2.4 was conducted by Dr Wai Kin Yiu at the University of Glasgow.

The electrical conductivity (σ) of a material describes how readily charge carriers move in response to an applied electric field. In the context of transport layers in perovskite solar cells, conductivity is a key parameter governing charge-extraction efficiency and resistive losses. A low conductivity can lead to increased series resistance and reduced fill factor, whereas higher conductivity facilitates efficient carrier transport.

Conductivity is inversely related to the resistivity (ρ) of a material, which quantifies the opposition to current flow [21]:

$$\sigma = \frac{1}{\rho}. \tag{3.17}$$

To determine the conductivity of thin films, a two-point probe configuration was employed on patterned ITO substrates. The etched geometry defines a known conduction pathway of length L and cross-sectional area A. A voltage bias was applied across the electrodes, and the resulting current was measured using an Ossila source-measure unit. Here, rapid voltage pulses were used rather than a voltage sweep to eliminate the effect of ionic conductivity and allow selective measurement of electron/hole conductivity.

For ohmic transport, the relationship between applied voltage V and current I is described by Ohm's law:

$$V = IR, \tag{3.18}$$

where R is the measured resistance. For a uniform film, the resistance is given by

$$R = \rho \frac{L}{A}, \tag{3.19}$$

where $A = w \times d$, with w representing the channel width and d the film thickness. Combining these expressions yields the conductivity:

$$\sigma = \frac{L}{RA}. \tag{3.20}$$

In practice, σ was extracted from the slope of the linear region of the measured I–V characteristics, assuming uniform film thickness and ohmic contact behaviour within the applied bias range.

3.3 Drift–Diffusion Modelling

Drift–diffusion simulations presented in this thesis were performed by Dr. Lucy J. F. Hart (Imperial College London) using DRIFTFUSION, a one-dimensional device simulator for ordered multilayer semiconductor stacks that can include mobile ionic charge within the perovskite absorber.[22] The purpose of these simulations is to provide a physics-based interpretation of experimental trends (rather than a unique fitted parameter set for any one device): the description below summarises the modelling approach and assumptions required to interpret the simulated datasets shown in Section 4.4 (adapted from Ref. [9] under CC BY 3.0).

Model framework and physical meaning

DRIFTFUSION is a one-dimensional drift–diffusion device model that solves electrostatics and charge transport together in a self-consistent manner.[9] In practical terms, the model calculates (i) the internal electric field set by the local space-charge distribution, (ii) the resulting electron and hole populations under illumination and applied bias, and (iii) the corresponding currents arising from field-driven drift and concentration-driven diffusion.[22] The governing equations are standard in semiconductor device physics; they are included here to define the quantities solved by the model and to show explicitly how mobile ionic charge modifies the internal electrostatics, rather than as original derivations.[22]

Electrostatics (Poisson equation). At the core of the model is Poisson's equation, which relates the local electrostatic potential $\phi(x)$ to the net space-charge density in the device:[22]

$$\frac{\mathrm{d}}{\mathrm{d}x}\left(\varepsilon\frac{\mathrm{d}\phi}{\mathrm{d}x}\right) = -q\left(p - n + N_{\mathrm{dop}} + N_{\mathrm{ion}}\right), \tag{3.21}$$

where ε is the permittivity, q is the elementary charge, n and p are the electron and hole densities, N_{dop} represents fixed dopant charge in the transport layers (where applicable), and N_{ion} is the net ionic charge density within the perovskite.

Poisson's equation therefore determines the internal electric field, $E = -\mathrm{d}\phi/\mathrm{d}x$, that drives charge separation and transport.[22] The central point for this thesis is that mobile ions directly contribute to the space-charge term through $N_{\mathrm{ion}}(x)$. As ions redistribute under bias, the internal field profile and interfacial band bending also change, which can in turn modify where carriers accumulate and how strongly recombination is expressed at interfaces.[22]

Carrier conservation (continuity equations). Electron and hole populations are governed by continuity equations that enforce charge conservation under illumination and applied bias.[22] In one dimension, these take the form:

$$\frac{\partial n}{\partial t} = \frac{1}{q}\frac{\mathrm{d}J_n}{\mathrm{d}x} + G - R, \tag{3.22}$$

$$\frac{\partial p}{\partial t} = -\frac{1}{q}\frac{\mathrm{d}J_p}{\mathrm{d}x} + G - R, \tag{3.23}$$

where n and p are the electron and hole densities, J_n and J_p are the corresponding current densities, G is the local photogeneration rate, and R is the total recombination rate.

In words, these equations state that carrier densities change when carriers flow into or out of a region (the current-gradient term), when carriers are created by light absorption (G), or when they are removed by recombination (R).[22] For steady-state J–V conditions, the time derivatives are approximately zero, meaning that the local balance between generation, recombination, and extraction determines the measured current and voltage. In particular, the simulated V_{OC} and the shape of the J–V curve reflect how efficiently photogenerated carriers can be maintained (i.e., how strongly recombination competes with extraction) under a given internal field profile.[22]

Transport (drift–diffusion currents). Charge transport is described using the drift–diffusion approximation, in which the total current arises from two physical driving forces: (i) drift in the internal electric field and (ii) diffusion down carrier concentration gradients.[22] For electrons and holes, the corresponding current densities are:

$$J_n = q\mu_n nE + qD_n \frac{\mathrm{d}n}{\mathrm{d}x}, \tag{3.24}$$

$$J_p = q\mu_p pE - qD_p \frac{\mathrm{d}p}{\mathrm{d}x}, \tag{3.25}$$

where $\mu_{n/p}$ are the carrier mobilities, $D_{n/p}$ are diffusion coefficients, n and p are the carrier densities, and E is the local electric field.

The first term in each expression represents field-driven drift: carriers are accelerated by the internal electric field, and the resulting current scales with both the mobility and the carrier density.[22] The second term represents diffusion: carriers also move from regions of high concentration to low concentration, producing a current even in the absence of an electric field.[22] In the context of this thesis, the important point is that mobile ions reshape $E(x)$ through Poisson's equation, which can shift the relative importance of drift and diffusion across the stack. This directly affects where electrons and holes accumulate and therefore how strongly interfacial recombination is expressed.[22]

Recombination and interfaces. Carrier recombination in the perovskite absorber is modelled using a combination of bulk monomolecular (Shockley–Read–Hall, SRH) recombination and radiative (bimolecular) recombination:[22]

$$R = R_{\mathrm{SRH}} + R_{\mathrm{rad}}. \tag{3.26}$$

Conceptually, SRH recombination captures trap-assisted carrier loss (i.e., recombination mediated by defect states), while radiative recombination captures band-to-band electron–hole recombination.[22] Together, these terms set the intrinsic recombination strength of the perovskite layer and therefore influence the carrier density that can be sustained under illumination.

In addition to bulk recombination, carrier loss at the perovskite/transport-layer interfaces was described using an effective surface recombination velocity (SRV).[22] The SRV provides a convenient way to capture the net recombination strength at an interface without specifying a detailed trap model: higher SRV corresponds to more rapid carrier loss at the interface, and therefore a stronger suppression of V_{OC} and device performance when interfacial recombination dominates.[22] In the parameter sweeps used in this thesis, SRV and the transport-layer energetic offset ΔE_{TL} were varied systematically to map performance regimes and to isolate how mobile ions modify device tolerance to interfacial recombination and energetic misalignment.[9]

Representation of mobile ionic charge

To capture the mixed ionic–electronic nature of perovskite absorbers, DRIFTFUSION treats mobile ionic defects as charged species that can redistribute within the perovskite layer under applied bias.[22] In the simulations used in this thesis, ionic carriers were modelled as Schottky defects, meaning that each mobile ionic defect is accompanied by an oppositely charged counter-defect that is assumed to be immobile (a fixed background charge).[9] A single *positively charged* mobile ionic species was included, consistent with the view that halide vacancies are typically the most abundant and most conductive ionic carrier in metal-halide perovskites.[22]

Mobile ions were assumed to remain confined within the perovskite absorber, and electrochemical interfacial reactions were not explicitly included.[9] As a result, the simulations isolate the *electrostatic* consequences of ionic redistribution (i.e., how the resulting space-charge term $N_{\mathrm{ion}}(x)$ reshapes the internal electric field and interfacial band bending) and how this feeds through to carrier extraction and recombination losses.[9] Irreversible degradation pathways are therefore not modelled directly; their practical effect is instead considered indirectly through increased recombination strength at interfaces (parameterised via SRV in the sweeps discussed below).[9]

Device stack and material parameters

The simulated device stack was treated as a laterally uniform, one-dimensional multilayer structure. The perovskite absorber was modelled as an intrinsic semiconductor, with bulk trap states represented by a mid-gap SRH recombination pathway.[9] The baseline absorber parameter set used for the Chapter 4 parameter sweeps (summarised in Table 3.2) corresponds to a 1.60 eV perovskite representative of MAPI.[9] Recombination within the transport layers was neglected in these simulations; instead, losses associated with the contacts were captured through an effective interfacial recombination strength at the perovskite/transport-layer interfaces (parameterised by SRV, as described above).[9]

Table 3.2: Perovskite-layer parameters used in the drift–diffusion simulations that generate the Chapter 4 parameter sweeps.

Parameter	Value	Reference
Band gap, E_g	1.60 eV	[23]
Valence band energy, E_V	-5.4 eV	[24]
Thickness, d	400 nm	*
Carrier mobility, μ	1.0 cm^2 V^{-1} s^{-1}	[25]
SRH lifetime, τ_{SRH}	100 ns	[26]
Radiative recombination constant, B	5×10^{-11} cm^3 s^{-1}	[27]
Relative permittivity, ε_r	25	[28]
Effective density of states, $N_C = N_V$	5×10^{18} cm^{-3}	[29]

* *Typical thickness for a perovskite layer.*

Only the doped-inorganic transport-layer parameter set is included here, as it most closely reflects the experimentally studied device architecture in this thesis.[9] Unless stated otherwise, the same transport-layer parameter values were applied symmetrically to the electron and hole transport layers (ETL and HTL, respectively).

Table 3.3: Transport-layer parameters used for the doped-inorganic simulations included in Chapter 4. E_C and E_V denote the transport-layer conduction and valence band energies, respectively.

Parameter	Value
Band gap, E_g	2.50 eV
ETL Fermi level	$E_C - 0.1$ eV
HTL Fermi level	$E_V + 0.1$ eV
Energy level of trap states	mid-gap
Thickness, d	100 nm
Carrier mobility, μ	10 cm^2 V^{-1} s^{-1}
Relative permittivity, ε_r	50
Effective density of states	5×10^{18} cm^{-3}

Bias protocols: steady-state ions and frozen-ion response

When mobile ions are included, the simulated J–V response depends on the distribution of ionic charge within the perovskite, which changes with the applied bias.[22] To obtain V_{OC} values representative of a *fully stabilised* device, the simulations were therefore carried out such that ions could reach steady state at each voltage point along the J–V curve. In practice, this was achieved by using an extremely slow scan rate of 0.1 mV s^{-1}.[9] As a result, the simulated J–V curves describe the steady-state device response after ionic re-equilibration, rather than the response typically measured during a conventional laboratory J–V scan (commonly ∼10–200 mV s^{-1}).

To emulate Stabilise and Pulse (SaP)-type conditions, ions were first allowed to equilibrate at a chosen stabilisation bias and were then immobilised ("frozen") by setting the ionic mobility to zero.[9] The electronic response at this fixed ionic configuration was subsequently evaluated either by explicitly simulating a short voltage pulse, or by performing a J–V sweep on the frozen-ion state (which provides higher voltage resolution while giving an equivalent electronic response).[9] This procedure allows direct comparison between a "mobile-ion" steady-state J–V and a "frozen-ion" J–V representative of rapid electronic probing at a fixed ionic distribution.

Parameter sweeps and definitions

To explore how mobile ions influence device tolerance to imperfect interfaces, two parameters were varied systematically to generate the datasets shown in Figures 4.12–4.13.[9]

- **Surface recombination velocity (SRV).** Interfacial recombination at the perovskite/transport-layer interfaces was described using an effective surface recombination velocity. In simple terms, SRV controls how quickly carriers are lost at an interface: a larger SRV corresponds to stronger interfacial recombination.[9] Mid-gap interfacial trap states were assumed, and SRVs were taken to be equal for electrons and holes, consistent with recombination via mid-gap defect states.[9]

- **Transport-layer energetic offset, ΔE_{TL}.** Energetic misalignment between the perovskite and the adjacent transport layers was captured using an effective energy offset ΔE_{TL} at the interfaces.[9] In the simulations, ΔE_{TL} was varied symmetrically at both interfaces while keeping the intrinsic carrier densities of the transport layers constant.[9] Where possible, the built-in voltage was held at $V_{\mathrm{BI}} = 1.1$ V; for sufficiently large ΔE_{TL} values, this constraint was relaxed due to limitations in modelling cases where an electrode work function lies within a transport-layer band.[9]

For these sweeps, the coloured curves correspond to different assumed mobile ion densities, while the dashed black curve indicates the otherwise equivalent "no ion" case.[9]

Alternative absorber parameter set used for Figure 4.13

Most simulations discussed in this thesis use the 1.60 eV absorber parameter set listed in Table 3.2. However, the efficiency maps in Figure 4.13 were generated using a parameter set intended to represent a higher-efficiency, narrower-band gap absorber ($FAPbI_3$-based).[9] Relative to the 1.60 eV case, the absorber band gap was reduced to 1.50 eV and the SRH lifetime was increased to 3 μs.[9] Increasing the SRH lifetime corresponds to a reduction in trap-assisted (monomolecular) recombination in the absorber, allowing higher steady-state carrier densities to be sustained under illumination; this typically increases the achievable quasi-Fermi level splitting and therefore improves V_{OC}, provided that interfacial recombination does not dominate.[9]

For these 1.50 eV simulations, the illumination intensity was set to 1.2× AM1.5G in order to reproduce literature-reported J_{SC} values.[9] This adjustment was made because suitable optical constants (n and k) for the specific absorber composition referenced were not available. Given the long diffusion length implied by the combination of mobility and lifetime used in this parameter set, variations in the detailed generation-rate profile are not expected to alter the qualitative trends of the parameter sweeps.[9]

Limitations. These simulations represent the device as a one-dimensional, laterally uniform stack. As a result, they do not capture microstructural heterogeneity (e.g., grain-to-grain variation), spatially localised defects, or current crowding effects that may be present in real devices.[9] In addition, electrochemical reactions at the perovskite/transport-layer interfaces and irreversible degradation pathways are not included explicitly; instead, their practical impact is approximated phenomenologically through changes in the interfacial recombination strength (SRV).[9] Accordingly, the simulations are used in this thesis to identify trends, operating regimes, and physical interpretations that support the experimental observations, rather than to provide a unique fitted parameter set for any specific device.[9]

3.4 Optical Characterisation

This section describes the optical characterisation techniques used throughout this thesis to probe radiative emission, recombination dynamics, and optical absorption in perovskite thin films and related materials. These measurements provide insight into the electronic structure, recombination behaviour, and overall suitability of the materials for photovoltaic applications, and enable correlations among optical properties, material quality, and device performance. A general description of each technique is provided first, followed by the specific experimental protocols, instrumentation, and measurement conditions used in the relevant results chapters where required.

3.4.1 Steady-state fluorescence

In steady-state photoluminescence (PL) measurements, a sample is excited with continuous light and the resulting emission spectrum is recorded as a function of wavelength. Upon photoexcitation, electrons are promoted to higher-energy states, generating electron–hole pairs. Radiative recombination of these carriers produces emitted photons whose energies reflect the electronic structure of the material.

The shape and peak position of the emission spectrum provide information about the nature of the optical transition and the relative energetic alignment of electronic states. The overall emission intensity reflects the balance between radiative and non-radiative recombination processes under constant excitation conditions. In dilute-solution measurements, intermolecular interactions and solid-state packing effects are minimised, so that the emission primarily reflects the intrinsic molecular electronic structure rather than morphology- or interface-dependent effects.

Chapter 6 PL

The PL measurement in Chapter 6 was conducted by Dr Dylan Wilkinson at the University of Glasgow.

Fluorescence emission spectra were recorded in dichloromethane at a concentration of 10^{-7} mol L^{-1} using an excitation wavelength of 391 nm.

3.4.2 Time-resolved Photoluminescence

In a time-resolved photoluminescence (TRPL) measurement, a short laser pulse photoexcites the sample, creating an excess population of electrons and holes. These charge carriers can then recombine through a range of pathways, which are summarised in Figure 3.6a. In *radiative* recombination, an electron and a hole recombine and emit a photon. In *non-radiative* recombination, the carrier energy is lost to heat without emitting light, as discussed in section 2.1.4. Although bimolecular recombination in semiconductors is commonly associated with radiative band-to-band recombination, the physical origin of an effective non-radiative bimolecular contribution in halide perovskites remains an area of ongoing discussion. Proposed mechanisms include multiphonon-assisted band-to-band recombination and defect-assisted Auger-like processes involving trapped carriers.[27] Within this work, the non-radiative bimolecular contribution is therefore treated as an effective carrier-density-dependent loss pathway rather than a uniquely identified microscopic recombination mechanism.

TRPL measures the photoluminescence intensity, $\Phi_{\mathrm{PL}}(t)$, as a function of time after the excitation pulse, such that the decay shape provides a time-resolved fingerprint of how quickly photoexcited carriers are removed. An illustrative example of a TRPL trace is shown in Figure 3.6b.

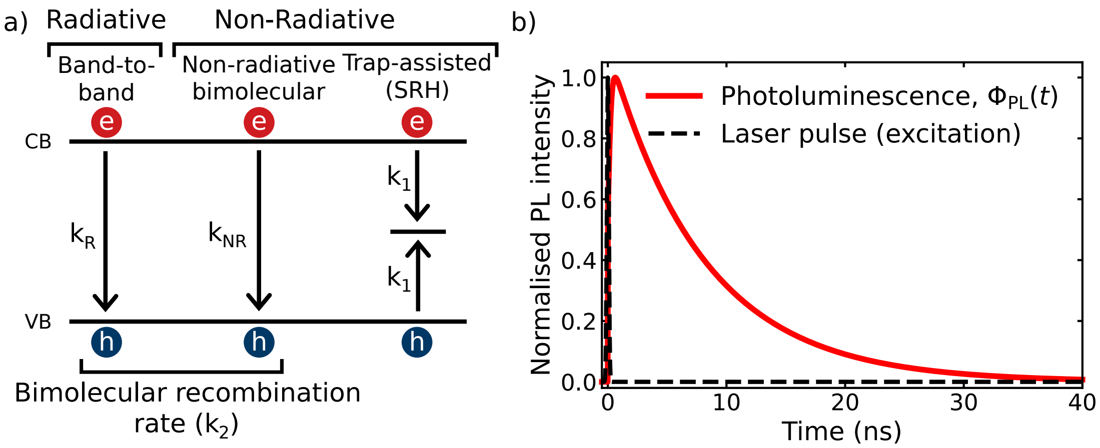

Figure 3.6: Schematic illustration of time-resolved photoluminescence (TRPL) and its connection to the rate-equation model. a) Following pulsed photoexcitation, excess electrons and holes recombine through radiative band-to-band recombination (k_{R}), effective carrier-density-dependent non-radiative loss pathways represented by k_{NR}, and trap-assisted (Shockley–Read–Hall, SRH) recombination represented here by an effective first-order loss term (k_1). Radiative recombination together with additional carrier-density-dependent non-radiative loss pathways contribute to the effective second-order term $k_2 n^2(t)$, while SRH/interfacial loss processes are captured by the first-order term $k_1 n(t)$. Adapted from Ref. [30] with permission from the PCCP Owner Societies. b) Illustrative TRPL trace showing the excitation pulse (dashed line) and the subsequent normalised photoluminescence decay, $\Phi_{\mathrm{PL}}(t)$ (solid line), measured as a function of time after excitation. The plotted decay is schematic and is included for clarity; it is not experimental data.

In an idealised single layer, a faster PL decay would indicate faster carrier loss. However, in the partial device stacks used throughout this thesis, the measured transient can reflect a combination of bulk recombination, interfacial non-radiative losses, and charge transfer into adjacent layers. This means that similar decay kinetics can originate from different physical processes. For this reason, TRPL is used here primarily as a comparative probe of how the buried interface influences carrier dynamics, and is interpreted alongside complementary analyses rather than treated as a unique measure of a single recombination lifetime.

In Chapters 5 and 6, the decays are analysed using a simple rate-equation model that captures the two dominant recombination behaviours typically observed in lead–halide perovskites over the excitation range used here: an approximately first-order loss channel (often associated with trap-assisted or interfacial recombination) and a second-order loss channel associated with electron–hole recombination.[31] The model is written as

$$\frac{dn}{dt} = -k_1 n(t) - k_2 n^2(t), \tag{3.27}$$

where $n(t)$ is the time-dependent excess carrier density generated by the laser pulse. Under TRPL conditions, the photoexcitation creates electrons and holes in pairs, such that the excess electron and hole densities are comparable ($\Delta n \approx \Delta p$). In this case, a recombination process that depends on the product of electron and hole densities reduces to a term proportional to n^2, motivating the bimolecular term $k_2 n^2(t)$.

The term $k_1 n(t)$ represents an *effective* first-order loss pathway for charge carriers. In practical terms, this contribution can arise from Shockley–Read–Hall (SRH) recombination via trap states, as well as recombination at interfaces, both of which typically scale approximately linearly with the excess carrier density.[30] The parameter k_1 should therefore not be interpreted as the rate constant of a single, specific defect. Instead, it captures the combined strength of all first-order processes that shorten the photoluminescence (PL) decay.[30]

The term $k_2 n^2(t)$ describes bimolecular recombination, which includes radiative band-to-band recombination as well as non-radiative processes involving the interaction of two charge carriers. In time-resolved photoluminescence (TRPL) measurements, the detected signal $\Phi_{\mathrm{PL}}(t)$ is proportional to the radiative component of this bimolecular recombination.[30] However, the overall *shape* of the decay is governed by the competition between all recombination pathways included in the rate equation, not solely the radiative contribution.

A useful feature of this model is that it naturally describes a change in the dominant recombination mechanism as the carrier density decreases following the pulse. At early times (high n), the n^2 term can dominate, making the decay more strongly density-dependent, whereas at later times (low n), the linear term can dominate, and the decay approaches an exponential form. Fitting the TRPL transients with Eq. (3.27) therefore provides a compact way to compare how strongly first-order and bimolecular losses contribute across different interfaces, and enables the relative weighting of the two terms to be reported consistently.

Chapter 5 TRPL

TRPL measurements in this chapter were conducted by Muhammad Umair Ali at the University of Hong Kong.

TRPL measurements in Chapter 5 were performed using a 375 nm pulsed laser diode (Edinburgh FLS1000 photoluminescence spectrometer). The laser pulse width was 200 ns, with switchable repetition rates of 1 MHz and 200 kHz.

Samples consisted of ITO/NiO$_x$ nanoparticle/SAM/perovskite half-stacks, fabricated by spin coating under the same conditions used for the corresponding solar cell devices.

Chapter 6 TRPL

TRPL measurements in this chapter were conducted by Dr Wenhui Li at the Institute of Chemical Research of Catalonia.

TRPL measurements in Chapter 6 were carried out using an Edinburgh Instruments LifeSpec-II system with 470 nm pulsed laser excitation. Excitation was performed through the glass/ITO side of the sample to probe the buried perovskite/contact interface.

3.4.3 Differential Lifetime Analysis

While direct fitting of TRPL transients yields effective recombination rate constants, additional insight can be obtained by examining the instantaneous decay rate over time. This is achieved through differential lifetime analysis, defined as

$$\tau_{\mathrm{PL}}(t) = -\left(\frac{d \ln \Phi_{\mathrm{PL}}(t)}{dt}\right)^{-1}, \tag{3.28}$$

where $\Phi_{\mathrm{PL}}(t)$ is the time-dependent photoluminescence intensity.[32]

Physically, $\tau_{\mathrm{PL}}(t)$ represents the instantaneous lifetime of the photoexcited carrier population at a given time after excitation. If recombination were governed purely by a single first-order process, τ_{PL} would be constant in time. Deviations from a constant lifetime therefore indicate density-dependent recombination behaviour.[32]

Within the framework of the rate equation introduced above,

$$\frac{dn}{dt} = -k_1 n - k_2 n^2, \tag{3.29}$$

the instantaneous lifetime can be expressed as

$$\tau(n) = \frac{1}{k_1 + k_2 n}. \tag{3.30}$$

This relationship highlights that the effective lifetime depends explicitly on carrier density. At early times, when n is large, the $k_2 n$ term can dominate and the lifetime decreases with increasing carrier density. At later times, as n decreases, the lifetime approaches $1/k_1$, corresponding to first-order recombination. Differential lifetime analysis, therefore, provides a direct way to visualise the transition between bimolecular-dominated and first-order-dominated regimes.[32]

Experimental Analysis Methodology

Direct numerical differentiation of raw TRPL data is highly sensitive to noise, particularly at late times where the signal approaches the detection limit. To obtain stable differential lifetime traces, the measured $\Phi_{\mathrm{PL}}(t)$ transients were first fitted using a multi-exponential analytical function of the form

$$\Phi_{\mathrm{fit}}(t) = \sum_{i=1}^{N} A_i \exp(-t/\tau_i), \tag{3.31}$$

where A_i and τ_i are positive fitting parameters. The logarithm of the fitted decay was then differentiated numerically with respect to time, and the differential lifetime was calculated as $\tau_{\mathrm{PL}}(t) = (-d \ln \Phi_{\mathrm{fit}}/dt)^{-1}$.

Rather than applying the differential lifetime method directly to the measured transient, a multi-exponential fitting approach was adopted in this work. This choice was motivated by the numerical behaviour of the differential method at late times. In that approach, the lifetime is obtained from the logarithmic slope of the signal,

$$\tau(t) = -\left(\frac{d\ \ln \Phi(t)}{dt}\right)^{-1} = -\frac{\Phi(t)}{d\Phi(t)/dt}, \tag{3.32}$$

which requires numerical differentiation of the measured data. While this performs well at early times, when the signal is large and smoothly varying, it becomes increasingly sensitive to noise as the photoluminescence intensity approaches the detection limit. Numerical differentiation amplifies small fluctuations, and because the expression for $\tau(t)$ involves division by $d\Phi/dt$, even minor noise-induced variations in the slope can lead to disproportionately large and unphysical excursions in the extracted lifetime.

In practice, this manifests as an apparent divergence or strong scatter in $\tau(t)$ at late times, not because the underlying recombination physics changes abruptly, but because the calculation becomes ill-conditioned as the signal-to-noise ratio decreases. The multi-exponential fitting approach used here instead models the decay directly, allowing the full transient to be described without relying on a noise-amplifying derivative operation. This provides a more stable and physically interpretable representation of the recombination dynamics across the entire time range.

3.4.4 Ultraviolet–Visible Absorption Spectroscopy

Ultraviolet–Visible Absorption Spectroscopy (UV–Vis) is used to probe the optical transitions of molecules and semiconducting materials. When light passes through a sample, photons with energies matching allowed electronic transitions are absorbed, promoting electrons from lower to higher energy states.

In molecular systems, absorption typically corresponds to transitions between frontier orbitals, such as from the highest occupied molecular orbital (HOMO) to the lowest unoccupied molecular orbital (LUMO). In semiconductors, absorption corresponds to transitions across the band gap, from the valence band to the conduction band.

The measured absorbance, A, is related to the incident and transmitted light intensities through the Beer–Lambert law,

$$A = \log_{10}\left(\frac{I_0}{I}\right), \tag{3.33}$$

where I_0 is the incident light intensity and I is the transmitted intensity.

Experimental Details

UV–Vis absorption spectra were recorded using a Shimadzu UV-3600 UV/visible/IR spectrometer.

In Chapter 5, the thin-film absorption measurements were performed on samples prepared under the same conditions as the corresponding solar cell devices. The double cation perovskite measurement was performed by Dr Wai Kin Yiu, and the methylammonium lead iodide (MAPI) film measurement was performed by me at the University of Glasgow.

In Chapter 6, absorption spectra of SAM molecules were measured in dichloromethane at a concentration of 10^{-6} mol L^{-1}, and the measurement was conducted by Dr Dylan Wilkinson at the University of Glasgow.

3.4.5 Tauc Analysis

Tauc analysis was used to estimate the optical band gap, E_g, from UV–Vis absorption spectra by analysing the absorption edge in photon-energy space.[33] Near the band edge, the Tauc relationship can be written as

$$(\alpha h\nu)^m \propto (h\nu - E_\mathrm{g}), \tag{3.34}$$

where α is the absorption coefficient, $h\nu$ is the photon energy, and m depends on the nature of the optical transition. In this work, a direct allowed transition was assumed and therefore $m = 2$.

In practice, the measured absorbance (A) was used as a proxy for the absorption coefficient, assuming a constant film thickness for comparative analysis. The wavelength axis was first converted to photon energy using

$$E(\mathrm{eV}) = \frac{1240}{\lambda(\mathrm{nm})}. \tag{3.35}$$

The absorbance data were baseline-corrected by subtracting the minimum absorbance value, ensuring that the absorption onset began from zero. The Tauc quantity was then calculated as $(AE)^2$, consistent with a direct allowed transition.

To extract the band gap, the analysis was restricted to the photon energy range 1.4–1.8 eV, which encompasses the absorption edge. Within this window, the region corresponding to the steepest part of the absorption edge was identified by calculating the gradient of $(AE)^2$ with respect to energy (dY/dE). Points where the gradient exceeded 60% of its maximum value were selected, and a linear fit was performed over this region. The optical band gap, E_g, was obtained from the intercept of the fitted line with the energy axis ($Y = 0$).

3.5 Chemical Characterisation

A range of chemical and surface-sensitive techniques were employed to characterise the electronic structure and interfacial properties of the materials used in this thesis. These measurements provide complementary information to device and optical measurements, enabling a more complete understanding of energy level alignment, interfacial chemistry, and molecular electronic properties. This section provides a general description of the measurement techniques used in the results chapters, followed by more specific experimental protocols, as needed.

3.5.1 Cyclic Voltammetry

Cyclic voltammetry (CV) is an electrochemical technique used to probe the redox behaviour of molecular species. In a typical measurement, the potential applied to the working electrode is swept linearly with time to a defined maximum value and then reversed, while the resulting current is recorded. Oxidation and reduction processes appear as peaks in the current–potential trace, corresponding to electron transfer between the analyte and the electrode.

In molecular semiconductors, the oxidation onset is commonly used to estimate the energy of the highest occupied molecular orbital (HOMO), while the reduction onset can be used to estimate the lowest unoccupied molecular orbital (LUMO).[34] CV therefore provides an electrochemical estimate of frontier orbital energies, which are relevant to understanding energy-level alignment in optoelectronic devices.

The oxidation onset potential ($E_{\text{ox}}^{\text{onset}}$) is used to estimate the HOMO energy according to

$$E_{\text{HOMO}} = -\left(E_{\text{ox}}^{\text{onset}} + E_{\text{ref}}\right)\ \text{eV}, \tag{3.36}$$

where E_{ref} is the energy level of the reference electrode relative to vacuum. When potentials are referenced to the ferrocene/ferrocenium (Fc/Fc$^+$) redox couple, the commonly used value of $E_{\text{ref}} = 4.8$ eV relative to vacuum is adopted. Where reduction processes were observed, the LUMO energy is estimated analogously using the reduction onset potential.

It is important to note that CV-derived energy levels represent electrochemical oxidation and reduction potentials in solution, and therefore reflect the energy required to remove or add an electron under those specific conditions. These values may differ from solid-state energy levels due to solvent effects, intermolecular interactions, and interfacial dipoles.

Experimental Details

CV measurements were carried out by Dr Dylan Wilkinson at the University of Glasgow.

Cyclic voltammetry measurements were carried out in dichloromethane at a concentration of 10^{-4} mol L^{-1} using 1 mol L^{-1} tetrabutylammonium hexafluorophosphate (TBAPF$_6$) as the supporting electrolyte. A scan rate of 0.1 V s^{-1} was employed. Potentials were referenced to the ferrocenium/ferrocene (Fc/Fc$^+$) redox couple. Observed differences in peak current magnitude between samples arise from variations in diffusion coefficients and electrochemical kinetics in solution, and do not directly reflect differences in orbital energies.

3.5.2 X-ray Photoelectron Spectroscopy

X-ray photoelectron spectroscopy (XPS) is a surface-sensitive technique used to determine elemental composition and chemical bonding environments. In XPS, a material is irradiated with monochromatic X-rays, causing the emission of core-level electrons via the photoelectric effect.[35] The kinetic energy of the emitted electrons is measured, and their binding energy is calculated according to

$$E_{\text{B}} = h\nu - E_{\text{K}} - \phi, \tag{3.37}$$

where E_B is the electron binding energy, $h\nu$ is the incident photon energy, E_K is the measured kinetic energy of the photoelectron, and ϕ is the spectrometer work function.

Because each element possesses characteristic core-level binding energies, XPS enables identification of the elemental composition of a surface. Additionally, small shifts in binding energy (chemical shifts) provide information about the chemical state of an element, such as oxidation state or bonding environment.[35]

Photoelectrons can only escape from a shallow depth within a material before losing energy through scattering. As a result, XPS primarily probes the top few nanometres of a surface. This shallow sampling depth makes the technique particularly useful for examining self-assembled molecules (SAMs) and interfacial chemistry, where the chemical composition and bonding at the outermost surface are of primary interest.

Experimental Details

XPS measurements were carried out and interpreted by Dr Marcin Giza and Dr Elisabetta Arca at the University of Glasgow.

XPS measurements were performed using a Kratos Analytical AXIS Supra+ system equipped with a monochromatic Al Kα X-ray source (1486.6 eV). No charge neutraliser was used. To ensure good electrical contact and minimise surface charging, samples were grounded using copper tape to provide direct contact between the sample, the mounting bar, and the instrument.

Samples were prepared using the same procedures as for solar cell fabrication (outlined in section 3.1.6) and measured as-deposited without further treatment. To minimise air exposure, sample preparation was carried out under a nitrogen atmosphere, and samples were transferred to the XPS chamber using a purge box directly attached to the instrument.

The chamber pressure during measurements was maintained between 8.3×10^{-8} and 1.3×10^{-7} torr.

3.5.3 Kelvin Probe Force Microscopy

Kelvin probe force microscopy (KPFM) is a scanning probe technique that measures local surface potential variations with nanometre-scale spatial resolution. KPFM operates as an extension of atomic force microscopy (AFM), in which a conductive cantilever tip scans across the surface while an electrical bias is applied between the tip and the sample.[36]

When the tip and sample are electrically connected, a contact potential difference (CPD) arises due to differences in their work functions. This potential difference generates an electrostatic force between the tip and sample. In KPFM, an external DC bias is applied to nullify this electrostatic interaction. The bias required to cancel the force corresponds to the local contact potential difference and is related to the work functions of the tip and sample by

$$\Phi_{\mathrm{sample}} = \Phi_{\mathrm{tip}} - V_{\mathrm{CPD}}, \tag{3.38}$$

where Φ_{tip} and Φ_{sample} are expressed in electron volts (eV), and V_{CPD} is the measured contact potential difference in volts.

The measured CPD, therefore, reflects variations in the surface work function.[36] Changes in surface chemistry, molecular dipoles, charge accumulation, or band bending can modify the local surface potential. As a result, KPFM provides spatially resolved information about interfacial energetics and electrostatic potential distributions.

Experimental Details

KPFM measurements were carried out and interpreted by Dr Tik Lun Leung and Professor Anita W. Y. Ho-Baillie at the University of Sydney.

KPFM measurements were performed using a Neaspec s-SNOM system equipped with a platinum–iridium (PtIr5, 95:5 Pt:Ir) coated conductive AFM probe (Arrow EFM, Nanoworld). Surface potential maps were acquired under illumination using the built-in LED within the sample compartment.

The tip work function was calibrated against a reference gold film prior to measurement. All samples were prepared with the structure ITO/NiO$_x$ nanoparticles/SAM/DC/PEAI via spin coating under the same conditions used for solar cell fabrication.

3.5.4 Density Functional Theory

Density functional theory (DFT) is a quantum mechanical method used to calculate the electronic structure of atoms and molecules. Rather than solving the many-electron Schrödinger equation directly, DFT describes the system in terms of its electron density. From this electron density, molecular geometries, orbital distributions, dipole moments, and total energies can be obtained.[37]

For molecular semiconductors, DFT is commonly used to determine optimised molecular structures and to estimate properties such as frontier orbital distributions and permanent dipole moments. These quantities provide insight into molecular electronic structure and can help rationalise experimentally observed trends in energy level alignment and interfacial behaviour.[37]

Computational Details

DFT calculations were performed by Dr Dylan Wilkinson at the University of Glasgow.

All calculations were performed using Gaussian 09 (Revision D.01).[38] Geometry optimisations were carried out using the B3LYP hybrid exchange–correlation functional with the 3-21G basis set.[39, 40]

B3LYP is a widely used hybrid functional that provides a good balance between computational efficiency and reliability for molecular geometry optimisation.[39] The 3-21G basis set was selected to obtain optimised structures and qualitative electronic properties at modest computational cost.[40] While larger basis sets can improve quantitative accuracy, the level of theory employed here is sufficient for comparative analysis of dipole magnitudes and orbital distributions.

All calculations were performed in the gas phase. The results are therefore interpreted as intrinsic molecular properties, with the understanding that solid-state packing and interfacial effects may modify these values in devices.

3.6 Structural & Morphological Characterisation

Understanding the structural and morphological properties of deposited films is essential for interpreting their electronic and optoelectronic behaviour within working devices. In perovskite solar cells, variations in surface roughness, grain size, crystallinity, and film uniformity can strongly influence interfacial contact quality, charge extraction, and recombination pathways. Structural and morphological characterisation, therefore, provides context for the electrical measurements discussed in subsequent sections, allowing correlations between film microstructure and device performance. This section provides a general description of the measurement techniques used in this thesis, followed by specific instrument details and experimental protocols.

3.6.1 X-ray Diffraction

X-ray diffraction (XRD) is a technique used to determine the crystal structure of materials. When X-rays are directed onto a crystalline sample, they are scattered by the regularly spaced atomic planes within the material.[41] At certain angles, the scattered waves interfere constructively, producing diffraction peaks. These angles are described by Bragg's law:

$$n\lambda = 2d \sin\theta, \tag{3.39}$$

where λ is the wavelength of the incident X-rays, d is the spacing between crystallographic planes, θ is the angle between the incident beam and the crystal planes, and n is an integer representing the diffraction order. A schematic illustration of X-ray diffraction is shown in Figure 3.7

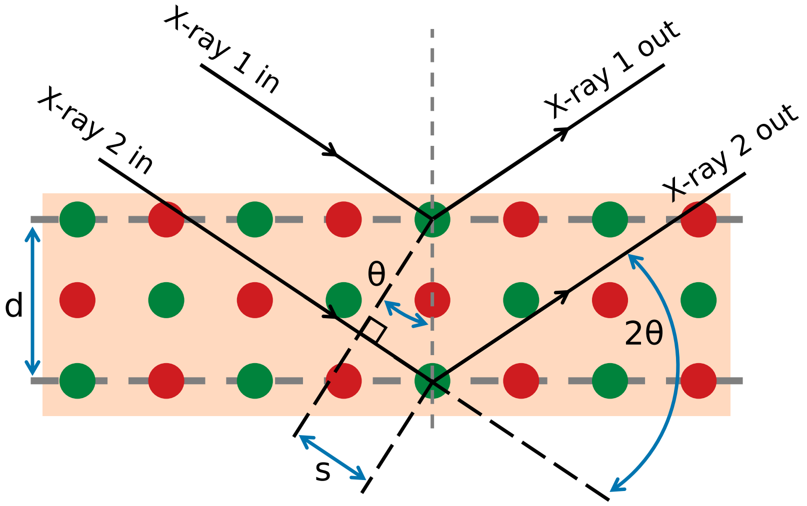

Figure 3.7: Schematic illustration of X-ray diffraction in a crystal lattice. The red and green circles represent atomic diffraction centres arranged in parallel crystallographic planes separated by an interplanar spacing d. An incident X-ray beam is reflected from lattice planes at the Bragg angle θ, producing a diffracted beam at a measured angle 2θ. The quantity s denotes half of the path difference between X-ray 1 and X-ray 2, such that constructive interference occurs when the total path difference equals $2d \sin\theta$, satisfying Bragg's law $n\lambda = 2d \sin\theta$.

By measuring the intensity of diffracted X-rays as a function of angle (typically reported as 2θ), a diffraction pattern is obtained. The positions of the peaks in this pattern are characteristic of the crystal structure and allow identification of the material phase. The relative intensities of the peaks provide information about preferred orientation within thin films, while changes in peak width can give qualitative insight into crystallite size and structural disorder.[41]

Experimental Details

XRD measurements were conducted by Dr Wai Kin Yiu at the University of Glasgow.

X-ray diffraction patterns were collected using a Rigaku MiniFlex600 diffractometer equipped with a Cu Kα X-ray source. Measurements were performed in θ–2θ scan mode over a range of 5° to 50°, with a step size of 0.01°.

Thin-film samples were prepared by spin coating using the same fabrication procedure employed for the corresponding solar cell devices and were measured as-deposited without further treatment.

3.6.2 Scanning Electron Microscopy

Scanning electron microscopy (SEM) is used to examine the surface morphology of materials with high spatial resolution. In SEM, a focused beam of high-energy electrons is scanned across the sample surface. As the electrons interact with the material, they generate a range of signals, including secondary electrons and backscattered electrons.[42] These emitted electrons are collected to form an image.

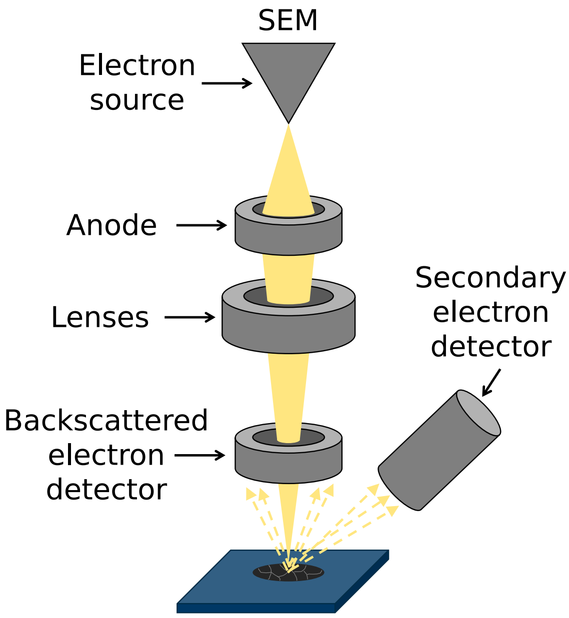

Figure 3.8: Simplified schematic of scanning electron microscopy (SEM). An electron beam is generated at the electron source and focused by a series of electromagnetic lenses onto the sample surface. Interactions between the primary beam and the sample produce secondary electrons and backscattered electrons, which are collected by dedicated detectors to generate contrast related to surface topography and compositional variation.

Secondary electrons are particularly sensitive to surface topography, as they originate from the near-surface region of the sample. As a result, SEM images obtained with secondary electron detection provide detailed information on surface features, including grain structure, film coverage, and morphological defects.[42]

Because the electron beam is scanned point-by-point across the surface, the technique produces high-resolution images that reveal microstructural features on the nanometre-to-micrometre scale. SEM is therefore well-suited to examining thin-film perovskite layers, where grain size, surface coverage, and uniformity are important for device performance.

Experimental Details

SEM measurements were conducted by Dr Wai Kin Yiu at the University of Glasgow.

Scanning electron microscopy images were acquired using a Hitachi S-4800 field-emission scanning electron microscope. An accelerating voltage of 5 kV was used for all measurements.

Samples were measured as-deposited, prepared under the same conditions as the corresponding solar cell devices.

3.6.3 Atomic Force Microscopy

Atomic force microscopy (AFM) is a scanning probe technique used to measure surface topography with nanometre-scale resolution. In AFM, a sharp tip mounted on a flexible cantilever is scanned across the sample surface. As the tip moves over surface features, interactions between the tip and the sample deflect the cantilever. This deflection is monitored using a laser reflected from the back of the cantilever onto a position-sensitive photodetector.[43]

By recording the cantilever response as the tip scans across the surface, a height map of the sample is reconstructed. The resulting image represents the local surface topography, allowing visualisation of grain structure, surface coverage, and nanoscale morphological features.[43]

AFM data can be displayed either as two-dimensional height maps or as three-dimensional renderings of the same topographic information. In addition to qualitative imaging, quantitative roughness metrics can be extracted. The root-mean-square (RMS) roughness, R_{RMS}, is defined as

$$R_{\mathrm{RMS}} = \sqrt{\frac{1}{N}\sum_{i=1}^{N}(z_i - \bar{z})^2}, \tag{3.40}$$

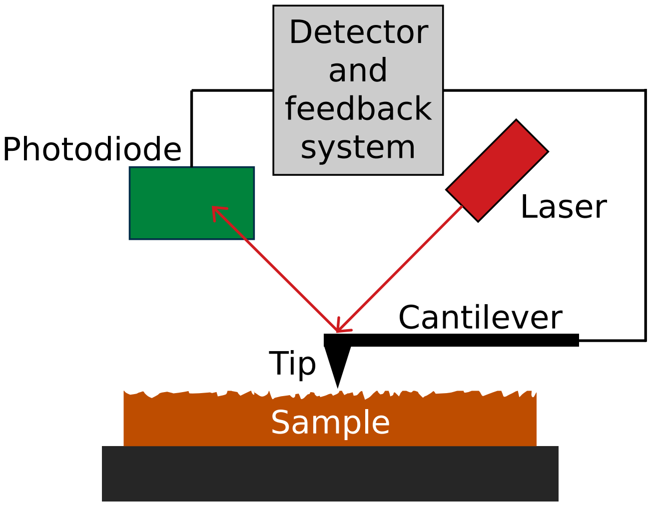

Figure 3.9: Simplified schematic of atomic force microscopy (AFM). A sharp tip mounted on a flexible cantilever interacts with the sample surface. Cantilever deflection is monitored by reflecting a laser beam onto a position-sensitive photodiode. The detected signal is fed into a feedback system that adjusts the tip–sample separation, allowing surface topography to be reconstructed with nanoscale resolution.

where z_i is the height at each measured point and $\bar{z}$ is the mean surface height. This parameter provides a statistical measure of surface roughness.

Experimental Details

AFM measurements shown in Chapter 5 were collected by Dr Tik Lun Leung at the University of Sydney; the measurements shown in Chapter 6 were collected by Dr Wenhui Li at the Institute of Chemical Research of Catalonia.

AFM topography images in Chapter 5 were obtained using a Neaspec s-SNOM system equipped with a PtIr5-coated AFM probe (Arrow EFM, Nanoworld). Height maps were acquired to characterise surface topography.

AFM topography images in Chapter 6 were acquired using an AFM NanoObserver (Concept Scientific Instruments, France) operated in resonant mode. The acquired images were analysed using the open-source software Gwyddion (Version 2.55).[44]

Three-dimensional renderings and RMS roughness values were generated from the measured topographic data using the instrument software.

Samples were prepared under the same conditions used for solar cell fabrication and were measured as-deposited.

3.6.4 Contact Angle Measurements

Contact angle measurements are used to evaluate a surface's wettability. When a liquid droplet is placed on a solid surface, it assumes a shape determined by the balance of interfacial tensions between the solid, the liquid, and the surrounding atmosphere. The contact angle, θ, is defined as the angle formed between the solid surface and the tangent to the liquid droplet at the contact point.[45]

The magnitude of the contact angle reflects the substrate's surface energy. A low contact angle indicates strong interaction between the liquid and the surface (high wettability), whereas a high contact angle indicates weaker interaction and a more hydrophobic surface. This relationship is described by Young's equation,

$$\gamma_{\mathrm{SV}} = \gamma_{\mathrm{SL}} + \gamma_{\mathrm{LV}} \cos\theta, \tag{3.41}$$

where γ_{SV}, γ_{SL}, and γ_{LV} are the solid–vapour, solid–liquid, and liquid–vapour interfacial tensions, respectively.[45]

Experimental Details

Contact angle measurements were collected by Dr Wenhui Li at the Institute of Chemical Research of Catalonia.

Contact angle measurements were performed using an optical tensiometer (Attension Theta Flex, Biolin Scientific, Sweden) employing the sessile drop method. Droplet profiles were analysed using the instrument software to extract static contact angle values.

References

(1) Vig, J.; LeBus, J. *IEEE Transactions on Parts, Hybrids, and Packaging* **1976**, *12*, 365–370.

(2) Ouedraogo, N. A. N.; Odunmbaku, G. O.; Guo, B.; Chen, S.; Lin, X.; Shumilova, T.; Sun, K. *ACS Applied Materials & Interfaces* **2022**, *14*, 34303–34327.

(3) Abate, A.; Leijtens, T.; Pathak, S.; Teuscher, J.; Avolio, R.; Errico, M. E.; Kirkpatrik, J.; Ball, J. M.; Docampo, P.; McPherson, I.; Snaith, H. J. *Physical Chemistry Chemical Physics* **2013**, *15*, 2572.

(4) Wang, Y.; Lin, J.; He, Y.; Zhang, Y.; Liang, Q.; Liu, F.; Zhou, Z.; Chan, C. C. S.; Li, G.; Feng, S.-P.; Ng, A. M. C.; Wong, K. S.; Popović, J.; Djurišić, A. B. *Solar RRL* **2022**, *6*, 2200224.

(5) You, J.; Meng, L.; Song, T.-B.; Guo, T.-F.; Yang, Y. (; Chang, W.-H.; Hong, Z.; Chen, H.; Zhou, H.; Chen, Q.; Liu, Y.; De Marco, N.; Yang, Y. *Nature Nanotechnology* **2016**, *11*, 75–81.

(6) Saliba, M.; Matsui, T.; Seo, J.-Y.; Domanski, K.; Correa-Baena, J.-P.; Nazeeruddin, M. K.; Zakeeruddin, S. M.; Tress, W.; Abate, A.; Hagfeldt, A.; Grätzel, M. *Energy & Environmental Science* **2016**, *9*, 1989–1997.

(7) Angus, F. J.; Yiu, W. K.; Mo, H.; Leung, T. L.; Ali, M. U.; Li, Y.; Wang, J.; Ho-Baillie, A. W. Y.; Cooke, G.; Djurišić, A. B.; Docampo, P. *The Journal of Physical Chemistry Letters* **2024**, *15*, 10686–10695.

(8) Hill, N. S.; Cowley, M. V.; Gluck, N.; Fsadni, M. H.; Clarke, W.; Hu, Y.; Wolf, M. J.; Healy, N.; Freitag, M.; Penfold, T. J.; Richardson, G.; Walker, A. B.; Cameron, P. J.; Docampo, P. *Advanced Materials* **2023**, *35*, 2302146.

(9) Hart, L. J. F.; Angus, F. J.; Li, Y.; Khaleed, A.; Calado, P.; Durrant, J. R.; Djurišić, A. B.; Docampo, P.; Barnes, P. R. F. *Energy & Environmental Science* **2024**, *17*, 7107–7118.

(10) Endres, J.; Egger, D. A.; Kulbak, M.; Kerner, R. A.; Zhao, L.; Silver, S. H.; Hodes, G.; Rand, B. P.; Cahen, D.; Kronik, L.; Kahn, A. *The Journal of Physical Chemistry Letters* **2016**, *7*, 2722–2729.

(11) Sherkar, T. S.; Momblona, C.; Gil-Escrig, L.; Ávila, J.; Sessolo, M.; Bolink, H. J.; Koster, L. J. A. *ACS Energy Letters* **2017**, *2*, 1214–1222.

(12) Jiang, C.-S.; Yang, M.; Zhou, Y.; To, B.; Nanayakkara, S. U.; Luther, J. M.; Zhou, W.; Berry, J. J.; van de Lagemaat, J.; Padture, N. P.; Zhu, K.; Al-Jassim, M. M. *Nature Communications* **2015**, *6*, 8397.

(13) Mantri, P.; Rizvi, S.; Mazhari, B. *Organic Electronics* **2013**, *14*, 2034–2038.

(14) Ravishankar, S.; Liu, Z.; Rau, U.; Kirchartz, T. *PRX Energy* **2022**, *1*, 013003.

(15) Almora, O.; Aranda, C.; Mas-Marzá, E.; Garcia-Belmonte, G. *Applied Physics Letters* **2016**, *109*, 173903.

(16) Peña-Camargo, F.; Thiesbrummel, J.; Hempel, H.; Musiienko, A.; Le Corre, V. M.; Diekmann, J.; Warby, J.; Unold, T.; Lang, F.; Neher, D.; Stolterfoht, M. *Applied Physics Reviews* **2022**, *9*, 021409.

(17) Pockett, A.; Eperon, G. E.; Sakai, N.; Snaith, H. J.; Peter, L. M.; Cameron, P. J. *Physical Chemistry Chemical Physics* **2017**, *19*, 5959–5970.

(18) Jacobs, D. A.; Wu, Y.; Shen, H.; Barugkin, C.; Beck, F. J.; White, T. P.; Weber, K.; Catchpole, K. R. *Physical Chemistry Chemical Physics* **2017**, *19*, 3094–3103.

(19) Wang, H.; Zhou, M.; Luo, H. *ACS Omega* **2018**, *3*, 1445–1450.

(20) Van Reenen, S.; Kemerink, M.; Snaith, H. J. *The Journal of Physical Chemistry Letters* **2015**, *6*, 3808–3814.

(21) Heaney, M. B. In *Electrical Measurement, Signal Processing, and Displays*, 2003, pp 7–1.

(22) Calado, P.; Gelmetti, I.; Hilton, B.; Azzouzi, M.; Nelson, J.; Barnes, P. R. F. *Journal of Computational Electronics* **2022**, *21*, 960–991.

(23) Yamada, Y.; Nakamura, T.; Endo, M.; Wakamiya, A.; Kanemitsu, Y. *Applied Physics Express* **2014**, *7*, 032302.

(24) Sharif, R.; Khalid, A.; Ahmad, S. W.; Rehman, A.; Qutab, H. G.; Akhtar, H. H.; Mahmood, K.; Afzal, S.; Saleem, F. *Nanoscale Advances* **2023**, *5*, 3803–3833.

(25) Lim, J.; Kober-Czerny, M.; Lin, Y.-H.; Ball, J. M.; Sakai, N.; Duijnstee, E. A.; Hong, M. J.; Labram, J. G.; Wenger, B.; Snaith, H. J. *Nature Communications* **2022**, *13*, 4201.

(26) Stranks, S. D.; Eperon, G. E.; Grancini, G.; Menelaou, C.; Alcocer, M. J. P.; Leijtens, T.; Herz, L. M.; Petrozza, A.; Snaith, H. J. *Science* **2013**, *342*, 341–344.

(27) Kirchartz, T.; Márquez, J. A.; Stolterfoht, M.; Unold, T. *Advanced Energy Materials* **2020**, *10*, 1904134.

(28) Bertoluzzi, L.; Boyd, C. C.; Rolston, N.; Xu, J.; Prasanna, R.; O'Regan, B. C.; McGehee, M. D. *Joule* **2020**, *4*, 109–127.

(29) Leijtens, T.; Eperon, G. E.; Barker, A. J.; Grancini, G.; Zhang, W.; Ball, J. M.; Kandada, A. R. S.; Snaith, H. J.; Petrozza, A. *Energy & Environmental Science* **2016**, *9*, 3472–3481.

(30) Péan, E. V.; Dimitrov, S.; De Castro, C. S.; Davies, M. L. *Physical Chemistry Chemical Physics* **2020**, *22*, 28345–28358.

(31) Péan, E. V.; Davies, M. L. *Journal of Chemical Information and Modeling* **2023**, *63*, 4477–4482.

(32) Krogmeier, B.; Staub, F.; Grabowski, D.; Rau, U.; Kirchartz, T. *Sustainable Energy & Fuels* **2018**, *2*, 1027–1034.

(33) Makuła, P.; Pacia, M.; Macyk, W. *The Journal of Physical Chemistry Letters* **2018**, *9*, 6814–6817.

(34) Bredas, J.-L. *Mater. Horiz.* **2014**, *1*, 17–19.

(35) Stevie, F. A.; Donley, C. L. *Journal of Vacuum Science & Technology A: Vacuum, Surfaces, and Films* **2020**, *38*, 063204.

(36) Melitz, W.; Shen, J.; Kummel, A. C.; Lee, S. *Surface Science Reports* **2011**, *66*, 1–27.

(37) Kohn, W.; Becke, A. D.; Parr, R. G. *The Journal of Physical Chemistry* **1996**, *100*, 12974–12980.

(38) M. J. Frisch et al., Gaussian 16, Revision C.01, Wallingford CT, 2016.

(39) Tirado-Rives, J.; Jorgensen, W. L. *Journal of Chemical Theory and Computation* **2008**, *4*, 297–306.

(40) Binkley, J. S.; Pople, J. A.; Hehre, W. J. *Journal of the American Chemical Society* **1980**, *102*, 939–947.

(41) Widjonarko, N. *Coatings* **2016**, *6*, 54.

(42) Zhou, W.; Apkarian, R.; Wang, Z. L.; Joy, D. In *Scanning Microscopy for Nanotechnology*; Springer New York: New York, NY, 2006, pp 1–40.

(43) Giessibl, F. J. *Reviews of Modern Physics* **2003**, *75*, 949–983.

(44) Nečas, D.; Klapetek, P. *Open Physics* **2012**, *10*, 181–188.

(45) Kwok, D.; Neumann, A. *Advances in Colloid and Interface Science* **1999**, *81*, 167–249.

Chapter 4

Investigating the Impact of Mobile Ions on Open-Circuit Voltage in Perovskite Solar Cells

The contents of this chapter are based upon the published research article, *"More is different: mobile ions improve the design tolerances of perovskite solar cells"*.[1] For this work, Dr Lucy J. F. Hart performed and analysed all the drift-diffusion simulations under the supervision of Dr Piers R. F. Barnes and Prof. James Durrant. Fraser J. Angus performed and analysed all stabilise and pulse measurements under the supervision of Prof. Pablo Docampo. The n–i–p perovskite solar cells were fabricated by Fraser J. Angus, and the p–i–n cells were fabricated by Yin Li and Abdul Khaleed under the supervision of Prof. Aleksandra B. Djurišić.

4.1 Field Screening and Ionic Effects in Perovskite Solar Cells

Metal-halide perovskite solar cells frequently exhibit unusual device behaviour, including current density–voltage (J–V) hysteresis and long-term performance instability. These phenomena have been widely linked to the presence of mobile ionic defects within the perovskite absorber. The redistribution of ionic charge under an applied voltage can modify the device's internal electrostatic potential by screening the electric field in the bulk of the perovskite (discussed in detail in Chapter 2).[2, 3] This field screening has been identified as a major contributor to J–V hysteresis,[4] and recent work has suggested that high densities of mobile ions may also contribute to device degradation and reduced stability following ageing.[5]

Mobile ionic species in perovskite solar cells are frequently associated with adverse device behaviour, particularly reduced charge-extraction efficiency and operational stability.[5–10] Although the severity of these effects is not universal, it depends on the material's quality and device design. When electronic charge carriers exhibit long diffusion lengths, extraction losses associated with ionic field screening can be substantially suppressed,[11] while instability to ionic motion may be alleviated through targeted passivation of defects and interfaces.[12–15]

While the detrimental effects of mobile ions have been widely discussed, far less emphasis has been placed on identifying regimes in which ionic motion could be advantageous. Addressing this possibility is essential, as the intrinsically low defect formation energies of metal-halide perovskites, as discussed in Section 2.2.2, imply that mobile ionic species are likely to remain an unavoidable feature of these materials.[16, 17] When assessing the influence of mobile ions on device performance, it is essential to consider their role in both charge extraction and recombination. Ionic field screening is generally associated with reduced charge extraction efficiency and, consequently, a decrease in the short-circuit current density. In contrast, the impact of mobile ions on recombination processes, and hence on the open-circuit voltage (V_{OC}), is less straightforward.

Halide vacancies have been shown to form shallow defects, such that their presence does not significantly limit bulk carrier lifetimes.[16, 18–20] As a result, any influence of mobile ions on V_{OC} is expected to arise primarily through modifications to the internal electrostatic potential of the device and the resulting redistribution of electronic charge carriers. In high-performing PSCs, recombination losses are often dominated by interface recombination, also known as surface recombination, rather than bulk processes. It has therefore been proposed that ionic charge accumulation at perovskite-transport layer interfaces may suppress surface recombination by reducing minority carrier concentration. This theory is analogous to field-effect passivation mechanisms employed in silicon photovoltaics.[21–27] Supporting this picture, recent modelling studies have demonstrated that ion redistribution can lead to substantial increases in V_{OC} and, consequently, power conversion efficiency in devices where the built-in potential is smaller than the achievable open-circuit voltage.[27] This regime is particularly relevant for perovskite solar cells, as high-efficiency devices frequently exhibit V_{OC} values that exceed the built-in potential, which is typically reported to lie in the range of 0.8–1.0 V.[28–30]

At present, direct experimental evidence demonstrating a beneficial influence of mobile ions on steady-state device performance remains limited. Previous research has indicated that incorporating alkali metal cations into methylammonium lead bromide can enhance the open-circuit voltage by an ionic modulation of interfacial recombination.[31] However, other studies focusing on steady-state operation have suggested that mobile ions do not substantially influence V_{OC}.[5, 6] These seemingly contradictory findings underscore the challenge of disentangling ionic effects from measurement history and transient behaviours.

In this chapter, we address this discrepancy by introducing a novel measurement approach based on 'pulsed' current density-voltage (J–V) scans, in which the mobile ion distribution is frozen during the J–V scan.[32, 33] This allows the photovoltaic performance to be measured under well-defined steady-state conditions. Using this approach, changes in V_{OC} associated with ionic redistribution are examined across both n–i–p and p–i–n device architectures and various perovskite compositions. In all cases, mobile ions are found to increase the steady-state open-circuit voltage, including in high-efficiency devices that exhibit negligible hysteresis.

To gain insight into how mobile ions may influence the open-circuit voltage in perovskite solar cells, it is helpful to draw an analogy with field-effect passivation in silicon photovoltaics. In silicon devices, this approach introduces a layer of fixed ionic charge at the interface between the absorber and a transport or passivation layer. The resulting electrostatic field formed repels the minority charge carriers from the interface, thereby reducing surface recombination and enhancing the achievable photovoltage.[34] To achieve this, the fixed charge must be of the same sign as the minority charge carrier that is intended to be repelled.

At first glance, this mechanism might appear incompatible with perovskite solar cells. When the applied voltage is below the built-in potential, the sign of the ionic space-charge region that forms at the perovskite-transport-layer interfaces is expected to match that of the majority charge carrier at those interfaces. This is schematically illustrated in Figure 4.1. In this case, ionic charge accumulation would not be expected to repel minority carriers, therefore, limiting the potential for field-effect-like passivation.

However, this picture changes when one considers that, in many high-performance perovskite solar cells, the V_{OC} is likely to exceed the built-in potential (V_{bi}). For perovskites with band gaps around 1.6 eV, open-circuit voltage values exceeding 1.1 V are commonly reported, whereas the V_{bi} is typically estimated to lie in the range of 0.8–1.0 V, as discussed above.[28–30] Furthermore, the mobile ionic charge in the perovskite will invert at an applied voltage above the flat-band condition (see Figure 4.1). Above the flat-band condition, the sign of the ionic space-charge regions becomes the same as that of the minority charge carriers at the interfaces. Under these conditions, the ionic charge can electrostatically substitute for the

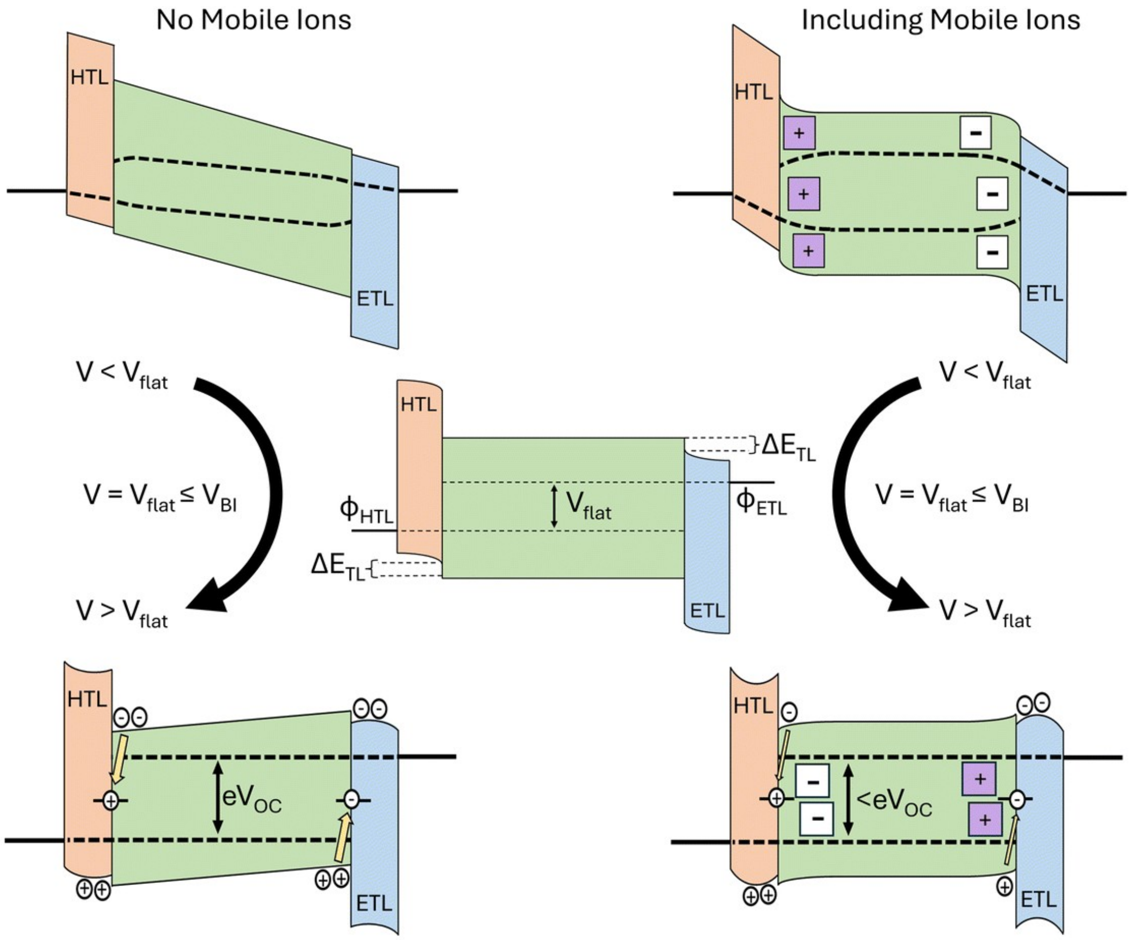

Figure 4.1: Illustration of the impact of mobile ions on solar cell band diagrams. In these figures, ΔE_{TL} is defined as the energetic offset between the perovskite's conduction (valence) band and that of the ETL (HTL). The built-in potential (V_{bi}) is defined as the difference in the equilibrium values of the anode and cathode work function (ϕ_{HTL} and ϕ_{ETL}, respectively). In the central panel, where the band diagrams of the devices with and without mobile ions look identical, the applied voltage, V_{flat}, corresponds to the flat-band condition in the active layer. In the bottom row, we illustrate how band bending induced by the redistribution of mobile ions can reduce minority-carrier accumulation at interfaces relative to an equivalent device without ions. This reduces the interfacial recombination rate at a given applied voltage, thereby increasing the device's open-circuit voltage. Adapted from Ref. [1] under a Creative Commons Attribution 3.0 Unported Licence.

minority-carrier space charge, thereby reducing interfacial recombination rates. This mechanism provides a plausible route by which mobile ions can enhance the open-circuit voltage in perovskite solar cells under steady-state operating conditions, as illustrated schematically in Figure 4.1.

Despite this clear physical motivation, directly verifying the influence of mobile ions on steady-state device performance remains experimentally challenging. Conventional J–V measurements are strongly influenced by measurement history and transient ionic motion, making it difficult to disentangle steady-state ionic effects from dynamic artefacts. As a result, experimental studies have reached differing conclusions regarding the role of mobile ions in determining V_{OC}. Addressing this challenge requires a measurement approach that can probe photovoltaic performance while the ionic distribution is held in a well-defined quasi-steady-state configuration.

In this chapter, the SaP method is introduced as a means of achieving this. Using this approach, the influence of mobile ions on the steady-state open-circuit voltage and interfacial recombination is examined systematically across multiple device architectures. To support the experimental findings, drift–diffusion simulations are also employed. These simulations reproduce the experimentally observed trends and provide mechanistic insight into how ionic redistribution modifies device electrostatics and recombination losses. Together, the experimental and simulated results establish how mobile ionic charge influences the steady-state open-circuit voltage of perovskite solar cells.

4.2 Isolating Ionic Effects Using the Stabilise and Pulse Technique

Separating the effects of mobile ions from the fast electronic response of a solar cell requires a measurement technique that decouples ionic and electronic processes. To achieve this, the Stabilise and Pulse (SaP) technique developed by Hill *et al.* is employed.[32] This method exploits the separation of timescales between ionic and electronic processes by combining prolonged bias stabilisation with rapid voltage pulses. The experimental implementation of the technique is described in detail in Chapter 3 (Section 3.2.2), while its application to the investigation of steady-state ionic effects is considered here.

In practice, the perovskite device is held at a fixed stabilisation voltage, V_{bias}, for a duration sufficient for the ionic distribution to reach quasi-steady-state (QSS) conditions at that bias. During this period, mobile ionic defects redistribute in response to the internal and applied electric fields, establishing a unique electrostatic profile within the device. This condition is reached once the measured current stabilises, indicating that further ionic redistribution no longer affects the extracted electronic current. Once this stabilised ionic configuration is established, a series of rapid voltage pulses is applied. The duration of these pulses is chosen so that the electronic current can fully respond while the ionic distribution remains effectively frozen. This can be achieved provided the pulses are sufficiently short, and the duty cycle remains small (<10%).[25, 32, 35, 36]

By recording the current response during each pulse and repeating this procedure across a range of applied bias voltages, it is possible to reconstruct a current-voltage curve corresponding to a single, well-defined ionic configuration. Repeating this process for different values of V_{bias} enables systematic exploration of how ionic distribution influences photovoltaic performance. Importantly, as each reconstructed J–V curve is obtained under fixed ionic conditions and there is no sweeping voltage, the influence of measurement history and scan-rate-dependent artefacts is substantially reduced.

In addition to enabling reconstruction of steady-state J–V characteristics, the SaP method can be used to extract the flat-band potential, V_{flat}, of a device.[32] As described in Section 4.1, the redistribution of mobile ions is expected to invert once the applied voltage exceeds the flat-band potential across the perovskite layer. Therefore, by selecting a wide range of stabilisation voltages, J–V curves can be reconstructed across the region surrounding the flat-band condition. The flat-band condition can then be extracted by analysing the change in gradient of the reconstructed J–V curves around V_{OC}, as discussed in Section 3.2.2. If V_{bias} is chosen to equal V_{flat}, the reconstructed J–V curve will be the one obtained with the ions distributed uniformly across the perovskite layer, and thus equivalent to the J–V curve which would be obtained for the same device structure, but without a mobile ionic species, as shown in the middle panel of Figure 4.1.

The current measured during the stabilisation period can be used to reconstruct a J–V curve corresponding to a quasi-steady-state (QSS) ionic configuration. By averaging the current measured during the final 30 seconds of the stabilisation step and plotting it as a function of the stabilisation voltage, a J–V curve representing the steady-state device behaviour can be obtained.[37, 38] In other words, the reconstructed QSS J–V curve reflects the true impact of mobile ions on device performance.

By comparing this QSS J–V curve with the reconstructed SaP J–V curve obtained at a stabilisation voltage close to the flat-band condition ($V_{\text{bias}} \approx V_{\text{flat}}$), it is possible to experimentally distinguish device behaviour with and without the influence of mobile ionic charge. Within this framework, the SaP J–V curve represents the purely electronic response of the device under a fixed ionic configuration, equivalent to the behaviour expected in the absence of mobile ions, while the QSS J–V curve captures the combined influence of both electronic transport and ionic redistribution on device performance.

An important aspect of this method is that the flat-band potential is determined directly from the experimental data rather than being assumed *a priori*. This method therefore has a clear advantage over the protocols used in previous studies, which employed fast and slow J–V sweeps to assess the impact of mobile ions on PSCs.[5, 6, 39] In these studies, device behaviour 'without mobile ions' was evaluated by stabilising the device under illumination at open-circuit conditions. This approach assumes that the open-circuit voltage is a reasonable approximation of the flat-band potential, so that stabilisation at V_{OC} would lead to a uniform distribution of ionic charge within the perovskite layer. However, as we will show in the following sections, this assumption does not generally hold, and in many perovskite solar cells, the V_{OC} typically exceeds the flat-band potential.

As a result, stabilisation at V_{OC} leads to a non-uniform ionic distribution, with positive ionic charge accumulating near the ETL and negative ionic charge near the HTL. A fast J–V sweep performed from this initial condition, therefore, does not represent the behaviour of a device without mobile ions. Instead, the accumulated ionic charge modifies the interfacial electrostatics, displacing minority carriers away from the interfaces and thereby reducing interfacial recombination. Consequently, the measured open-circuit voltage may exceed that of an equivalent device in the absence of mobile ions.

However, when the stabilisation potential is chosen to be equal to the open-circuit voltage, the measured V_{OC} is necessarily identical for both slow and fast J–V scans. In both cases, the applied voltage fixes the device configuration at the same operating point, as seen in refs. [5, 6, 39]. Under these conditions, fast-scan measurements cannot reveal whether the steady-state ionic distribution modifies the open-circuit voltage relative to an ion-free device.

This limitation highlights the importance of measurement protocols that do not rely on assumptions about the relationship between V_{OC} and the flat-band condition.

Using the Stabilise and Pulse technique, the experiments presented here provide the first direct experimental evidence that the presence of mobile ions can increase the steady-state V_{OC} relative to equivalent devices without mobile ions. It is hypothesised that the magnitude of this effect depends strongly on the extent to which recombination is limited by the perovskite–transport-layer interfaces, as illustrated in Figure 4.1.

To test this hypothesis, SaP measurements are applied to devices with different architectures and interfacial layers, including structures with and without interfacial passivation layers. Measurements are also performed on high-efficiency inverted devices that exhibit minimal hysteresis to determine whether mobile ions remain relevant to steady-state performance under more optimal operating conditions. Together, these experiments establish a systematic framework for evaluating the role of mobile ions in perovskite solar cells.

4.3 Experimental Evidence for Ion-Induced Enhancement of the Open-Circuit Voltage

4.3.1 Extracting the Flat-Band Potential

Mobile ionic charge can modify the steady-state open-circuit voltage of perovskite solar cells by altering the device's internal electrostatics. To investigate this effect experimentally, devices with the structure FTO/TiO_2/(SAM)/MAPI/Spiro-OMeTAD/Au were fabricated. MAPI was chosen here as it is widely reported to have a high mobile ion density (10^{17}–10^{19} cm^{-3}).[16, 40, 41] Although this limits the maximum achievable device efficiency, simulations (discussed in more detail in Section 4.4) suggest that a higher mobile ion density will increase the effect of mobile ions on V_{OC}, making it easier to detect experimentally. For the SAM layer, we used the benzoic acid derivative of C_{60} (C_{60}-BA), which has been shown to enhance the efficiency of electron extraction and to passivate shallow trap states at the perovskite/TiO_2 interface.[42–44] Thus, this should limit any performance gains from mobile ions, as surface recombination will already be reduced and therefore the reduction in minority carrier accumulation will bear less impact. A summary of device parameters for all TiO_2 devices used is shown in Table 4.1 and for passivated devices, Table 4.2.

We begin by extracting the flat-band potential from the SaP data, following the method outlined in Section 3.2.2. The reconstructed SaP J–Vs are shown in Figure 4.2a and Figure 4.2c for devices without and with the C_{60} passivation layer, respectively. From this dataset, we perform the gradient analysis as discussed in Section 3.2.2 to extract V_{flat} for both devices without and with passivation, as shown in Figure 4.2b and Figure 4.2d, respectively. From this data, it is clear that the C_{60} passivation layer also creates a slight shift in the energetics at the ETL interface as the V_{flat} is increased from 0.68 to 0.74 V. This is even clearer when averaged over a range of devices. The V_{flat} for devices without C_{60} was found to be 0.66 ± 0.03 V and 0.74 ± 0.02 V with the passivation layer present (see Table 4.1 and Table 4.2).

To confirm the reliability of the SaP measurement and to ensure that ion motion is restricted during the pulsing section, the measurement is conducted both in a forward and reverse pulsed J–V. As shown in Figure 4.3a-b, for both devices, with and without the passivation layer, the forward and reverse pulsed J–Vs at all stabilisation biases show negligible hysteresis. This strongly suggests that no ionic motion occurs during the measurement. This is in stark contrast to the results obtained from the traditional J–V sweeps measured, where a significant amount of hysteresis is present for both devices, demonstrating a large amount of ionic motion can occur in these devices (Figure 4.A1).

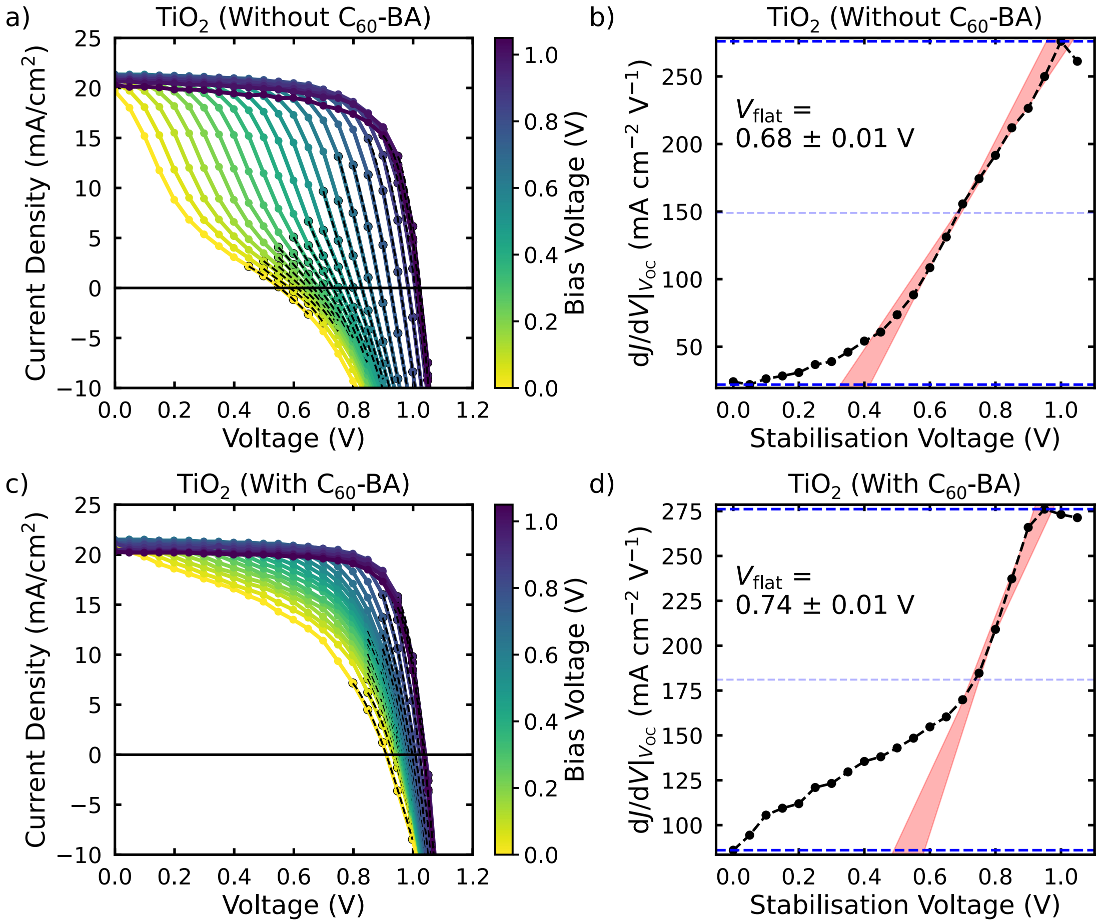

Figure 4.2: Stabilise and Pulse measurements for TiO_2-based n–i–p devices (a,b) without and (c,d) with C_{60}-BA passivation. (a,c) SaP J–V curves acquired following stabilisation at different bias voltages. (b,d) Corresponding open-circuit voltage gradient analysis, $\mathrm{d}J/\mathrm{d}V|_{V_{\mathrm{OC}}}$, used to extract the flat-band potential, V_{flat}, from the SaP data. The extracted values are $V_{\mathrm{flat}} = 0.68 \pm 0.01$ V for the unpassivated device and $V_{\mathrm{flat}} = 0.74 \pm 0.01$ V for the C_{60}-BA passivated device. The uncertainty reflects the range of linear fits used in the gradient analysis, as indicated by the red-shaded regions. Further details of the fitting procedure are provided in Section 3.2.2. Adapted from Ref. [1] under a Creative Commons Attribution 3.0 Unported Licence.

It is worth noting that, for the n–i–p devices used here, in both cases the V_{flat} lies significantly below the V_{OC} under traditional operating conditions (see Table 4.1 and Table 4.2). This therefore supports the hypothesis that, in perovskite solar cells, there is a clear distinction between open-circuit voltage and flat-band conditions. With the experimentally obtained V_{flat}, we now seek to extract the QSS J–V performance for comparison. Thus allowing us to extract, within the same device, the performance with mobile ions contributing and with the device held at flat-band conditions and therefore not contributing.

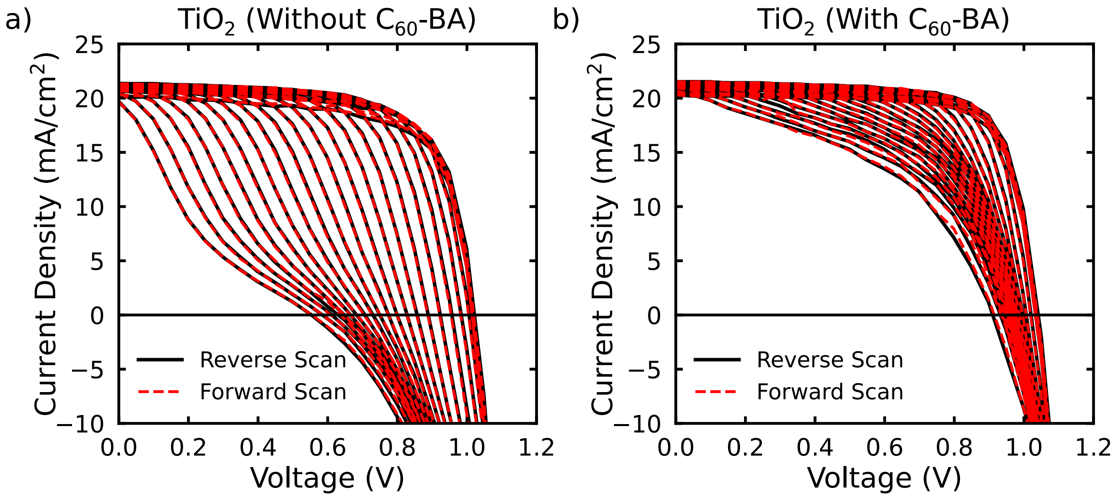

Figure 4.3: Stabilise and Pulse J–V data for TiO_2 devices a) without and b) with C_{60}-BA passivation, shown for both forward (red dashed) and reverse (black solid) pulsed voltage directions. The overlap of the forward and reverse scans demonstrates the absence of hysteresis during the SaP measurement, indicating that ionic redistribution does not occur on the timescale of the voltage pulse. This confirms that the SaP method probes an ion-frozen electronic configuration in both passivated and unpassivated devices. Adapted from Ref. [1] under a Creative Commons Attribution 3.0 Unported Licence.

4.3.2 Reconstructing the Quasi-Steady-State J–V Curve

The quasi-steady-state (QSS) J–V curve represents the true device performance when mobile ions have reached their equilibrium distribution at each applied bias. To extract this behaviour from the SaP measurement, it is necessary to consider how the ionic distribution evolves at each applied stabilisation voltage. When a voltage is applied to the device, mobile ions move to screen the external electric field and, if given sufficient time, reach a quasi-steady-state position corresponding to that bias. As discussed previously, this condition can be identified by a stable current output at a given voltage, indicating that further ionic motion no longer influences the extracted photocurrent. By extracting the stabilised current at each applied voltage, the J–V curve can therefore be reconstructed with the ions held at steady-state conditions. This reconstructed curve represents the device performance in the presence of mobile ionic charge.

The current output over the range of applied voltages for devices without and with the passivation layer are shown in Figure 4.4a and Figure 4.4c, respectively. Additionally, the average current minus the mean current across the final 30 seconds before pulsing is displayed in Figure 4.4b and Figure 4.4d for devices with and without the passivation layer, respectively. It is clear that the current is slightly less stable at higher bias voltages. However, the passivation layer does appear to improve stability,

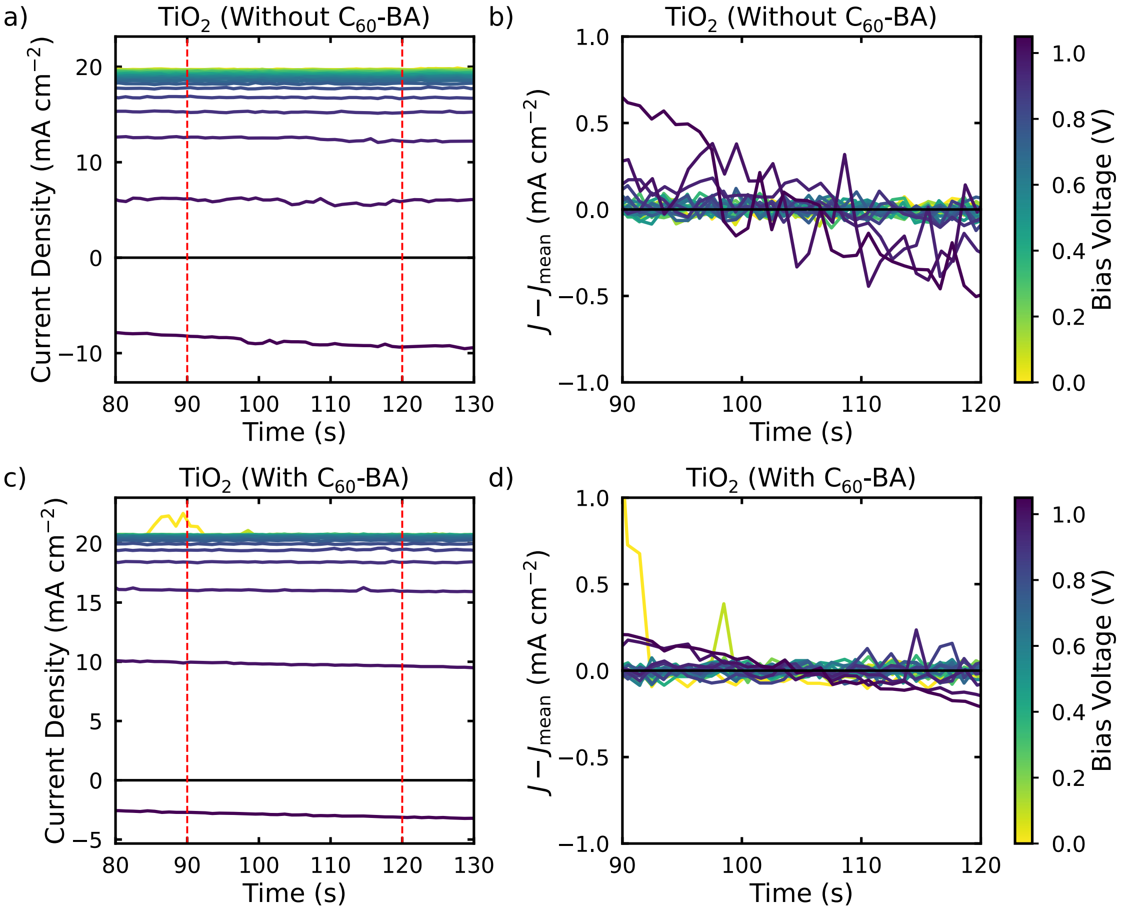

Figure 4.4: Measured current density during the stabilisation phase of Stabilise and Pulse measurements for TiO_2 devices (a-b) without and (c-d) with C_{60}-BA passivation. a, c) Current density recorded before pulsing, with the vertical red dashed lines indicating the 30 s time window over which the steady-state current was averaged. b, d) Deviation of the measured current from its mean value over the same time window, highlighting the stability of the current during stabilisation. The current is slightly less stable at higher stabilisation biases, while devices incorporating C_{60}-BA exhibit improved current stability. Adapted from Ref. [1] under a Creative Commons Attribution 3.0 Unported Licence.

suggesting that the TiO_2-perovskite interface may be linked to these changes.[42–44] However, despite this reduced stability at high applied voltages, the pulsed J–V curves obtained still showed little to no hysteresis as shown in Figure 4.3. This suggests that the apparent current instability may be linked to an electrochemical process occurring at high voltages and under illumination. The stabilised current output obtained over the final 30 seconds for each bias voltage was then used to reconstruct the J–V curves for both devices. The reconstructed QSS J–V curves are superimposed on the SaP data for direct comparison, as displayed in Figure 4.5a and Figure 4.5c, for devices without and with the passivation layer, respectively. Additionally, this data provides an extra check to confirm that the ions had not redistributed during the pulsing section.

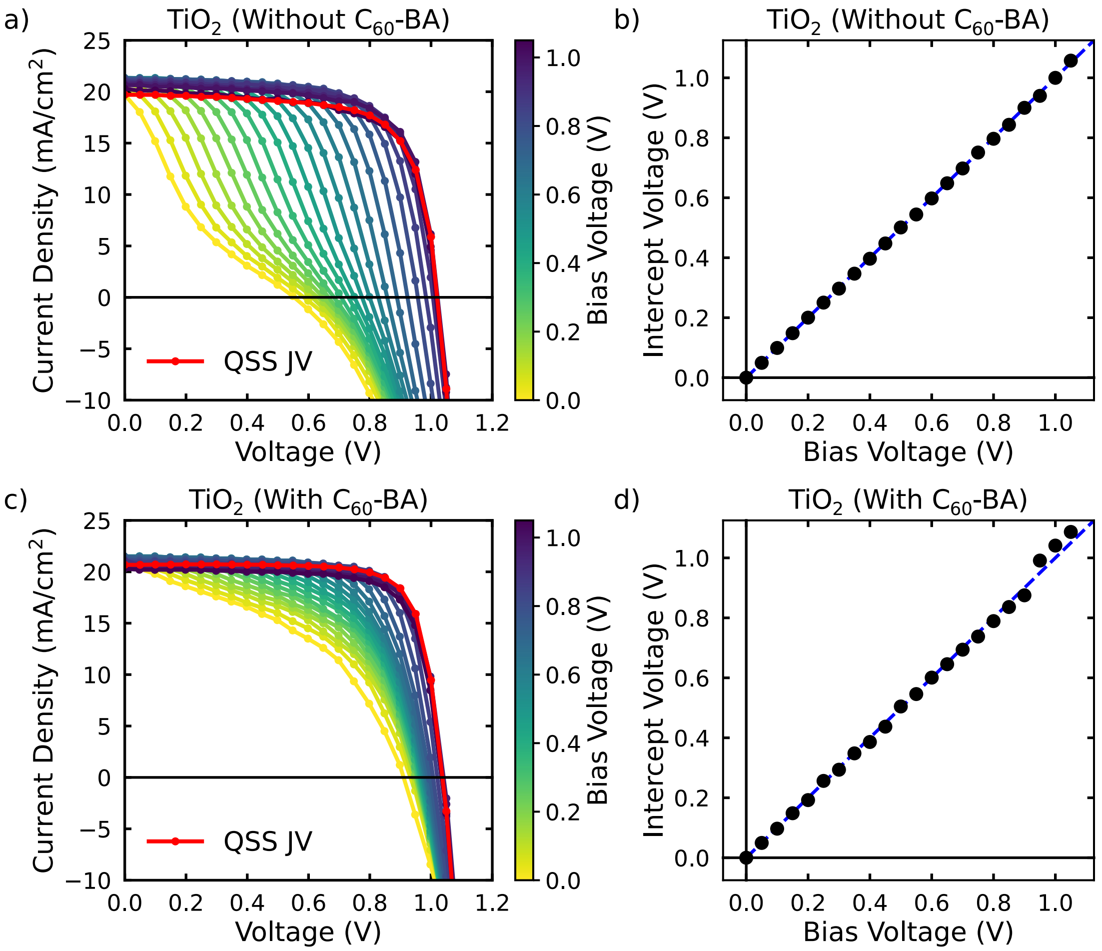

Figure 4.5: Stabilise and Pulse measurements for TiO_2 devices without and with a C_{60}-BA passivation layer. Panels (a) and (c) show the SaP J–V curves obtained after stabilisation at different bias voltages, with the quasi-steady-state (QSS) J–V curve overlaid in red for comparison. Panels (b) and (d) show the intercept voltage determined by identifying the bias at which the current density from the SaP curve intercepts the QSS curve ($J_{\mathrm{SaP}} = J_{\mathrm{QSS}}$). The dashed blue line indicates $y = x$. The close agreement between the extracted intercept voltage and the applied stabilisation bias demonstrates that each SaP J–V curve intersects the QSS curve at the stabilisation voltage, confirming that the ionic configuration established during stabilisation remains effectively unchanged during the voltage pulse. Adapted from Ref. [1] under a Creative Commons Attribution 3.0 Unported Licence.

As discussed, the stabilisation voltage sets the ionic configuration. Therefore, the QSS J–V should intercept the SaP J–V exactly at the applied bias voltage and the same current should be obtained. We find this to be true by plotting this intercept value for both devices, as shown in Figure 4.5b (without C_{60}-BA) and

Figure 4.5d (with C_{60}-BA). Here, the values are extremely close to the true intercept value, except for a few high-voltage points in the passivated device. However, when zoomed in, this is found to be due to a discrepancy of $\sim$ 0.2–0.4 $\mathrm{mA\,cm^{-2}}$. At this point, the current is also rapidly dropping; it is less likely that the intercept will occur exactly. However, this data supports the hypothesis that the ions are held at a quasi-steady-state position, and, as stated, the applied voltage determines the ionic configuration. These results also provide further explanation for why the measurement protocols used in references [5, 6, 39] show little effect of mobile ions on V_{OC}.

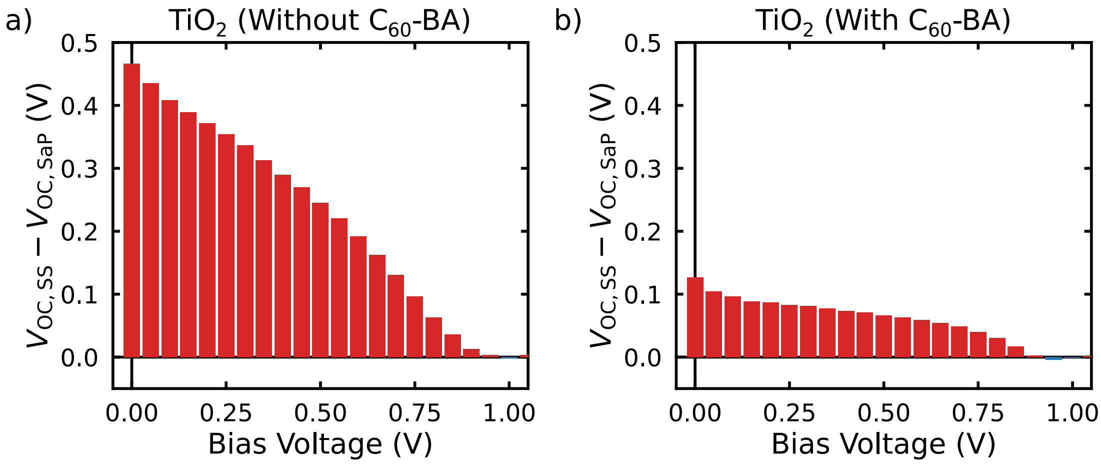

Figure 4.6: Bias dependence of the difference between the steady-state and flat-band open-circuit voltage, $V_{\mathrm{OC,SS}} - V_{\mathrm{OC,SaP}}$, for TiO_2-based n–i–p devices a) without and b) with a C_{60}-BA passivation layer. The voltage difference is obtained by comparing quasi-steady-state J–V measurements with Stabilise and Pulse J–V measurements at each stabilisation bias. Positive values (red) indicate an enhancement of the steady-state open-circuit voltage due to ionic redistribution, while negative values (blue) indicate a reduction in open-circuit voltage relative to the flat-band condition. The reduced magnitude of the voltage enhancement in passivated devices highlights the sensitivity of ion-mediated photovoltage gains to interfacial recombination. Adapted from Ref. [1] under a Creative Commons Attribution 3.0 Unported Licence.

With the consistency of the SaP method established relative to previous attempts to measure the impact of mobile ions, we now compare the reconstructed J–V curves of the device at QSS and flat-band conditions. We first quantify the effect of mobile ions on V_{OC} as a function of V_{bias}. This is done by calculating the difference between the V_{OC} at QSS ($V_{\mathrm{OC,SS}}$) and that determined from the SaP J–Vs for each V_{bias} ($V_{\mathrm{OC,SaP}}$). The resulting difference is shown in Figure 4.6a–b.

The data show that, in the presence of mobile ions, the V_{OC} is significantly increased across almost all applied voltages. Only at stabilisation voltages close to 1 V do mobile ions appear to slightly reduce V_{OC}. The measurements also reveal a much larger variation in V_{OC} for devices without the C_{60} passivation layer, particularly at lower applied voltages. This behaviour indicates that the magnitude of the ionic modulation of V_{OC} in PSCs is strongly correlated with the fraction of the total recombination current that proceeds via surface recombination, which is discussed further in Section 4.4. These results therefore support the hypothesis that mobile ions suppress surface recombination through a field-effect passivation-like mechanism, as illustrated in Figure 4.1.

4.3.3 Quantifying the Effect of Mobile Ions on Solar Cell Performance

Having established that the presence of a mobile ionic species can enhance the open-circuit voltage for almost all applied stabilisation voltages, we now look to extract the exact gain in comparison to an 'ion-free' device, as well as the difference in device performance. To achieve this, we compare the results of the QSS J–V directly with the J–V curve obtained at V_{flat}. The resulting J–V curves are displayed in Figure 4.7. Here, it can clearly be seen that the QSS J–V curve, and therefore including a mobile ionic species, has a significantly improved V_{OC} in comparison to the V_{flat} J–V curve.

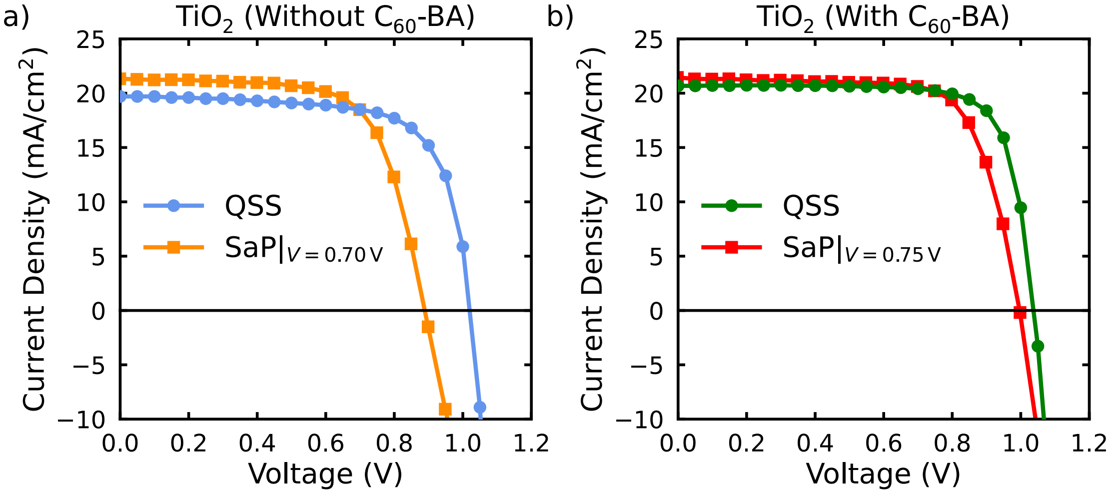

Figure 4.7: Comparison of quasi-steady-state and Stabilise and Pulse J–V characteristics for TiO_2 devices a) without and b) with a C_{60}-BA passivation layer. In each case, the SaP J–V curve corresponds to the flat-band potential ($V_{\mathrm{bias}} = 0.70$ V without C_{60}-BA and $V_{\mathrm{bias}} = 0.75$ V with C_{60}-BA), while the QSS J–V curve reflects steady-state operation with mobile ions. When the exact voltage was not obtained during the SaP measurement, the closest V_{bias} value is used. The uncertainty associated with each extracted QSS data point is smaller than the marker size and is therefore not visible. Adapted from Ref. [1] under a Creative Commons Attribution 3.0 Unported Licence.

Overall, three key observations emerge from these plots. First, a clear reduction in the measured current density is observed in both device architectures when mobile ions are present. This occurs because ionic charge accumulation screens the internal electric field within the perovskite layer, shifting charge transport from a drift-dominated regime to one governed primarily by diffusion. As a result, photogenerated carriers are extracted less efficiently, thereby reducing photocurrent.

Second, a single crossover point is observed in both cases, occurring at the applied stabilisation voltage of the SaP curve. At this voltage point, the ionic distribution corresponds to the stabilisation condition used during the measurement, meaning the reconstructed QSS and SaP J–V curves coincide.

Third, the presence of mobile ions leads to a clear increase in the measured voltage and fill factor. This behaviour reflects modifications in interfacial electrostatics induced by ionic charge accumulation, which reduce interfacial recombination and enable the device to achieve a higher photovoltage.

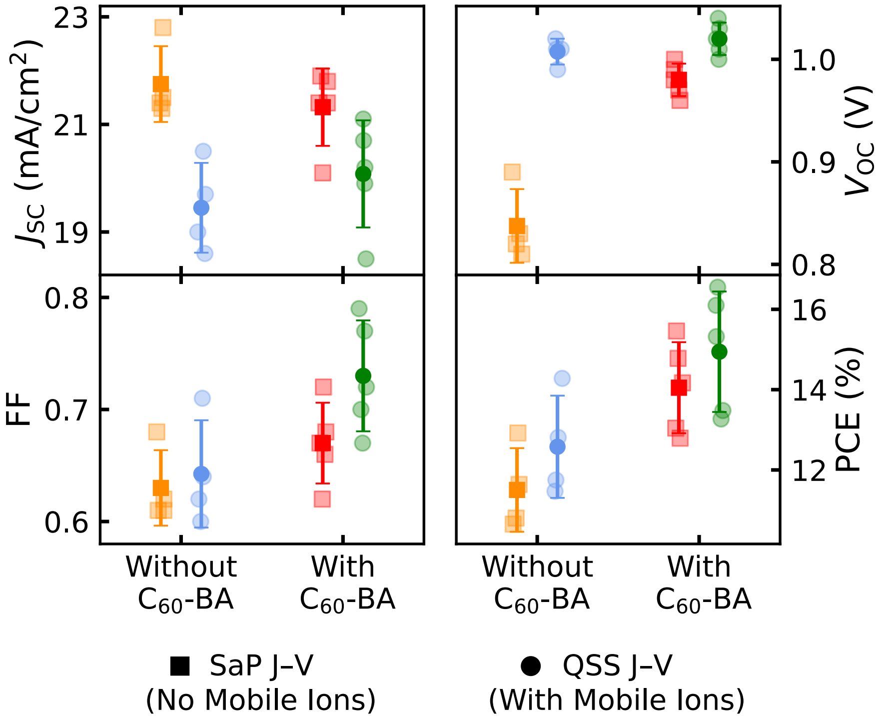

Figure 4.8: Comparison of photovoltaic performance parameters extracted from Stabilise and Pulse (SaP) at V_{flat} and quasi-steady-state (QSS) J–V measurements for devices fabricated with and without the C$_{60}$-BA interfacial passivation layer. Shown are the short-circuit current density (J_{SC}), open-circuit voltage (V_{OC}), fill factor (FF), and power conversion efficiency (PCE). It is clear that the addition of C$_{60}$-BA leads to systematic improvements in V_{OC}, FF, and PCE under QSS conditions, highlighting the enhanced steady-state performance arising from reduced interfacial recombination in the presence of mobile ionic redistribution. Error bars represent the standard deviation across multiple devices. Adapted from Ref. [1] under a Creative Commons Attribution 3.0 Unported Licence.

We find that when evaluated at $V_{\text{bias}} = V_{\text{flat}}$, the average increase in V_{OC} is 158 ± 22 mV for devices without C_{60}-BA and 38 ± 10 mV for devices including the C_{60}-BA passivation. In fact, we find that, with mobile ions contributing to device performance, the boost in open-circuit voltage and fill factor is enough to offset the current loss. As shown in Figure 4.8, the average PCE is greater for the devices with ions contributing. What is even more striking is the device-by-device comparison, which reveals that for all devices in this study, the PCE is greater in every individual case when mobile ions are present. This data is shown in Table 4.1 for devices without C_{60}-BA and in Table 4.2 for devices with C_{60}-BA passivation.

Table 4.1: Summary of device performance parameters for TiO_2 only devices. J–V parameters are given in three cases: as measured under the Solar Simulator using the protocol described in Chapter 3 (parameters taken from the reverse scan), as measured with the mobile ions at QSS (QSS J–V) and as measured using SaP measurements carried out at $V_{\text{bias}} = V_{\text{flat}}$ (SaP J–V). The parameters corresponding to the devices discussed in Section 4.3 are given in bold, and data for all other devices are shown in Appendix 4.A2. Additionally, the V_{flat} value obtained from the SaP analysis is provided; here, the error corresponds to the statistical uncertainty associated with the local fitting procedure (see Section 3.2.2). Adapted from Ref. [1] under a Creative Commons Attribution 3.0 Unported Licence.

Device	V_{flat} (V)	Method	J_{SC} (mA cm^{-2})	V_{OC} (V)	FF	PCE (%)
1	**0.68 ± 0.01**	**Solar Sim**	**21.3**	**1.13**	**0.75**	**17.90**
		QSS J–V	**19.7**	**1.02**	**0.71**	**14.26**
		SaP J–V	**21.3**	**0.89**	**0.68**	**12.92**
2	0.64 ± 0.01	Solar Sim	20.8	1.08	0.71	16.00
		QSS J–V	18.6	0.99	0.64	11.75
		SaP J–V	21.5	0.83	0.61	10.80
3	0.63 ± 0.03	Solar Sim	21.9	1.08	0.70	16.47
		QSS J–V	20.5	1.01	0.62	12.81
		SaP J–V	22.8	0.82	0.62	11.64
4	0.69 ± 0.04	Solar Sim	21.8	1.08	0.71	16.68
		QSS J–V	19.0	1.01	0.60	11.47
		SaP J–V	21.3	0.86	0.62	11.38

These results unequivocally show that the presence of mobile ions can improve device performance compared to an equivalent device without mobile ions. The data also revealed a strong dependence on surface recombination: when the TiO_2 layer was passivated with the C_{60}-BA layer, the magnitude of the V_{OC} gain was significantly reduced. However, these results were also obtained using MAPI, which is known to have a high mobile-ion density, raising the question: are mobile ions relevant to the steady-state performance of the highest-efficiency PSCs?

Table 4.2: Summary of device performance parameters for TiO_2 with C_{60}-BA. J–V parameters are given in three cases: as measured under the Solar Simulator using the protocol described in Chapter 3 (parameters taken from the reverse scan), as measured with the mobile ions at QSS (QSS J–V) and as measured using SaP measurements carried out at $V_{\text{bias}} = V_{\text{flat}}$ (SaP J–V). The parameters corresponding to the devices discussed in Section 4 are given in bold, and data for all other devices are shown in Appendix 4.A4. Additionally, the V_{flat} value obtained from the SaP analysis is provided; here, the error corresponds to the statistical uncertainty associated with the local fitting procedure (see Section 3.2.2). Adapted from Ref. [1] under a Creative Commons Attribution 3.0 Unported Licence.

Device	V_{flat} (V)	Method	J_{SC} (mA cm^{-2})	V_{OC} (V)	FF	PCE (%)
1	**0.74 ± 0.01**	**Solar Sim**	**21.3**	**1.10**	**0.74**	**17.34**
		QSS J–V	**19.9**	**1.04**	**0.77**	**16.55**
		SaP J–V	**21.4**	**1.00**	**0.72**	**15.46**
2	0.77 ± 0.01	Solar Sim	20.1	1.10	0.71	16.55
		QSS J–V	19.9	1.03	0.79	16.10
		SaP J–V	21.9	0.99	0.68	14.78
3	0.75 ± 0.01	Solar Sim	21.2	1.08	0.73	16.69
		QSS J–V	20.2	1.00	0.67	13.48
		SaP J–V	21.4	0.98	0.62	13.04
4	0.73 ± 0.01	Solar Sim	22.3	1.09	0.71	17.29
		QSS J–V	20.7	0.99	0.64	13.16
		SaP J–V	22.1	0.94	0.60	12.49
5	0.72 ± 0.01	Solar Sim	21.7	1.07	0.74	17.24
		QSS J–V	21.1	1.01	0.72	15.32
		SaP J–V	21.8	0.97	0.67	14.17

4.3.4 Ionic Effects in High-Efficiency p–i–n Devices

Until now, we have focused on the pronounced effects of mobile ions in devices using MAPI as the active layer. However, the most efficient devices commonly employ more complex perovskite compositions, which are reported to have lower concentrations of mobile ions.[40] The amount of field-effect passivation effect from the presence of mobile ions would therefore be reduced in a device with fewer mobile ions (this is discussed further in Section 4.4). To address this, we performed SaP on high efficiency p–i–n devices (PCE = 21.5 %, V_{OC} = 1.17 V, J_{SC} = 24 mA cm^{-2} and FF = 0.76, see Figure 4.A7 and Table 4.A1) with the structure ITO/NiO_x/2PACz/perovskite/PEAI/PCBM/BCP/Ag. The perovskite used was $Cs_{0.05}(FA_{0.87}MA_{0.13})Pb(I_{0.87}Br_{0.13})_3$ and therefore a triple cation composition. This device showed little J–V hysteresis across a scan rate range of 0.01–0.50 V s^{-1} (see Figure 4.A7).

The full Stabilise and Pulse data for this device is shown in Figure 4.9a with the extracted V_{flat} value of 0.94 V displayed in Figure 4.9b. This value represents a notable increase compared to the n–i–p devices measured in the previous sections and may be linked to improved device performance. We note that the SaP measurement was conducted at $\approx$ 0.5 Suns, as a precaution due to the prolonged 600-second stabilisation time. Therefore, to prevent degradation that could impact the results, a lower light intensity was used.[32] A longer stabilisation time was used because we hypothesised that the lower density of mobile ions would increase the time required for the current to stabilise. An important note to make on these results is the clear change in the SaP J–V curves obtained for the different stabilisation biases, in stark contrast to the no-hysteresis J–V curve measured under standard conditions. This result unequivocally shows that, even in high-efficiency 'optimised' devices, there is still a noticeable amount of ionic motion, even if it does not appear in traditional J–V sweep measurements.

We first verify that the device remains stable during the measurement and that the ions are held at quasi-steady state. As shown in Figure 4.9c–d, the current output remains stable throughout the stabilisation period. Notably, the current of this optimised device is significantly higher than that of the n–i–p devices discussed previously, even at applied voltages above the open-circuit voltage. This behaviour is consistent with reports in the literature, which show that improved device stability is often correlated with higher efficiency. These measurements therefore confirm that the ionic distribution reaches a steady-state configuration for each applied voltage during the pulsing regime following the ten-minute stabilisation period.

Figures 4.10a–b provide further confirmation that the ions occupy a steady-state configuration. Here, the QSS J–V characteristic is overlaid with the reconstructed SaP J–V curves, and the intercept voltage for each stabilisation bias is shown. The QSS characteristic closely intersects the corresponding SaP curve at the same bias, demonstrating that the applied voltage determines the ionic configuration within the device.

Finally, Figure 4.10c shows that when mobile ions contribute to device operation, the open-circuit voltage increases for almost all stabilisation voltages and is only slightly reduced above 1.2 V. When compared to the J–V curve obtained at V_{flat}, the increase in V_{OC} is approximately 30 mV. This behaviour is consistent with expectations: the lower ion density, together with likely improved interface quality in these optimised devices, reduces recombination rates, and therefore the magnitude of the ionic enhancement is smaller than that observed in the earlier n–i–p devices. Nevertheless, these results show that even in high-efficiency devices, mobile ions remain beneficial under steady-state operating conditions.

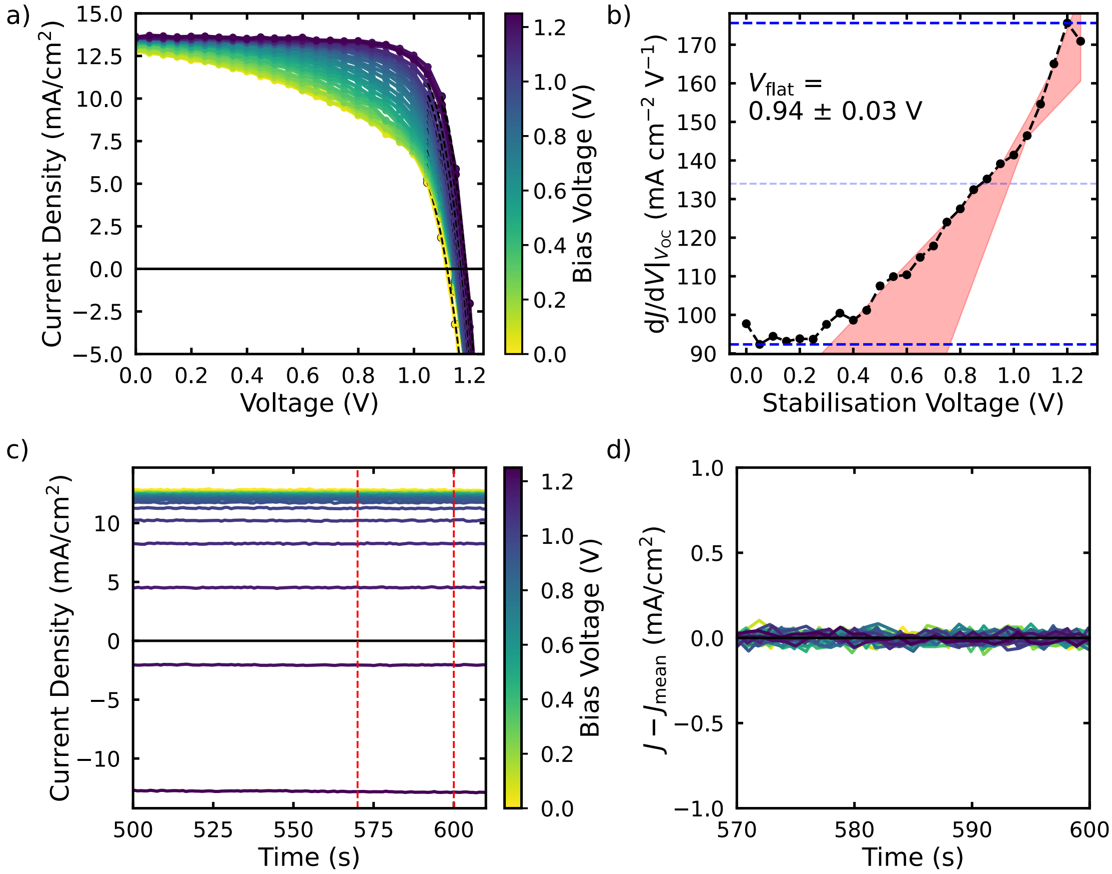

Figure 4.9: Stabilise and Pulse analysis of a p–i–n perovskite solar cell. a) SaP J–V curves acquired at different stabilisation voltages. b) Differential gradient analysis of the pulsed J–V curves used to extract the flat-band potential, V_{flat}. The error here is associated with the range of fits used to extract the value of V_{flat}. c) Measured current densities for each applied bias, demonstrating that the electronic current reaches a steady value prior to the pulsing regime. This is zoomed in on the final stages of the stabilisation period, before pulsing beginning at 600 seconds, and the final 30 seconds highlighted with vertical red dashed lines as the area where the current is used for the quasi-steady state J–V. d) The difference between the measured current and its mean value over the time window highlighted in (c). Showing negligible ionic redistribution during the pulsing, as the current does not deviate. Adapted from Ref. [1] under a Creative Commons Attribution 3.0 Unported Licence.

A comparison of the overall device performance further supports this conclusion. The J–V curve obtained at V_{flat} (i.e., in the absence of ions impacting performance) yields a PCE of 11.15%, whereas the QSS curve yields 11.25%. Although this improvement is modest, it demonstrates that mobile ions do not hinder device performance relative to an equivalent device without ionic motion. With these experimental observations established, the following section uses drift–diffusion simulations implemented in Driftfusion to investigate further the mechanisms underlying these results.

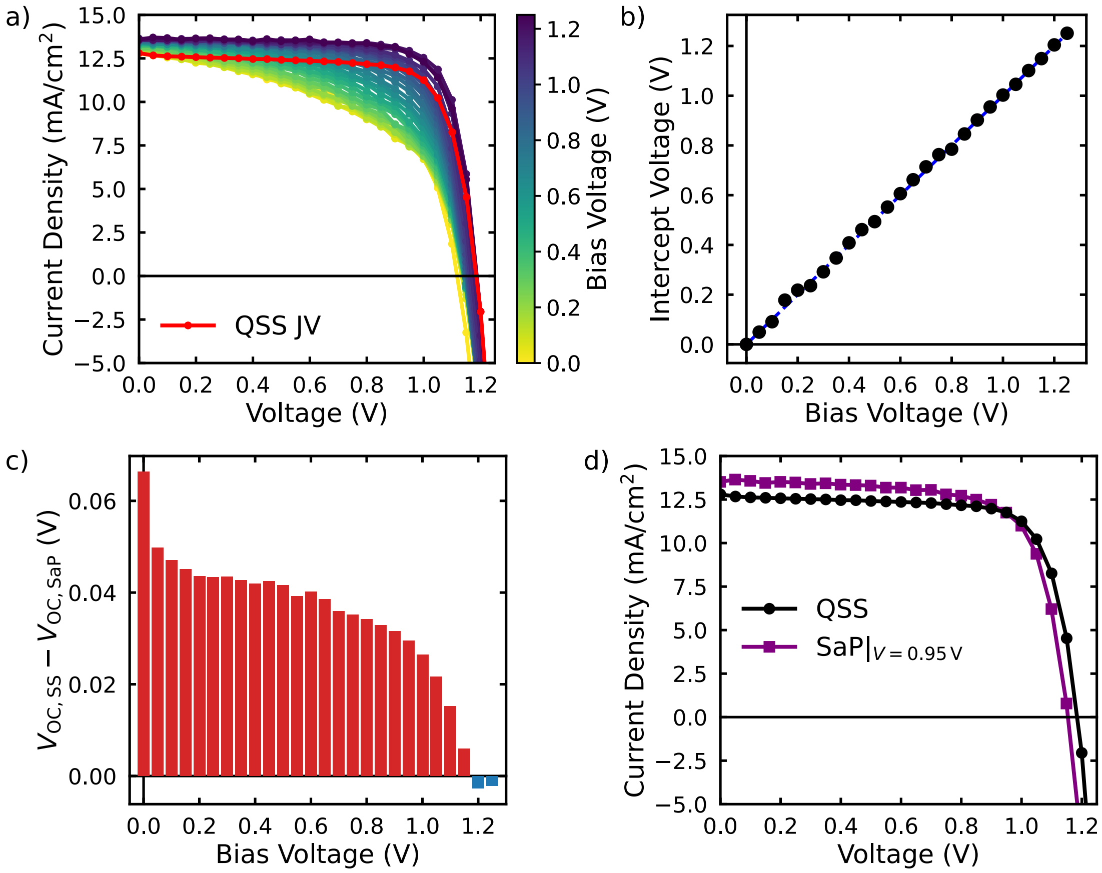

Figure 4.10: Comparison of quasi-steady-state and Stabilise and Pulse J–V characteristics for a p–i–n perovskite solar cell. a) SaP J–V curves, with the quasi-steady-state J–V curve superimposed in red for reference. b) Extracted intercept voltage as a function of stabilisation bias, demonstrating a linear correspondence and confirming that the applied stabilisation voltage defines the ionic configuration before pulsing. c) Difference between the steady-state and flat-band open-circuit voltage, $V_{\mathrm{OC,SS}} - V_{\mathrm{OC,SaP}}$, as a function of stabilisation bias, revealing a systematic enhancement of the steady-state photovoltage across a wide bias range. d) Direct comparison of the quasi-steady-state J–V curve with the SaP J–V curve acquired at $V_{\mathrm{bias}} = 0.95$ V, illustrating the voltage enhancement arising from ionic redistribution under steady-state operation. The uncertainty associated with each extracted QSS data point is smaller than the marker size and is therefore not visible. Adapted from Ref. [1] under a Creative Commons Attribution 3.0 Unported Licence.

4.4 Drift–Diffusion Simulations of Ionic Effects

The simulations in this section were performed by Dr Lucy J F Hart, and are included here solely to support the experimental results discussed in this chapter. Full details of the simulation methodology and underlying assumptions are provided in Ref. [1], and are not repeated here.

To further support the experimental observations in Section 4.3, drift-diffusion simulations were employed to independently assess the impact of mobile ionic charge on device electrostatics and recombination losses. Importantly, the purpose of these simulations is not to reproduce the absolute performance of the experimental results, but rather to isolate the influence of mobile ions on surface recombination and energetic alignment. In this way, they serve as a mechanistic test of the hypothesis and results observed using the Stabilise and Pulse method. All simulation results discussed in this section correspond to devices with doped transport layers, representative of the experimental architecture used in Section 4.3, which employ a metal oxide, TiO_2, as the electron transport layer and heavily doped Spiro-OMeTAD as the hole transport layer.[45–49]

Figure 4.11a shows the simulated J–V characteristics for a device with (solid line) and without mobile ions (dashed line). This simulated device has symmetric energetic offsets between the perovskite and transport layers. In the absence of mobile ions, the open-circuit voltage is limited by interfacial recombination and the built-in electrostatic potential. When mobile ions are included, a clear increase in V_{OC} is observed, despite no change in the electronic structure or recombination parameters of the contacts. This behaviour mirrors the experimentally observed enhancement in quasi-steady-state open-circuit voltage relative to the flat-band condition.

The physical origin of the enhancement in open-circuit voltage gained from the presence of mobile ions is illustrated in Figures 4.11c and d, which show the simulated electrostatic potential and excess carrier density across the device under short-circuit conditions (0 V applied), flat-band (0.9 V in this device), and open-circuit conditions (1.12 V). In the case of mobile ions, ionic redistribution under an applied bias modifies the internal electric field. This, in turn, reduces carrier accumulation at the interfaces and suppresses interfacial recombination, leading to greater accumulation of photogenerated charge and, consequently, increased quasi-Fermi level splitting. Importantly, Figures 4.11c and d also demonstrate that at a voltage equal to the flat-band potential, the electrostatic potential across the perovskite layer is null. Additionally, there is no accumulation of ion density at either interface in comparison to the short-circuit and open-circuit conditions.

Figure 4.11b addresses an important experimental consideration, which is the validity of the SaP method in devices with non-ideal energetic alignment. The simulated J–V curves are shown for transport layers with no energetic offset and for a transport layer with a significant energetic offset at one interface, both with no ions present. Fortunately, simulations suggest that the SaP remains viable in these situations, as the electronic doping of the perovskite bulk means that the interface with the worst energetic alignment dominates surface recombination.[1] This can be matched to the no mobile ions case by selecting the voltage which corresponds to

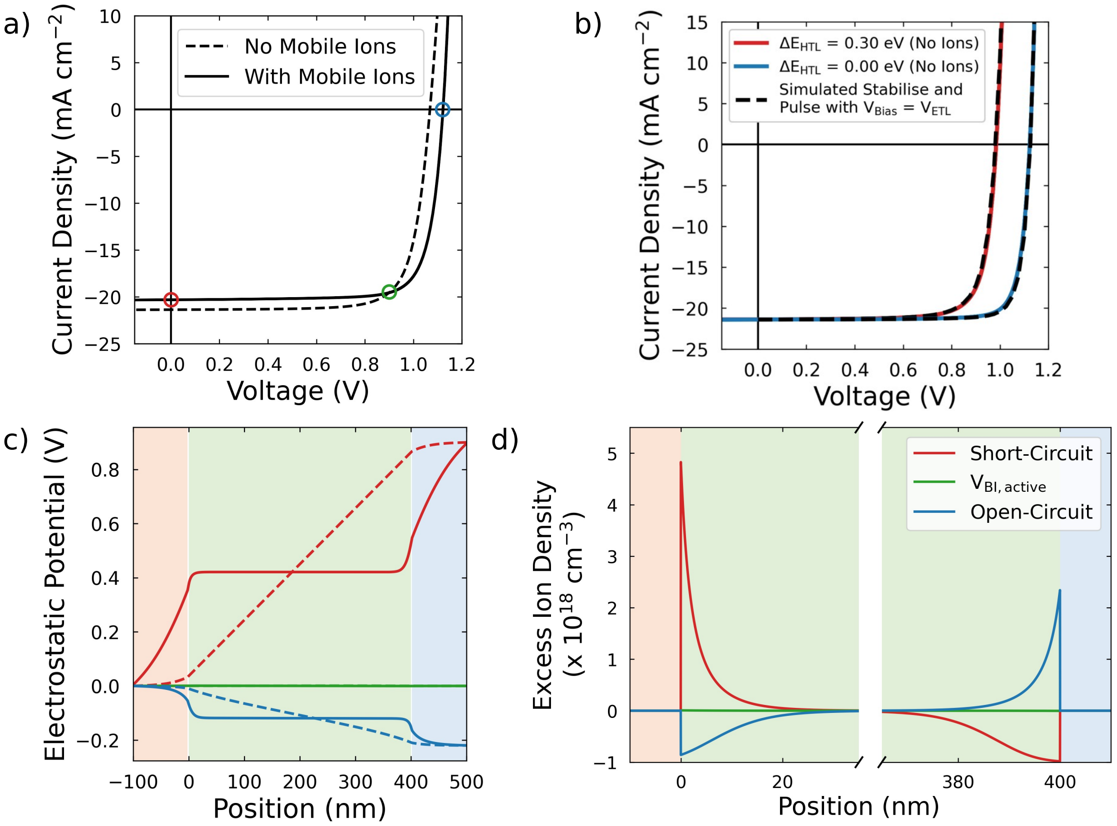

Figure 4.11: Drift–diffusion simulation results illustrating the influence of mobile ionic charge on device electrostatics and open-circuit voltage. a) Simulated J–V characteristics for devices with and without mobile ions, showing an increase in the open-circuit voltage when ionic redistribution is allowed. b) Simulated Stabilise and Pulse J–V curves for devices with different transport layer energetic offsets. c) Simulated electrostatic potential across the device under short-circuit, flat-band, and open-circuit conditions, highlighting the modification of the internal electric field due to ionic redistribution. d) Corresponding excess ionic charge density profiles under the same operating conditions, showing the accumulation of mobile ions at the interfaces and their role in shaping the device electrostatics. I acknowledge that the simulations and data collection were conducted by Lucy J. F. Hart from Imperial College London. Adapted from Ref. [1] under a Creative Commons Attribution 3.0 Unported Licence.

the flat-band potential on that side of the device. This is shown to match the J–V of an equivalent device with no mobile ions, as shown in Figure 4.11b. Importantly, simulations show that the difference in inversion voltages for the ETL and HTL varied only by 0.01 V over a range of ion densities. This implies that a single V_{flat} is therefore not a bad approximation, thereby validating the experimental results.

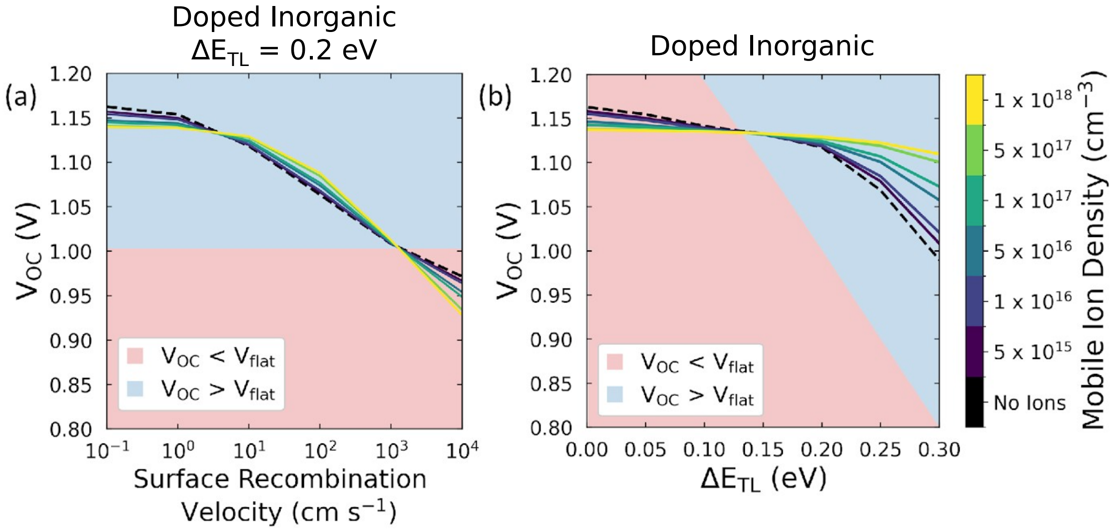

Figure 4.12: Drift–diffusion simulation results showing the dependence of the open-circuit voltage on interfacial recombination and energetic alignment for doped inorganic transport layer devices. a) Simulated V_{OC} as a function of surface recombination velocity for a fixed transport layer offset of $\Delta E_{\text{TL}} = 0.2$ eV. b) Simulated V_{OC} as a function of the transport layer energetic offset, ΔE_{TL}, for a fixed surface recombination velocity. Coloured curves correspond to different mobile ion densities, while the dashed black curve represents an equivalent device without mobile ions. The shaded regions indicate regimes where the open-circuit voltage lies below ($V_{\text{OC}} < V_{\text{flat}}$) or above ($V_{\text{OC}} > V_{\text{flat}}$) the flat-band condition. I acknowledge that the simulations and data collection were conducted by Lucy J. F. Hart from Imperial College London. Adapted from Ref. [1] under a Creative Commons Attribution 3.0 Unported Licence.

Next, we consider the magnitude of the ionic contribution to the open-circuit voltage as a function of surface recombination (Figure 4.12a) and energetic offset (Figure 4.12b). In both cases, the simulations reveal two distinct regimes. When the open-circuit voltage lies below the flat-band potential ($V_{\text{OC}} < V_{\text{flat}}$), the presence of mobile ions slightly reduces the achievable V_{OC}. In contrast, when the open-circuit voltage exceeds the flat-band potential ($V_{\text{OC}} > V_{\text{flat}}$), mobile ions increase V_{OC}.

Furthermore, the magnitude of this enhancement depends strongly on the energetic offset relative to the transport layers. As shown in Figure 4.12b, increasing the energetic offset leads to a larger improvement in V_{OC}. This behaviour is also strongly influenced by the mobile ion density. Devices with a higher mobile ion density exhibit a greater enhancement in V_{OC}, as more ionic charge is available to compensate minority carriers at the interfaces electrostatically.

Ions are therefore most beneficial in devices with large energetic offsets ($\Delta\mathrm{E}_{\mathrm{TL}}$), where the built-in potential is restricted, and recombination at the interfaces becomes significant. Under these conditions, ionic charge accumulation mitigates surface recombination by modifying the interfacial electrostatics. Consequently, the presence of mobile ions allows the open-circuit voltage to exceed the flat-band potential, demonstrating that ionic redistribution can partially decouple V_{OC} from V_{flat}.

In Figure 4.12a, the presence of mobile ions improves the open-circuit voltage in cases where the surface recombination velocity is between 1–1000 cm s^{-1}. In this region, the field-effect passivation-like mechanism discussed is strongest, and therefore the reduction in minority charge accumulation is enough to improve the V_{OC}. Below this region SRH recombination dominates, and so the field-effect passivation effect does not provide any benefit. These results explicitly support the experimental results, as they show that if passivation via the C_{60}-BA layer reduces recombination or decreases the energetic offset, then a reduction in the V_{OC} gain will be observed.

While the primary experimental focus of this chapter is on the open-circuit voltage, the broader performance implications of the presence of mobile ions are illustrated in Figure 4.13. These plots show the simulated power conversion efficiency as a function of the surface recombination velocity and the energetic offset of the transport layers for doped inorganic transport layers, both with and without ions.

It is clear from this result that mobile ionic modulation of V_{OC} shifts the parameter space where PSCs can achieve high power conversion efficiencies. Specifically, Figure 4.13 shows that the presence of mobile ions reduces the dependence of PCE on the energetic offset to the transport layers. This is because the redistribution of ions in these devices suppresses surface recombination currents and, therefore, allows them to maintain high open-circuit voltages even at larger energetic offsets to the transport layers. Thus, although the maximum achievable efficiency is similar with and without ions, devices containing ions outperform those without ions at higher energetic offsets.

However, this improved tolerance to energetic offset comes at a cost of greater sensitivity to the rate of surface recombination. Devices that contain a mobile ionic species lose PCE more rapidly than those without as surface recombination increases. This result implies that greater gains in PCE can be achieved by passivating the active/transport layer interfaces than by improving the energetic alignment between these layers. Thus, the results in this section show that the presence of a mobile ionic species alters the design criteria relative to a device without a mobile ionic charge.

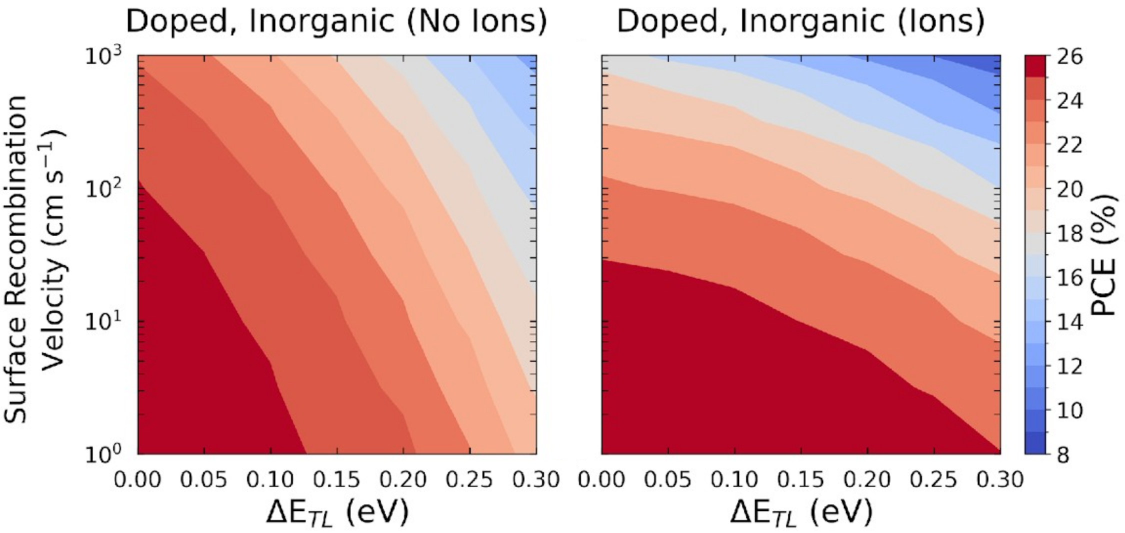

Figure 4.13: Drift–diffusion simulation results showing the impact of mobile ions on power conversion efficiency for doped inorganic transport layer devices. Shown are contour maps of the simulated power conversion efficiency as a function of surface recombination velocity and transport layer energetic offset, ΔE_{TL}, for devices without mobile ions (left) and with mobile ions (right). In the absence of mobile ions, high efficiency is confined to a narrow region of parameter space characterised by low surface recombination velocities and near-ideal energetic alignment. When mobile ions are included, the high-efficiency region expands, indicating that ionic redistribution relaxes constraints on energetic alignment while increasing the device's sensitivity to surface recombination. These results demonstrate that mobile ions can modify the design regime in which high efficiency is achieved, consistent with the experimentally observed steady-state voltage enhancement. I acknowledge that the simulations and data collection were conducted by Lucy J. F. Hart from Imperial College London. Adapted from Ref. [1] under a Creative Commons Attribution 3.0 Unported Licence.

4.5 Conclusions

In this chapter, the role of mobile ionic charge in determining the steady-state operation of perovskite solar cells has been examined experimentally using the Stabilise and Pulse technique. By decoupling ionic and electronic effects, this approach enables direct comparison of flat-band and steady-state device characteristics, providing a method for measuring the impact of ionic redistribution under operating conditions.

This is the first experimental demonstration that the presence of mobile ions systematically increases steady-state open-circuit voltage relative to equivalent devices without mobile ions. This observation provides direct experimental evidence that mobile ionic redistribution modifies the device's internal electrostatics, reducing minority-carrier accumulation and suppressing interfacial recombination. Importantly, this enhancement in V_{OC} is not an isolated effect, but was observed across devices with different transport layers, perovskite compositions, and both n–i–p and p–i–n configurations.

By comparing devices with differing levels of interfacial passivation, it was further demonstrated that the magnitude of the steady-state voltage enhancement is strongly dependent on the surface recombination rate. Devices with reduced interfacial recombination exhibited smaller gains in V_{OC} relative to the flat-band condition. Crucially, the influence of mobile ions persisted in high-efficiency devices, which showed negligible hysteresis under traditional measurement techniques. In such devices, the SaP analysis revealed that the presence of mobile ions boosted the voltage up to and beyond the flat-band condition, demonstrating that ionic motion remains relevant even when hysteresis is suppressed. Additionally, the SaP analysis of this device highlights an important distinction between hysteresis and ion motion; the absence of hysteresis does not imply that mobile ions are inactive or that their impact on device performance is negligible. Although the magnitude of the effect is reduced in mixed-cation systems, the underlying mechanism remains the same.

Drift-diffusion simulations reproduce the key trends observed experimentally and provide a mechanistic interpretation of the results. A key result is that the presence of mobile ions does not *a priori* reduce the maximum achievable efficiency of perovskite solar cells; however, mobile ions shift the design regime where this maximum efficiency is attained. It is demonstrated that this is due to the size of interfacial recombination currents in perovskite solar cells, which are less sensitive to energetic misalignments at the perovskite/transport layer interfaces than in an equivalent device with no mobile ions, provided that the V_{OC} exceeds the flat-band condition. This increases the range of energetic offsets at which perovskite solar cells can achieve high efficiencies. However, it reduces their tolerance to high surface recombination velocities, which explains the field's recent focus on minimising interfacial recombination.

Taken together, the results in this chapter demonstrate that mobile ions are not necessarily detrimental to the performance of perovskite solar cells. Instead, they modify the regime in which high performance is attained by redistributing internal electric fields and suppressing interfacial recombination under steady-state conditions. While ionic field screening reduces photocurrent, these losses can be compensated by ion-mediated increases in photovoltage. These findings establish that the impact of mobile ions on steady-state performance must be considered holistically and provide an experimental foundation for interpreting ionic effects in perovskite devices beyond the conventional hysteresis framework.

4.A Appendix

4.A.1 Additional Figures

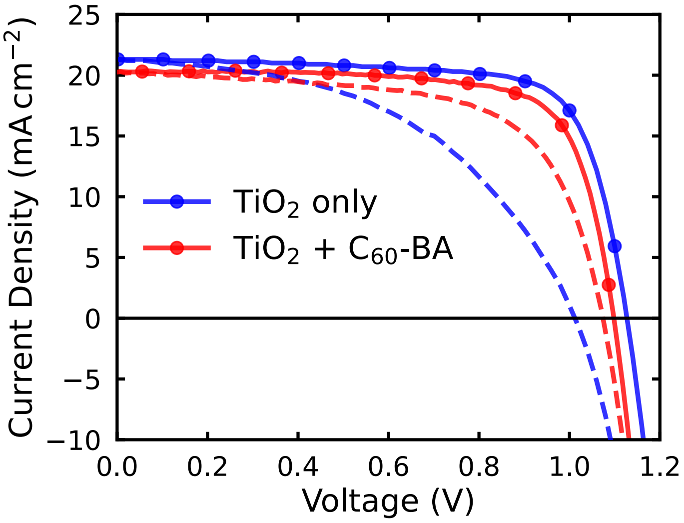

Figure 4.A1: Comparison of forward and reverse J–V characteristics for TiO_2 devices without and with a C_{60}-BA passivation layer. Solid lines correspond to the forward scan, while dashed lines represent the reverse scan.

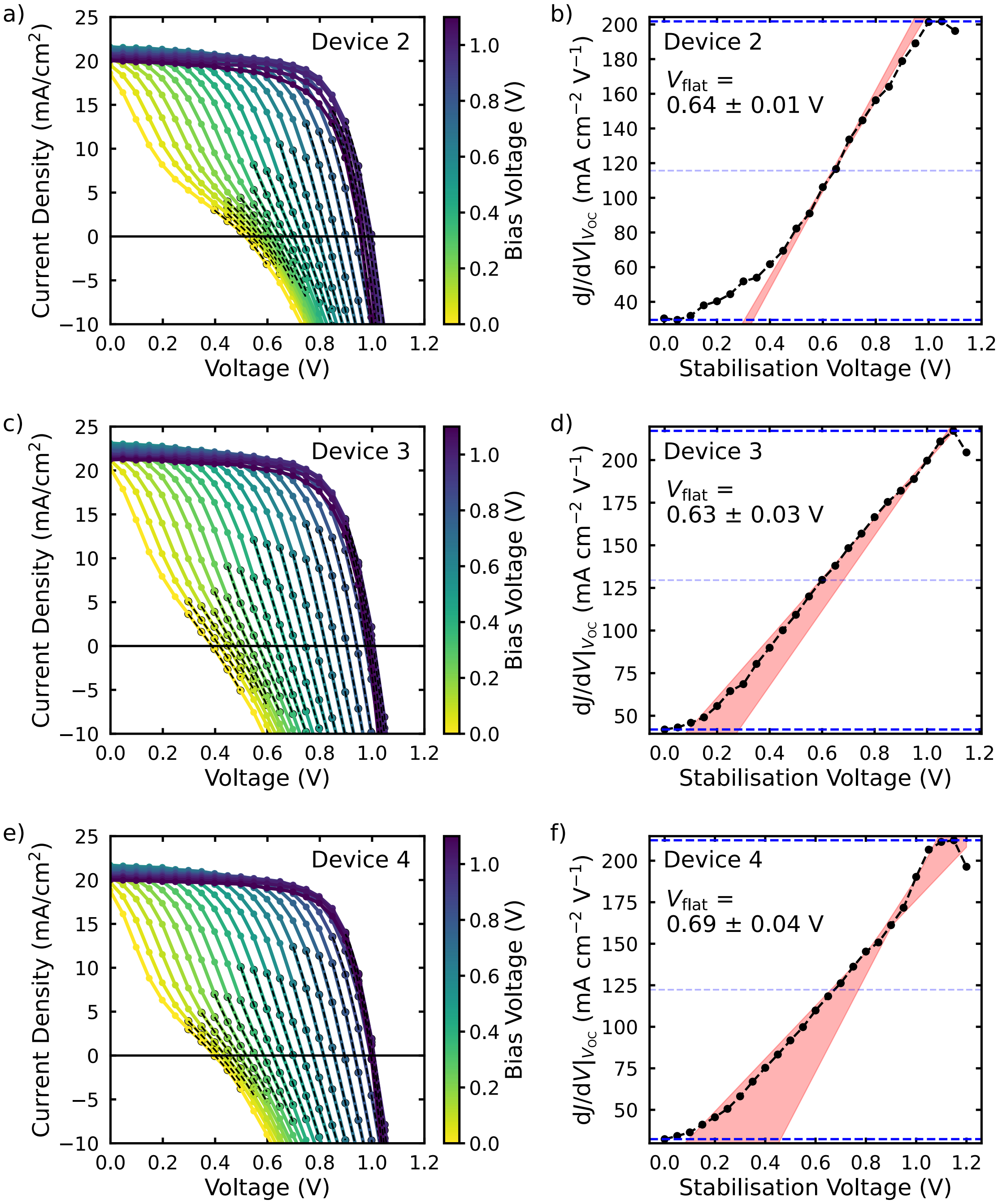

Figure 4.A2: Stabilise and Pulse (SaP) current–voltage curves and corresponding differential gradient analysis for TiO_2-only Devices 2–4, as summarised in Table 4.1. (a,c,e) SaP J–V curves measured at increasing stabilisation voltages, with the colour scale indicating the applied bias. (b,d,f) Gradient analysis (dJ/dV) as a function of stabilisation voltage used to extract V_{flat}. The linear fitting region employed to determine V_{flat} is highlighted, and the extracted value is indicated in each panel.

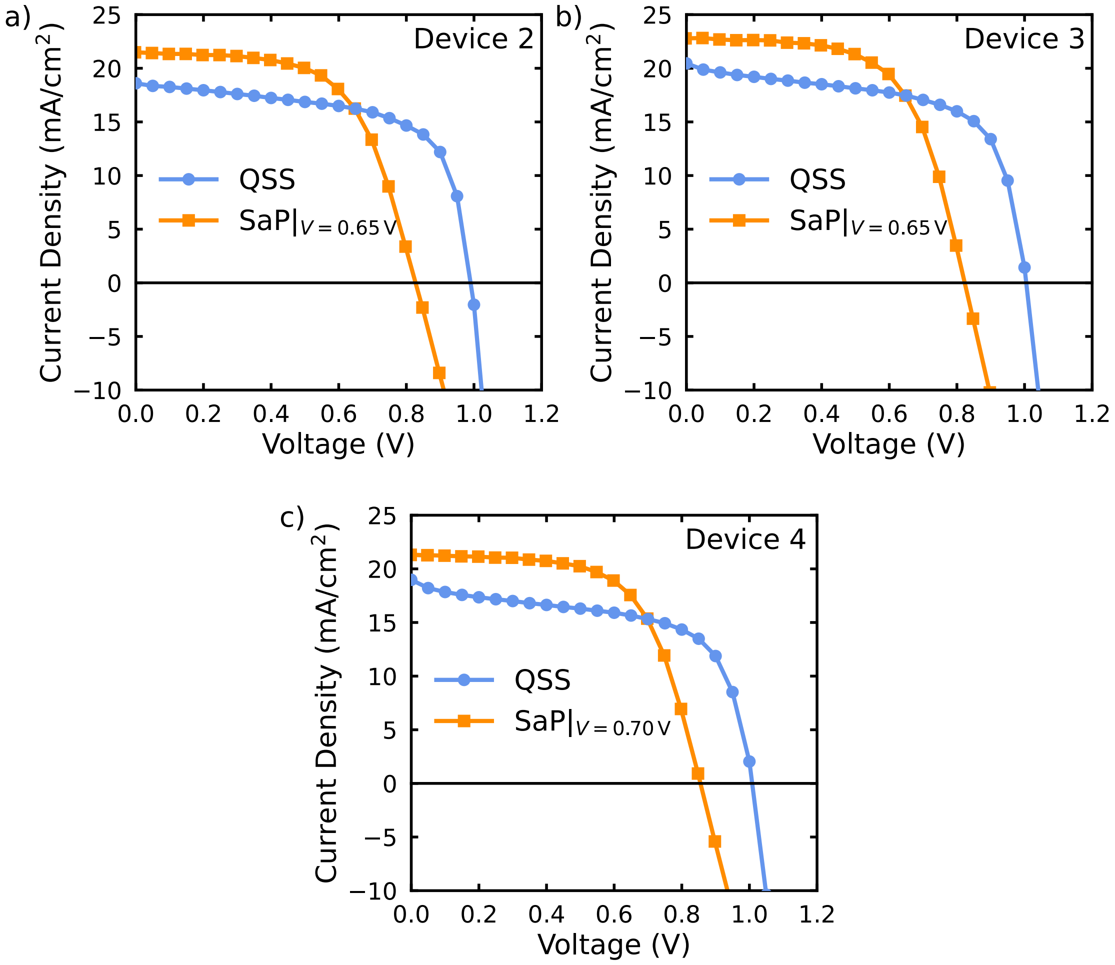

Figure 4.A3: Comparison of quasi-steady-state (QSS) and Stabilise and Pulse current–voltage curves for TiO_2 control devices (Devices 2–4). In each panel, the Stabilise and Pulse J–V curve corresponds to the extracted flat-band potential ($V_{\text{bias}} \approx 0.65$ V), while the QSS J–V curve reflects steady-state operation in the presence of mobile ions. Where the exact flat-band potential was not directly measured during the Stabilise and Pulse measurement, the closest available V_{bias} value was used. The uncertainty associated with each extracted QSS data point is smaller than the marker size and is therefore not visible.

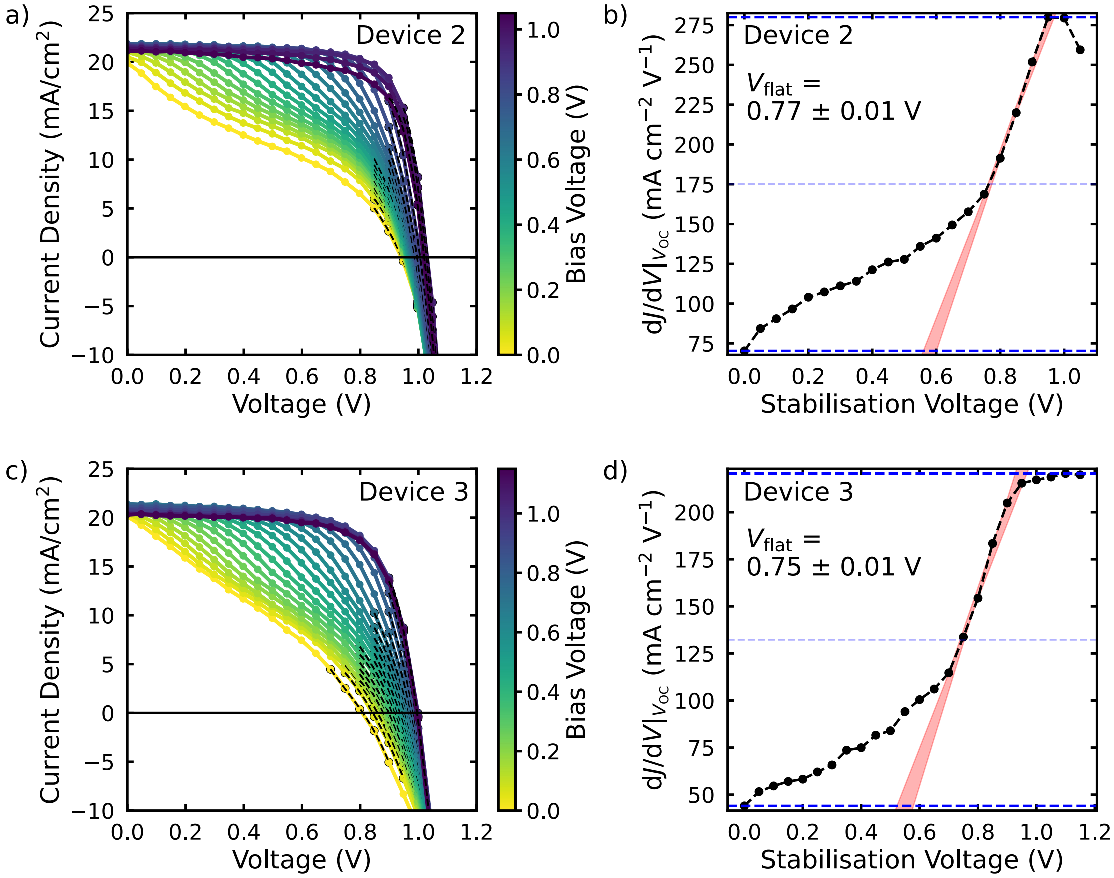

Figure 4.A4: Stabilise and Pulse (SaP) current–voltage curves and corresponding differential gradient analysis for TiO_2 + C_{60}-BA passivated Devices 2 and 3, as summarised in Table 4.2. (a,c) SaP J–V curves measured at incrementally increasing stabilisation voltages, with the colour scale indicating the applied bias. (b,d) Gradient analysis (dJ/dV) as a function of stabilisation voltage used to extract V_{flat}. The linear fitting region employed to determine V_{flat} is highlighted, and the extracted value is indicated in each panel.

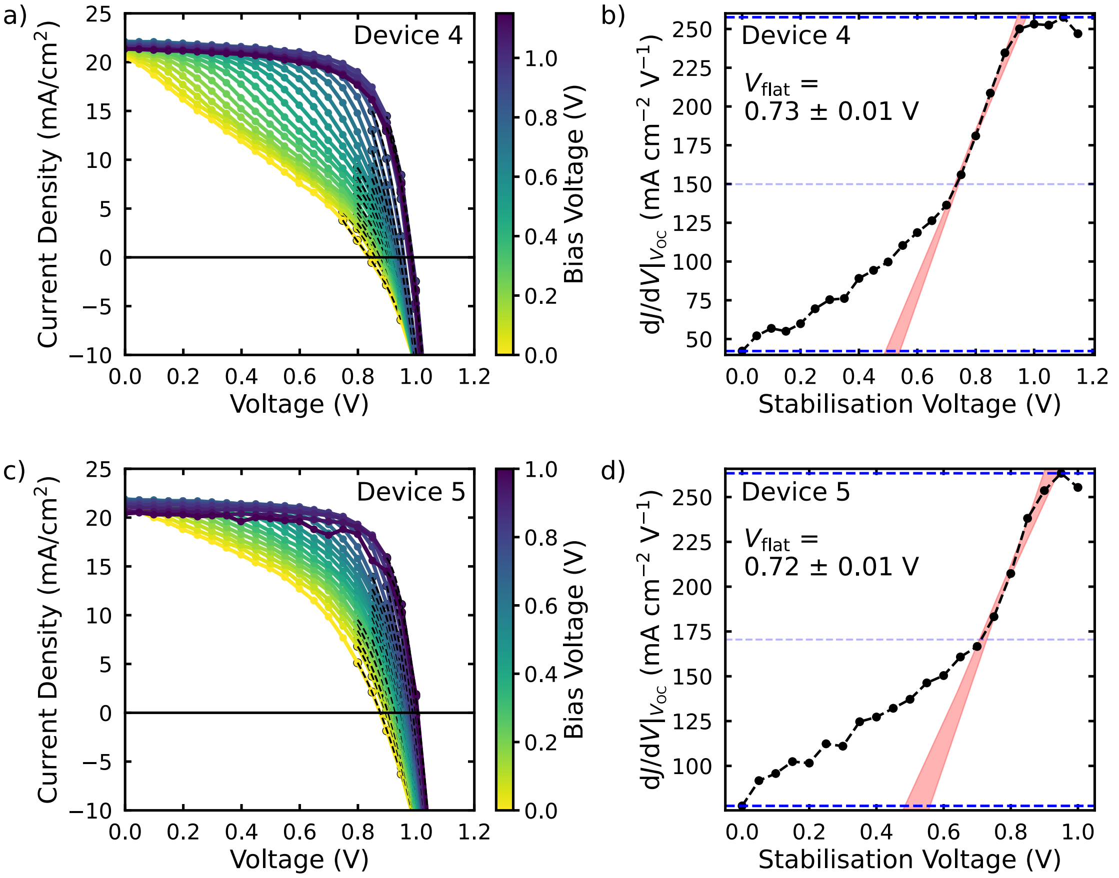

Figure 4.A5: Stabilise and Pulse (SaP) current–voltage curves and corresponding differential gradient analysis for TiO_2 + C_{60}-BA passivated Devices 4 and 5, as summarised in Table 4.2. (a,c) SaP J–V curves measured at incrementally increasing stabilisation voltages, with the colour scale indicating the applied bias. (b,d) Gradient analysis (dJ/dV) as a function of stabilisation voltage used to extract V_{flat}. The linear fitting region employed to determine V_{flat} is highlighted, and the extracted value is indicated in each panel.

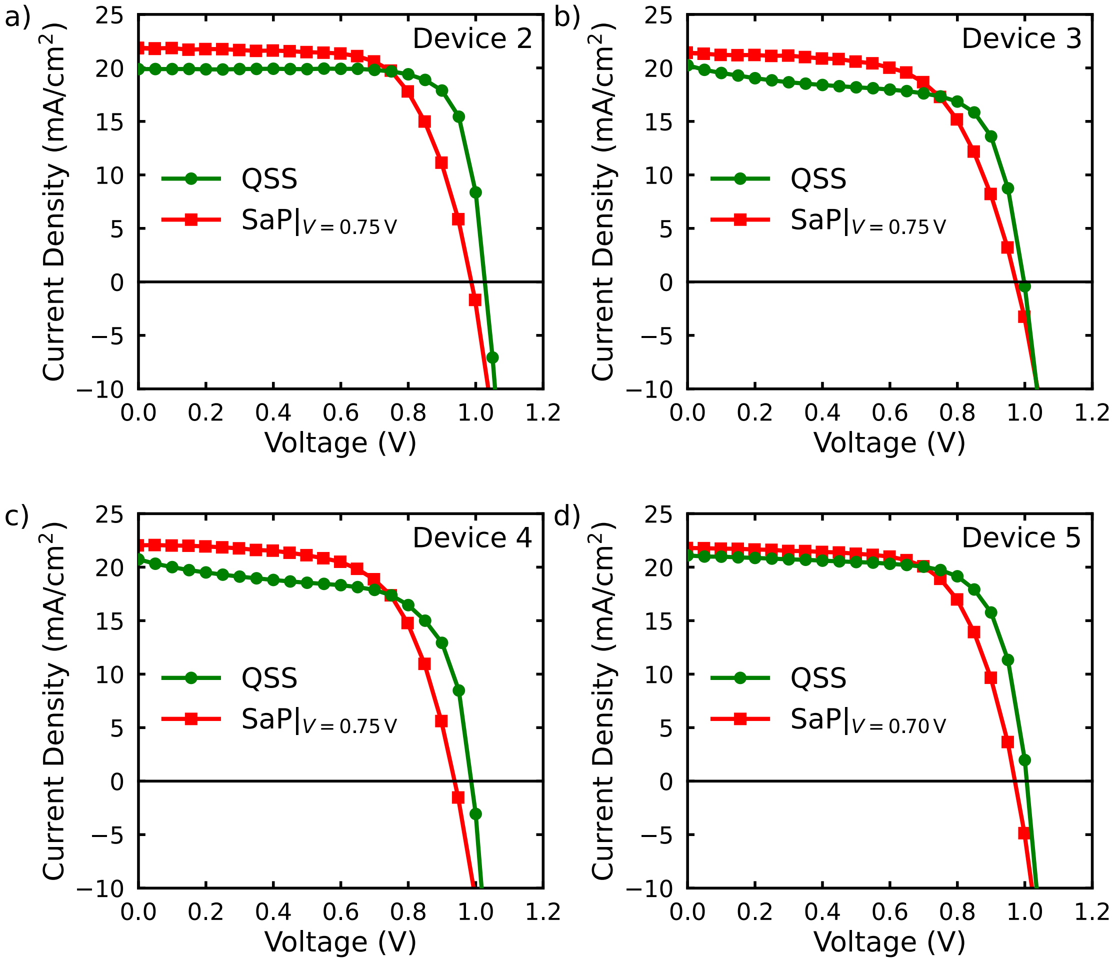

Figure 4.A6: Comparison of quasi-steady-state (QSS) and Stabilise and Pulse current–voltage curves for TiO_2 + C_{60}-BA control devices (Devices 2–5). In each panel, the Stabilise and Pulse J–V curve corresponds to the extracted flat-band potential ($V_{\mathrm{bias}} \approx 0.75$ V), while the QSS J–V curve reflects steady-state operation in the presence of mobile ions. Where the exact flat-band potential was not directly measured during the Stabilise and Pulse measurement, the closest available V_{bias} value was used. The uncertainty associated with each extracted QSS data point is smaller than the marker size and is therefore not visible.

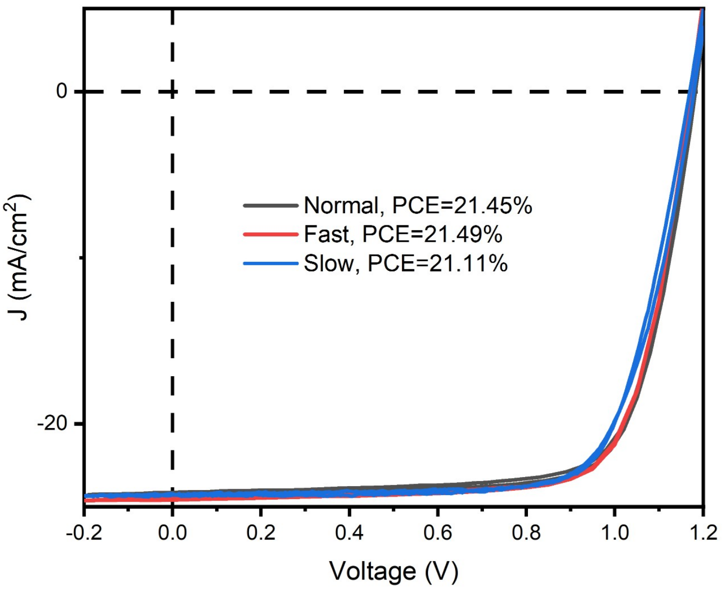

Figure 4.A7: Current–voltage characteristics of the p–i–n device with architecture ITO/NiO$_x$/2PACz/perovskite/PEAI/PCBM/BCP/Ag measured under different scan conditions (Normal, Fast, and Slow), as detailed in the corresponding appendix Table 4.A1. Dashed lines indicate $J = 0$ and $V = 0$ for clarity. Reported PCE values are indicated in the legend for each scan condition.

4.A.2 Additional Tables

Table 4.A1: Device performance metrics of the p–i–n architecture (ITO/NiO$_x$/2PACz/perovskite/PEAI/PCBM/BCP/Ag) measured under different scan conditions (Normal, Fast, and Slow). The scan step size and delay time used for each condition are listed alongside the extracted photovoltaic parameters: V_{OC}, J_{SC}, power conversion efficiency (PCE), and fill factor (FF).

Scan	Direction	Step (V)	Delay (ms)	V_{OC} (V)	J_{SC} (mA cm^{-2})	PCE (%)	FF
Normal	Reverse	0.03	10	1.17	24.00	21.45	0.76
	Forward	0.03	10	1.19	24.00	21.13	0.73
Fast	Reverse	0.05	0.01	1.15	24.58	21.49	0.76
	Forward	0.05	0.01	1.15	24.58	21.59	0.76
Slow	Reverse	0.005	500	1.18	24.33	20.90	0.73
	Forward	0.005	500	1.17	24.33	21.11	0.74

References

(1) Hart, L. J. F.; Angus, F. J.; Li, Y.; Khaleed, A.; Calado, P.; Durrant, J. R.; Djurišić, A. B.; Docampo, P.; Barnes, P. R. F. *Energy & Environmental Science* **2024**, *17*, 7107–7118.

(2) Eames, C.; Frost, J. M.; Barnes, P. R. F.; O'Regan, B. C.; Walsh, A.; Islam, M. S. *Nature Communications* **2015**, *6*, 7497.

(3) Moia, D.; Gelmetti, I.; Calado, P.; Hu, Y.; Li, X.; Docampo, P.; de Mello, J.; Maier, J.; Nelson, J.; Barnes, P. R. F. *Physical Review Applied* **2022**, *18*, 044056.

(4) Snaith, H. J.; Abate, A.; Ball, J. M.; Eperon, G. E.; Leijtens, T.; Noel, N. K.; Stranks, S. D.; Wang, J. T.-W.; Wojciechowski, K.; Zhang, W. *The Journal of Physical Chemistry Letters* **2014**, *5*, 1511–1515.

(5) Thiesbrummel, J. et al. *Advanced Energy Materials* **2021**, *11*, 2101447.

(6) Le Corre, V. M.; Diekmann, J.; Peña-Camargo, F.; Thiesbrummel, J.; Tokmoldin, N.; Gutierrez-Partida, E.; Peters, K. P.; Perdigón-Toro, L.; Futscher, M. H.; Lang, F.; Warby, J.; Snaith, H. J.; Neher, D.; Stolterfoht, M. *Solar RRL* **2022**, *6*, 2100772.

(7) Xu, W.; Hart, L. J. F.; Moss, B.; Caprioglio, P.; Macdonald, T. J.; Furlan, F.; Panidi, J.; Oliver, R. D. J.; Pacalaj, R. A.; Heeney, M.; Gasparini, N.; Snaith, H. J.; Barnes, P. R. F.; Durrant, J. R. *Advanced Energy Materials* **2023**, *13*, 2301102.

(8) Kim, S.; Bae, S.; Lee, S.-W.; Cho, K.; Lee, K. D.; Kim, H.; Park, S.; Kwon, G.; Ahn, S.-W.; Lee, H.-M.; Kang, Y.; Lee, H.-S.; Kim, D. *Scientific Reports* **2017**, *7*, 1200.

(9) Li, J.; Dong, Q.; Li, N.; Wang, L. *Advanced Energy Materials* **2017**, *7*, 1602922.

(10) Lee, J.-W.; Kim, S.-G.; Yang, J.-M.; Yang, Y.; Park, N.-G. *APL Materials* **2019**, *7*, 041111.

(11) Akel, S.; Kulkarni, A.; Rau, U.; Kirchartz, T. *PRX Energy* **2023**, *2*, 013004.

(12) Bi, E.; Chen, H.; Xie, F.; Wu, Y.; Chen, W.; Su, Y.; Islam, A.; Grätzel, M.; Yang, X.; Han, L. *Nature Communications* **2017**, *8*, 15330.

(13) Wang, R. et al. *Joule* **2019**, *3*, 1464–1477.

(14) Zhu, H.; Teale, S.; Lintangpradipto, M. N.; Mahesh, S.; Chen, B.; McGehee, M. D.; Sargent, E. H.; Bakr, O. M. *Nature Reviews Materials* **2023**, *8*, 569–586.

(15) Wu, S.; Chen, R.; Zhang, S.; Babu, B. H.; Yue, Y.; Zhu, H.; Yang, Z.; Chen, C.; Chen, W.; Huang, Y.; Fang, S.; Liu, T.; Han, L.; Chen, W. *Nature Communications* **2019**, *10*, 1161.

(16) Walsh, A.; Scanlon, D. O.; Chen, S.; Gong, X. G.; Wei, S.-H. *Angewandte Chemie International Edition* **2015**, *54*, 1791–1794.

(17) Kim, J.; Lee, S.-H.; Lee, J. H.; Hong, K.-H. *The Journal of Physical Chemistry Letters* **2014**, *5*, 1312–1317.

(18) Yin, W.-J.; Shi, T.; Yan, Y. *Applied Physics Letters* **2014**, *104*, 063903.

(19) Meggiolaro, D.; Motti, S. G.; Mosconi, E.; Barker, A. J.; Ball, J.; Andrea Riccardo Perini, C.; Deschler, F.; Petrozza, A.; De Angelis, F. *Energy & Environmental Science* **2018**, *11*, 702–713.

(20) Du, M.-H. *The Journal of Physical Chemistry Letters* **2015**, *6*, 1461–1466.

(21) Courtier, N. *Physical Review Applied* **2020**, *14*, 024031.

(22) Ahläng, C.; Nyman, M.; Österbacka, R. *Physical Review Applied* **2021**, *16*, 014041.

(23) Mozaffari, N.; Walter, D.; White, T. P.; Bui, A. D.; Tabi, G. D.; Weber, K.; Catchpole, K. R. *Solar RRL* **2022**, *6*, 2101087.

(24) Wu, N.; Walter, D.; Fell, A.; Wu, Y.; Weber, K. *The Journal of Physical Chemistry C* **2020**, *124*, 219–229.

(25) Jacobs, D. A.; Wu, Y.; Shen, H.; Barugkin, C.; Beck, F. J.; White, T. P.; Weber, K.; Catchpole, K. R. *Physical Chemistry Chemical Physics* **2017**, *19*, 3094–3103.

(26) Tress, W. *The Journal of Physical Chemistry Letters* **2017**, *8*, 3106–3114.

(27) Córdoba, M.; Taretto, K. *Solar RRL* **2024**, *8*, 2300742.

(28) Lin, S.; Yang, B.; Qiu, X.; Yan, J.; Shi, J.; Yuan, Y.; Tan, W.; Liu, X.; Huang, H.; Gao, Y.; Zhou, C. *Organic Electronics* **2018**, *53*, 235–241.

(29) Gong, X.; Sun, Q.; Liu, S.; Liao, P.; Shen, Y.; Grätzel, C.; Zakeeruddin, S. M.; Grätzel, M.; Wang, M. *Nano Letters* **2018**, *18*, 3969–3977.

(30) Huang, X.; Du, J.; Guo, X.; Lin, Z.; Ma, J.; Su, J.; Feng, L.; Zhang, C.; Zhang, J.; Chang, J.; Hao, Y. *Solar RRL* **2020**, *4*, 1900336.

(31) Aranda, C. A.; Alvarez, A. O.; Chivrony, V. S.; Das, C.; Rai, M.; Saliba, M. *Joule* **2024**, *8*, 241–254.

(32) Hill, N. S.; Cowley, M. V.; Gluck, N.; Fsadni, M. H.; Clarke, W.; Hu, Y.; Wolf, M. J.; Healy, N.; Freitag, M.; Penfold, T. J.; Richardson, G.; Walker, A. B.; Cameron, P. J.; Docampo, P. *Advanced Materials* **2023**, *35*, 2302146.

(33) Duijnstee, E. A.; Ball, J. M.; Le Corre, V. M.; Koster, L. J. A.; Snaith, H. J.; Lim, J. *ACS Energy Letters* **2020**, *5*, 376–384.

(34) Bonilla, R. S.; Hoex, B.; Hamer, P.; Wilshaw, P. R. *physica status solidi (a)* **2017**, *214*, 1700293.

(35) Wang, H.; Zhou, M.; Luo, H. *ACS Omega* **2018**, *3*, 1445–1450.

(36) Van Reenen, S.; Kemerink, M.; Snaith, H. J. *The Journal of Physical Chemistry Letters* **2015**, *6*, 3808–3814.

(37) Christians, J. A.; Manser, J. S.; Kamat, P. V. *The Journal of Physical Chemistry Letters* **2015**, *6*, 852–857.

(38) Dunbar, R. B. et al. *Journal of Materials Chemistry A* **2017**, *5*, 22542–22558.

(39) Thiesbrummel, J. et al. *Nature Energy* **2024**, *9*, 664–676.

(40) Bertoluzzi, L.; Boyd, C. C.; Rolston, N.; Xu, J.; Prasanna, R.; O'Regan, B. C.; McGehee, M. D. *Joule* **2020**, *4*, 109–127.

(41) Sajedi Alvar, M.; Blom, P. W.; Wetzelaer, G.-J. A. H. *Advanced Electronic Materials* **2020**, *6*, 1900935.

(42) Wojciechowski, K.; Stranks, S. D.; Abate, A.; Sadoughi, G.; Sadhanala, A.; Kopidakis, N.; Rumbles, G.; Li, C.-Z.; Friend, R. H.; Jen, A. K.-Y.; Snaith, H. J. *ACS Nano* **2014**, *8*, 12701–12709.

(43) Gao, Z.-W.; Wang, Y.; Choy, W. C. H. *Advanced Energy Materials* **2022**, *12*, 2104030.

(44) Liu, X.; Tsai, K.-W.; Zhu, Z.; Sun, Y.; Chueh, C.-C.; Jen, A. K.-Y. *Advanced Materials Interfaces* **2016**, *3*, 1600122.

(45) Van Daal, H. J. *Journal of Applied Physics* **1968**, *39*, 4467–4469.

(46) Chen, Y.; Meng, Q.; Zhang, L.; Han, C.; Gao, H.; Zhang, Y.; Yan, H. *Journal of Energy Chemistry* **2019**, *35*, 144–167.

(47) Yokoyama, T.; Nishitani, Y.; Miyamoto, Y.; Kusumoto, S.; Uchida, R.; Matsui, T.; Kawano, K.; Sekiguchi, T.; Kaneko, Y. *ACS Applied Materials & Interfaces* **2020**, *12*, 27131–27139.

(48) Rombach, F. M.; Haque, S. A.; Macdonald, T. J. *Energy & Environmental Science* **2021**, *14*, 5161–5190.

(49) Nakka, L.; Cheng, Y.; Aberle, A. G.; Lin, F. *Advanced Energy and Sustainability Research* **2022**, *3*, 2200045.

Chapter 5

Understanding the Impact of the Fermi Level of Transport Layers on Perovskite Solar Cell Device Performance

The contents of this chapter are based upon the published research article, *"Understanding the Impact of SAM Fermi Levels on High Efficiency p–i–n Perovskite Solar Cells"*.[1] This work was conceptualised by Prof. Pablo Docampo, Dr Wai Kin Yiu, Prof. Aleksandra B. Djurišić and Fraser J. Angus. Fraser J. Angus performed all Stabilise and Pulse measurements, interpreted the results, constructed the energy level diagrams, and analysed the J–V and TRPL data. Solar cell devices were fabricated and measured by Dr Wai Kin Yiu and Yin Li under the supervision of Prof. Aleksandra B. Djurišić. Dr Wai Kin Yiu performed the XRD and SEM measurements. Muhammad Umair Ali performed the TRPL measurement under the supervision of Prof. Aleksandra B. Djurišić. Hongbo Mo performed the UV–Vis absorption of the double cation perovskite and prepared the samples for KPFM. Jingbo Wang prepared the NiO_x nanoparticles. Tik Lun Leung performed and interpreted the KPFM measurements under the supervision of Prof. Anita W. Y. Ho-Baillie.

5.1 Probing Interfacial Energetics Using the Stabilise and Pulse Technique

The energetic alignment between the perovskite absorber and the charge-selective transport layers is critical to device performance. In this chapter, the Stabilise and Pulse (SaP) technique is used to probe interfacial energetics in operating perovskite solar cells directly. By manipulating the ionic distribution within the device, the SaP method enables quantification of the electrostatic potential drop across the perovskite layer. This quantity can then be directly related to the energetic properties of the charge-selective interfaces.

Interfaces between the perovskite absorber and the transport layers strongly influence photovoltaic performance by shaping interfacial recombination, passivation, and band bending.[2–4] In metal-halide perovskites, the presence of mobile ions alters the way energetic offsets influence device behaviour, making these devices less sensitive to energetic misalignment but more sensitive to interfacial recombination.[5] Consequently, strategies that improve interfacial passivation have become a major focus of the field. Examples include forming low-dimensional, layered perovskites at the absorber surface or using surface adsorption to passivate defect states, both of which can substantially improve device performance.[6, 7]

A widely adopted strategy for improving charge extraction in high-efficiency perovskite solar cells is the incorporation of self-assembled molecular (SAM) layers.[8–10] When bound to the surface of a typical charge-extraction contact, such as indium-doped tin oxide (ITO), these molecules form interfacial dipoles that modify the contact's effective work function, thereby inducing band bending.[11, 12] A dipole consists of a spatial separation between positive and negative charges, characterised by both magnitude and direction. When many molecules assemble in an ordered fashion, their individual dipoles add collectively, producing an electrostatic potential at the interface.[13] In the context of perovskite solar cells, a dipole-induced work function shift alters the band bending at the perovskite-electrode interface and therefore influences charge extraction and interfacial recombination. Such dipole-induced energetic shifts can dramatically improve the collection efficiency of an otherwise non-selective electrode.[14] Among the various molecular systems explored, carbazole-based phosphonic acid SAMs have yielded particularly high-performance devices, often attributed to reduced interfacial recombination and to enhanced charge extraction through favourable energetic alignment.[15–17]

Despite their widespread success, establishing a clear link between a SAM's molecular properties and the resulting device performance remains challenging. The power conversion efficiency of SAM-based devices is highly sensitive to the perovskite composition and device architecture.[18, 19] As a result, empirical trial-and-error approaches frequently guide optimisation. This difficulty is compounded by the inherent uncertainty in energy-level diagrams, which are typically constructed from measurements on partial device stacks, such as X-ray photoelectron spectroscopy (XPS) or electroabsorption spectroscopy, rather than from measurements on complete, operating devices.[20, 21] Furthermore, in the commonly employed p–i–n device architecture, the work functions of the ITO anode and the silver cathode differ by only a few tenths of an electronvolt.[22, 23] According to the conventional wisdom of solar cells, this would result in an exceptionally small built-in potential. Nevertheless, such devices routinely exhibit extremely high open-circuit voltages and negligible hysteresis, raising fundamental questions about the true driving forces governing charge extraction and recombination.

The Stabilise and Pulse technique provides a route to address these challenges by exploiting the sensitivity of mobile ions in the perovskite to the internal and applied external fields.[5, 24] As discussed in Chapter 4, the SaP method utilises the effects of ion accumulation at device interfaces on charge extraction and recombination. By applying a sequence of stabilisation biases followed by rapid voltage pulses, SaP enables the identification of the applied bias at which the ionic distribution within the perovskite becomes spatially uniform, corresponding to the flat-band potential, V_{flat}.[24] As the V_{flat} is closely related to the Fermi level positions of the adjacent charge-extraction layers, it provides a direct experimental handle on small changes in device energetics.[5]

In this chapter, SaP measurements are used to establish a direct link between the energetics imposed by charge-extraction layers and the resulting photovoltaic behaviour in high-efficiency, hysteresis-free perovskite solar cells. A series of chemically related carbazole-based SAM layers with systematically varied dipole strengths is employed to tune the interfacial electrostatics. We show that the built-in potential in p–i–n devices is far above the potential difference of the electrodes, ranging from 0.6–1.0 V. Furthermore, we show that the built-in potential in these devices is directly linked to the dipole strength of the SAM used. Additionally, we combine complementary characterisation using time-resolved photoluminescence (TRPL) and current density–voltage (J–V) curve analysis, which enables us to distinguish between increased recombination and efficient charge extraction and to identify the formation of potential barriers at device interfaces. The results in this chapter provide insights into the device physics of p–i–n perovskite solar cells, highlighting the role of interfacial energetics on device performance.

5.2 Influence of SAM Layers on Perovskite Solar Cell Energetics and Performance

5.2.1 Bulk Perovskite Properties on SAM-Modified Substrates

Before attributing any differences in device energetics or photovoltaic performance to the self-assembled molecular layers, it is necessary to exclude changes in the structural or optical properties of the perovskite absorber. In this section, the morphology of perovskite films deposited on different SAM-modified substrates is examined. Establishing that the bulk perovskite properties remain unchanged provides a baseline for interpreting subsequent electrical and optical measurements in terms of interfacial energetics rather than variations in the absorber itself.

Perovskite Film Morphology on SAM-Modified Substrates

To investigate how SAM dipole strength influences the Fermi level of the underlying metal oxide, we utilise the following molecules: [2-(9H-carbazol-9-yl)ethyl]phosphonic acid (2PACz), [2-(3,6-dimethoxy-9H-carbazol-9-yl)ethyl] phosphonic acid (MeO-2PACz), and [4-(3,6-dimethyl-9H-carbazol-9-yl)butyl]phosphonic acid (Me-4PACz). These materials have been extensively studied in the literature and thus serve as important benchmarks while delivering high power conversion efficiencies.[25–31] Furthermore, these SAMs exhibit a clear trend in dipole strength, going from 2PACz > Me-4PACz > MeO-2PACz, which will result in well-differentiated Fermi level shifts upon anchoring on a metal oxide surface.[32, 33] This effect has been well characterised via ultraviolet photoelectron spectroscopy (UPS) and X-ray photoelectron spectroscopy (XPS) measurements.[34] These SAM layers, therefore, provide an ideal starting point for increasing our understanding of device energetics.

Figure 5.1 shows the molecular structures of the three self-assembled molecules used throughout this chapter. All three molecules contain a carbazole-based hole-transporting unit and a phosphonic acid anchoring group for attachment to the substrate surface. The primary structural differences arise from the functional substituents attached to the carbazole unit and the length of the molecular linker. MeO-2PACz contains electron-donating methoxy groups, while Me-4PACz contains methyl substituents and an extended butyl linker. These structural modifications alter the molecular dipole moment and interfacial energetics, thereby influencing the electronic properties of the resulting interface.

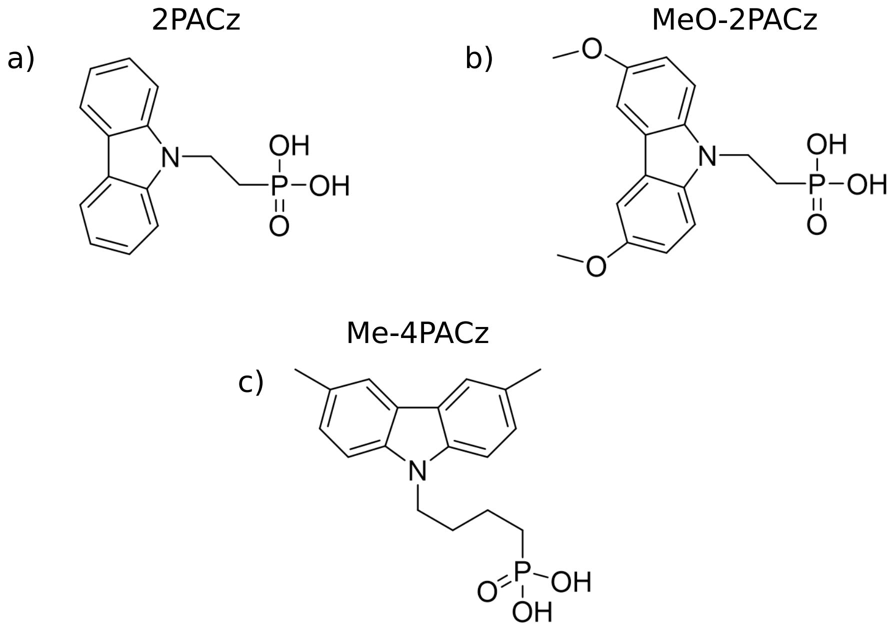

Figure 5.1: Molecular structures of the self-assembled molecules used for substrate modification: a) 2PACz, b) MeO-2PACz, and c) Me-4PACz.

The performance of perovskite solar cells is highly sensitive to the microstructure and surface morphology of the absorber layer.[35, 36] Variations in grain size, grain boundaries, and surface roughness can strongly influence both bulk and interfacial recombination processes. In particular, increased grain-boundary density is commonly associated with enhanced non-radiative recombination, whereas incomplete surface coverage or pinhole formation can lead to shunting pathways or poorly defined electrical contacts.[37, 38] Establishing that the incorporation of different SAM layers does not significantly alter the morphology of the perovskite film is therefore a necessary step before attributing any changes in device performance to interfacial energetics. In this chapter, we focus on a p–i–n configuration where nickel oxide (NiO_x) is used as the hole-transporting layer, which has been shown to improve surface coverage and efficiency of perovskite solar cells compared to bare indium-doped tin oxide (ITO).[39]

Scanning electron microscopy (SEM) and X-ray diffraction (XRD) were used to characterise the morphology of the archetypal methylammonium lead iodide (MAPI) and an optimised formulation that incorporates a double cation composition of formamidinium and caesium ($FA_{0.9}Cs_{0.1}PbI_{2.9}Br_{0.1}$), which is abbreviated to "DC" for the remainder of this chapter. The perovskite films were deposited on top of the NiO_x modified ITO, which had been treated with the different carbazole-based SAMs. The resulting SEM images and XRD diffractograms for both MAPI and DC perovskites on all SAMs are shown in Figures 5.2 and 5.3, respectively.

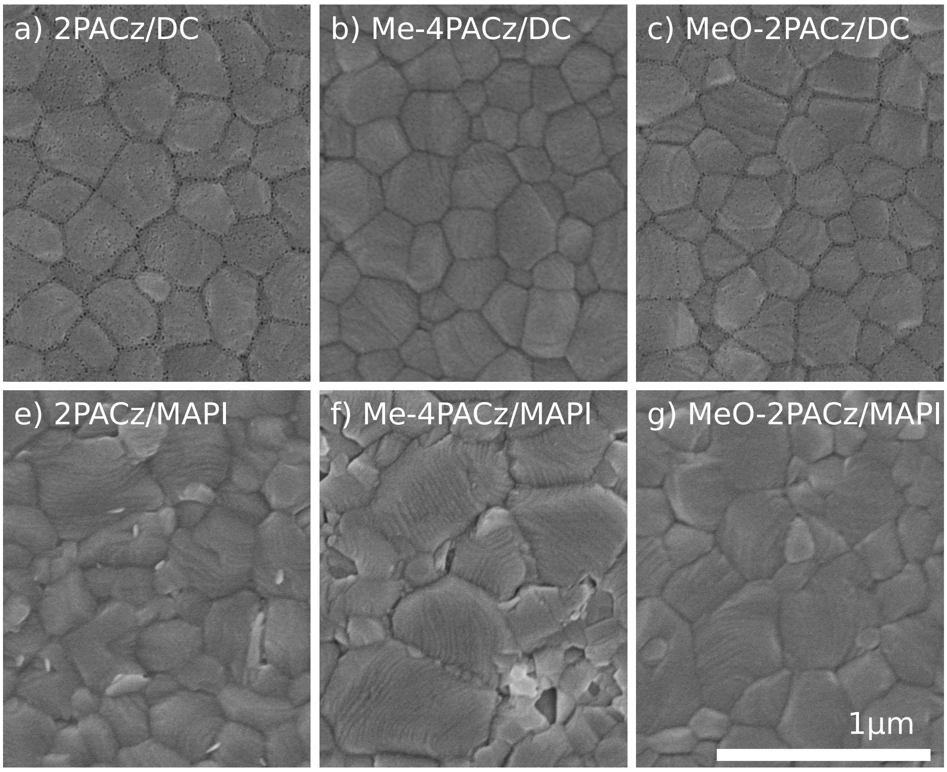

Figure 5.2: Scanning electron microscopy (SEM) images of perovskite films deposited on NiO$_x$-modified indium-doped tin oxide (ITO) substrates treated with different carbazole-based self-assembled molecules (SAMs). The top row shows double-cation (DC) perovskite films deposited on a) 2PACz, b) Me-4PACz, and c) MeO-2PACz, while the bottom row shows the corresponding methylammonium lead iodide (MAPI) films deposited on e) 2PACz, f) Me-4PACz, and g) MeO-2PACz. All films exhibit compact morphologies with comparable grain sizes across the different SAMs. The scale bar in g) corresponds to $\sim$1 μm and applies to all SEM images. I acknowledge that this data was collected by Wai Kin Yiu at the University of Hong Kong. Figure adapted from Ref. [1] (CC BY 4.0).

Across all samples, compact, continuous, high-quality films were obtained, with no evidence of pinholes or large-scale morphological defects. To quantify grain size from SEM images, we selected and measured $\sim$120 grains for DC perovskite and $\sim$70 for MAPI. The grain size distributions were comparable for all SAMs, with the average difference being smaller than the standard deviation values as shown in Table 5.1.

Table 5.1: Average grain size extracted for MAPI and DC perovskite films deposited on different SAMs. Values are reported as mean ± standard deviation. I acknowledge that this data was collected by Wai Kin Yiu at the University of Hong Kong.

Perovskite	**2PACz (nm)**	**MeO-2PACz (nm)**	**Me-4PACz (nm)**
MAPI	302.8 ± 81.6	289.5 ± 104.8	276.6 ± 100.1
DC	274.6 ± 57.5	253.0 ± 60.6	258.6 ± 64.6

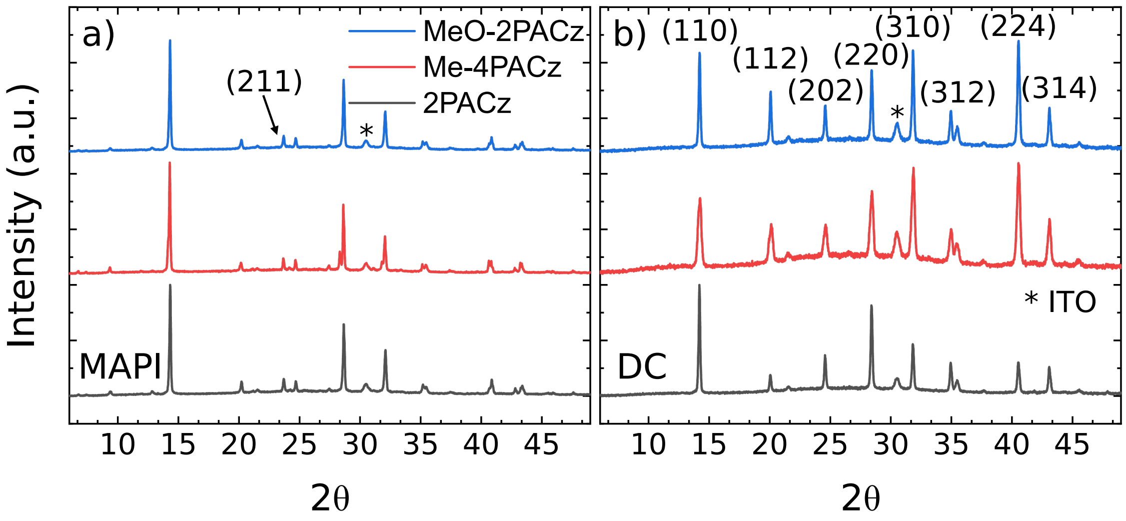

Figure 5.3: X-ray diffraction (XRD) patterns of perovskite films deposited on NiO$_x$-modified indium-doped tin oxide (ITO) substrates treated with different carbazole-based self-assembled molecules (SAMs). Panel a) shows methylammonium lead iodide (MAPI) perovskite films deposited on 2PACz, Me-4PACz, and MeO-2PACz, while panel b) shows the corresponding double-cation (DC) perovskite films deposited on the same SAMs. The diffraction peaks correspond to the expected perovskite crystal reflections, confirming the formation of phase-pure perovskite films across all SAMs. Peaks marked with an asterisk (*) originate from the underlying ITO substrate. I acknowledge that this data was collected by Wai Kin Yiu at the University of Hong Kong. Figure adapted from Ref. [1] (CC BY 4.0).

Additionally, the XRD diffractograms for both perovskite (Figures 5.3a and b) compositions reveal a phase-pure structure with no notable differences when the perovskite is grown on the different SAM layers. The only exception here is the DC perovskite when grown on Me-4PACz, which resulted in a relative loss of intensity for the peak at 13.8° 2θ compared to the other reflections. This loss of intensity indicates that the crystallites in this film are more disordered, with fewer crystals preferentially oriented along the 110 direction. These observations indicate that the chemical modification of the NiO$_x$ surface through SAM attachment does not disrupt the crystallisation process of the perovskite under the fabrication conditions used, which are described in Section 3.1.6. This is an important result, as it rules out morphology-driven explanations for differences in photovoltaic performance, such as changes in grain boundary density or surface coverage. Consequently, any trends in open-circuit voltage, short-circuit current density, or recombination dynamics discussed in later sections can be interpreted with confidence as not resulting from differences in film quality.

5.2.2 Impact of SAM Layers on Device Electrical and Optical Behaviour

To understand how carbazole-based self-assembled molecular layers influence device operation, the electrical and optical behaviour of complete perovskite solar cells is examined. Conventional photovoltaic measurements are combined with time-resolved photoluminescence and Kelvin probe microscopy to probe charge extraction, recombination dynamics, and interfacial energetics. These complementary measurements provide insight into how the choice of SAM layer governs device performance beyond what can be inferred from current–voltage characteristics alone.

Photovoltaic Performance of SAM-Based Devices

Complete perovskite solar cells with the architecture ITO/NiO_x/SAM/perovskite /PCBM/BCP/Ag were fabricated and characterised. In this structure, indium-doped tin oxide (ITO) and NiO_x form the hole-selective contact, while [6,6]-phenyl-C_{61}-butyric acid methyl ester (PCBM) and bathocuproine (BCP) act as the electron-transport layers beneath the silver (Ag) top electrode. The resulting J–V curves measured under AM 1.5 simulated sunlight are shown in Figure 5.4 for DC and MAPI devices. Champion devices exceed 22% power conversion efficiency for DC and 20% for MAPI. A summary of the champion device metrics for each SAM is provided in Table 5.2.

Table 5.2: Photovoltaic parameters of the champion devices corresponding to the J–V curves shown in Figure 5.4 for double-cation (DC) and MAPI perovskite devices employing carbazole-based self-assembled molecules.

SAM	J_{SC} (mA/cm^2)	V_{OC} (V)	FF	PCE (%)
DC perovskite				
2PACz	24.6	1.09	0.79	21.2
Me-4PACz	25.5	1.09	0.81	22.6
MeO-2PACz	25.8	1.07	0.82	22.7
MAPI perovskite				
2PACz	21.6	1.08	0.77	18.0
Me-4PACz	23.1	1.09	0.82	20.5
MeO-2PACz	21.6	1.05	0.81	18.4

Devices incorporating MAPI exhibit clear hysteresis under standard scan-rate conditions, whereas the DC composition shows hysteresis-free behaviour, consistent with previous reports for these material systems.[40] Full device fabrication and measurement details are provided in Section 3.1.6 and Section 3.2.1, respectively.

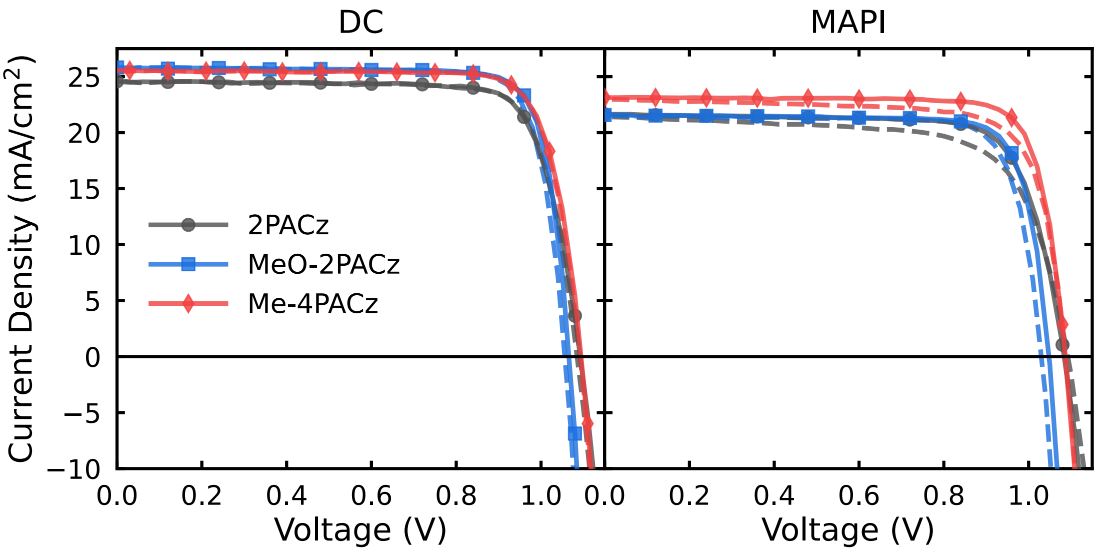

Figure 5.4: Current density–voltage (J–V) characteristics of p–i–n perovskite solar cells incorporating carbazole-based self-assembled molecules (SAMs) with different dipole strengths: a) double-cation (DC) perovskite devices and b) MAPI devices. Devices employ 2PACz, MeO-2PACz, and Me-4PACz as the hole-selective SAM layer. Forward scans are shown as dashed lines, while reverse scans are shown as solid lines. While all devices exhibit minimal hysteresis under standard measurement conditions, systematic differences in current density, voltage, and fill factor are observed as a function of SAM choice and perovskite composition. Figure adapted from Ref. [1] (CC BY 4.0).

To understand the differences resulting from incorporating these SAMs, it is necessary to examine statistics across the entire series. Full device statistics for the DC-containing devices are shown in Figure 5.5. Here, it is evident that Me-4PACz consistently produces the highest-performing devices, with the MeO-2PACz device at 22.7% being a statistical outlier. This increase in average efficiency is associated with a higher average open-circuit voltage than in 2PACz and MeO-2PACz. The current density obtained for all SAMs was relatively uniform; however, a clear change in fill factor also affected PCE. Devices containing MeO-2PACz displayed a greater FF compared to Me-4PACz, which was in turn greater than 2PACz.

This comparison is supported by statistical analysis of the device utilising MAPI as the absorber, which also shows similar trends. Again, a clear voltage boost is observed, primarily with Me-4PACz but also with 2PACz present. Additionally, the trend in fill factor is very similar to MeO-2PACz and Me-4PACz, achieving greater fill factors than 2PACz. Interestingly, for MAPI devices, utilising Me-4PACz results in a clear increase in the achievable short-circuit current density. Overall, Me-4PACz

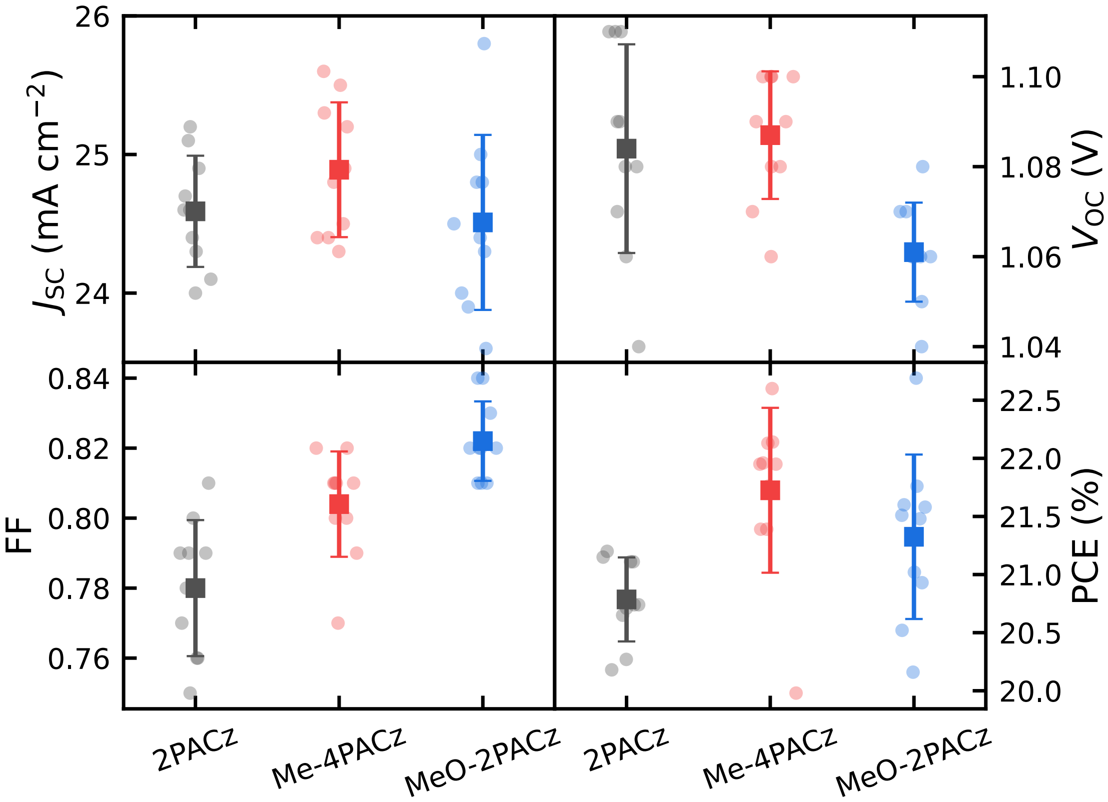

Figure 5.5: Statistical distribution of photovoltaic performance parameters for double-cation (DC) perovskite solar cells incorporating carbazole-based self-assembled molecules (SAMs). Shown are the short-circuit current density (J_{SC}), open-circuit voltage (V_{OC}), fill factor (FF), and power conversion efficiency (PCE) for devices using 2PACz, Me-4PACz, and MeO-2PACz as the hole-selective SAM. For each SAM, data are shown for ten independent devices. Individual device values are displayed as semi-transparent points, while square markers represent the mean value and error bars denote the standard deviation. Figure adapted from Ref. [1] (CC BY 4.0).

yields a higher power conversion efficiency in devices using either DC or MAPI. We note that the V_{OC} in these devices is likely limited by PCBM, as is widely observed in the literature, which explains the small difference in this parameter between the DC- and MAPI-containing devices.[41, 42]

While J–V measurements provide a convenient metric for device performance, they do not directly distinguish between changes in recombination dynamics, charge extraction, or interfacial band bending. For this reason, complementary time-resolved measurements are required to determine the origins of performance differences across the different SAMs.

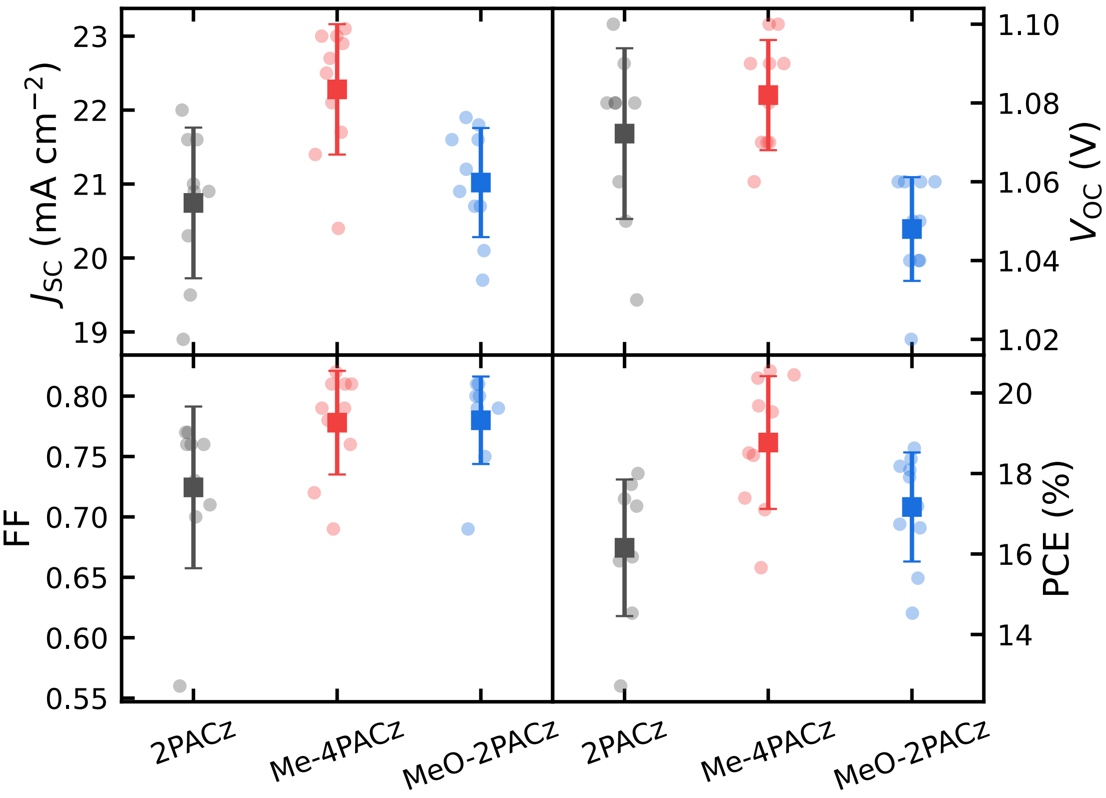

Figure 5.6: Statistical distribution of photovoltaic performance parameters for methylammonium lead iodide (MAPI) perovskite solar cells incorporating carbazole-based self-assembled molecules (SAMs). Shown are the short-circuit current density (J_{SC}), open-circuit voltage (V_{OC}), fill factor (FF), and power conversion efficiency (PCE) for devices using 2PACz, Me-4PACz, and MeO-2PACz as the hole-selective SAM. For the 2PACz devices, data are shown for 9 independent devices, whereas 10 devices are shown for Me-4PACz and MeO-2PACz. Individual device values are displayed as semi-transparent points, while square markers represent the mean value and error bars denote the standard deviation. Figure adapted from Ref. [1] (CC BY 4.0).

Recombination Dynamics from Time-Resolved Photoluminescence

Time-resolved photoluminescence (TRPL) measurements were employed to probe the recombination dynamics of perovskite films deposited on different SAM-modified substrates. To keep this measurement as directly related to device performance as possible, the stack used was ITO/NiO_x/SAM/perovskite. The resulting decay curves for both DC and MAPI are presented in Figures 5.7a and 5.7b, respectively.

Although relative PL intensity can provide additional information about differences in radiative yield and non-radiative loss, the available TRPL datasets were not acquired as calibrated absolute PL intensity measurements. In particular, the total-count comparison is sensitive to acquisition conditions such as excitation power, detector gain, collection alignment, and background offset. For this reason, the analysis in this chapter does not use absolute PL counts as quantitative evidence for differences in bulk perovskite properties. Instead, the TRPL data are normalised and used to compare decay dynamics, while the similarity of the bulk perovskite layers is primarily assessed from the SEM and XRD measurements discussed above.

The measured photoluminescence decays were analysed using a rate-equation model incorporating monomolecular (first-order) and bimolecular (second-order) recombination terms.[43] A detailed discussion on this model is provided in Section 3.4.2. The extracted parameters from the rate equation fit to the decay curves for DC and MAPI are displayed in Table 5.3. As these fits were performed on single-fluence TRPL decays without independently calibrated carrier densities, the extracted k_1 and k_2 values should be interpreted as effective fitting parameters rather than absolute recombination rate constants. The rate-equation analysis is therefore used only to compare the relative shape of the decay dynamics across the different SAM layers.

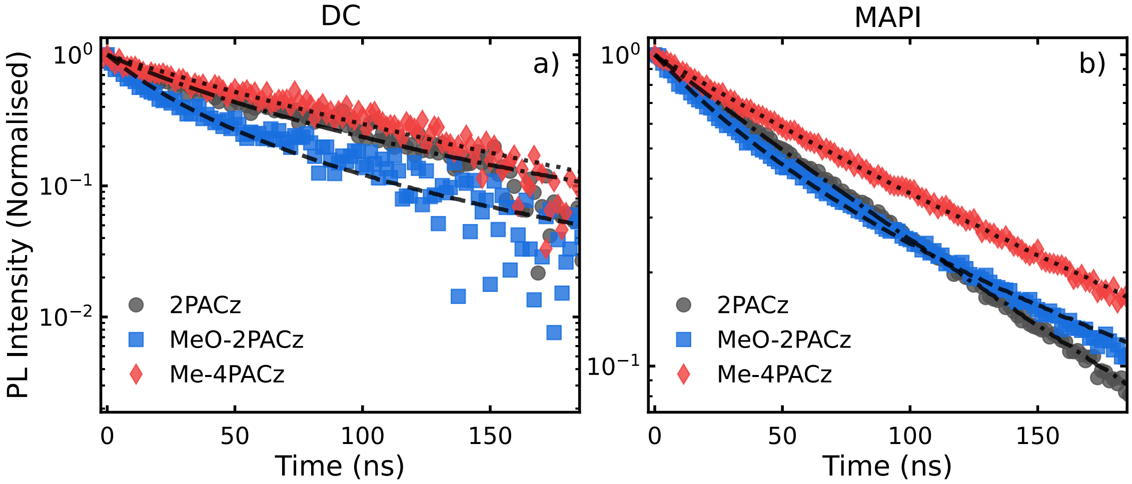

Figure 5.7: Normalised time-resolved photoluminescence (TRPL) decays measured for perovskite films deposited on partial device stacks comprising ITO/NiO$_x$/SAM/ perovskite: a) double-cation (DC) perovskite films and b) methylammonium lead iodide (MAPI) films. Measurements were performed on substrates modified with 2PACz, MeO-2PACz, and Me-4PACz SAMs. The photoluminescence intensity is normalised to its maximum value to enable direct comparison of decay dynamics across samples. Solid markers represent the measured TRPL data, while dashed lines show fits obtained using a rate-equation model incorporating monomolecular and bimolecular recombination terms. The extracted rate constants from these fits are summarised in Table 5.3. I acknowledge that this data was collected by Wai Kin Yiu at the University of Hong Kong. Figure adapted from Ref. [1] (CC BY 4.0).

For the MAPI films, the transient decay measured for the sample containing MeO-2PACz is described within this model by a larger relative contribution from the second-order term than the corresponding 2PACz and Me-4PACz decays. In contrast, the Me-4PACz and 2PACz films require a larger effective first-order contribution to reproduce the measured decay shape. This indicates that the normalised TRPL decays are sensitive to the underlying SAM layer, although the fitted parameters should not be interpreted as direct microscopic recombination constants.

A similar trend is observed for the DC perovskite films. Again, the MeO-2PACz decay is described by a stronger effective second-order contribution within the fitting model, while the 2PACz and Me-4PACz decays show a more comparable balance between the effective first- and second-order terms. The consistency of this behaviour across the two perovskite compositions suggests that the observed differences in the normalised TRPL dynamics are attributable to the underlying SAM-modified interface rather than solely to changes in the bulk absorber.

Table 5.3: Extracted TRPL rate constants for DC and MAPI perovskites using the bimolecular–trapping rate equation model, which is displayed above the table. Here, k_1 and k_2 are effective first- and second-order fitting parameters, respectively, extracted using an assumed photoexcited carrier concentration of $n = 10^{15}\,\mathrm{cm}^{-3}$, and t is time. *The k_1 value for MeO-2PACz with DC was fixed to provide a non-zero number whilst retaining a reasonable fit to the data.

$$\frac{dn}{dt} = -k_1 n(t) - k_2 n^2(t)$$

SAM	k_1 (ns^{-1})	k_1 (%)	$1/k_1$ (ns)	k_2 (cm^{3}ns^{-1})	k_2 (%)	r^2
			DC perovskite			
2PACz	4.69×10^{-3}	58.1	213.2	5.02×10^{-18}	41.9	0.948
*MeO-2PACz	5.00×10^{-4}	4.3	2000	1.84×10^{-18}	95.7	0.959
Me-4PACz	3.66×10^{-3}	50.0	273.2	5.39×10^{-18}	50.0	0.947
			MAPI perovskite			
2PACz	5.66×10^{-3}	83.2	176.7	3.24×10^{-19}	16.8	0.999
MeO-2PACz	2.87×10^{-4}	4.2	3484.3	1.93×10^{-18}	95.8	0.999
Me-4PACz	3.37×10^{-3}	67.1	296.7	4.51×10^{-19}	32.9	0.999

Although the fitted trends show clear SAM-dependent differences in the normalised TRPL decay shapes, it is essential to emphasise that the extracted coefficients are obtained from single-fluence transient decays measured under pulsed, open-circuit conditions. Without global fluence-dependent fitting and independently calibrated carrier densities, these values should not be assigned strict microscopic meaning or used to quantify absolute recombination pathway contributions. This limitation is particularly important for multilayer perovskite stacks, where transient PL measurements can probe a mixture of recombination, charge transfer, detrapping, and capacitive effects rather than isolating a unique recombination lifetime relevant to photovoltaic operation.[34]

The TRPL analysis therefore shows that the different SAM-modified interfaces produce measurably different decay dynamics, but it does not by itself determine whether these differences arise from changes in carrier overlap, charge separation, interfacial transfer, or trap-mediated recombination. The results are instead treated as comparative evidence that the buried SAM/perovskite interface influences carrier dynamics in the partial device stacks. This interpretation is consistent with previous reports that SAM layers can affect interfacial passivation and charge extraction, while also recognising that normalised TRPL decays do not necessarily correlate directly with steady-state quantities such as the quasi-Fermi level splitting, open-circuit voltage, or device efficiency.[34, 44]

To further investigate how these interface-dependent differences relate to charge separation and accumulation under illumination, Kelvin probe force microscopy (KPFM) measurements were performed. By mapping illumination-induced changes in surface potential, KPFM provides complementary, spatially resolved insight into carrier redistribution and band bending at the perovskite/SAM interface.

Kelvin probe force microscopy

To further investigate the influence of the SAM layers on charge extraction and recombination, KPFM measurements were performed. The resulting surface potential maps, recorded both in the dark and under illumination, are shown in Figure 5.8. This measurement was performed using the DC perovskite composition; further details on the measurement technique are provided in Section 3.5.3.

For perovskite films deposited on MeO-2PACz (Figure 5.8g-i), no significant change in surface potential is observed upon illumination.[45] The absence of an illumination-induced surface potential shift suggests that photogenerated charge does not lead to the formation of an internal electric field at the perovskite/SAM interface. Instead, this behaviour is consistent with rapid recombination of photogenerated charge carriers, preventing the build-up of a measurable surface potential. This could arise from greater overlap between the electron and hole populations, consistent with the pronounced bimolecular recombination contribution observed in the TRPL analysis.

In contrast, the perovskite films, including 2PACz (Figure 5.8a-c) or Me-4PACz (Figure 5.8d-f), exhibit a clear illumination-induced surface potential difference. The presence of surface photovoltage indicates that photogenerated carriers are more effectively separated, thereby enabling band bending at the perovskite/SAM interface.

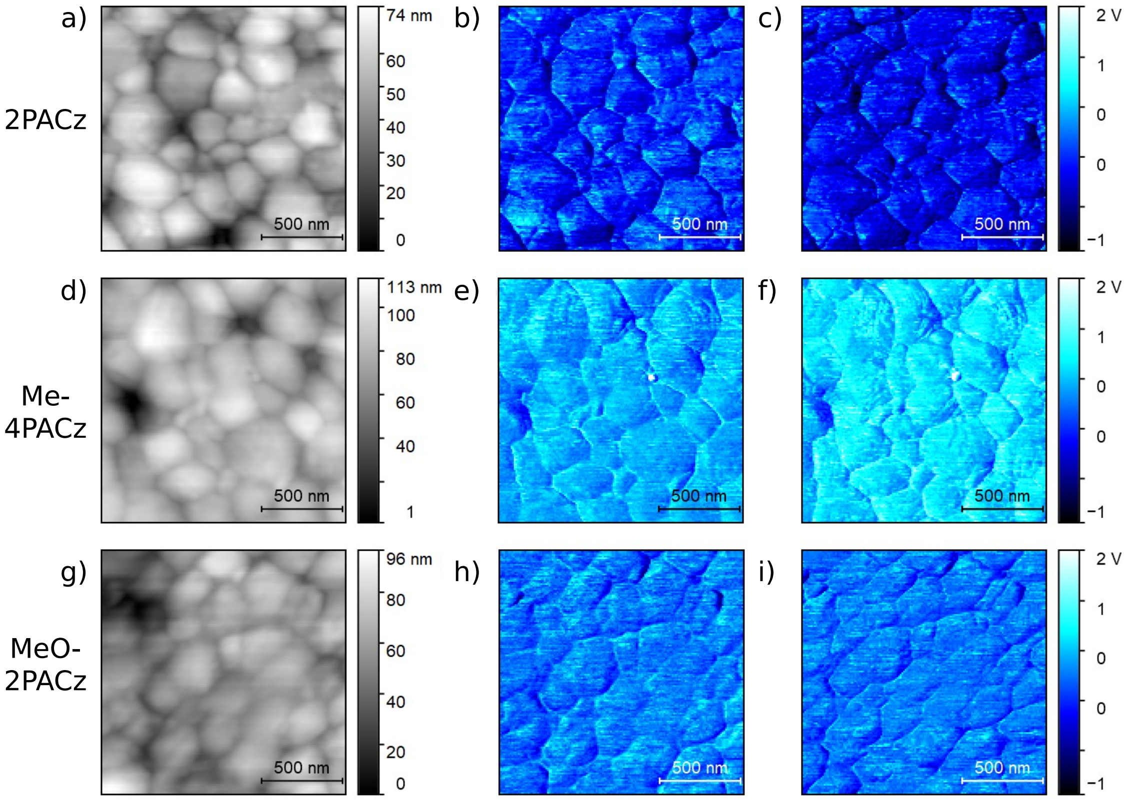

Figure 5.8: Atomic force microscopy (AFM) and Kelvin probe force microscopy (KPFM) measurements performed on double-cation (DC) perovskite films deposited on substrates comprising ITO/NiO$_x$/SAM/DC/PEAI. AFM images (left column) show the surface morphology of DC perovskite films formed on 2PACz, Me-4PACz, and MeO-2PACz. Corresponding KPFM surface potential maps acquired in the dark (middle column) and under illumination (right column) are shown for each SAM. All images were acquired over identical scan areas and are displayed using a common colour scale. Differences between the dark and illuminated surface potential maps reflect changes in local electrostatic potential induced by photo-generated charge accumulation at or near the perovskite surface. I acknowledge that this data was collected by Tik Lun Leung at The University of Sydney. Figure adapted from Ref. [1] (CC BY 4.0).

Importantly, this observation again does not imply the absence of carrier accumulation for these SAMs. Instead, it suggests that accumulated charge is spatially separated in a manner that supports an internal electric field while limiting electron-hole overlap and the associated bimolecular recombination losses. This interpretation is entirely consistent with the reduced bimolecular recombination contribution observed in the TRPL transients for both 2PACz and Me-4PACz, as well as with literature reports highlighting the role of selective interfaces in promoting carrier separation rather than simply extending PL lifetimes.

It is important to emphasise that KPFM measurements on half-cells do not capture the full complexity of device operation, particularly in inverted architectures that employ SAMs and three-dimensional perovskite absorbers. As discussed in the literature, such systems can exhibit complex energy-level alignment and interfacial behaviour that may differ from that of complete devices.[46] Nevertheless, the qualitative trends observed here provide valuable, spatially resolved insight into how different SAMs influence charge separation and accumulation under illumination, complementing the transient recombination dynamics obtained from the TRPL measurements.

Taken together, the KPFM and TRPL results support a consistent picture in which MeO-2PACz is associated with limited charge separation and enhanced carrier recombination. At the same time, 2PACz and Me-4PACz promote spatial separation of photogenerated charge carriers, enabling band bending at the interface and suppressing bimolecular recombination without eliminating carrier accumulation.

5.2.3 Probing SAM-Induced Energetic Differences Using the Stabilise and Pulse Technique

The Stabilise and Pulse (SaP) technique is used here to directly probe how different self-assembled molecular layers modify the internal energetics of operating perovskite solar cells.[5, 24] Conventional photovoltaic measurements, time-resolved photoluminescence, and Kelvin probe microscopy provide strong evidence that the choice of SAM influences charge extraction and recombination. However, these techniques do not directly quantify how these differences arise from changes in the device's internal electrostatics. This limitation arises because they probe either steady-state electrical behaviour or partial device stacks and therefore do not fully capture the influence of mobile ionic charge. The SaP technique is highly sensitive to small energetic differences and is therefore well suited to probing how ionic charge accumulation modifies interfacial energetics.[24]

The SaP measurement exploits ionic migration within the perovskite layer to extract energetic offsets at device interfaces. For each SAM, measurements are performed on both perovskite compositions investigated in this chapter, MAPI and DC. Devices are first held at a defined stabilisation bias, V_{bias}, allowing the ionic distribution to reach quasi-steady-state before short voltage pulses are applied. During these pulses, the ionic configuration remains effectively fixed, meaning the resulting J–V curve reflects the electronic response of the device under that specific ionic configuration. Full SaP J–V curves for each SAM on DC and MAPI are shown in Figures 5.9a and 5.9b. Complete measurement details are provided in Section 3.2.2.

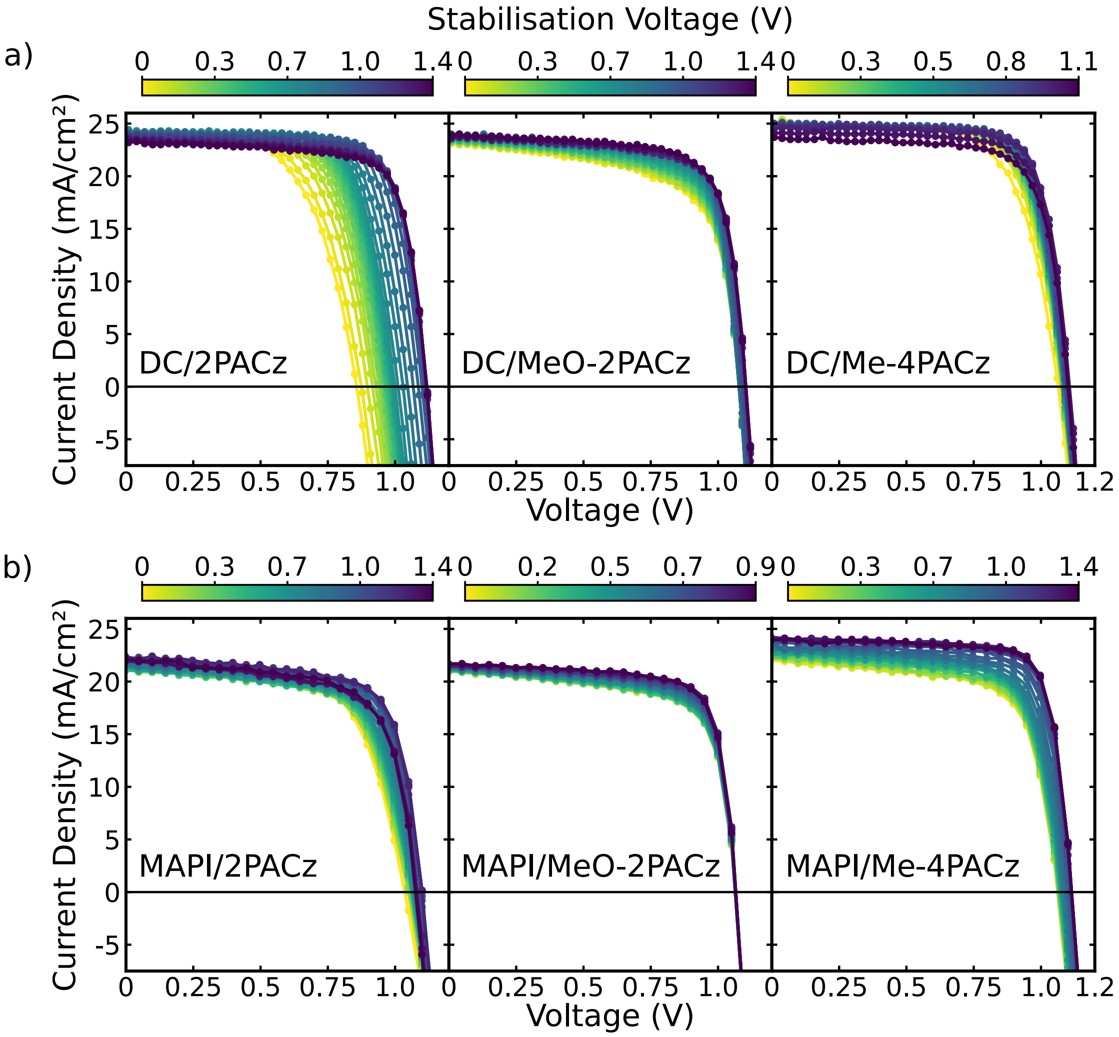

Figure 5.9: Stabilise and Pulse (SaP) current density–voltage (J–V) curves measured for perovskite solar cells incorporating carbazole-based SAMs: a) double-cation (DC) devices and b) methylammonium lead iodide (MAPI) devices. For each SAM (2PACz, MeO-2PACz, and Me-4PACz), devices were held at a series of stabilisation biases before the application of rapid voltage pulses. The resulting J–V curves reflect device operation under distinct ionic distributions. The colour scale indicates the applied stabilisation bias. Systematic changes in the J–V characteristics with stabilisation bias demonstrate the influence of mobile ionic charge on charge extraction and recombination, even in devices exhibiting minimal hysteresis under standard J–V sweep measurements. Figure adapted from Ref. [1] (CC BY 4.0).

The resulting SaP J–V demonstrate that even in high efficiency (>22%) optimised perovskite compositions such as DC, there is still a degree of ionic motion that impacts the J–V curves. This is similar to the result shown in Section 4.3.4, where a high-efficiency perovskite solar cell with minimal hysteresis under a standard J–V sweep measurement shows a clear impact of mobile ionic charge on recombination and extraction. This result again shows that simply eliminating hysteresis from J–V sweep measurements via passivation or careful tuning of scan rate does not suppress ionic motion. Nevertheless, it is important to ensure the reliability of these measurements by carefully verifying the data obtained. To provide reassuring evidence that mobile ions were not redistributing during the pulsing regime, a forward and reverse scan was taken. The resulting SaP measurement, with a clearer distinction between forward and reverse scans, is shown in Figure 5.10a-b for devices containing Me-4PACz. Full forward and reverse J–V scans for devices incorporating MeO-2PACz and 2PACz SAM layers are provided in Figure 5.A1.

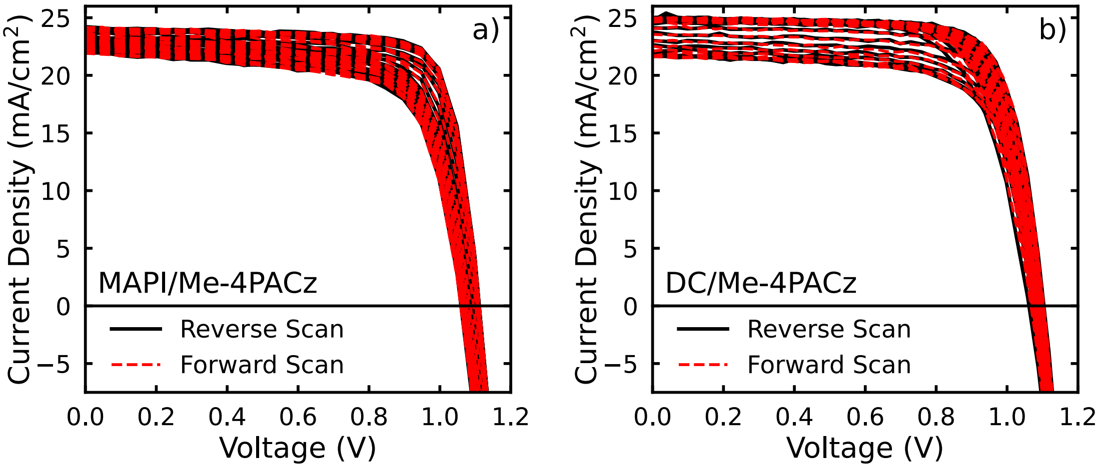

Figure 5.10: Comparison of forward and reverse Stabilise and Pulse (SaP) current density–voltage (J–V) measurements for devices incorporating Me-4PACz: a) methylammonium lead iodide (MAPI) devices and b) double-cation (DC) devices. Forward scans are shown as dashed red lines, while reverse scans are shown as solid black lines. For each device, SaP measurements were performed across a range of stabilisation biases. The close overlap between forward and reverse scans at all stabilisation voltages indicates that ionic redistribution is suppressed during the pulsing regime, confirming that the measured J–V curves correspond to fixed ionic configurations rather than scan-direction-dependent artefacts. Figure adapted from Ref. [1] (CC BY 4.0).

From Figure 5.10 it is clear that there is no hysteresis in the measurement across the range of applied biases, indicating that ionic motion is hindered during the pulsing. The lack of hysteresis here is distinctly different from a traditional J–V sweep hysteresis, as there are clear differences in the J–V curves for each applied bias. To further confirm the reliability of the results, and before extracting information on the built-in potential, we can observe the response during the stabilisation period preceding pulsing. The stabilised current obtained for MAPI and DC devices containing Me-4PACz is shown in Figures 5.11a-b for MAPI and 5.11c-d for DC. The full stabilisation data for devices utilising MeO-2PACz and 2PACz are provided in Figure 5.A2 and Figure 5.A3 for MAPI and DC, respectively.

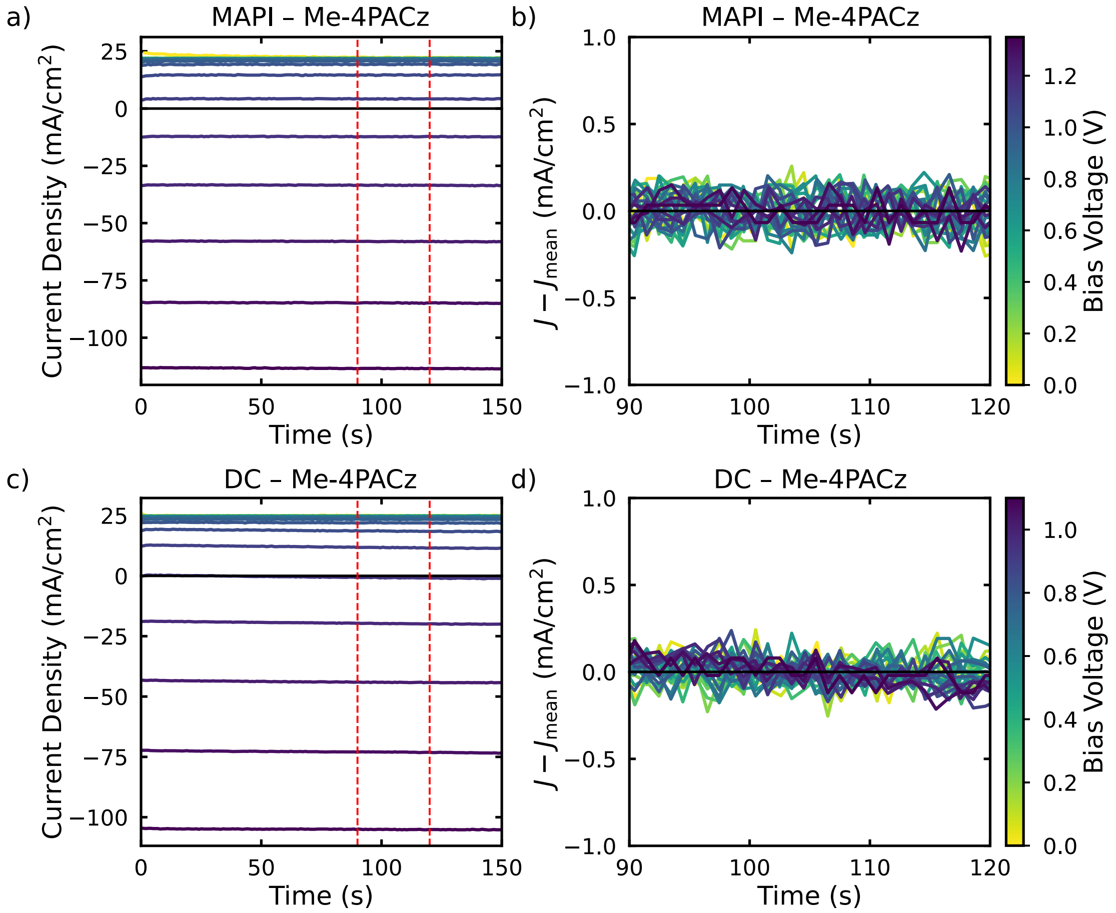

Figure 5.11: Current density measured during the stabilisation period of the Stabilise and Pulse (SaP) measurements for devices incorporating Me-4PACz: a,b) methylammonium lead iodide (MAPI) devices and (c,d) double-cation (DC) devices. Panels a) and c) show the stabilised current density as a function of time for a range of applied stabilisation biases. Panels b) and d) show the corresponding current density during the final 30 s of the stabilisation period, plotted relative to the mean current density over this same 30 s interval. The red dashed lines in a) and c) indicate the 30 s window used for this analysis. The absence of systematic deviation from zero in b) and d) demonstrates that no measurable current drift occurs immediately before pulsing, confirming that devices reach a quasi-steady-state ionic configuration during the measurement. Figure adapted from Ref. [1] (CC BY 4.0).

From Figures 5.11a-d, it is clear that there is no significant change in the stabilised current obtained before the pulsing stage. This result confirms that the devices reached a quasi-steady-state under the applied bias. Interestingly, all devices using either MAPI or DC perovskites are shown to be particularly stable across a range of applied biases. This increased stability, even when using MAPI, demonstrates the high quality of the devices in this study, as it has been shown previously that a close link exists between high efficiency and device stability.

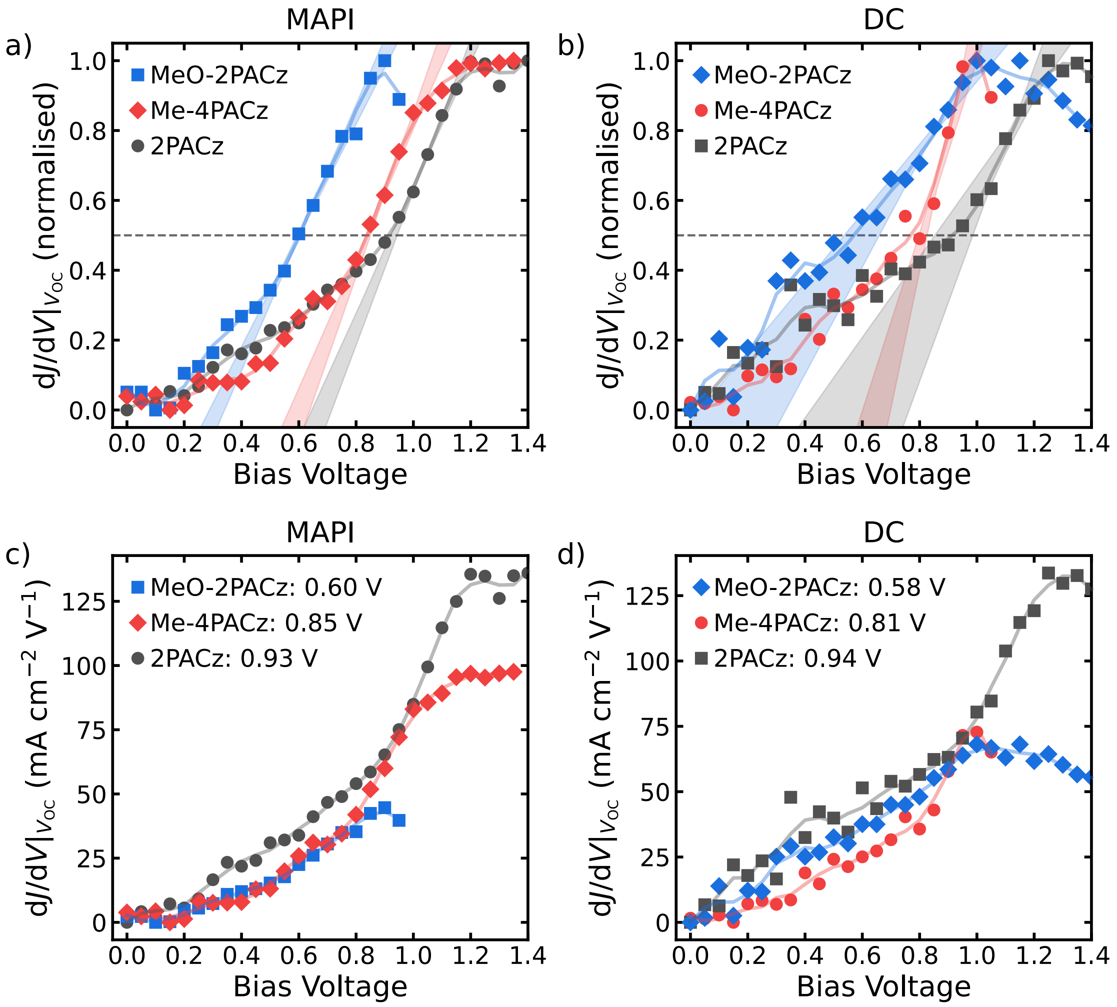

Figure 5.12: Gradient analysis of the SaP current density–voltage curves evaluated at the open-circuit voltage, $\mathrm{d}J/\mathrm{d}V|_{V=V_{\mathrm{OC}}}$, used to extract the flat-band (voltage) potential, V_{flat}, for devices incorporating different carbazole-based SAMs: a,c) methylammonium lead iodide (MAPI) devices and (b,d) double-cation (DC) devices. Panels a) and b) show the normalised $\mathrm{d}J/\mathrm{d}V|_{V=V_{\mathrm{OC}}}$ response as a function of applied stabilisation bias, enabling direct comparison of the bias dependence across SAMs. Panels c) and d) show the same data plotted after offset normalisation, where the minimum value is subtracted ($\mathrm{d}J/\mathrm{d}V|_{V=V_{\mathrm{OC}}}-\mathrm{min}$), to highlight differences in the absolute magnitude of the response. Discrete symbols represent experimental data, while lighter shaded curves show Savitzky–Golay smoothed traces included as a guide to the eye. The horizontal grey dashed line indicates the mid-point used in combination with linear fits (shaded regions) to determine the flat-band potential, V_{flat}. The extracted V_{flat} values are indicated in the legends. Figure adapted from Ref. [1] (CC BY 4.0).

With the device stability confirmed, the flat-band potential (V_{flat}) was extracted for each device following the procedure established in Chapter 3. The resulting gradient analysis around the open-circuit voltage is shown in Figure 5.12 for all SAMs and both perovskite compositions. An excellent agreement is observed between the two perovskite compositions for each SAM layer used, with the V_{flat} values obtained for 2PACz being 0.93 V with MAPI and 0.94 V with DC. Similarly, the V_{flat} value for MeO-2PACz was 0.60 V with MAPI and 0.58 V with DC, and Me-4PACz was 0.85 V with MAPI and 0.81 V with DC. This remarkable consistency across the two perovskite compositions is to be expected, as this measurement is a direct probe of the difference in Fermi levels between the charge extraction layer adjacent to the perovskite.[1] Since the same device structure was used in both cases, except for the perovskite used, a close agreement can be expected. Additionally, this is supported by the close value in band gap obtained for both MAPI and the DC perovskites as shown by the Tauc analysis in Figure 5.13a-b for MAPI and DC, respectively (the UV–Vis data is shown in Figure 5.A4). This close agreement in band gap indicates this will not be a limiting factor impacting the results of the SaP measurement and V_{flat} analysis.

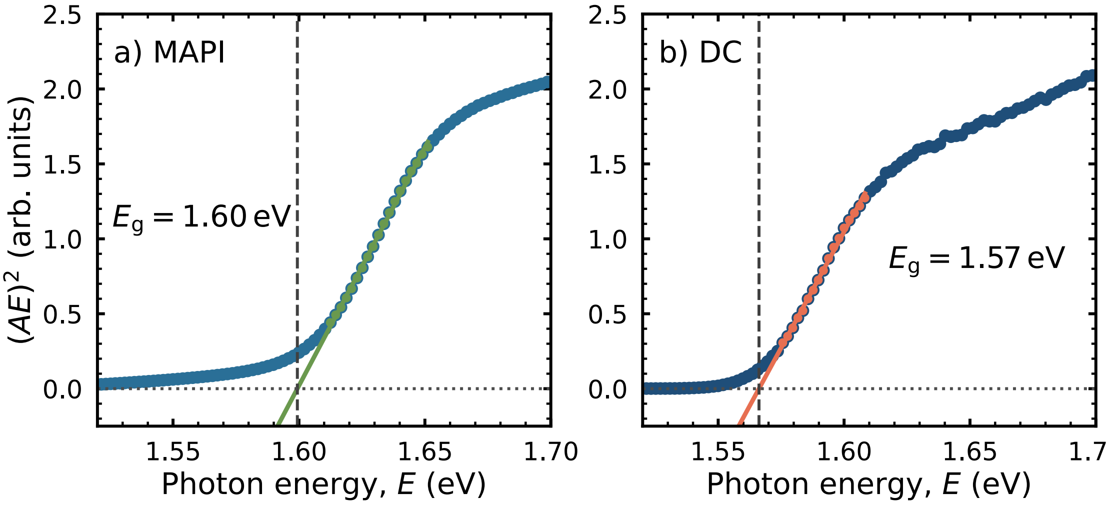

Figure 5.13: Direct Tauc plots, $(AE)^2$ versus photon energy E, for a) MAPI and b) DC perovskite films. In this context, A represents the measured absorbance, which serves as a proxy for the absorption coefficient. The band gap energy E_g is extracted from the x-intercept of a linear fit to the steepest region of the absorption edge (highlighted points). The dashed vertical line indicates the extracted E_g, while the dotted horizontal line marks $(AE)^2 = 0$. The use of absorbance rescales the Tauc plot by a constant factor but does not affect the extracted band gap. Figure adapted from Ref. [1] (CC BY 4.0).

By taking a closer look at the gradient analysis and V_{flat} extraction, a clear ordering of magnitude appears. When plotted with a common scale and all curves starting at y=0, we observe how the different SAMs respond during the SaP measurement. The $\mathrm{d}J/\mathrm{d}V$ analysis provides insights into the effects of ion accumulation at interfaces on charge extraction and recombination. The slope of the $\mathrm{d}J/\mathrm{d}V$ curve therefore

---

[1] We also note here that the same result was recorded for the p–i–n device used in Section 4.3.4, which utilised 2PACz and PCBM and a V_{flat} of 0.94 V was obtained.

represents the interplay between ion-modulated interfacial charge recombination and bulk losses. As bulk recombination increases, the interface becomes less dominant, resulting in a smaller slope magnitude. For both perovskite compositions, 2PACz clearly exhibits the steepest response, followed by Me-4PACz and finally MeO-2PACz, which displays the shallowest gradient. The larger gradient observed for 2PACz indicates a stronger sensitivity to interfacial recombination. In contrast, the more gradual response observed for MeO-2PACz suggests reduced sensitivity to interfacial recombination, leading to a larger relative contribution from bulk recombination pathways. This finding aligns with the analysis of the TRPL and KPFM data, which suggested increased overlap between photogenerated electrons and holes for MeO-2PACz and reduced monomolecular contributions.

5.2.4 SAM Dipole Strength and the Flat-Band Potential

The extracted V_{flat} values exhibit a systematic dependence on the self-assembled molecular layer, indicating that the flat-band potential is primarily governed by the energetic alignment imposed by the transport layers adjacent to the perovskite. This behaviour is analogous to the built-in potential in conventional semiconductor devices. To interpret these results, the measured V_{flat} values are compared with literature reports of SAM dipole strengths and experimentally determined Fermi levels.

Carbazole-based phosphonic acid SAMs are known to induce work-function shifts when bound to ITO substrates. The SAMs used in this study exhibit a clear trend in dipole strength, with 2PACz > Me-4PACz > MeO-2PACz. Correspondingly, the measured potential drop across the perovskite layer increases with the dipole strength of the underlying SAM. A summary of this relationship is presented in Table 5.4.

This trend is further supported by measurements on a chlorine-substituted carbazole SAM, Cl-2PACz, which has a dipole moment of approximately 4.6 D.[47, 48] Devices incorporating Cl-2PACz exhibit V_{flat} values exceeding 1.15 V for both MAPI and DC compositions. The full SaP and $\mathrm{d}J/\mathrm{d}V$ analysis for these devices is shown in Figure 5.A5. Although the extracted V_{flat} values of 1.30 V for DC and 1.15 V for MAPI lie slightly outside the expected uncertainty range, the key result is the consistent correlation between SAM dipole strength and the V_{flat} values obtained from the SaP analysis.

Overall, these results indicate that the built-in potential of these devices is determined entirely by the Fermi levels of the charge-extraction layers, rather than by the difference in the electrodes' work functions, which is reported to be approximately 0.2 eV in this system. To further investigate this hypothesis, we compare the extracted V_{flat} values with expected energetic offsets of the transport layers. We

Table 5.4: Summary of reported dipole moments for carbazole-based self-assembled molecules (SAMs) and the corresponding flat-band potentials, V_{flat}, extracted from Stabilise and Pulse measurements for double-cation (DC) and methylammonium lead iodide (MAPI) perovskite devices. Dipole moment values are taken from literature reports, while V_{flat} values are obtained from the $\mathrm{d}J/\mathrm{d}V$ gradient analysis. The quoted uncertainties in V_{flat} reflect the error corresponding to the uncertainty in the intercept extraction as described in Section 3.2.2.

SAM	Dipole Moment (D)	DC V_{flat} (V)	MAPI V_{flat} (V)	Ref.
Cl-2PACz	~ 4.6	1.33 ± 0.01	1.15 ± 0.01	[47, 48]
2PACz	~ 2	0.94 ± 0.03	0.93 ± 0.01	[32]
Me-4PACz	~ 1.5	0.81 ± 0.01	0.85 ± 0.01	[33]
MeO-2PACz	~ 0.2	0.58 ± 0.07	0.60 ± 0.01	[32]

reference values obtained by Siekmann et al., who conducted a thorough XPS/UPS analysis of the same SAM layers used in this Chapter.[34] Siekmann et al. identified that 2PACz induced the deepest Fermi level shift at ~ -5.2 eV, followed by Me-4PACz at ~ -5.0 eV and finally MeO-2PACz at ~ -4.8 eV. This trend again correlates with the strength of the SAM layers' dipole moment: a stronger dipole shifts the Fermi level to deeper energy values.[34]

In the devices in this Chapter, we utilised PCBM as the electron-transporting layer, which is *a priori* expected to be an intrinsic layer, as no chemical dopants are added during fabrication. However, it has been reported that exposure to air can induce n-doping in PCBM.[49, 50] Our fabrication protocol includes transferring samples from the glovebox to an evaporator and subsequently exposing them to air. We have verified that this exposure leads to a substantial increase in the conductivity of PCBM measured across a patterned ITO substrate, from $6.75 \times 10^{-8}\,\mathrm{S\,cm^{-1}}$ to $1.97 \times 10^{-6}\,\mathrm{S\,cm^{-1}}$, as shown in Figure 5.14.

Therefore, this measurement confirms that PCBM undergoes unintentional n-type doping upon exposure to oxygen, leading to a measurable increase in the conductivity and a corresponding shift in the effective Fermi level. Using the literature-reported value of doped PCBM of approximately -4.2 eV, we obtain a conservative yet reasonable estimate of the difference in Fermi levels between the charge-extraction layers.[49, 51] Using the values reported for the SAM layers and those for PCBM, we find Fermi-level differences of 1 eV for 2PACz, 0.80 eV for Me-4PACz, and 0.60 eV for MeO-2PACz. These values are in excellent agreement with our extracted V_{flat} values of 0.94, 0.81, and 0.58 V obtained for 2PACz, Me-4PACz, and MeO-2PACz, respectively, for DC and very similar results for MAPI. This remarkable agreement between measurements highlights the robustness of the Stabilise and Pulse technique.

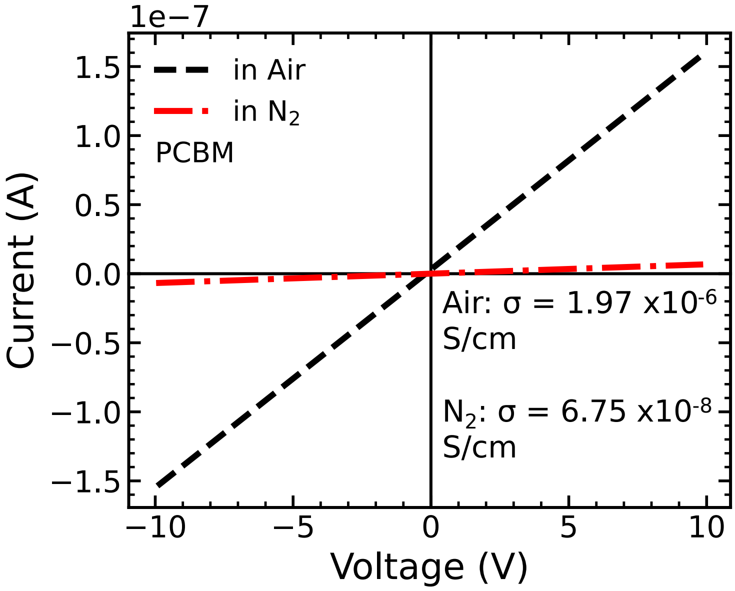

Figure 5.14: Conductivity measurement of pristine PCBM films deposited on patterned ITO substrates, acquired under ambient air and nitrogen (N_2) atmospheres. Linear fits to the I–V data are used to extract the electrical conductivity, σ, of the PCBM films under each condition. Exposure to air results in a substantial increase in conductivity compared to measurements performed under N_2, indicating unintentional n-type doping of PCBM upon oxygen exposure. The extracted conductivity values are annotated on the plot. I acknowledge that this data was collected by Wai Kin Yiu at the University of Glasgow. Figure adapted from Ref. [1] (CC BY 4.0).

Taken together, we demonstrate that the SaP measurement can accurately determine interfacial energetic modifications, even in highly efficient perovskite solar cells. These results also confirm that the extracted V_{flat} value reflects the difference in Fermi levels imposed on the perovskite layer by the adjacent transport layers.

With these results in hand, we can now correlate the effect of the anchored SAM's Fermi level on the metal oxide with device performance. To support this, we use cartoon energy-level diagrams based on Fermi-level values from Siekmann et al. for the perovskite and SAM layers.[34] The corresponding energy level diagrams for the SAM layers are presented in Figure 5.15.

From the device parameters, it was found that incorporating MeO-2PACz results in a clear loss of V_{OC} and J_{SC} relative to 2PACz and Me-4PACz. Notably, the loss in J_{SC} is unintuitive based on the energetic picture shown in Figure 5.15. Conventional wisdom would anticipate that this device configuration would lead to the highest J_{SC} due to the offset at the SAM/perovskite interface, which, in principle, should provide a driving force for charge extraction.[52] However, this result can be understood in terms of the built-in potential. Previous work has shown that in high-injection-limited cases, where interfacial recombination is not the limiting factor, reducing the

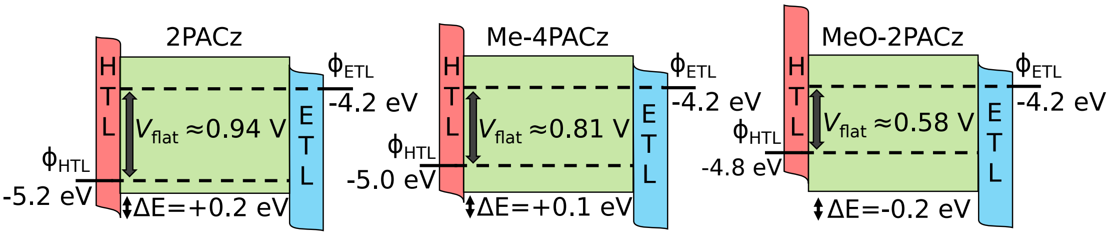

Figure 5.15: Schematic energy-level diagrams illustrating the interfacial energetics of p–i–n perovskite solar cells incorporating different carbazole-based SAMs. The hole-transport layer (HTL) represents the NiO_x/SAM interface, while the electron-transport layer (ETL) represents n-doped PCBM. The perovskite valence-band edge is reported to be approximately −5.4 eV in the literature. The electrostatic potential drop across the perovskite layer extracted from Stabilise and Pulse measurements is labelled as V_{flat}. The energetic offset between the perovskite valence band and the valence band of the HTL is denoted ΔE and is estimated from literature-reported energetic alignments for the corresponding SAMs. These diagrams are intended as conceptual representations to contextualise the experimentally extracted V_{flat} values and device performance trends, rather than as absolute band alignments. Figure adapted from Ref. [1] (CC BY 4.0).

built-in potential leads to a loss in both V_{OC} and J_{SC}.[5] This loss arises from ionic field screening, which increases overlap between the electron and hole populations, thereby triggering higher bulk recombination rates. Considering that MeO-2PACz resulted in the lowest V_{flat}, this aligns with the TRPL data, which indicated a very small monomolecular contribution, and with the KPFM results, which showed no surface potential difference before and after illumination, indicating weak charge separation and minimal carrier accumulation at the interface.

In contrast, the device containing 2PACz showed the largest V_{flat} value, approaching 1 V due to the larger dipole moment. This resulted in devices showing an increase in V_{OC} but a decrease in J_{SC} compared to the MeO-2PACz devices, a trend frequently observed in the literature.[32] Based on the proposed energy level diagrams in Figure 5.15, we can assign the loss in current to the formation of a small energetic barrier at the interface. Due to the increased strength of the dipole, the valence band (VB) of the SAM-modified NiO_x interface is expected to be deeper than the VB of the perovskite. This would, in principle, lead to increased hole accumulation at the 2PACz/perovskite interface and thus increased monomolecular recombination.

Finally, Me-4PACz-based devices exhibit the highest average current and voltage among the device series. We can now understand that this improvement is a result of better alignment of the VB of the SAM-modified NiO_x interface with the VB of the perovskite. The marginal energetic offset reduces the accumulation at the interface relative to 2PACz and, therefore, the monomolecular recombination rate, in agreement with the TRPL results. However, the large built-in potential of ~ 0.85 allows the device to sustain high voltages. Additionally, the KPFM results showed a charge buildup at the exposed perovskite surface after illumination, consistent with a small potential barrier to charge extraction at the interface.

Interestingly, the device results in this Chapter show that the presence of an energetic barrier to charge extraction does not hinder performance. Similar observations were made by Xu et al., who utilised an electron transport layer that formed an energetic barrier to charge extraction, yet achieved highly efficient perovskite solar cells.[53] In fact, a small, energetic offset at the interface may be beneficial for boosting the open-circuit voltage, as observed by Chen et al. for devices incorporating a series of layered perovskites as interface modifiers.[54] This is again consistent with the increased V_{OC} observed for devices incorporating 2PACz and Me-4PACz in this Chapter.

5.2.5 Diagnosing Interfacial Recombination from QSS and Flat-Band Conditions

Comparing device performance at quasi-steady-state (QSS) conditions with that obtained at the flat-band potential provides a direct diagnostic of how mobile ions influence recombination and device operation.[5] When mobile ions accumulate at the interfaces, they modify the interfacial electrostatics and can suppress surface recombination. The difference in performance between QSS and flat-band conditions therefore provides a diagnostic of whether device performance is limited by interfacial recombination.

The magnitude of the open-circuit voltage enhancement produced by mobile ions depends on several factors, including the mobile ion density, the surface recombination velocity, and the energetic offsets at the transport layers. By comparing the J–V characteristics obtained with ions in their quasi-steady-state configuration to those obtained at the flat-band potential, the influence of mobile ions on device performance can therefore be evaluated.

Using this approach, the device performance for all SAMs was extracted under both QSS and flat-band conditions. A summary of the resulting device parameters for both perovskite compositions is presented in Table 5.5. The corresponding comparisons between QSS and V_{flat} J–V curves for devices employing DC and MAPI absorbers are shown in Figures 5.A6 and 5.A7, respectively.

Across all SAMs, clear differences are observed between the QSS and V_{flat} operation, with the magnitude and direction of the changes dependent on the interfacial energetics imposed by the SAM. Devices employing 2PACz and Me-4PACz showed a clear increase in the open-circuit voltage across both perovskite compositions, with

Table 5.5: Summary of photovoltaic performance parameters extracted from Stabilise and Pulse measurements for double-cation (DC) and methylammonium lead iodide (MAPI) perovskite solar cells incorporating different carbazole-based SAMs. Device performance is reported under quasi-steady-state (QSS) conditions and under flat-band conditions (V_{flat}). The parameters, fill factor (FF), open-circuit voltage (V_{OC}), short-circuit current density (J_{SC}), and power conversion efficiency (PCE) are extracted from the corresponding flat-band SaP J–V curve and reconstructed QSS J–V. Comparing QSS and V_{flat} operation enables the impact of mobile ionic charge on device performance to be assessed as a function of interfacial energetics.

SAM	Condition	FF	V_{OC} (V)	J_{SC} (mA cm^{-2})	PCE (%)
			DC perovskite		
Me-4PACz	QSS	0.77	1.10	24.9	21.07
	V_{flat}	0.76	1.09	25.0	20.81
2PACz	QSS	0.72	1.12	24.3	19.43
	V_{flat}	0.76	1.09	24.2	19.99
MeO-2PACz	QSS	0.75	1.09	23.1	19.10
	V_{flat}	0.70	1.08	23.5	18.00
Cl-2PACz	QSS	0.64	1.08	22.1	15.43
	V_{flat}	0.60	1.09	20.2	13.11
			MAPI perovskite		
Me-4PACz	QSS	0.80	1.11	22.2	19.73
	V_{flat}	0.74	1.09	23.2	18.58
2PACz	QSS	0.70	1.10	21.7	16.67
	V_{flat}	0.72	1.09	21.8	17.08
MeO-2PACz	QSS	0.80	1.04	21.3	17.55
	V_{flat}	0.72	1.07	21.4	16.50
Cl-2PACz	QSS	0.62	1.09	17.8	12.03
	V_{flat}	0.71	1.10	21.3	16.73

ions contributing to performance. However, 2PACz devices, despite the gain in V_{OC} still exhibited a loss in power conversion efficiency relative to the flat-band condition. In contrast, devices utilising MeO-2PACz showed little enhancement in V_{OC} under QSS conditions, and the MAPI device showed a loss of V_{OC} relative to the flat-band potential response. Similarly, the devices employing the large dipole Cl-2PACz SAM showed a loss in V_{OC} for both perovskite compositions.

These results can all be explained when considering the results from Chapter 4. It was shown that if the flat-band potential lies above the open-circuit voltage, the presence of mobile ions reduces the open-circuit voltage, as there is no inversion of the ionic population before reaching open-circuit conditions.[5] Therefore, mobile ions do not repel minority charge carriers, thereby reducing surface recombination. This is observed in the Cl-2PACz device, where the flat-band potential exceeds the achieved open-circuit voltage for both perovskite compositions.

The loss in power conversion efficiency when utilising 2PACz is unsurprising. Despite the modest gain in open-circuit voltage under quasi-steady-state conditions, the surface recombination velocity when this SAM is used is too high to offset the gains provided by mobile ions. This result is in agreement with the TRPL and KPFM analysis, as well as the magnitude of the $\mathrm{d}J/\mathrm{d}V$ analysis, which all indicate that 2PACz results in a large accumulation of charge and therefore a large ratio of surface recombination. Finally, the Me-4PACz-containing devices illustrate an optimal balance between the extremes discussed. The modest gains in open-circuit voltage due to mobile ionic charge, accompanied by a slight increase in accumulation arising from a small energetic barrier, are sufficient to outperform the device under flat-band conditions. The loss in open-circuit voltage observed when employing the MeO-2PACz SAM indicates that this device is in a bulk recombination-dominated regime. This is consistent with the absence of significant interfacial band bending and carrier accumulation at device interfaces as inferred from the TRPL and KPFM results. The loss of V_{OC} with mobile ions present suggests that this device is limited by Shockley-Read-Hall recombination, again consistent with the interpretation that bulk recombination dominates with this SAM present.[5]

An additional point is that the observable impact of mobile ions on device performance is greater in MAPI-based perovskite devices. As discussed, this perovskite composition is expected to have a higher density of mobile ionic charge than more optimised perovskite compositions, such as the DC perovskite used.[55–58] This is evident in the case of MeO-2PACz, where a large loss in V_{OC} is observed and again in the Cl-2PACz device, where a large loss in performance is observed with mobile ions included.

By comparing the QSS and V_{flat} J–V characteristics, this study demonstrates that this method can complement traditional measurement techniques, such as TRPL and KPFM, in identifying dominant recombination regimes. In devices with a higher degree of surface recombination, mobile ions can increase the open-circuit voltage; however, they cannot sufficiently suppress the losses to compensate and increase the power conversion efficiency. In devices limited by bulk recombination, mobile ions reduce the open-circuit voltage; when the flat-band potential exceeds the open-circuit voltage, they further degrade it and potentially the power conversion efficiency.

5.3 Conclusions

In this chapter, the role of transport-layer energetics in governing the performance of high-efficiency p–i–n perovskite solar cells has been systematically investigated using a combination of electrical, optical, and electrostatic characterisation techniques. By employing a series of carbazole-based self-assembled molecular layers, it has been possible to directly tune the energetic alignment at the perovskite/transport-layer interface. A central result of this chapter is the direct experimental determination of the flat-band potential, V_{flat}, using the Stabilise and Pulse technique. Across two distinct perovskite compositions, MAPI and a mixed double cation perovskite, the V_{flat} was found to vary systematically with the dipole strength of the underlying SAM. Approximate values of 0.60 V for MeO-2PACz, 0.85 V for Me-4PACz, and 0.93 V for 2PACz indicate that the built-in potential in these devices is entirely driven by the Fermi levels of the adjacent transport layers rather than by the electrode work functions.

Device performance analysis reveals a clear dependence on V_{flat} with devices incorporating MeO-2PACz exhibiting the lowest V_{flat} and consistently suffering losses in both J_{SC} and V_{OC}, indicating an insufficient driving force for charge separation and extraction. Increasing the V_{flat} to an intermediate value using Me-4PACz results in simultaneous improvements in current density, open-circuit voltage, and power conversion efficiency, yielding, on average, the highest-performing devices across both perovskite compositions. However, further increases in V_{flat}, achieved using high-dipole SAMs such as 2PACz or Cl-2PACz, do not lead to continued performance gains and instead introduce significant losses.

The loss in performance when utilising 2PACz or Cl-2PACz is attributed to the formation of an interfacial energetic barrier arising from an excessive shift of the Fermi level due to the large dipole moment of the SAM. Kelvin probe force microscopy measurements reveal a significant difference in surface potential between dark and illuminated conditions for 2PACz, consistent with increased charge accumulation. Time-resolved photoluminescence measurements further indicate altered recombination dynamics that are consistent with impeded charge extraction and increased carrier accumulation. Together, these results demonstrate that while a large built-in potential enhances photovoltage, excessively strong interfacial dipoles can introduce significant energetic barriers that limit charge collection, thereby offsetting the gains.

By comparing the performance of the SAMs at quasi-steady-state and under flat-band conditions, this interpretation is further reinforced. Devices that exhibited gains in open-circuit voltage under quasi-steady-state conditions were 2PACz and Me-4PACz, which, from TRPL and KPFM results, showed increased sensitivity to surface recombination and charge accumulation. Conversely, when V_{flat} is too small, and the device is limited by bulk recombination processes, the presence of mobile ions hinders the open-circuit voltage. This framework aligns with the established results in Chapter 4. Optimal performance is therefore achieved in an intermediate regime where the built-in potential is large enough to support high photovoltages and charge separation, but not so large as to introduce a significant energetic barrier to charge extraction.

The results presented in this chapter provide a physical interpretation of why different SAMs yield optimal device performance, depending on the device architecture. For wide-band-gap or bromide-rich absorbers, larger dipole moments and therefore higher V_{flat} values may be advantageous. In contrast, for lower-band-gap perovskites, excessive dipoles are more likely to induce significant energetic barriers to charge extraction. This underscores the need not to rely on a single, universally optimal SAM, but to tailor it to the energetics of a specific perovskite composition.

Overall, this chapter demonstrates that the performance of p–i–n perovskite solar cells is governed by a delicate mix of interfacial dipoles, built-in potentials, and recombination dynamics. The SaP method and V_{flat} extraction is established as a framework for understanding how transport-layer design influences charge extraction, recombination, and ultimately device performance in perovskite solar cells.

5.A Appendix

5.A.1 Additional Figures

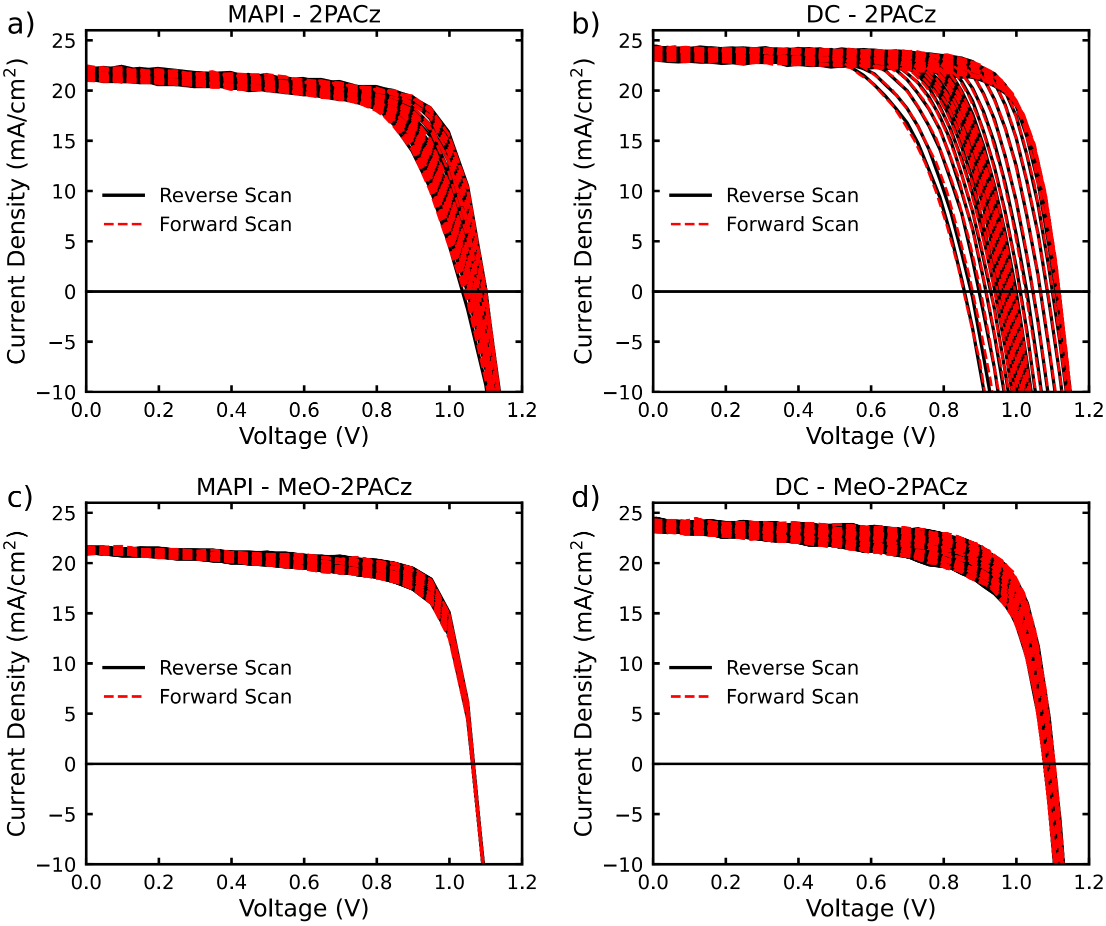

Figure 5.A1: Comparison of forward and reverse Stabilise and Pulse current density–voltage (J–V) measurements for devices incorporating 2PACz and MeO-2PACz: (a) MAPI–2PACz, (b) DC–2PACz, (c) MAPI–MeO-2PACz, and (d) DC–MeO-2PACz. Forward scans are shown as dashed red lines, while reverse scans are shown as solid black lines. For each device, Stabilise and Pulse measurements were performed across a range of stabilisation biases. The strong overlap between forward and reverse scans at all stabilisation voltages indicates that ionic redistribution is suppressed during the pulsing regime.

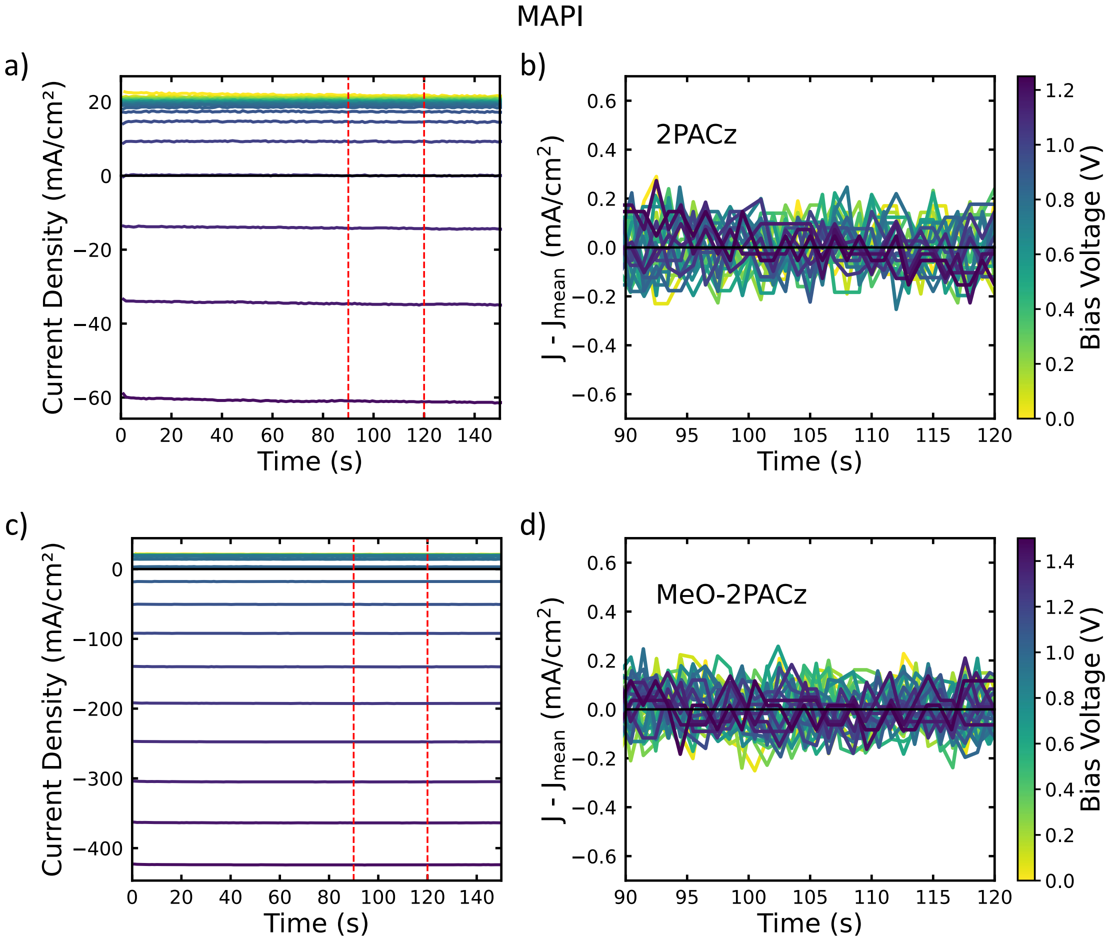

Figure 5.A2: Current density measured during the stabilisation period of the Stabilise and Pulse (SaP) measurements for MAPI devices incorporating 2PACz (a,b) and MeO-2PACz (c,d). Panels a) and c) show the stabilised current density as a function of time for a range of applied stabilisation biases. Panels b) and d) show the corresponding current density during the final 30 s of the stabilisation period, plotted relative to the mean current density over this same 30 s interval. The red dashed lines in a) and c) indicate the 30 s window used for this analysis. The absence of systematic deviation from zero in b) and d) demonstrates that no measurable current drift occurs immediately before the voltage pulse, confirming that devices reach a quasi-steady-state ionic configuration before the pulse is applied.

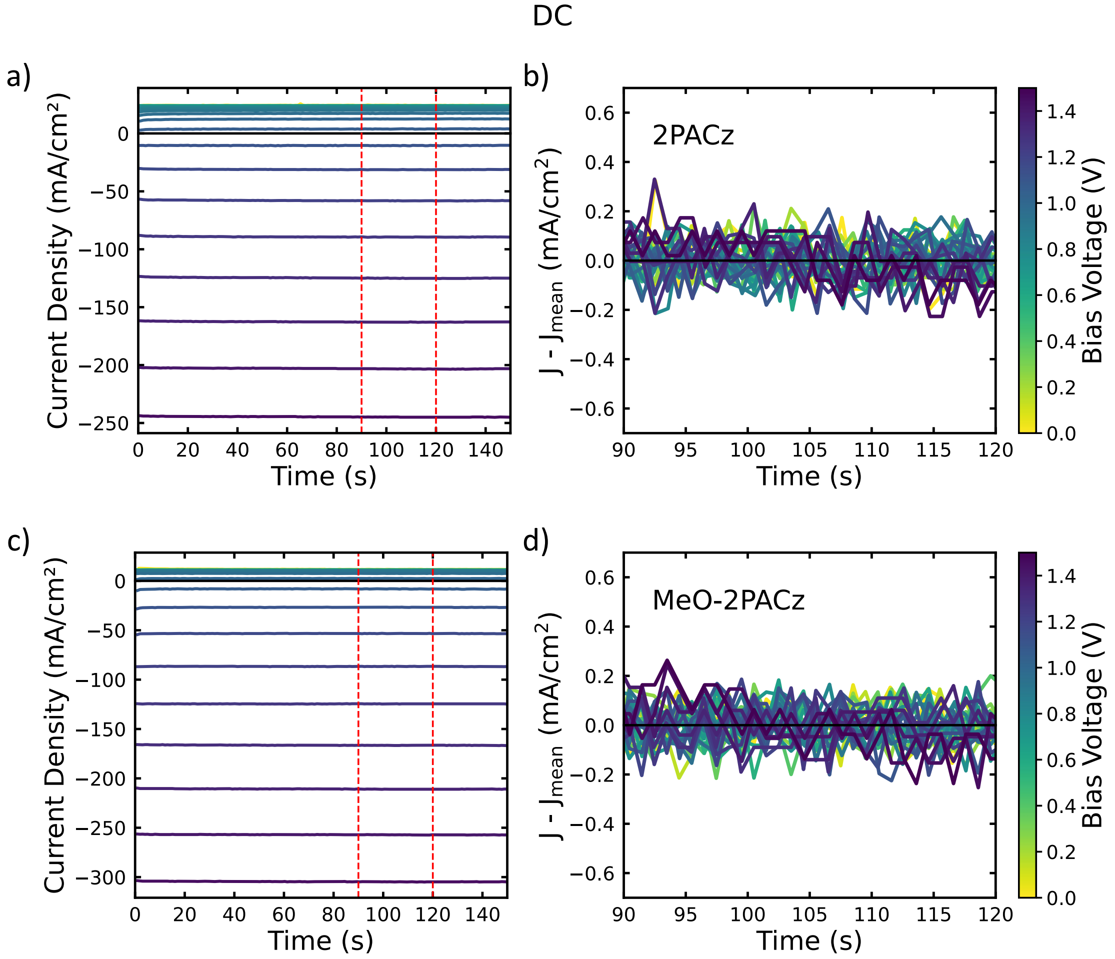

Figure 5.A3: Current density measured during the stabilisation period of the Stabilise and Pulse (SaP) measurements for double cation (DC) devices incorporating 2PACz (a,b) and MeO-2PACz (c,d). Panels a) and c) show the stabilised current density as a function of time for a range of applied stabilisation biases. Panels b) and d) show the corresponding current density during the final 30 s of the stabilisation period, plotted relative to the mean current density over this same 30 s interval. The red dashed lines in a) and c) indicate the 30 s window used for this analysis. The absence of systematic deviation from zero in b) and d) confirms that no measurable current drift occurs immediately before pulsing, indicating that the devices have reached a stable ionic configuration under the applied bias.

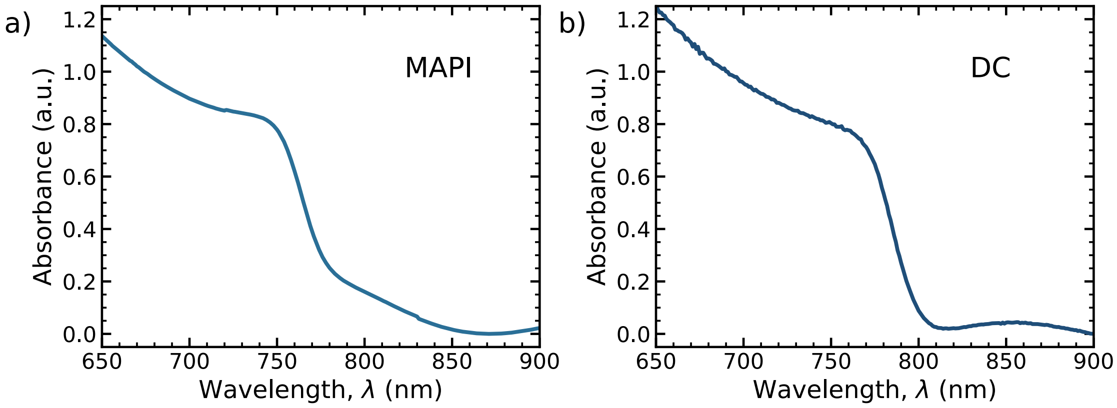

Figure 5.A4: UV–Vis absorbance spectra of (a) methylammonium lead iodide (MAPI) and (b) double cation (DC) perovskite films used for the Tauc band gap analysis. Absorbance data were baseline-corrected by subtracting the minimum absorbance value before plotting. The spectra are shown over the near-band-edge wavelength range (650–900 nm), which is used to convert photon energy in the direct Tauc analysis.

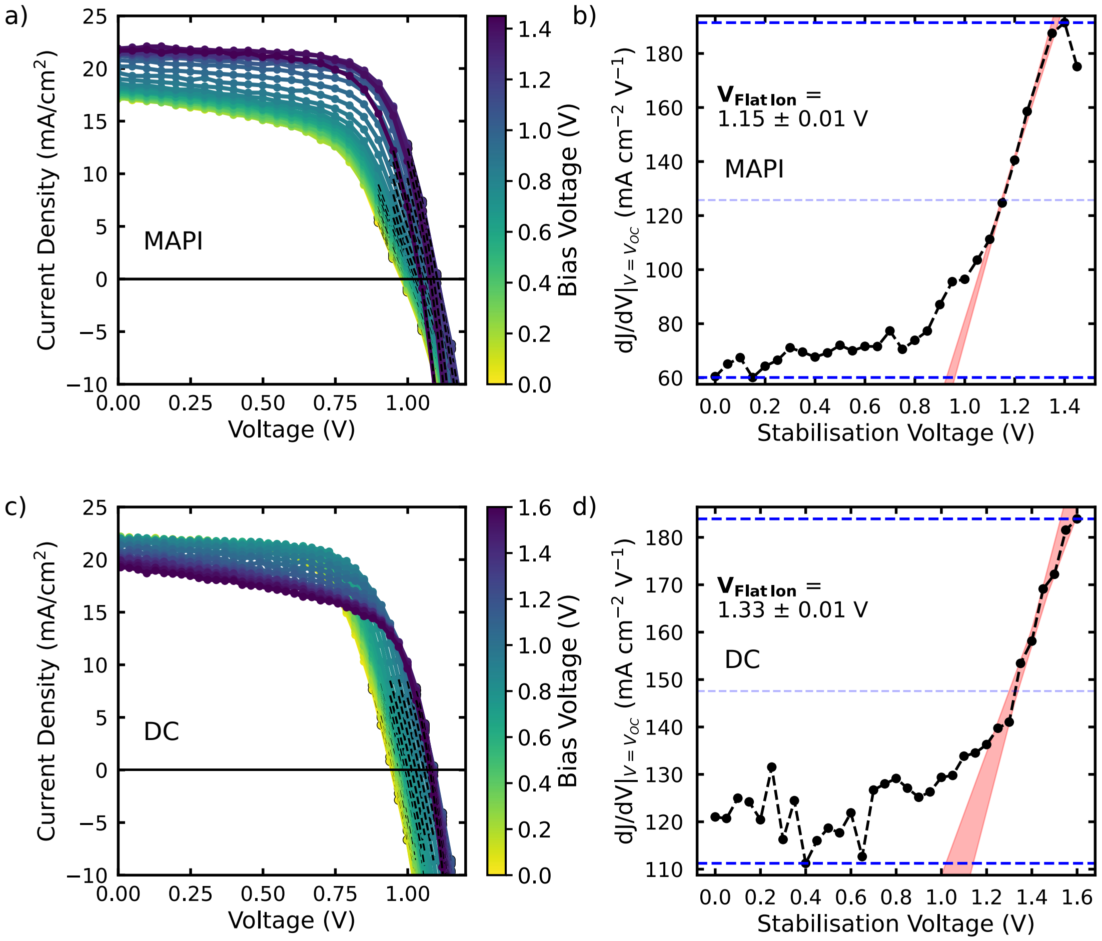

Figure 5.A5: Stabilise and Pulse measurements and corresponding gradient analysis for devices incorporating the Cl-2PACz self-assembled molecule on (a,b) MAPI and (c,d) double-cation (DC) perovskites. Panels a) and c) show the Stabilise and Pulse J–V characteristics measured at incrementally increasing stabilisation biases, with the colour scale indicating the applied bias voltage. Panels b) and d) show the corresponding $\mathrm{d}J/\mathrm{d}V|_{V=V_{\mathrm{OC}}}$ values plotted as a function of stabilisation voltage, with the linear fitting region highlighted for extraction of V_{flat}. The extracted flat-band potentials are indicated in each panel.

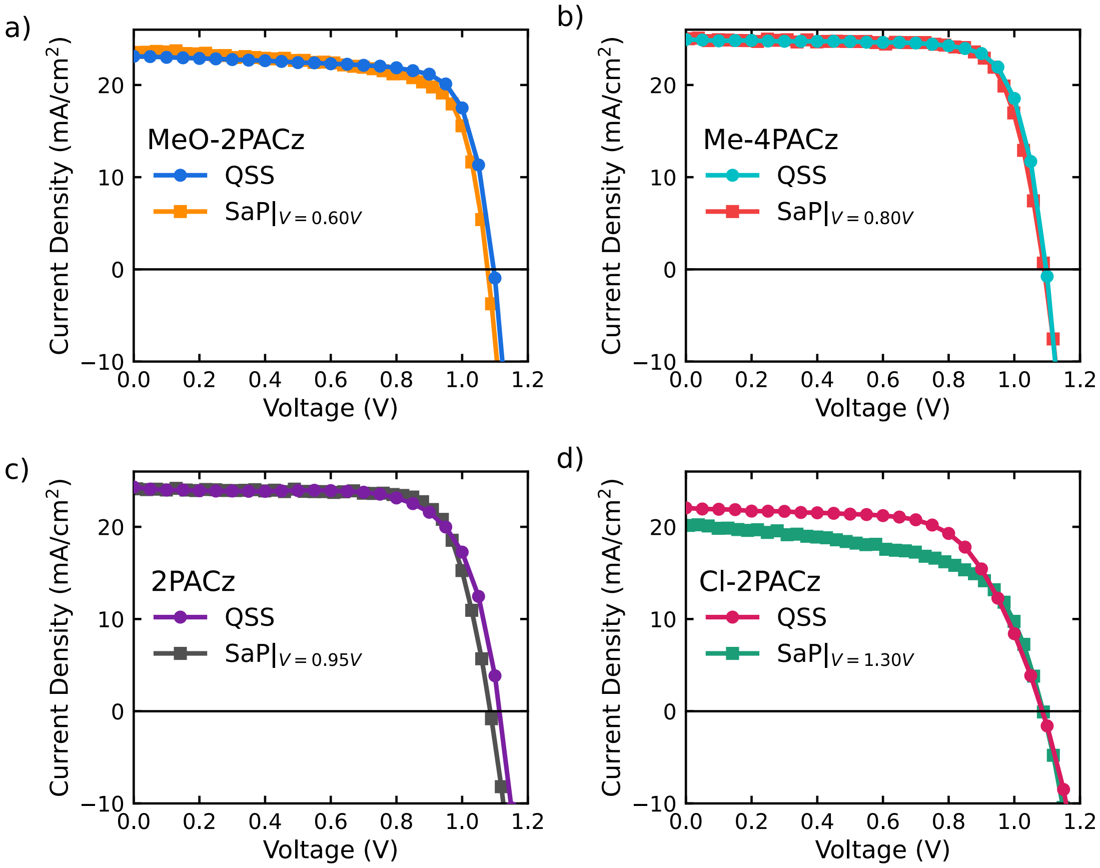

Figure 5.A6: Comparison of quasi-steady-state (QSS) and Stabilise and Pulse J–V characteristics at the extracted flat-band potential ($V = V_{\text{flat}}$) for double-cation (DC) perovskite devices incorporating different self-assembled molecules: (a) MeO-2PACz, (b) Me-4PACz, (c) 2PACz, and (d) Cl-2PACz. In each panel, the Stabilise and Pulse curve corresponds to the J–V measured at the extracted V_{flat}, while the QSS curve reflects steady-state operation in the presence of mobile ions.

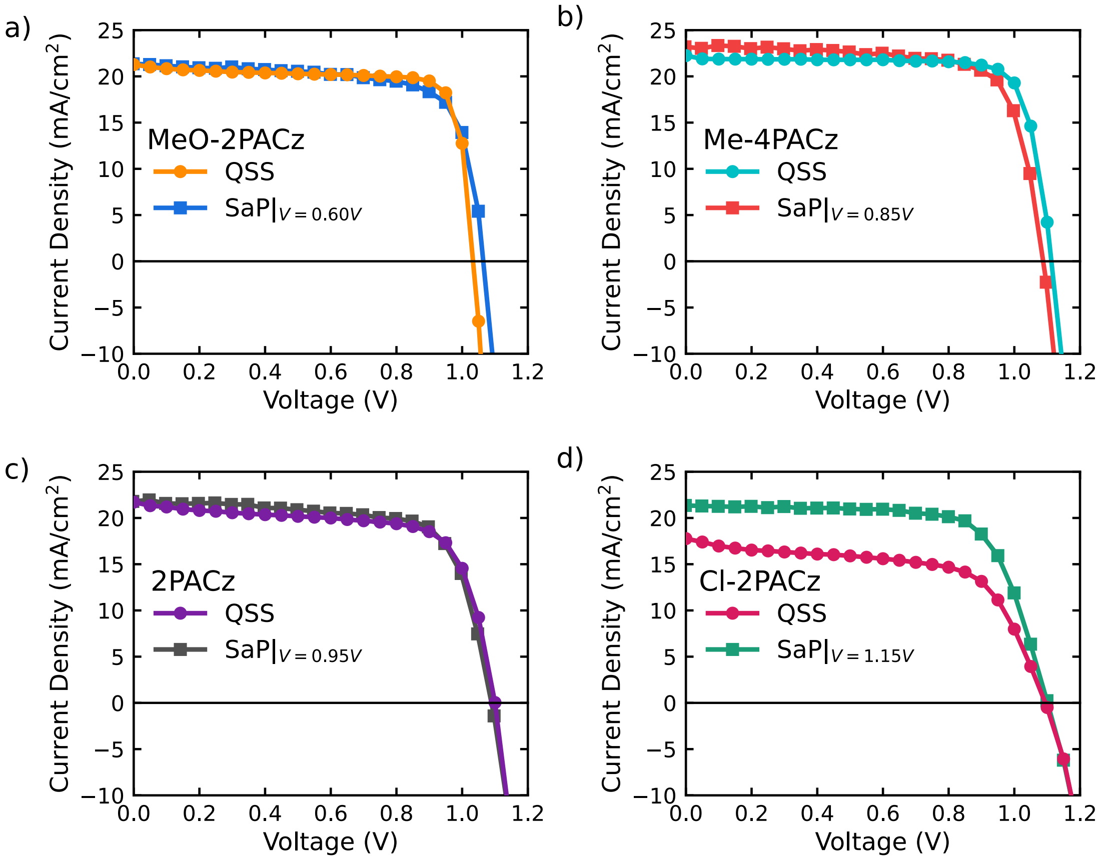

Figure 5.A7: Comparison of quasi-steady-state (QSS) and Stabilise and Pulse J–V characteristics at the extracted flat-band potential ($V = V_{\mathrm{flat}}$) for methylammonium lead iodide (MAPI) perovskite devices incorporating different self-assembled molecules: (a) MeO-2PACz, (b) Me-4PACz, (c) 2PACz, and (d) Cl-2PACz. In each panel, the Stabilise and Pulse curve corresponds to the J–V measured at the extracted V_{flat}, while the QSS curve reflects steady-state operation in the presence of mobile ions.

References

(1) Angus, F. J.; Yiu, W. K.; Mo, H.; Leung, T. L.; Ali, M. U.; Li, Y.; Wang, J.; Ho-Baillie, A. W. Y.; Cooke, G.; Djurišić, A. B.; Docampo, P. *The Journal of Physical Chemistry Letters* **2024**, *15*, 10686–10695.

(2) Chen, H. et al. *Science* **2024**, *384*, 189–193.

(3) Zhou, H.; Chen, Q.; Li, G.; Luo, S.; Song, T.-b.; Duan, H.-S.; Hong, Z.; You, J.; Liu, Y.; Yang, Y. *Science* **2014**, *345*, 542–546.

(4) Bai, Y.; Meng, X.; Yang, S. *Advanced Energy Materials* **2018**, *8*, 1701883.

(5) Hart, L. J. F.; Angus, F. J.; Li, Y.; Khaleed, A.; Calado, P.; Durrant, J. R.; Djurišić, A. B.; Docampo, P.; Barnes, P. R. F. *Energy & Environmental Science* **2024**, *17*, 7107–7118.

(6) Hu, Y.; Schlipf, J.; Wussler, M.; Petrus, M. L.; Jaegermann, W.; Bein, T.; Müller-Buschbaum, P.; Docampo, P. *ACS Nano* **2016**, *10*, 5999–6007.

(7) Jiang, Q.; Zhao, Y.; Zhang, X.; Yang, X.; Chen, Y.; Chu, Z.; Ye, Q.; Li, X.; Yin, Z.; You, J. *Nature Photonics* **2019**, *13*, 460–466.

(8) Kim, S. Y.; Cho, S. J.; Byeon, S. E.; He, X.; Yoon, H. J. *Advanced Energy Materials* **2020**, *10*, 2002606.

(9) Abrusci, A.; Stranks, S. D.; Docampo, P.; Yip, H.-L.; Jen, A. K.-Y.; Snaith, H. J. *Nano Letters* **2013**, *13*, 3124–3128.

(10) Dai, Z.; Yadavalli, S. K.; Chen, M.; Abbaspourtamijani, A.; Qi, Y.; Padture, N. P. *Science* **2021**, *372*, 618–622.

(11) Suo, J.; Yang, B.; Bogachuk, D.; Boschloo, G.; Hagfeldt, A. *Advanced Energy Materials* **2025**, *15*, 2400205.

(12) Zuo, L.; Gu, Z.; Ye, T.; Fu, W.; Wu, G.; Li, H.; Chen, H. *Journal of the American Chemical Society* **2015**, *137*, 2674–2679.

(13) Kwok Kwok Ng; Simon Sze, *Physics of Semiconductor Devices*, 2008.

(14) Ali, F.; Roldán-Carmona, C.; Sohail, M.; Nazeeruddin, M. K. *Advanced Energy Materials* **2020**, *10*, 2002989.

(15) Zhang, S.; Wu, R.; Mu, C.; Wang, Y.; Han, L.; Wu, Y.; Zhu, W.-H. *ACS Materials Letters* **2022**, *4*, 1976–1983.

(16) Park, S. M. et al. *Nature* **2023**, *624*, 289–294.

(17) Liu, S. et al. *Nature* **2024**, *632*, 536–542.

(18) Mishima, R.; Hino, M.; Kanematsu, M.; Kishimoto, K.; Ishibashi, H.; Konishi, K.; Okamoto, S.; Irie, T.; Fujimoto, T.; Yoshida, W.; Uzu, H.; Adachi, D.; Yamamoto, K. *Applied Physics Express* **2022**, *15*, 076503.

(19) Kim, D.-H.; Lee, H.-J.; Lee, S.-H.; Kang, Y.-J.; Kwon, S.-N.; Kim, D.-H.; Na, S.-I. *Solar RRL* **2024**, *8*, 2400067.

(20) Ou, Q.; Zhang, Y.; Wang, Z.; Yuwono, J. A.; Wang, R.; Dai, Z.; Li, W.; Zheng, C.; Xu, Z.-Q.; Qi, X.; Duhm, S.; Medhekar, N. V.; Zhang, H.; Bao, Q. *Advanced Materials* **2018**, *30*, 1705792.

(21) Li, C.; Tscheuschner, S.; Paulus, F.; Hopkinson, P. E.; Kießling, J.; Köhler, A.; Vaynzof, Y.; Huettner, S. *Advanced Materials* **2016**, *28*, 2446–2454.

(22) Singh, N.; Mohapatra, A.; Chu, C.-W.; Tao, Y.-T. *Organic Electronics* **2021**, *98*, 106297.

(23) Yue, S.; Lu, S.; Ren, K.; Liu, K.; Azam, M.; Cao, D.; Wang, Z.; Lei, Y.; Qu, S.; Wang, Z. *Small* **2017**, *13*, 1700007.

(24) Hill, N. S.; Cowley, M. V.; Gluck, N.; Fsadni, M. H.; Clarke, W.; Hu, Y.; Wolf, M. J.; Healy, N.; Freitag, M.; Penfold, T. J.; Richardson, G.; Walker, A. B.; Cameron, P. J.; Docampo, P. *Advanced Materials* **2023**, *35*, 2302146.

(25) Li, D. et al. *Nature Communications* **2024**, *15*, 7605.

(26) Mao, L. et al. *Advanced Materials* **2022**, *34*, 2206193.

(27) Levine, I.; Al-Ashouri, A.; Musiienko, A.; Hempel, H.; Magomedov, A.; Drevilkauskaite, A.; Getautis, V.; Menzel, D.; Hinrichs, K.; Unold, T.; Albrecht, S.; Dittrich, T. *Joule* **2021**, *5*, 2915–2933.

(28) Peng, W. et al. *Energy & Environmental Science* **2025**, *18*, 874–883.

(29) Hossain, K.; Kulkarni, A.; Bothra, U.; Klingebiel, B.; Kirchartz, T.; Saliba, M.; Kabra, D. *ACS Energy Letters* **2023**, *8*, 3860–3867.

(30) Farag, A. et al. *Advanced Energy Materials* **2023**, *13*, 2203982.

(31) Phung, N.; Verheijen, M.; Todinova, A.; Datta, K.; Verhage, M.; Al-Ashouri, A.; Köbler, H.; Li, X.; Abate, A.; Albrecht, S.; Creatore, M. *ACS Applied Materials & Interfaces* **2022**, *14*, 2166–2176.

(32) Al-Ashouri, A. et al. *Energy & Environmental Science* **2019**, *12*, 3356–3369.

(33) Sun, A. et al. *Advanced Energy Materials* **2024**, *14*, 2303941.

(34) Siekmann, J.; Kulkarni, A.; Akel, S.; Klingebiel, B.; Saliba, M.; Rau, U.; Kirchartz, T. *Advanced Energy Materials* **2023**, *13*, 2300448.

(35) De Quilettes, D. W.; Vorpahl, S. M.; Stranks, S. D.; Nagaoka, H.; Eperon, G. E.; Ziffer, M. E.; Snaith, H. J.; Ginger, D. S. *Science* **2015**, *348*, 683–686.

(36) Im, J.-H.; Kim, H.-S.; Park, N.-G. *APL MATERIALS* **2014**, *2*, 081510.

(37) Zhang, H.; Cheng, J.; Lin, F.; He, H.; Mao, J.; Wong, K. S.; Jen, A. K.-Y.; Choy, W. C. H. *ACS Nano* **2016**, *10*, 1503–1511.

(38) Kim, H.-S.; Park, N.-G. *The Journal of Physical Chemistry Letters* **2014**, *5*, 2927–2934.

(39) Sajid, S.; Elseman, A. M.; Huang, H.; Ji, J.; Dou, S.; Jiang, H.; Liu, X.; Wei, D.; Cui, P.; Li, M. *Nano Energy* **2018**, *51*, 408–424.

(40) Kang, D.-H.; Park, N.-G. *Advanced Materials* **2019**, *31*, 1805214.

(41) Sun, X.; Li, Y.; Liu, D.; Liu, R.; Zhang, B.; Tian, Q.; Fan, B.; Wang, X.; Li, Z.; Shao, Z.; Wang, X.; Cui, G.; Pang, S. *Advanced Energy Materials* **2023**, *13*, 2302191.

(42) Stolterfoht, M. et al. *Energy & Environmental Science* **2019**, *12*, 2778–2788.

(43) Péan, E. V.; Davies, M. L. *Journal of Chemical Information and Modeling* **2023**, *63*, 4477–4482.

(44) Al-Ashouri, A. et al. *Science* **2020**, *370*, 1300–1309.

(45) Hellmann, T.; Das, C.; Abzieher, T.; Schwenzer, J. A.; Wussler, M.; Dachauer, R.; Paetzold, U. W.; Jaegermann, W.; Mayer, T. *Advanced Energy Materials* **2020**, *10*, 2002129.

(46) Wang, Y.; Lin, J.; He, Y.; Zhang, Y.; Liang, Q.; Liu, F.; Zhou, Z.; Chan, C. C. S.; Li, G.; Feng, S.-P.; Ng, A. M. C.; Wong, K. S.; Popović, J.; Djurišić, A. B. *Solar RRL* **2022**, *6*, 2200224.

(47) Lin, Y. et al. *Advanced Energy Materials* **2022**, *12*, 2202503.

(48) Wang, Y.; Jiang, W.; Liu, S.-C.; Lin, C.-T.; Fan, B.; Li, Y.; Gao, H.; Liu, M.; Lin, F. R.; Jen, A. K.-Y. *Advanced Energy Materials* **2024**, *14*, 2303354.

(49) Reiser, P. et al. *Chemistry of Materials* **2019**, *31*, 4213–4221.

(50) Seemann, A.; Egelhaaf, H.-J.; Brabec, C. J.; Hauch, J. A. *Organic Electronics* **2009**, *10*, 1424–1428.

(51) Lee, J. H.; Shin, J.-H.; Song, J. Y.; Wang, W.; Schlaf, R.; Kim, K. J.; Yi, Y. *The Journal of Physical Chemistry C* **2012**, *116*, 26342–26348.

(52) Mohan, M.; Nandal, V.; Paramadam, S.; Reddy, K. P.; Ramkumar, S.; Agarwal, S.; Gopinath, C. S.; Nair, P. R.; Namboothiry, M. A. G. *The Journal of Physical Chemistry C* **2017**, *121*, 5523–5530.

(53) Xu, W.; Hart, L. J. F.; Moss, B.; Caprioglio, P.; Macdonald, T. J.; Furlan, F.; Panidi, J.; Oliver, R. D. J.; Pacalaj, R. A.; Heeney, M.; Gasparini, N.; Snaith, H. J.; Barnes, P. R. F.; Durrant, J. R. *Advanced Energy Materials* **2023**, *13*, 2301102.

(54) Chen, H. et al. *Nature* **2023**, *613*, 676–681.

(55) Bertoluzzi, L.; Boyd, C. C.; Rolston, N.; Xu, J.; Prasanna, R.; O'Regan, B. C.; McGehee, M. D. *Joule* **2020**, *4*, 109–127.

(56) Sajedi Alvar, M.; Blom, P. W.; Wetzelaer, G.-J. A. H. *Advanced Electronic Materials* **2020**, *6*, 1900935.

(57) Walsh, A.; Scanlon, D. O.; Chen, S.; Gong, X. G.; Wei, S.-H. *Angewandte Chemie International Edition* **2015**, *54*, 1791–1794.

(58) McCallum, S. G.; Nicholls, O.; Jensen, K. O.; Cowley, M. V.; Lerpinière, J. E.; Walker, A. B. *Journal of Physics: Energy* **2024**, *6*, 015005.

Chapter 6

The Case Against Hole Injection Through Self-Assembled Molecules in Perovskite Solar Cells

The contents of this chapter are based upon the published research article, *"The case against hole injection through SAMs in perovskite solar cells"*.[1] This work was conceptualised by Prof. Graeme Cooke, Prof. Pablo Docampo, Dr Wenhui Li, Dr Lewis Mackenzie, and Fraser J. Angus. Dr Lewis Mackenzie designed and synthesised the molecule under the supervision of Prof. Graeme Cooke. Dr Dylan Wilkinson and Dr Lewis Mackenzie characterised the new material under the supervision of Prof. Graeme Cooke. Dr Wenhui Li fabricated the devices and measured them under the supervision of Prof. Emilio Palomares. Fraser J. Angus performed the SaP characterisation and interpreted the results under the supervision of Prof. Pablo Docampo. Marcin Giza performed the XPS measurements and interpreted the results under the supervision of Prof. Pablo Docampo and Dr Elisabetta Arca. Fraser J. Angus and Prof. Pablo Docampo conceived the experiments for the characterisation in this work.

6.1 Do SAM Energy Levels Control Charge Extraction in Perovskite Solar Cells?

Self-assembled molecules (SAMs) have become a central component in the design of high-performance inverted (p–i–n) perovskite solar cells (PSCs), where they are typically employed as hole-selective contacts.[2–4] Their widespread adoption is largely motivated by their ability to modify the work function of transparent conducting oxides (i.e. indium-doped tin oxide (ITO)), passivate interfacial defects, and provide favourable energetic alignment between the perovskite absorber and the charge extraction electrode.[5–9] In many reports, improvements in device performance achieved through the addition of a SAM layer are rationalised in terms of enhanced charge extraction, arising from careful alignment of the highest occupied molecular orbital (HOMO) of the SAM with the valence band of the perovskite.[10–13]

This design philosophy implicitly assumes that efficient hole injection through the SAM layer is a necessary, or at least desirable, condition for achieving high power conversion efficiencies. Such an assumption is intuitive and historically grounded in the design principles established for dye-sensitised solar cells (DSSCs), in which strong electronic coupling and favourable energy-level alignment between the dye and the charge-extraction electrode are critical for suppressing recombination and maximising photocurrent.[14] The most effective dyes incorporated both an energetically favourable transition and molecular orbital overlap with the electrode.[15–17] This combination promotes ultrafast charge extraction from the dyes, as rapid electron transfer outcompetes recombination, enabling high photogenerated current densities and maximising performance.[18–20]

However, device performance in perovskite solar cells is not determined solely by charge extraction efficiency, but rather by a balance among charge generation, recombination, and accumulation.[21, 22] Under conditions of selective contacts, the open-circuit voltage (V_{OC}) of a PSC reflects the quasi-Fermi level splitting (QFLS) within the absorber, which depends sensitively on charge carrier density.[23, 24] Efficient extraction pathways, while beneficial for current collection, can reduce carrier density in the perovskite and thereby limit the achievable QFLS if they dominate over recombination.[24]

Recent results have shown that SAM-induced dipoles can introduce energetic offsets at the interface between the perovskite and the charge extraction contact. These offsets promote the accumulation of photogenerated charge within the absorber, thereby increasing the open-circuit voltage.[22] Full details of this behaviour are discussed in Chapter 5.

In contrast, the lack of such a barrier reduced the charge density in the film and therefore reduced the open-circuit voltage as a result of a reduced QFLS.[22] In previous work by Cariello *et al.*, a novel SAM material (Spiro-A) was synthesised by the mono-demethylation of commercially available Spiro-OMeTAD, which features a carboxylic acid anchoring group.[25] This material is a classic example of following traditional design paradigms, in which the HOMO overlaps with the charge-extraction electrode. The resulting p–i–n perovskite solar cells showed efficiencies comparable to that of a poly[bis(4-phenyl) (2,4,6-trimethylphenyl)amine] (PTAA)-based device; however, they did not outperform competing carbazole-based SAM materials. This raises an important question: Is injection through the SAM, to promote charge extraction, necessary or even desirable?

In this chapter, this question is addressed directly by deliberately testing the assumption that efficient hole injection through a SAM is required for high-performance perovskite solar cells. Two structurally related Spiro-OMeTAD-based SAMs are investigated, designed to isolate the role of spatial and electronic coupling between the SAMs' HOMO and the underlying ITO electrode. A novel Spiro moiety, Spiro-B, was synthesised, featuring a hexyl alkyl chain spacer, which creates a spatial gap between the HOMO of the SAM and the ITO anode when incorporated in solar cells. Both Spiro moieties are compared against a carbazole-based reference SAM, [4-(3,6-dimethyl-9H-carbazol-9-yl)butyl]phosphonic acid (Me-4PACz). We hypothesise that Spiro-A will promote efficient charge injection with a direct HOMO-valence band overlap at the interface. In contrast, Spiro-B, which lacks this orbital overlap, may lead to charge accumulation at the interface.

To disentangle the relationship between SAM structure and device performance, we employ a combination of spectroscopic and electronic techniques, including X-ray photoelectron spectroscopy (XPS), time-resolved photoluminescence (TRPL), and Stabilise and Pulse (SaP) measurements. Standard current density–voltage (J–V) scans show that Spiro-B achieves higher open-circuit voltages and overall power conversion efficiencies than Spiro-A, while Me-4PACz delivers the best performance overall.

However, SaP measurements reveal that the Spiro-B derivative produces a lower built-in potential (V_{bi}) than Spiro-A, despite its higher V_{OC} and improved device performance. Both Spiro derivatives are also outperformed by the carbazole SAM Me-4PACz. These observations indicate that promoting charge extraction in PSCs is not necessarily a driver of higher device performance and challenge conventional molecular design strategies.

This chapter, therefore, investigates how the degree of electronic coupling between a SAM and the underlying electrode influences charge extraction, charge accumulation, and ultimately the open-circuit voltage of perovskite solar cells.

6.2 Charge Extraction and Interfacial Energetics in Spiro SAM Devices

6.2.1 Molecular Design of Spiro SAMs for Controlled Charge Injection

Charge injection through the self-assembled molecular layer is often assumed to play a critical role in determining device performance. To directly probe this assumption, two structurally related Spiro-OMeTAD derivatives were selected to isolate the effect of spatial and electronic coupling between the molecule and the underlying ITO electrode. These materials, denoted Spiro-A and Spiro-B, share the same Spiro core and therefore exhibit very similar intrinsic electronic properties, while deliberately differing in how the HOMO is spatially positioned relative to the electrode surface.

The previously synthesised Spiro-A is anchored directly to the ITO substrate through a carboxylic acid functional group attached to the triphenylamine unit, placing the Spiro core, and therefore its HOMO, in close spatial proximity to the electrode.[25] This configuration is expected to promote strong electronic coupling and facilitate efficient hole injection from the perovskite through the SAM into the ITO. In contrast, Spiro-B is bonded to a benzoic acid group through a hexyl alkyl chain separator, introducing a deliberate physical separation between the HOMO and the electrode surface. The chemical structures of the Spiro moieties are shown in Figure 6.1.

To verify that these structural modifications do not alter the intrinsic electronic properties of the molecules, the optical and electronic characteristics of Spiro-A and Spiro-B were investigated using ultraviolet–visible absorption spectroscopy (UV–Vis), fluorescence spectroscopy, and cyclic voltammetry (CV). The absorption and emission spectra of Spiro-B match those of Spiro-A and Spiro-OMeTAD, indicating that the introduction of the alkyl spacer does not significantly impact the electronic structure of the Spiro core, as shown in Figure 6.2.

Similarly, the cyclic voltammetry measurements reveal that both Spiro-moieties exhibit similar electrochemical behaviour, as shown in Figure 6.3. Taken together, these results indicate that any changes in device performance are unlikely to originate from changes in intrinsic molecular energetics.

While the optical and electrochemical measurements of the two Spiro SAMs indicate no substantial difference in the electronic properties, density functional theory (DFT) calculations reveal a pronounced difference in their molecular dipole moments. Spiro-A exhibits a large calculated dipole moment of approximately 8.2 D. In contrast, Spiro-B possesses a substantially smaller dipole moment of approximately

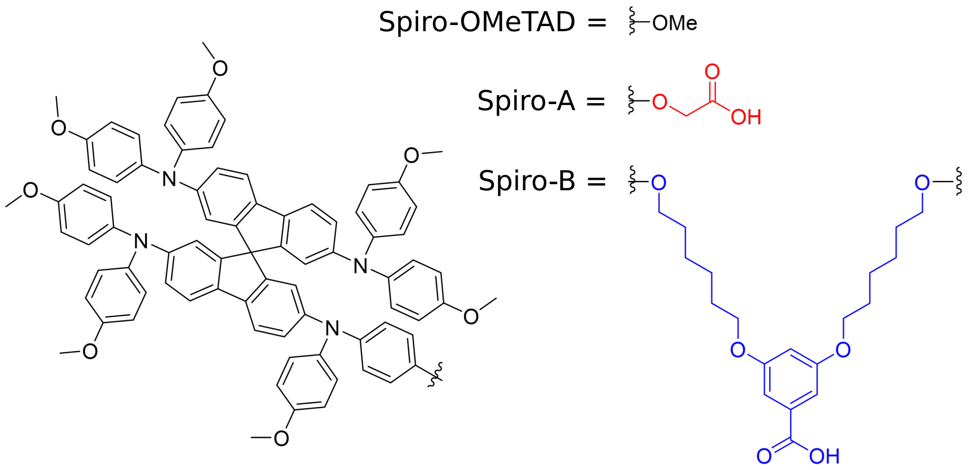

Figure 6.1: Molecular structures of Spiro-OMeTAD and its carboxylic acid-functionalised derivatives, Spiro-A and Spiro-B. Spiro-A consists of a Spiro-OMeTAD core bearing a short carboxylic acid anchoring group, enabling binding to the indium tin oxide (ITO) surface. In contrast, Spiro-B incorporates a longer alkyl spacer terminated with a carboxylic acid group, thereby increasing the spatial separation between the spiro core and the substrate. I acknowledge that Dr Dylan Wilkinson prepared this figure at the University of Glasgow. Adapted from Ref. [1] under a Creative Commons Attribution 3.0 Unported Licence.

2.1 D. This contrast arises from the differing configurations of the two molecules and is therefore expected to strongly influence the work function of the underlying ITO once deposited.[26, 27] As discussed in Chapter 5, such dipole-induced work function shifts can significantly modify the built-in potential of the device.

Taken together, this molecular design strategy provides a controlled method for disentangling the roles of dipole-induced modifications to the work function and spatial electronic coupling in device performance. By comparing two Spiro SAM moieties with similar intrinsic electronic characteristics but markedly different dipole moments and injection pathways, it is possible to test whether promoting efficient hole injection through a SAM is a necessary condition for achieving high-performance perovskite solar cells.

6.2.2 Evidence for Anchoring of Spiro SAMs on ITO Substrates

To attribute differences in device behaviour to electronic effects rather than morphological variations, it is first necessary to confirm that the Spiro molecules form self-assembled layers on the ITO surface. The presence of the Spiro SAMs was verified using X-ray photoelectron spectroscopy (XPS), contact angle measurements, and atomic force microscopy (AFM). The C 1s spectra for bare ITO, ITO/Spiro-A, and ITO/Spiro-B are provided in Figure 6.A1. While the Spiro-A sample does not

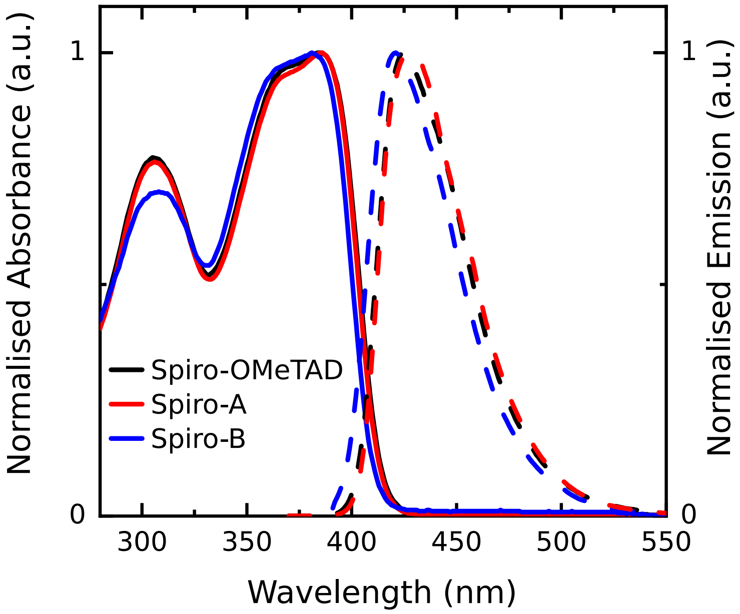

Figure 6.2: Normalised UV–Vis absorption (solid lines) and steady-state fluorescence emission spectra (dashed lines) of Spiro-OMeTAD, Spiro-A and Spiro-B. The absorption profiles of all three molecules exhibit similar spectral features, indicating that functionalisation with carboxylic acid anchoring groups and the introduction of an alkyl spacer in Spiro-B do not substantially change the electronic structure of the core. Likewise, the emission spectra show only minor shifts, consistent with comparable optical band gaps across the series. I acknowledge that this data was collected by Dr Dylan Wilkinson at the University of Glasgow. Adapted from Ref. [1] under a Creative Commons Attribution 3.0 Unported Licence.

exhibit additional distinguishable C 1s features relative to the ITO reference, the presence of Spiro-B is evident from the appearance of a distinct C–O component at approximately 286.3 eV and an aromatic satellite feature at approximately 291.6 eV. The assignments of XPS peaks associated with the Spiro moieties were established by measuring a thin reference film of Spiro-OMeTAD, shown in Figure 6.A2. These reference measurements allow the additional components to be confidently attributed to the molecular backbone of the Spiro SAMs.

More definitive evidence of the Spiro SAM attachment is observed in the O 1s spectra, shown in Figure 6.4. The bare ITO substrate exhibits a peak corresponding to bulk indium–oxygen bonds (~ 530.4), oxygen adjacent to oxygen-deficient sites (~ 531.2), and surface hydroxy–indium bonds (~ 532.1).[28] Following the deposition of either Spiro-A or Spiro-B, an additional contribution appears at approximately 533.1 eV, which is attributed to C–O species within the Spiro molecules. The emergence of this component confirms the presence of the Spiro SAMs on the ITO surface.

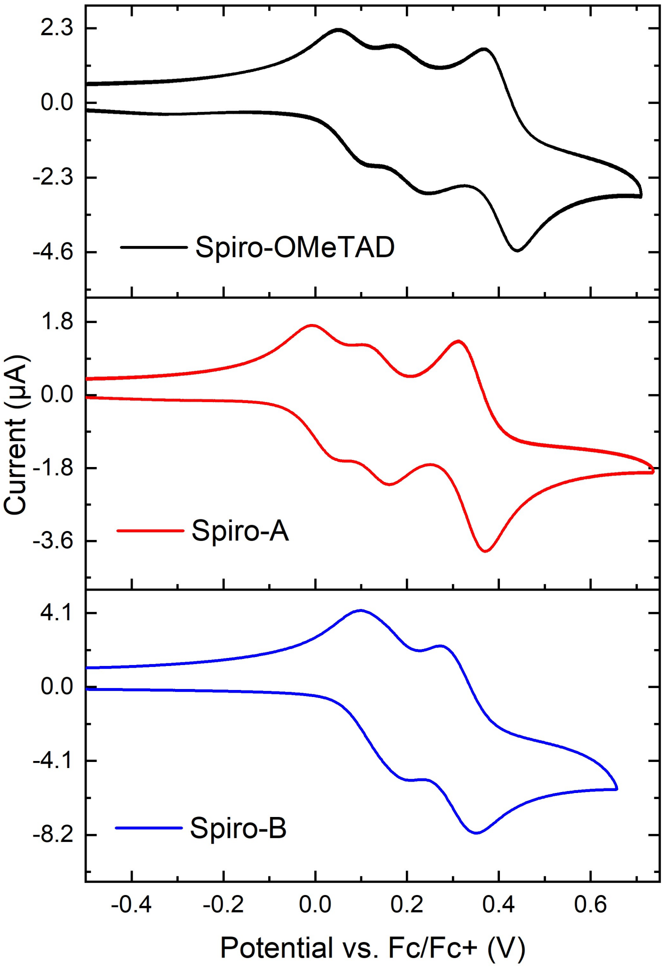

Figure 6.3: Cyclic voltammograms of Spiro-OMeTAD, Spiro-A and Spiro-B recorded versus the ferrocene/ferrocenium (Fc/Fc$^+$) redox couple. All three molecules exhibit comparable oxidation features, indicating that functionalisation with carboxylic acid anchoring groups and the incorporation of an alkyl spacer in Spiro-B do not significantly alter the molecular orbital energetics of the Spiro-OMeTAD core. I acknowledge that this data was collected by Dr Dylan Wilkinson at the University of Glasgow. Adapted from Ref. [1] under a Creative Commons Attribution 3.0 Unported Licence.

Further confirmation is provided by the N 1s spectra in Figure 6.4, where the bare ITO substrate shows no detectable nitrogen signal, whereas both Spiro-A and Spiro-B samples exhibit peaks centred at approximately 400.1 eV, associated with C-N environments within the Spiro structure. A secondary component at approximately 400.8 eV is attributed to residual dimethylformamide (DMF) solvent.[29] The complete XPS peak data is provided in Table 6.A1.

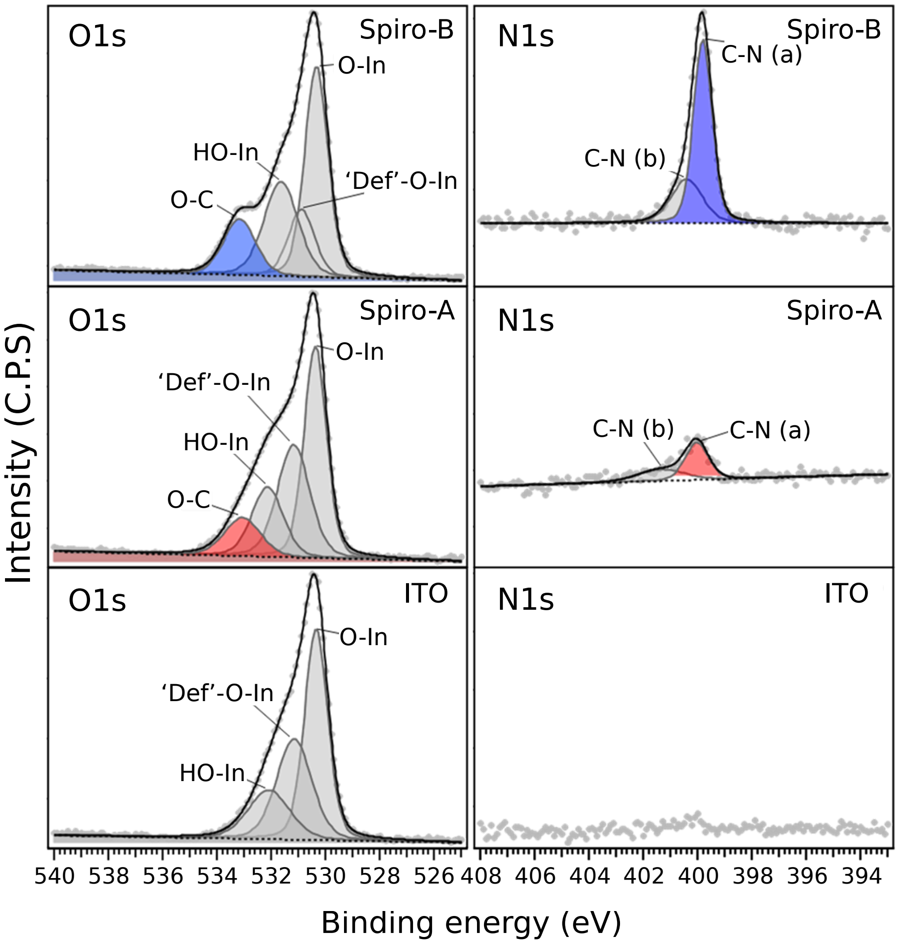

Figure 6.4: High-resolution O 1s and N 1s X-ray photoelectron spectroscopy (XPS) spectra of bare indium tin oxide (ITO) and ITO substrates coated with Spiro-A or Spiro-B. ITO components (e.g., O–In and defect-associated O–In species) are shown in grey, while additional features arising from the self-assembled molecular layers are highlighted in red (Spiro-A) and blue (Spiro-B) for clarity. The appearance of N 1s signals and modified O 1s components confirms successful surface functionalisation of ITO by both carboxylic acid-terminated Spiro derivatives. I acknowledge that this data was collected by Dr Marcin Giza at the University of Glasgow. Adapted from Ref. [1] under a Creative Commons Attribution 3.0 Unported Licence.

To assess the uniformity of surface coverage, contact angle measurements and atomic force microscopy (AFM) were performed, with the results shown in Figure 6.5. Deposition of either Spiro-A or Spiro-B increases the water contact angle on the ITO surface from approximately 30° to approximately 74°, indicating successful modification of the initially hydrophilic oxide surface to a more hydrophobic interface. The contact angles of Spiro-A and Spiro-B are comparable, suggesting similar macroscopic surface wettability.

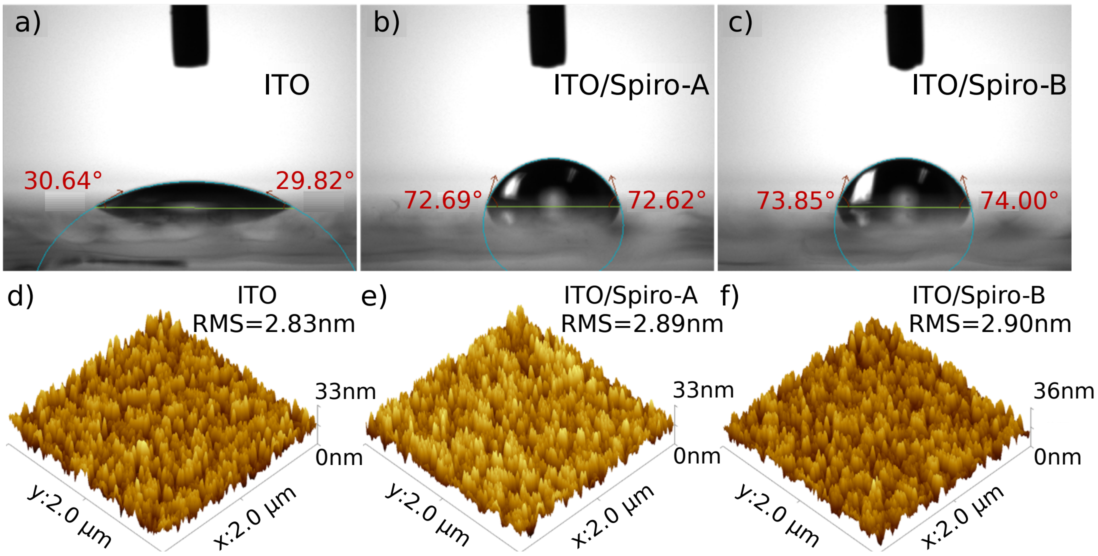

Figure 6.5: (a–c) Contact angle measurements of bare indium-doped tin oxide (ITO), ITO/Spiro-A, and ITO/Spiro-B, respectively. The increased contact angle following deposition of the Spiro derivatives indicates successful surface modification and enhanced surface hydrophobicity relative to bare ITO. (d–f) Atomic force microscopy (AFM) topography images of ITO, ITO/Spiro-A, and ITO/Spiro-B. Root-mean-square (RMS) roughness values are reported for each sample and indicate that deposition of the molecular layers does not significantly alter the substrate morphology. I acknowledge that this data was collected by Dr Wenhui Li at the Institute of Chemical Research of Catalonia. Adapted from Ref. [1] under a Creative Commons Attribution 3.0 Unported Licence.

AFM analysis reveals that the root-mean-square (RMS) roughness remains effectively unchanged upon SAM deposition (Figure 6.5), with values ranging from 2.83 nm for bare ITO to 2.89 nm and 2.90 nm for ITO/Spiro-A and ITO/Spiro-B, respectively. No significant alteration in surface topology is observed. Taken together, these measurements confirm that both Spiro-A and Spiro-B form anchored, uniformly distributed layers on the ITO surface. The similarity in surface wettability and roughness indicates that subsequent differences in perovskite growth and photovoltaic performance cannot be readily attributed to morphological effects, but instead must arise from differences in interfacial electronic structure and charge-transfer behaviour.

6.2.3 Photovoltaic Performance of Spiro SAM Devices

To determine how the molecular structure of the Spiro SAM influences device behaviour, inverted p–i–n perovskite solar cells were fabricated using ITO substrates treated with either Spiro-A, Spiro-B, or the carbazole-based reference SAM Me-4PACz as the hole-selective layer. The perovskite absorber employed was an optimised triple-cation composition, $Cs_{0.05}(FA_{0.95}MA_{0.05})_{0.95}Pb(I_{0.95}Br_{0.05})_3$, selected for its established stability and high performance. The electron-transporting layer consisted of [6,6]-phenyl-C_{61}-butyric acid methyl ester (PCBM) and bathocuproine (BCP), and devices were completed with a silver cathode. Full fabrication and measurement details are provided in Section 3.2.1.

The current density–voltage (J–V) characteristics of representative champion devices measured under simulated 1 Sun illumination (AM1.5G, 100 mW cm^{-2}) are shown in Figure 6.6. The champion device incorporating Spiro-A achieved a power conversion efficiency (PCE) of 19.7%, with a short-circuit current density (J_{SC}) of 23.8 mA cm^{-2}, an open-circuit voltage (V_{OC}) of 0.99 V, and a fill factor (FF) of 83.9. In contrast, the device incorporating Spiro-B yielded an improved PCE of 20.8%, with a J_{SC} of 24.0 mA cm^{-2}, a V_{OC} of 1.03 V, and a fill factor of 84.5. The reference device based on Me-4PACz achieved the highest overall performance, reaching a PCE of 23.2%, with a J_{SC} of 24.7 mA cm^{-2}, a V_{OC} of 1.13 V, and a fill factor of 82.9.

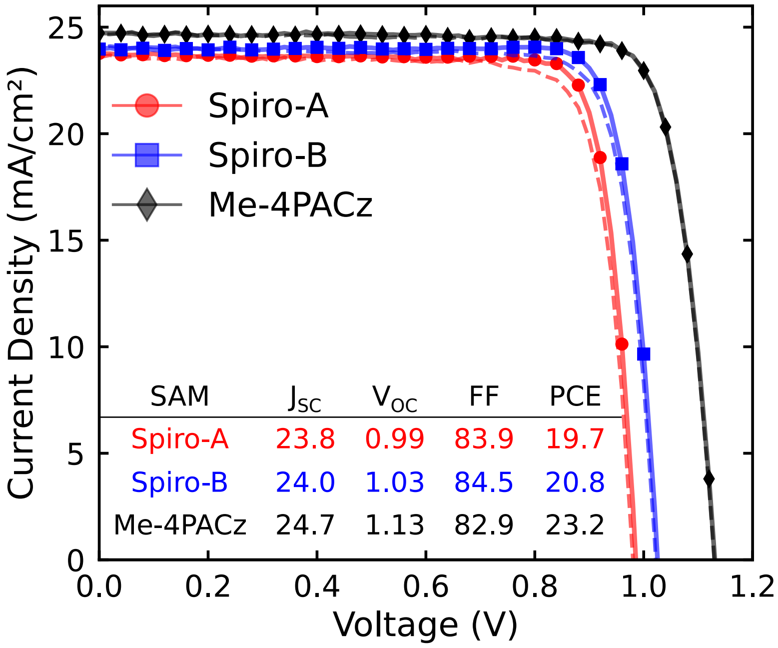

SAM	J_{SC}	V_{OC}	FF	PCE
Spiro-A	23.8	0.99	83.9	19.7
Spiro-B	24.0	1.03	84.5	20.8
Me-4PACz	24.7	1.13	82.9	23.2

Figure 6.6: Current density–voltage (J–V) characteristics of champion perovskite solar cells incorporating Spiro-A, Spiro-B and Me-4PACz as the hole-transport layer. Reverse scans are shown as solid lines with markers, and forward scans as dashed lines. The inset table summarises the champion device parameters, including short-circuit current density (J_{SC}, mA cm^{-2}), open-circuit voltage (V_{OC}, V), fill factor (FF, %), and power conversion efficiency (PCE, %). Devices incorporating Spiro-B exhibit an enhanced V_{OC} and fill factor relative to Spiro-A, despite comparable J_{SC}, leading to an overall improvement in PCE. I acknowledge that this data was collected by Dr Wenhui Li at the Institute of Chemical Research of Catalonia. Adapted from Ref. [1] under a Creative Commons Attribution 3.0 Unported Licence.

The statistical distribution of the photovoltaic parameters is presented in Figure 6.7. The short-circuit current densities are broadly similar across all three systems, varying within a narrow range of 23.1–24.7 mA cm^{-2}. More pronounced differences are observed in the open-circuit voltage, where a clear increase in V_{OC} is observed when moving from Spiro-A (0.99 V) to Spiro-B (1.03 V), with Me-4PACz yielding the highest value (1.13 V). The improvement in PCE from Spiro-A to Spiro-B therefore arises primarily from increases in both V_{OC} and FF, rather than from changes in J_{SC}. Notably, the fill factor of Spiro-B devices is slightly higher than that of Spiro-A, which in turn is greater than that of Me-4PACz. Additionally, minimal hysteresis is observed in all devices studied here under standard J–V scan conditions.

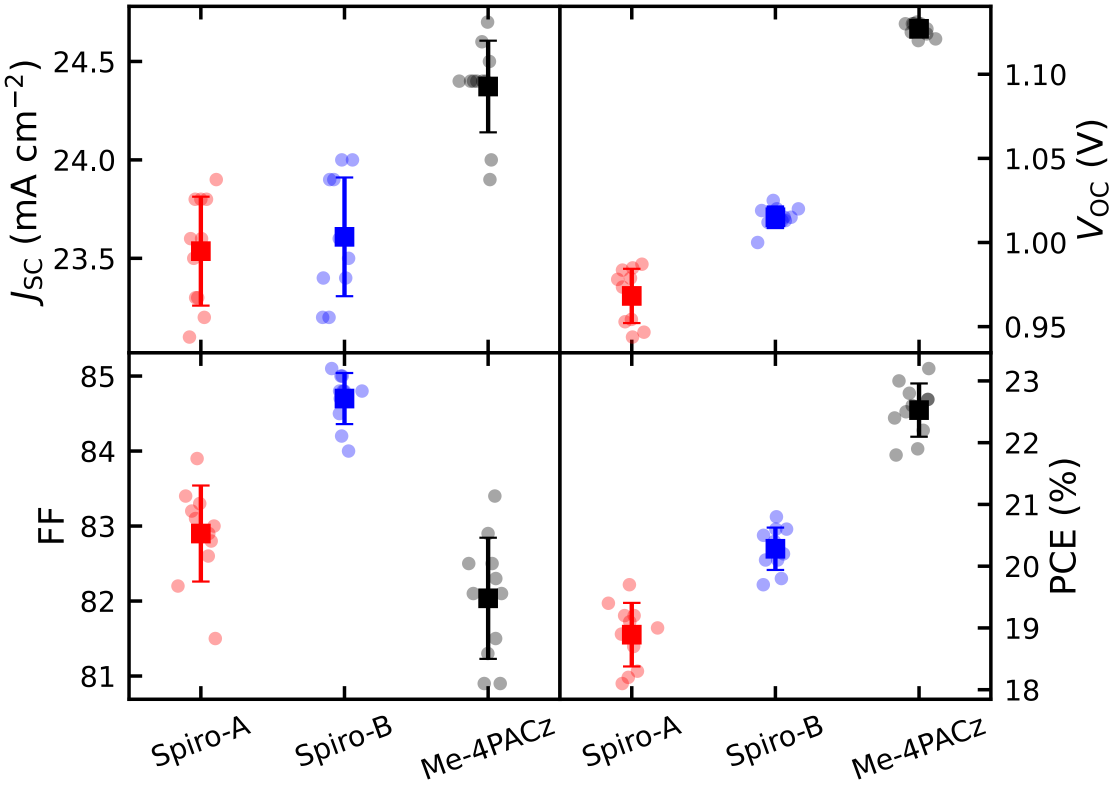

Figure 6.7: Statistical distribution of photovoltaic parameters for perovskite solar cells incorporating Spiro-A, Spiro-B, and Me-4PACz as the hole-transport layer (11 devices per SAM). Box plots show: short-circuit current density (J_{SC}, mA cm^{-2}), open-circuit voltage (V_{OC}, V), fill factor (FF, %), and power conversion efficiency (PCE, %). Boxes represent the interquartile range (25th–75th percentile); the central marker indicates the median; whiskers denote the full data range; and markers correspond to individual devices. Adapted from Ref. [1] under a Creative Commons Attribution 3.0 Unported Licence.

At first glance, the ordering of device performance may appear counterintuitive. Spiro-A, which places the Spiro core in closer proximity to the ITO surface and is therefore expected to promote more efficient hole injection, does not yield superior device metrics. Instead, Spiro-B, which incorporates a spatial separator between the Spiro core and the electrode, delivers a higher V_{OC} and improved overall efficiency. This observation suggests that maximising interfacial charge injection alone is not sufficient to optimise device performance, and that additional interfacial processes must be considered. To further elucidate the origin of these differences, the impact of the SAMs on charge carrier recombination dynamics is explained in the following section using time-resolved photoluminescence (TRPL) measurements.

6.2.4 Interfacial Recombination Dynamics in Spiro SAM Devices

To identify the origin of the performance differences between the Spiro-based devices, time-resolved photoluminescence (TRPL) spectroscopy is used to probe charge-carrier recombination dynamics at the interface between the SAM and the perovskite. The normalised TRPL decays for perovskite films deposited on Spiro-A and Spiro-B are shown in Figure 6.8. To analyse the decay behaviour, a rate-equation model based on bimolecular, trapping, and Auger recombination processes was employed. The extracted parameters are summarised in Table 6.1.[30, 31]

Using this model, Spiro-B exhibits both a larger effective first-order recombination coefficient (k_1) and a larger bimolecular recombination coefficient (k_2) than Spiro-A. The characteristic lifetime ($1/k_1$) is therefore significantly shorter for Spiro-B (112 ns) than for Spiro-A (763 ns). While both systems remain predominantly dominated by bimolecular recombination under the measurement conditions used, Spiro-B shows a noticeably greater contribution from first-order recombination.

The TRPL curves show that both Spiro derivatives exhibit a rapid initial decay. This contrasts with Me-4PACz, which is known to extend monomolecular lifetimes significantly.[32, 33] Despite these shorter lifetimes, devices employing Spiro-A and Spiro-B still achieve relatively high photovoltaic performance. This observation raises an important question: why does Me-4PACz outperform the Spiro derivatives? One may assume that, *a priori*, a faster decay could be linked to faster extraction.

The Spiro-based SAMs were designed following principles inspired by dye-sensitised solar cells, in which strong electronic coupling between the light absorber and the contact facilitates charge injection. In this context, stronger electronic coupling at the interface may accelerate carrier transfer away from the perovskite, potentially leading to faster photoluminescence decay. We therefore postulate that, for Spiro-A

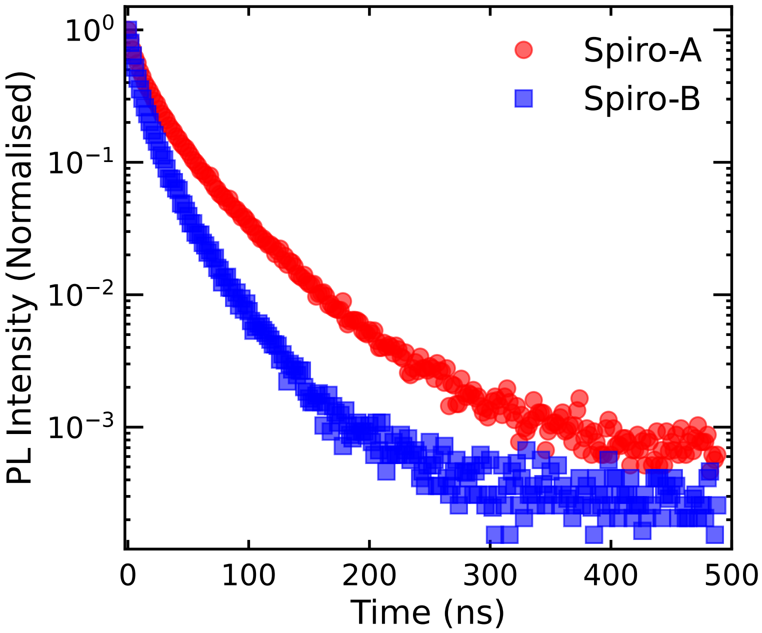

Figure 6.8: Normalised time-resolved photoluminescence (TRPL) decays of perovskite films deposited on ITO/Spiro-A and ITO/Spiro-B substrates. I acknowledge that this data was collected by Dr Wenhui Li at the Institute of Chemical Research of Catalonia. Adapted from Ref. [1] under a Creative Commons Attribution 3.0 Unported Licence.

and Spiro-B, charge injection will occur through the SAM layer.[14] However, TRPL alone cannot distinguish between rapid interfacial charge transfer and rapid interfacial recombination. A faster decay, therefore, does not necessarily imply beneficial charge extraction; it may also reflect increased non-radiative losses at the interface.[31]

Table 6.1: Extracted TRPL decay rate constants obtained by fitting the photoluminescence transients using the rate equation model shown above, $\frac{dn}{dt} = -k_1 n(t) - k_2 n^2(t)$. All measurements were performed on half-cell structures comprising ITO/SAM/perovskite. In this model, k_1 represents the monomolecular (trap-assisted) recombination rate constant, k_2 corresponds to the bimolecular recombination rate constant, n is the photoexcited carrier concentration, and t denotes time. The percentage contributions indicate the relative weighting of each recombination pathway within the fitted decay dynamics. Adapted from Ref. [1] under a Creative Commons Attribution 3.0 Unported Licence.

$$\frac{dn}{dt} = -k_1 n(t) - k_2 n^2(t)$$

SAM	k_1 (ns^{-1})	$1/k_1$ (ns)	k_1 (%)	k_2 (cm^3 s^{-1})	k_2 (%)	r^2
Spiro-A	1.31×10^{-3}	763.4	5.8	3.92×10^{-18}	94.2	0.996
Spiro-B	8.92×10^{-3}	112.1	22.0	5.51×10^{-18}	78.0	0.999

The rapid initial decay observed for both Spiro derivatives, unlike that typically seen for Me-4PACz, suggests that recombination at the interfaces is significantly different from that in the carbazole SAM. This observation is consistent with the lower V_{OC} observed for the Spiro-based devices. However, a further complexity arises: although Spiro-B exhibits a faster decay than Spiro-A, it delivers a higher V_{OC}. This behaviour appears counterintuitive if photoluminescence lifetime is interpreted as being representative of recombination losses, which govern the photovoltage. To resolve this apparent contradiction, differential lifetime analysis is employed to examine how the recombination dynamics evolve as the carrier density decreases.[34] The differential lifetime analysis provides the instantaneous recombination timescale without imposing a predefined number of exponential components. Further discussion on this analysis is provided in Section 3.4.3. The resulting differential lifetime traces are shown in Figure 6.9. The differential lifetime analysis is restricted to delay times below approximately 300 ns, as the PL signal approaches the noise floor at longer times and the resulting late-time rise in τ_{PL} is not considered physically meaningful.

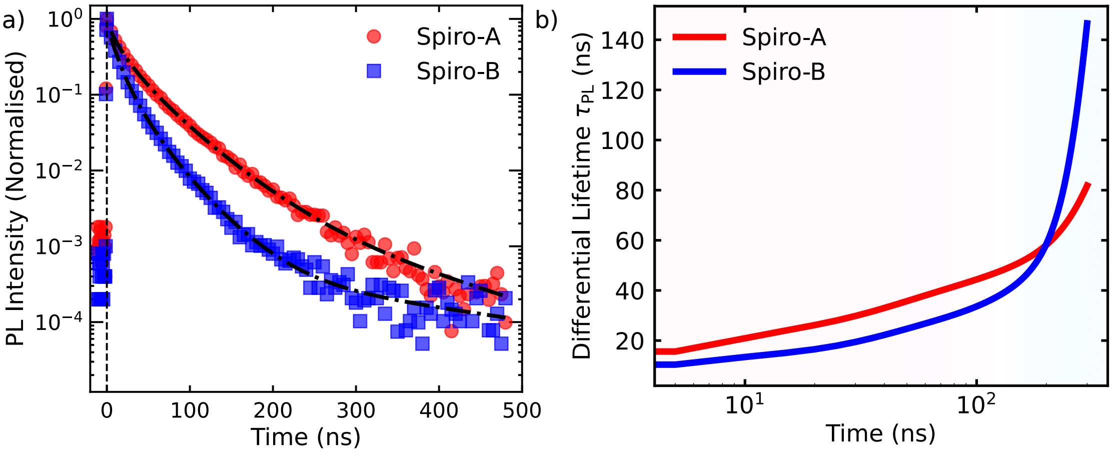

Figure 6.9: a) Normalised time-resolved photoluminescence (TRPL) decays of perovskite films deposited on ITO/Spiro-A and ITO/Spiro-B substrates. The x-axis is extended before $t = 0$ to show the pre-excitation baseline and noise level prior to the PL decay. Black dashed lines represent multi-exponential fits used to capture the decay dynamics across the analysed time window. b) Differential photoluminescence lifetime (τ_{PL}) extracted from the fitted decays, plotted as a function of time. The differential lifetime analysis is restricted to delay times below approximately 300 ns, beyond which the PL signal approaches the noise floor and the extracted differential lifetime becomes unreliable. Adapted from Ref. [1] under a Creative Commons Attribution 3.0 Unported Licence.

At early times and intermediate times, the differential lifetime of Spiro-B remains slightly below that of Spiro-A, which is consistent with the larger effective recombination coefficients extracted from the rate equation analysis. However, at later times, which corresponds with lower carrier densities, the differential lifetime of Spiro-B increases more sharply and exceeds that of Spiro-A. This divergence indicates that the two interfaces enter distinct low-carrier-density recombination regimes.

Importantly, differential lifetime analysis alone cannot unambiguously identify the physical origin of the regimes. Variations may arise from differences in interfacial recombination pathways, carrier transfer dynamics, or carrier accumulation effects at the perovskite/SAM interface. As shown by Krückemeier *et al.*, transient photoluminescence measurements in multilayer perovskite stacks reflect a combination of radiative and non-radiative recombination, interfacial charge transfer, and carrier redistribution.[31] As a consequence, similar decay kinetics may emerge from fundamentally different processes. In particular, a rapid decay component may indicate enhanced interfacial recombination, but it may also result from efficient charge transfer into an adjacent transport layer. Likewise, late-time behaviour can be shaped by carrier reinjection or interfacial accumulation. The divergence observed here at low carrier densities, therefore, does not establish a specific recombination regime. However, the combination of larger effective first-order recombination contributions in Spiro-B and a distinct late-time differential-lifetime behaviour strongly suggests that the recombination dynamics at the Spiro-B interface differ from those in Spiro-A.

When considered alongside the device results presented in Section 6.2.3, an apparent discrepancy emerges. Although Spiro-B devices exhibit faster recombination dynamics under TRPL measurements, they display a higher open-circuit voltage than Spiro-A devices. This observation indicates that the relationship between transient recombination dynamics and device performance is not trivial. This may also be, in part, due to TRPL measurements using half-cells and, therefore, the absence of a built-in field. To resolve this discrepancy and directly probe how the interfacial energetics influence steady-state recombination under operating conditions, Stabilise and Pulse (SaP) measurements and $\mathrm{d}J/\mathrm{d}V$ analysis are employed in the following section.

6.2.5 Probing the Flat-Band Potential in Spiro SAM Devices

To understand how the different Spiro SAMs influence the internal energetics of operating devices, the Stabilise and Pulse (SaP) technique is applied to complete perovskite solar cells incorporating Spiro-A, Spiro-B, and Me-4PACz.[21, 35] This method exploits ionic field screening to probe how the internal electrostatic potential and recombination dynamics depend on the charge-extraction layer. The measurement, therefore, provides direct insight into how the molecular structure of the SAM modifies the device's built-in electrostatics. Full details of the Stabilise and Pulse method are provided in Section 3.2.2.

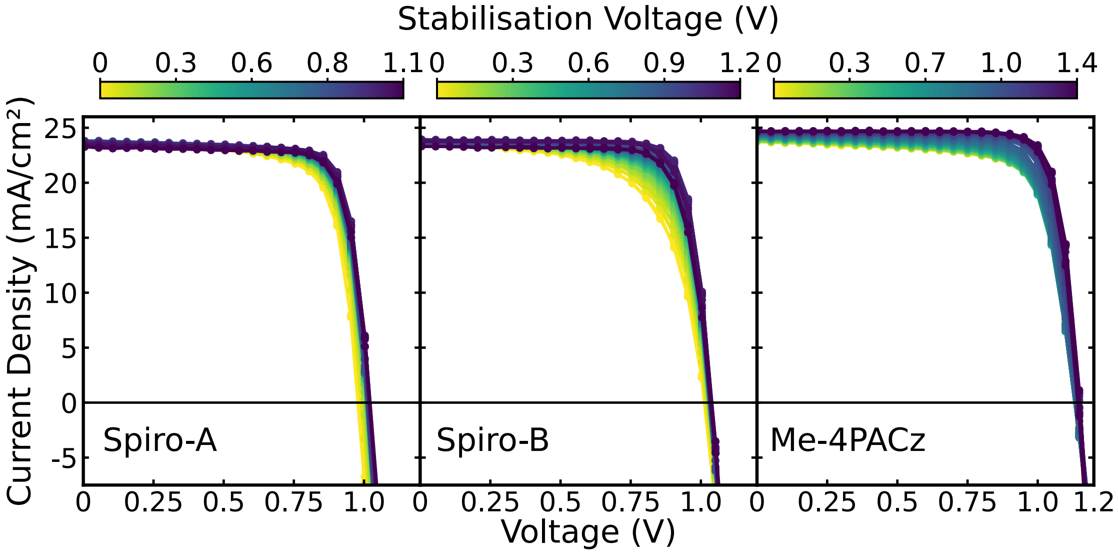

Figure 6.10: Fully reconstructed Stabilise and Pulse (SaP) current density–voltage (J–V) curves measured across a range of stabilisation voltages for devices incorporating Spiro-A, Spiro-B and Me-4PACz. The colour scale indicates the applied stabilisation voltage before the voltage pulses, with yellow corresponding to low stabilisation voltages and purple to high stabilisation voltages, as shown in the colour bars above each panel. The evolution of the reconstructed J–V curves with stabilisation bias reflects changes in the internal electric field and charge distribution within the device. Adapted from Ref. [1] under a Creative Commons Attribution 3.0 Unported Licence.

The reconstructed J–V curves obtained from the SaP measurements across a range of stabilisation voltages for representative devices incorporating Spiro-A, Spiro-B, and Me-4PACz are shown in Figure 6.10. Clear differences in the reconstructed SaP J–V curves are observed as the stabilisation voltage is varied. This behaviour demonstrates that ionic redistribution continues to influence charge extraction even in optimised p–i–n perovskite solar cells. Consequently, the absence of observable hysteresis in conventional J–V sweeps does not imply that ionic motion has been suppressed.[36, 37]

To ensure that any observed differences in the obtained V_{flat} or gradient analysis are not artefacts arising from the measurement, the forward and reverse scans are shown in a clearer contrasting colour in Figure 6.11. This figure clearly demonstrates that, for each applied voltage, the forward and reverse pulsed J–V curves overlap, indicating that during the pulsing regime ionic motion is suppressed.

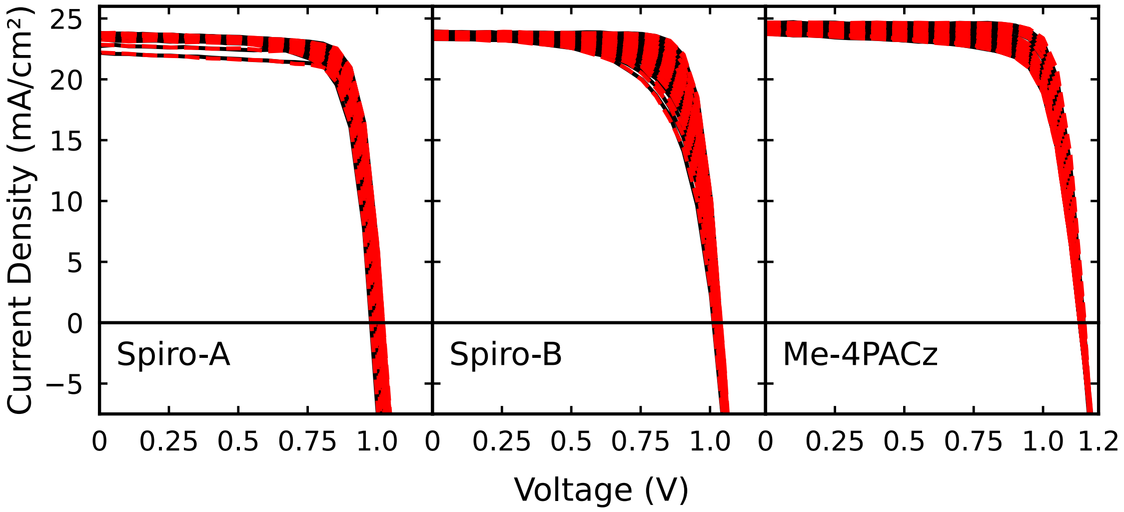

Figure 6.11: Reconstructed forward and reverse current density–voltage (J–V) scans obtained from Stabilise and Pulse (SaP) measurements for devices incorporating (a) Spiro-A, (b) Spiro-B and (c) Me-4PACz. Reverse scans are shown as solid black lines and forward scans as dashed red lines for a range of applied stabilisation voltages. Adapted from Ref. [1] under a Creative Commons Attribution 3.0 Unported Licence.

To further ensure that ionic motion is fixed during the stabilisation phase and before pulsing, the current obtained for each stabilisation voltage is shown in Figures 6.12a and c for Spiro-A and Spiro-B, respectively (stabilisation data for Me-4PACz is shown in Figure 6.A3 for brevity). Additionally, the current minus the average current obtained during the final 30 seconds before pulsing is shown in Figures 6.12b and d for Spiro-A and Spiro-B, respectively. From this data, it is clear that no deviation in current was observed at any stabilisation voltage; therefore, ionic motion was suppressed before reconstructing the pulsed J–V curve for the given ionic configuration.

With the validity of the SaP data checked, we now look to extract the built-in potential of these devices by analysing the change in gradient around the open-circuit voltage ($\mathrm{d}J/\mathrm{d}V|_{V=V_{\mathrm{OC}}}$) for each quasi-steady state J–V curve. The resulting V_{flat} analysis is shown in Figure 6.13. Further discussion of the extraction of this parameter is provided in Section 3.2.2. As established in Chapter 5, the extracted flat-band potential in these devices is equal to the difference in the Fermi level position of the adjacent transport layers and therefore equivalent to the built-in potential in these devices.[21, 22]

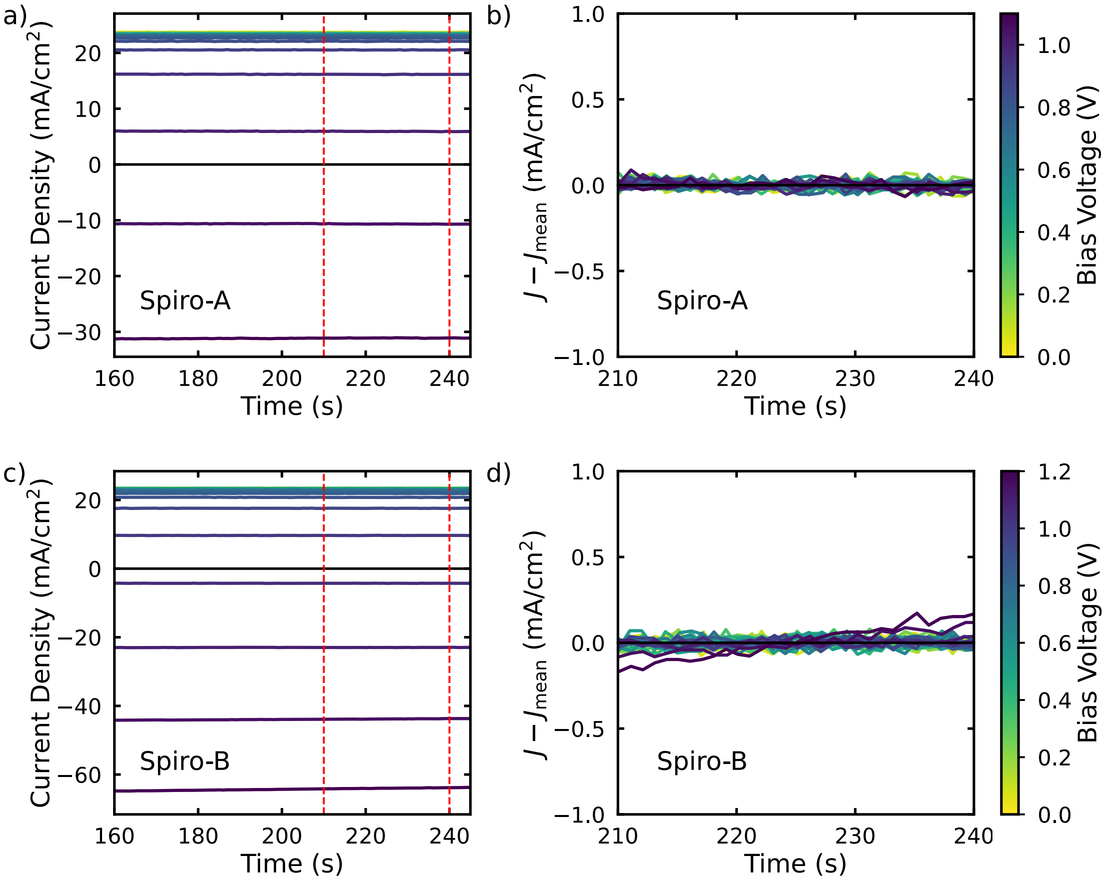

Figure 6.12: (a,c) Full stabilisation current transients recorded during Stabilise and Pulse (SaP) measurements for devices incorporating Spiro-A and Spiro-B, respectively, shown for a range of applied stabilisation voltages. The dashed red lines indicate the time window used to define the steady-state current before pulsing. (b,d) Current deviation from the mean stabilised current ($J - J_{\mathrm{mean}}$) over the final 30 seconds of the stabilisation period for Spiro-A and Spiro-B devices. The small fluctuations about zero confirm that the devices are in a steady-state condition before the voltage pulse sequence. Adapted from Ref. [1] under a Creative Commons Attribution 3.0 Unported Licence.

We will first consider Figure 6.13a, which shows the normalised gradient analysis and extracted V_{flat} values for devices incorporating Spiro-A, Spiro-B, and Me-4PACz. A clear observation is a significant shift in V_{flat} across different SAMs. A change in V_{flat} reflects a shift in the internal energetics of the device. The extracted values of 0.41 V for Spiro-B, 0.73 V for Spiro-A, and 1.10 V for Me-4PACz (summarised in Table 6.2) demonstrate that the choice of SAM strongly influences the energetics.

This result is surprising for several reasons, the first being that the Spiro derivatives displayed similar HOMO levels as measured by cyclic voltammetry in Section 6.2.1. This difference, however, can be explained through the molecular dipole moments obtained by DFT. Spiro-A was found to have a significantly larger dipole at approximately 8.1 D. In comparison, Spiro-B was found to be proportionally

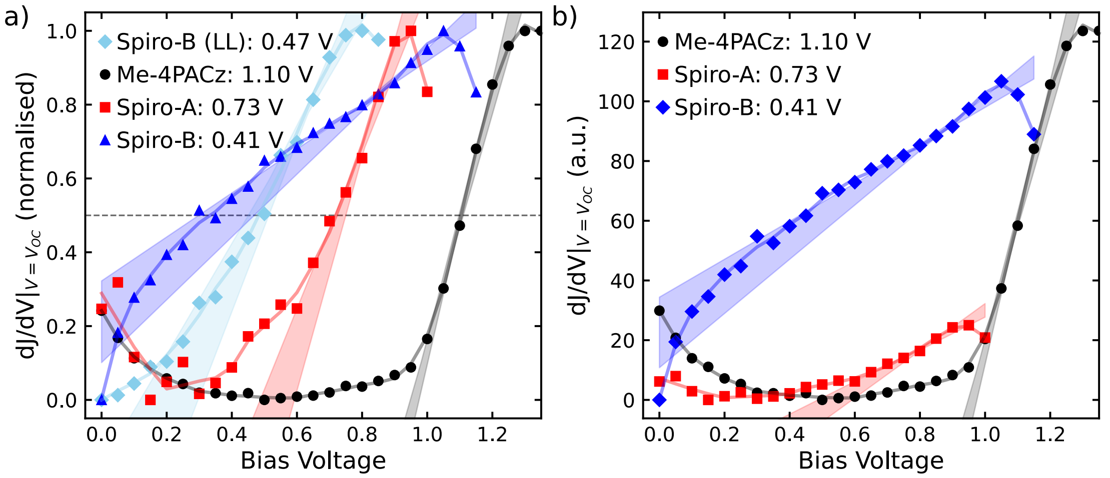

Figure 6.13: (a) Normalised gradient analysis of the Stabilise and Pulse (SaP) data around the open-circuit voltage, showing $\mathrm{d}J/\mathrm{d}V|_{V=V_{\mathrm{OC}}}$ as a function of applied bias for all samples. Markers represent the measured data points, while the lighter solid lines indicate Savitzky–Golay smoothing applied for visual guidance. The midpoint between the local maxima and minima is indicated by a horizontal grey dashed line. The shaded region represents the range of fits considered in determining V_{flat}. Light blue data for Spiro-B (LL) correspond to low-light measurements (~ 0.3 Suns), while dark blue represents standard 1 Sun measurements. (b) The same data plotted after offset normalisation, where the minimum value is subtracted, $\mathrm{d}J/\mathrm{d}V|_{V=V_{\mathrm{OC}}} - \min$, to emphasise differences in the absolute magnitude of the response. Low-light data are omitted in panel (b) for clarity. The extracted V_{flat} values and their associated uncertainties are summarised in Table 6.2. Adapted from Ref. [1] under a Creative Commons Attribution 3.0 Unported Licence.

lower at approximately 2.9 D. A stronger dipole will induce a greater shift in the ITO work function, thereby increasing the V_{flat} value, as was established in Chapter 5 with the carbazole SAMs.[22] Additionally, the extracted value for Me-4PACz is significantly higher than what was obtained in the previous Chapters. This result may be linked to the device not utilising a NiO_x layer. Additionally, the PCBM may be more heavily doped than the previously used devices, as they were obtained from different laboratories and therefore underwent different fabrication procedures.

We will first consider Figure 6.13a, which shows the normalised gradient analysis and extracted V_{flat} values for devices incorporating Spiro-A, Spiro-B, and Me-4PACz. A clear shift in V_{flat} is observed when different SAMs are employed. Since V_{flat} reflects the internal device energetics, this result indicates that the choice of interfacial molecule significantly modifies the electrostatic potential within the device. The extracted values of 0.41 V for Spiro-B, 0.73 V for Spiro-A, and 1.10 V for Me-4PACz (summarised in Table 6.2) demonstrate that the interfacial energetics are strongly dependent on the molecular properties of the SAM.

At first glance, this behaviour is somewhat unexpected, as the Spiro derivatives exhibit similar HOMO levels when measured using cyclic voltammetry (Section 6.2.1). However, the difference can be rationalised by considering the molecular dipole moments obtained from density functional theory calculations. Spiro-A was found to possess a substantially larger dipole moment of approximately 8.1 D, while Spiro-B exhibits a smaller dipole moment of approximately 2.9 D. A larger dipole induces a stronger shift in the ITO work function, which in turn increases the V_{flat} value. This behaviour is consistent with the trend established in Chapter 5 for the carbazole-based SAMs.[22]

Interestingly, Me-4PACz exhibits the highest extracted V_{flat} despite possessing a substantially smaller dipole moment than Spiro-A (Table 6.2). This observation suggests that the interfacial energetics of carbazole-based and Spiro-based SAMs may not be solely determined by their molecular dipole moments. Instead, additional interfacial factors, such as differences in molecular packing, electronic coupling, or energy-level alignment with the perovskite absorber, likely influence the effective electrostatic potential at the interface. A similar distinction between the behaviour of carbazole and Spiro SAMs was observed in the TRPL measurements discussed earlier, further indicating that the interfacial electronic structure differs between these two classes of hole-selective layers.

Table 6.2: Summary of reported dipole moments for devices employing the Spiro-SAMs and Me-4PACz and the corresponding flat-band potentials, V_{flat}, extracted from Stabilise and Pulse measurements. The V_{flat} values are obtained from the $\mathrm{d}J/\mathrm{d}V$ gradient analysis. The quoted uncertainties reflect the error corresponding to the uncertainty in the intercept extraction as described in Section 3.2.2.

SAM	Dipole Moment (D)	V_{flat} (V)
Spiro-A	8.1	0.73 ± 0.01
Spiro-B	2.9	0.41 ± 0.04
Spiro-B (LL)	2.9	0.47 ± 0.02
Me-4PACz	1.5 [38]	1.10 ± 0.01

We note that the Spiro-B measurement was conducted at both 1 Sun and approximately 0.3 Suns, corresponding to the low-light (LL) measurement. This was due to a large error in the Spiro-B device V_{flat} extraction under 1 Sun conditions. Regardless, the measurement conducted under lower light yields a clearer analysis, with the values obtained showing overlap in the associated fit errors. The observation that the low-light measurement yields a clearer fit is likely due to changes in the film's charge density: bulk recombination processes are limited by the square of the charge density, whereas monomolecular processes depend on a single charge carrier.[39]

Therefore, in this measurement, where ion-modulated surface recombination produces a clear change in the J–V curve, reducing the light intensity will yield a clearer result by shifting the balance towards monomolecular processes. The full SaP and V_{flat} extraction at low light can be seen in Figure 6.A4.

Secondly, we consider the results of the gradient analysis, $\mathrm{d}J/\mathrm{d}V|_{V=V_{\text{OC}}}$, without normalisation, shown in Figure 6.13b. Interestingly, a clear difference is observed between Spiro-A and Spiro-B in the magnitude of the gradient change. As discussed in Chapter 5, the magnitude of the gradient analysis represents the interplay between ion-modulated interfacial charge recombination and bulk losses. If bulk recombination dominates, the impact of ions at the device interfaces will be reduced, resulting in a smaller magnitude. Figure 6.13b clearly shows that Spiro-B has a far greater magnitude than Spiro-A, which is significantly smaller. This result indicates that Spiro-A is more likely to be bulk-limited, consistent with the TRPL analysis, which showed a significantly lower ratio of monomolecular to bimolecular loss. In contrast, Spiro-B appears to show a larger contribution of ion-modulated surface recombination, which is again consistent with the TRPL analysis, which indicated a larger contribution of monomolecular losses in comparison to Spiro-A. Additionally, Me-4PACz shows a significant gradient magnitude; this result is not unexpected, as previous results indicated that Me-4PACz induces a slight energetic barrier at the interface, which increases charge accumulation and, consequently, the V_{OC}; however, it also increases sensitivity to surface recombination.[21, 22]

With these results in hand, we now consider the broader physical implications of the observed shift in V_{flat} and how these results relate to the TRPL observations and overall device performance. The following section looks to consolidate the findings to distinguish charge extraction from charge accumulation in determining device photovoltage.

6.2.6 Charge Accumulation Versus Extraction in Spiro SAM Devices

The SaP measurements show that the dipole strength of the SAM layer primarily governs the flat-band potential. Spiro-A, which has the larger calculated dipole moment, produces a higher V_{flat} than Spiro-B, consistent with dipole-induced modifications of the ITO work function. Surprisingly, however, maximising spatial and energetic overlap between the HOMO of the SAM and the charge-extraction contact does not yield the best device performance. Instead, the Spiro-A devices exhibit a lower open-circuit voltage than Spiro-B devices, despite their larger flat-band potential. This observation indicates that the built-in potential alone does not determine the photovoltage of Spiro SAM devices.

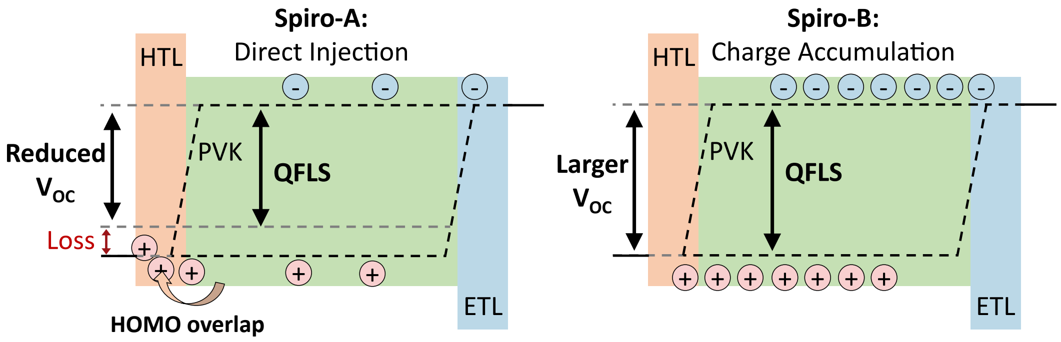

Figure 6.14: Schematic illustration of the difference in quasi-Fermi level splitting (QFLS) for devices incorporating Spiro-A and Spiro-B. In the case of Spiro-A, strong energetic overlap between the Spiro-A HOMO and the perovskite valence band facilitates direct hole injection, reducing the carrier population within the perovskite and leading to a smaller QFLS and lower V_{OC}. In contrast, the increased spatial separation introduced by Spiro-B suppresses direct interfacial injection, promoting charge accumulation within the perovskite layer. This results in a larger QFLS and enhanced V_{OC}, despite a lower built-in potential. The schematic highlights the interplay between interfacial energetics, charge extraction, and recombination dynamics. Adapted from Ref. [1] under a Creative Commons Attribution 3.0 Unported Licence.

Under conditions of selective contacts, the open-circuit voltage reflects the quasi-Fermi level splitting (QFLS) within the perovskite absorber.[23, 24] For a given illumination intensity, a higher charge-carrier density corresponds to a larger QFLS and therefore a higher open-circuit voltage.[40–42] The voltage is therefore determined by the balance between charge generation, recombination, and extraction.

For Spiro-A, two competing effects influence the V_{OC}. The molecular architecture promotes strong electronic coupling between the Spiro HOMO and the ITO contact.[43–45] This configuration facilitates efficient interfacial charge extraction and reduces charge accumulation at the interface. While efficient extraction can improve current collection, it also reduces the carrier density within the perovskite. The resulting reduction in carrier accumulation limits the achievable QFLS and suppresses the V_{OC}.[23, 24]

This interpretation is supported by both the TRPL analysis and the $\mathrm{d}J/\mathrm{d}V|_{V=V_{OC}}$ analysis, which indicate that Spiro-A devices are more strongly influenced by bulk recombination than by interfacial recombination. The relatively large V_{flat} measured for the Spiro-A devices would normally suggest a higher open-circuit voltage.[22] However, the efficient charge-extraction pathway dominates the device behaviour and offsets the benefit of the increased flat-band potential, resulting in the observed reduction in V_{OC}.

In contrast, when the charge-extraction pathway is hindered, as expected for Spiro-B due to the alkyl spacer separating the HOMO from the electrode, additional charge accumulation occurs at the interface. This increased carrier accumulation enhances the QFLS, thereby increasing the open-circuit voltage.[40, 41] The TRPL analysis shows that Spiro-B exhibits a larger effective first-order recombination contribution and a distinct low-carrier-density recombination regime, while the SaP gradient analysis reveals a stronger dependence on ion-modulated interfacial recombination. Together, these observations are consistent with charge carriers accumulating at the perovskite/SAM interface due to hindered extraction.

This mechanism is illustrated schematically in Figure 6.14. Spiro-B allows greater interfacial charge accumulation, increasing the relative QFLS and therefore enabling a larger V_{OC} despite its smaller dipole moment and lower flat-band potential. The reference system, Me-4PACz, further supports this interpretation. This SAM introduces a moderate energetic barrier at the interface, promoting controlled charge accumulation and enhancing the device photovoltage. Consequently, Me-4PACz again produces the highest open-circuit voltage among the devices studied.

A key outcome of this work is therefore that the HOMO energy of the SAM molecule, as inferred from solution-phase measurements, plays only a minor role in determining the built-in potential of complete perovskite solar cells. Instead, the dominant parameter is the dipole strength of the anchored molecule. Furthermore, maximising direct HOMO overlap with the charge-extraction contact does not necessarily maximise device voltage or performance. Introducing a physical spacer between the HOMO and the electrode can instead promote controlled interfacial charge accumulation and improve device behaviour.

These results highlight that the design of transport layers should focus on how a molecule alters the device's energetics when bound to a surface, rather than solely on optimising energy-level alignment based on isolated molecular orbitals. This conclusion is consistent with the broader observation that perovskite solar cells tolerate significant energetic offsets due to the presence of mobile ionic charge, which can suppress surface recombination losses.

6.3 Conclusions

This chapter demonstrates that maximising electronic coupling and direct HOMO overlap between a self-assembled molecule (SAM) layer and the charge extraction contact does not necessarily lead to improved performance in inverted perovskite solar cells. Through the synthesis and systematic comparison of two Spiro-based SAMs, Spiro-A and Spiro-B, we have isolated the impact of spatial coupling while maintaining comparable intrinsic molecular energetics.

The Spiro-A derivative has the Spiro core directly anchored to the ITO substrate via a carboxylic acid moiety, thereby placing the HOMO level in close proximity to the ITO. In contrast, Spiro-B incorporates an alkyl spacer group that spatially separates the HOMO from the ITO. When incorporated in perovskite solar cells, Spiro-B achieved a higher overall power conversion efficiency and open-circuit voltage in comparison to the Spiro-A derivative, despite both molecules exhibiting nearly identical optical properties and energy level alignment as estimated via cyclic voltammetry and light absorption measurements. The Spiro-A moiety produced a larger interfacial dipole, as confirmed by Stabilise and Pulse measurements that revealed a larger built-in potential than Spiro-B, which showed a low dipole moment and consequently a low built-in potential.

Here, we propose that Spiro-A's HOMO overlaps with the ITO, promoting efficient charge extraction and thereby reducing the photogenerated charge density in the perovskite. In contrast, Spiro-B, which lacks this HOMO overlap due to the alkyl spacer, results in increased accumulation and, consequently, higher QFLS, thereby improving the open-circuit voltage and boosting the power conversion efficiency.

Transient photoluminescence measurements reveal that Spiro-B exhibits a larger effective contribution from monomolecular recombination pathways compared to Spiro-A. This was supported by the SaP measurement and subsequent open-circuit voltage gradient analysis, which revealed a strong influence of ion-modulated surface recombination for Spiro-B, and a bulk-dominated regime for Spiro-A. Differential lifetime analysis of the TRPL revealed a distinct low-carrier-density regime in Spiro-B, suggesting that charge carriers may persist longer when using this SAM than Spiro-A. These observations indicate that the spacer group in Spiro-B clearly alters interfacial recombination and promotes charge accumulation, thereby explaining the observed increase in the device's open-circuit voltage.

However, the reference SAM, Me-4PACz, outperforms both Spiro derivatives in all metrics bar fill factor. This emphasises the significance of controlled interfacial recombination and charge accumulation in improving the QFLS. These findings challenge the conventional focus on maximising charge injection efficiency and highlight the importance of balancing interfacial energy barriers, molecular dipole strength, and recombination dynamics in SAM design to optimise device performance.

6.A Appendix

6.A.1 Additional Figures

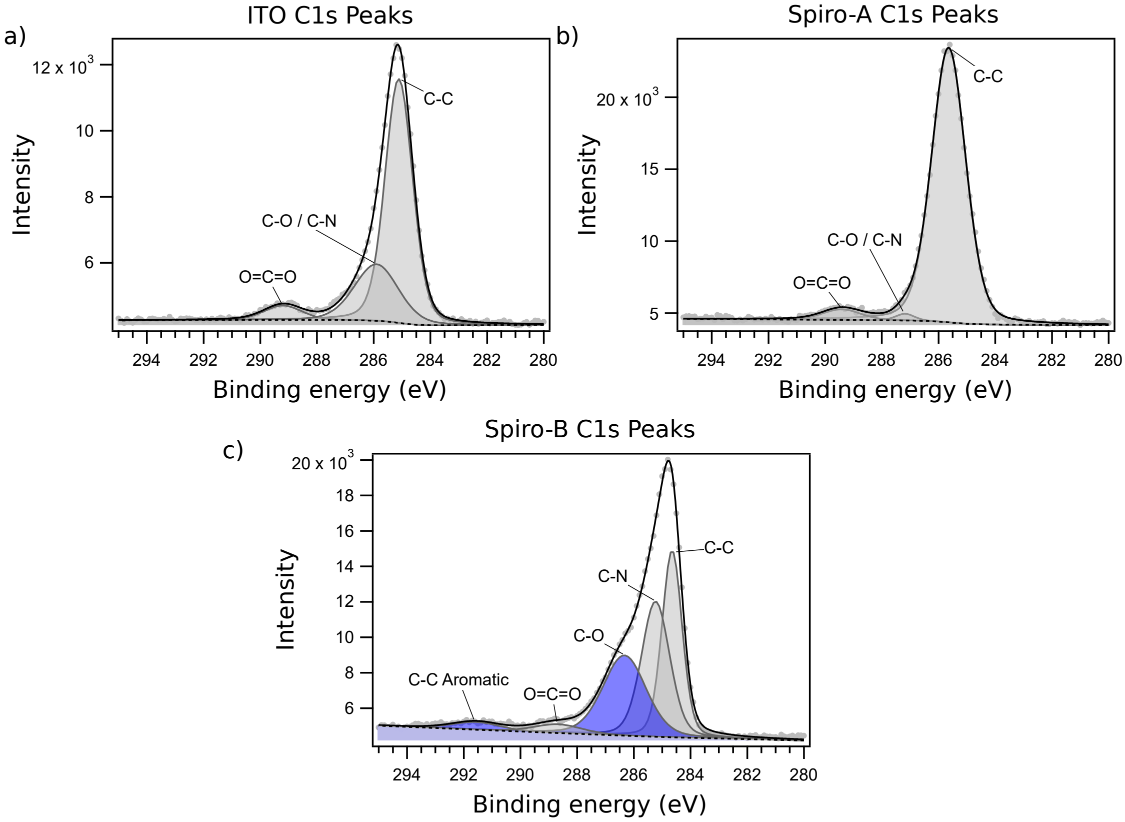

Figure 6.A1: High-resolution C 1s X-ray photoelectron spectroscopy (XPS) spectra of (a) a bare ITO substrate, (b) ITO coated with Spiro-A, and (c) ITO coated with Spiro-B. The appearance and relative intensities of the peaks in panels (b) and (c) confirm successful deposition of the Spiro-based self-assembled molecules on the ITO surface.

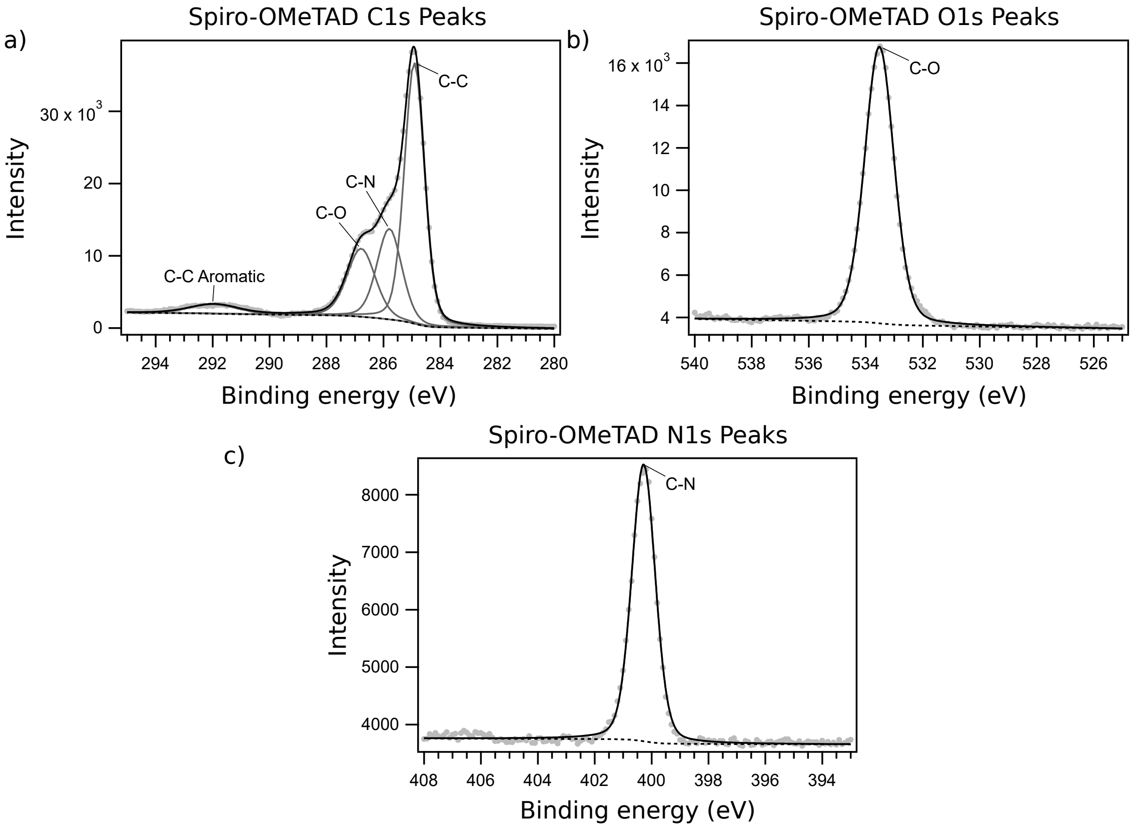

Figure 6.A2: High-resolution X-ray photoelectron spectroscopy (XPS) spectra of a thin film of spin-coated Spiro-OMeTAD showing the (a) C 1s, (b) O 1s, and (c) N 1s core-level regions

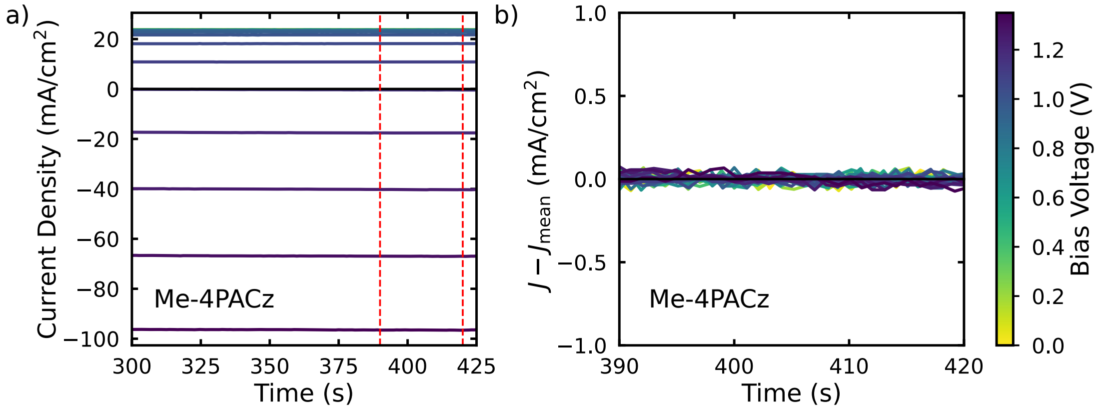

Figure 6.A3: Current density measured during the stabilisation period of the Stabilise and Pulse measurements for the device incorporating Me-4PACz. (a) Stabilised current density as a function of time for a range of applied stabilisation biases. The red-dashed lines indicate the 30 s window used for analysis, immediately prior to the voltage pulse. (b) Corresponding current density during the final 30 s of the stabilisation period, plotted relative to the mean current density over this same interval. The absence of systematic deviation from zero confirms that no measurable current drift occurs prior to pulsing, indicating that the device reaches a stable ionic configuration under the applied bias.

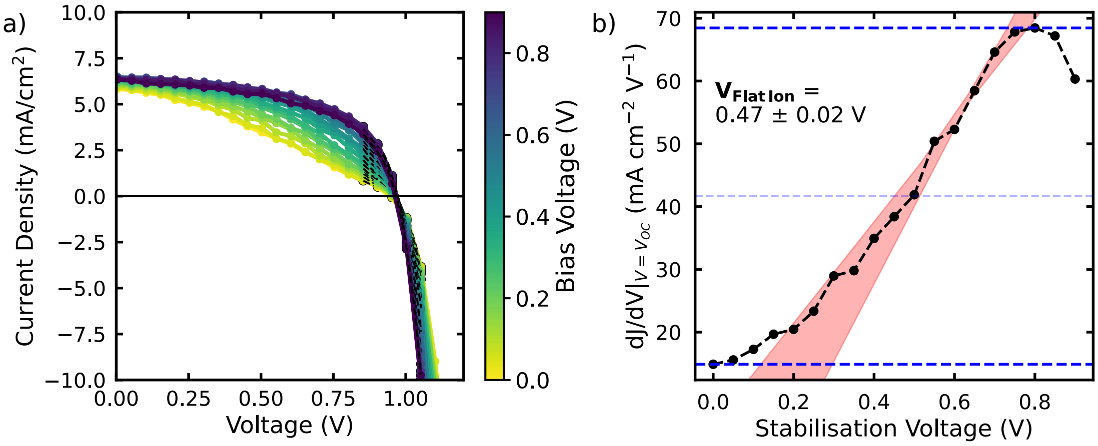

Figure 6.A4: Stabilise and Pulse (SaP) analysis of a Spiro-B device measured at approximately 0.3 suns illumination. a) Reconstructed J–V curves obtained following stabilisation at different bias voltages, with the colour scale indicating the applied stabilisation voltage. b) Corresponding $\mathrm{d}J/\mathrm{d}V|_{V=V_{\mathrm{OC}}}$ as a function of stabilisation voltage. The linear transition region used to extract the flat-band potential is indicated by the shaded region. The extracted flat-band potential is $V_{\mathrm{flat}} = 0.47 \pm 0.02$ V, where the uncertainty reflects the error associated with the linear regression used to determine the intercept.

6.A.2 Additional Tables

Table 6.A1: Fitted XPS peak positions (binding energy, eV) for reference ITO substrates and substrates coated with Spiro-OMeTAD, Spiro-A, and Spiro-B. Peaks in the C 1s, N 1s, and O 1s regions correspond to the chemical environments identified during peak fitting. For the In 3d and Sn 3d regions, the reported binding energies correspond to the spin–orbit split doublet components ($3d_{5/2}$ and $3d_{3/2}$) obtained from the fitted spectra.

Material	C–C	C–N	C–O	O–C–O	C (Aro)
ITO-Ref	285.11	285.9	–	289.2	–
Spiro-OMeTAD	284.91	285.79	286.78	–	291.96
Spiro-A	285.64	–	287.18	289.42	–
Spiro-B	284.65	285.21	286.34	288.66	291.57

Material	N 1s (a)	N 1s (b)
ITO-Ref	–	–
Spiro-OMeTAD	400.28	–
Spiro-A	400.02	401.18
Spiro-B	399.82	400.38

Material	O–In	O–In-Def	HO–In	O–C
ITO-Ref	530.36	531.17	532.1	–
Spiro-OMeTAD	–	–	–	533.52
Spiro-A	530.39	531.19	532.15	533.07
Spiro-B	530.35	530.9	531.65	533.18

Material	In $3d_{5/2}$	In $3d_{3/2}$	Sn $3d_{5/2}$	Sn $3d_{3/2}$
ITO-Ref	444.96	452.51	487.13	495.54
Spiro-OMeTAD	–	–	–	–
Spiro-A	444.95	452.50	487.11	495.54
Spiro-B	444.90	452.45	487.04	495.46

References

(1) Angus, F. J.; Mackenzie, L.; Giza, M.; Wilkinson, D.; Arca, E.; Palomares, E.; Li, W.; Docampo, P.; Cooke, G. *Journal of Materials Chemistry A* **2025**, *13*, 38140–38148.

(2) Abrusci, A.; Stranks, S. D.; Docampo, P.; Yip, H.-L.; Jen, A. K.-Y.; Snaith, H. J. *Nano Letters* **2013**, *13*, 3124–3128.

(3) Kim, S. Y.; Cho, S. J.; Byeon, S. E.; He, X.; Yoon, H. J. *Advanced Energy Materials* **2020**, *10*, 2002606.

(4) Suo, J.; Yang, B.; Bogachuk, D.; Boschloo, G.; Hagfeldt, A. *Advanced Energy Materials* **2025**, *15*, 2400205.

(5) Tang, H.; Shen, Z.; Shen, Y.; Yan, G.; Wang, Y.; Han, Q.; Han, L. *Science* **2024**, *383*, 1236–1240.

(6) Dai, Z.; Yadavalli, S. K.; Chen, M.; Abbaspourtamijani, A.; Qi, Y.; Padture, N. P. *Science* **2021**, *372*, 618–622.

(7) Yang, G.; Wang, C.; Lei, H.; Zheng, X.; Qin, P.; Xiong, L.; Zhao, X.; Yan, Y.; Fang, G. *Journal of Materials Chemistry A* **2017**, *5*, 1658–1666.

(8) Aktas, E.; Phung, N.; Köbler, H.; González, D. A.; Méndez, M.; Kafedjiska, I.; Turren-Cruz, S.-H.; Wenisch, R.; Lauermann, I.; Abate, A.; Palomares, E. *Energy & Environmental Science* **2021**, *14*, 3976–3985.

(9) Cao, Q. et al. *Advanced Materials* **2024**, *36*, 2311970.

(10) Zheng, X. et al. *Nature Energy* **2023**, *8*, 462–472.

(11) Torres Merino, L. V. et al. *Joule* **2024**, *8*, 2585–2606.

(12) Chen, C.-H.; Liu, G.-W.; Chen, X.; Deger, C.; Jin, R.-J.; Wang, K.-L.; Chen, J.; Xia, Y.; Huang, L.; Yavuz, I.; Fan, J.; Wang, Z.-K. *Angewandte Chemie International Edition* **2025**, *64*, e202419375.

(13) Ullah, A. et al. *Advanced Functional Materials* **2022**, *32*, 2208793.

(14) Koops, S. E.; O'Regan, B. C.; Barnes, P. R. F.; Durrant, J. R. *Journal of the American Chemical Society* **2009**, *131*, 4808–4818.

(15) Wooh, S.; Kim, T.-Y.; Song, D.; Lee, Y.-G.; Lee, T. K.; Bergmann, V. W.; Weber, S. A. L.; Bisquert, J.; Kang, Y. S.; Char, K. *ACS Applied Materials & Interfaces* **2015**, *7*, 25741–25747.

(16) Koops, S. E.; Barnes, P. R. F.; O'Regan, B. C.; Durrant, J. R. *The Journal of Physical Chemistry C* **2010**, *114*, 8054–8061.

(17) Sánchez-de-Armas, R.; Oviedo, J.; San Miguel, M. Á.; Sanz, J. F. *The Journal of Physical Chemistry C* **2011**, *115*, 11293–11301.

(18) Ghadiri, E.; Zakeeruddin, S. M.; Hagfeldt, A.; Grätzel, M.; Moser, J.-E. *Scientific Reports* **2016**, *6*, 24465.

(19) Zhang, L.; Favereau, L.; Farré, Y.; Mijangos, E.; Pellegrin, Y.; Blart, E.; Odobel, F.; Hammarström, L. *Physical Chemistry Chemical Physics* **2016**, *18*, 18515–18527.

(20) Antila, L. J.; Myllyperkiö, P.; Mustalahti, S.; Lehtivuori, H.; Korppi-Tommola, J. *The Journal of Physical Chemistry C* **2014**, *118*, 7772–7780.

(21) Hart, L. J. F.; Angus, F. J.; Li, Y.; Khaleed, A.; Calado, P.; Durrant, J. R.; Djurišić, A. B.; Docampo, P.; Barnes, P. R. F. *Energy & Environmental Science* **2024**, *17*, 7107–7118.

(22) Angus, F. J.; Yiu, W. K.; Mo, H.; Leung, T. L.; Ali, M. U.; Li, Y.; Wang, J.; Ho-Baillie, A. W. Y.; Cooke, G.; Djurišić, A. B.; Docampo, P. *The Journal of Physical Chemistry Letters* **2024**, *15*, 10686–10695.

(23) Caprioglio, P.; Stolterfoht, M.; Wolff, C. M.; Unold, T.; Rech, B.; Albrecht, S.; Neher, D. *Advanced Energy Materials* **2019**, *9*, 1901631.

(24) Warby, J.; Shah, S.; Thiesbrummel, J.; Gutierrez-Partida, E.; Lai, H.; Alebachew, B.; Grischek, M.; Yang, F.; Lang, F.; Albrecht, S.; Fu, F.; Neher, D.; Stolterfoht, M. *Advanced Energy Materials* **2023**, *13*, 2303135.

(25) Cariello, M.; Pant, N.; Harkiss, A. H.; Tracey, F. M.; Cameron, J.; Skabara, P. J.; Holliman, P. J.; Docampo, P.; Cooke, G. *Molecular Systems Design & Engineering* **2022**, *7*, 899–905.

(26) Zhang, C.; Son, Y.; Kim, H.; Lee, S.-H.; Liang, X.; Fu, G.; Lee, S.-U.; Park, D.-A.; Jiang, Q.; Zhu, K.; Park, N.-G. *Joule* **2024**, *8*, 1394–1411.

(27) Wang, S. et al. *Advanced Functional Materials* **2024**, *34*, 2316202.

(28) Donley, C.; Dunphy, D.; Paine, D.; Carter, C.; Nebesny, K.; Lee, P.; Alloway, D.; Armstrong, N. R. *Langmuir* **2002**, *18*, 450–457.

(29) Basta, L.; Moscardini, A.; Fabbri, F.; Bellucci, L.; Tozzini, V.; Rubini, S.; Griesi, A.; Gemmi, M.; Heun, S.; Veronesi, S. *Nanoscale Advances* **2021**, *3*, 5841–5852.

(30) Péan, E. V.; Davies, M. L. *Journal of Chemical Information and Modeling* **2023**, *63*, 4477–4482.

(31) Krückemeier, L.; Krogmeier, B.; Liu, Z.; Rau, U.; Kirchartz, T. *Advanced Energy Materials* **2021**, *11*, 2003489.

(32) Al-Ashouri, A. et al. *Science* **2020**, *370*, 1300–1309.

(33) Yuan, Y.; Yan, G.; Dreessen, C.; Rudolph, T.; Hülsbeck, M.; Klingebiel, B.; Ye, J.; Rau, U.; Kirchartz, T. *Nature Materials* **2024**, *23*, 391–397.

(34) Krogmeier, B.; Staub, F.; Grabowski, D.; Rau, U.; Kirchartz, T. *Sustainable Energy & Fuels* **2018**, *2*, 1027–1034.

(35) Hill, N. S.; Cowley, M. V.; Gluck, N.; Fsadni, M. H.; Clarke, W.; Hu, Y.; Wolf, M. J.; Healy, N.; Freitag, M.; Penfold, T. J.; Richardson, G.; Walker, A. B.; Cameron, P. J.; Docampo, P. *Advanced Materials* **2023**, *35*, 2302146.

(36) Richardson, G.; O'Kane, S. E. J.; Niemann, R. G.; Peltola, T. A.; Foster, J. M.; Cameron, P. J.; Walker, A. B. *Energy & Environmental Science* **2016**, *9*, 1476–1485.

(37) Calado, P.; Telford, A. M.; Bryant, D.; Li, X.; Nelson, J.; O'Regan, B. C.; Barnes, P. R. *Nature Communications* **2016**, *7*, 13831.

(38) Sun, A. et al. *Advanced Energy Materials* **2024**, *14*, 2303941.

(39) Péan, E. V.; Dimitrov, S.; De Castro, C. S.; Davies, M. L. *Physical Chemistry Chemical Physics* **2020**, *22*, 28345–28358.

(40) Chen, H. et al. *Nature* **2023**, *613*, 676–681.

(41) Xu, W.; Hart, L. J. F.; Moss, B.; Caprioglio, P.; Macdonald, T. J.; Furlan, F.; Panidi, J.; Oliver, R. D. J.; Pacalaj, R. A.; Heeney, M.; Gasparini, N.; Snaith, H. J.; Barnes, P. R. F.; Durrant, J. R. *Advanced Energy Materials* **2023**, *13*, 2301102.

(42) Stolterfoht, M. et al. *Energy & Environmental Science* **2019**, *12*, 2778–2788.

(43) He, L.; Guo, Y.; Kloo, L. *Physical Chemistry Chemical Physics* **2021**, *23*, 27171–27184.

(44) Maggio, E.; Martsinovich, N.; Troisi, A. *The Journal of Physical Chemistry C* **2012**, *116*, 7638–7649.

(45) Nguyen, H. M.; Nguyen, D. N.; Kim, N. *Advances in Natural Sciences: Nanoscience and Nanotechnology* **2010**, *1*, 025001.

Chapter 7

Conclusions and Outlook

Metal-halide perovskite solar cells have progressed rapidly in recent years, with certified power conversion efficiencies now exceeding 27%, placing them among the highest-performing single-junction photovoltaic technologies.[1] Despite this remarkable progress, these materials remain fundamentally distinct from conventional semiconductors. The soft ionic lattice and low defect formation energies intrinsic to metal-halide perovskites give rise to high densities of mobile ionic species.[2, 3] Ion migration through the perovskite lattice is known to induce effects such as current density–voltage (J–V) hysteresis and long-term stability challenges.[4, 5] However, ionic motion cannot be entirely suppressed without fundamentally altering the material itself; instead, it must be understood. The question is therefore not whether ions influence device performance, but how that influence can be quantified and interpreted.

This thesis sought to determine what physical information can be extracted from ion migration in perovskite solar cells, and whether mobile ionic charge should be regarded solely as a parasitic feature or as a diagnostic of internal device energetics. Through a combination of Stabilise and Pulse measurements, time-resolved photoluminescence, and systematic variation of interfacial materials, a consistent picture has emerged: mobile ions do not merely perturb device performance, but encode information about interfacial recombination, charge accumulation, and energetic alignment.

By isolating ionic and electronic contributions using the Stabilise and Pulse technique, Chapter 4 demonstrated that mobile ions do not inherently limit performance and can, under steady-state conditions, increase the open-circuit voltage relative to an equivalent "ion-free" configuration of the same device. We provide the first direct experimental evidence that mobile ionic charge can enhance the open-circuit voltage in a working device. This approach did not simply quantify an ionic effect, but used controlled ionic redistribution as a probe of the internal electric field and interfacial recombination processes. Direct experimental evidence showed that ionic screening can reduce interfacial recombination losses by modifying the internal electrostatics. In fact, despite the well-known effect of mobile ions reducing the extracted short-circuit current density, the boost in photovoltage resulting from ionic field screening in the devices measured in Chapter 4 was sufficient to increase the relative overall power conversion efficiency. The drift-diffusion simulations performed showed that mobile ions relax the requirement for perfect energetic alignment at perovskite/transport-layer interfaces by screening internal fields and redistributing charge under steady-state conditions, thereby allowing larger energetic offsets to be tolerated. However, this increased flexibility in energetic alignment also enhances the device's sensitivity to interfacial defect states. It is therefore unsurprising that much of the recent literature has focused on interfacial passivation, which we interpret as a response to this enhanced sensitivity to defect-mediated recombination.

In Chapter 5, controlled variation of carbazole-based self-assembled molecules was used to deliberately tune the interfacial dipole and, consequently, the internal electrostatics of the device. By applying the Stabilise and Pulse technique to these devices, the flat-band potential was directly measured under operational conditions, enabling the energetic impact of each transport layer to be quantified in situ. Ionic redistribution was therefore not merely observed, but used as a sensitive probe of how molecular dipole moment modifies band bending at the perovskite/transport-layer interface. A clear correlation between dipole strength and flat-band potential was established, confirming that the effective built-in potential is governed by the Fermi level of the transport layers rather than solely by electrode work function. However, device performance was not maximised at the largest dipole moment. While increasing dipole strength raises the flat-band potential, excessive energetic offsets introduce interfacial barriers that promote charge accumulation and enhance recombination losses. These results demonstrate that in mixed ionic–electronic systems, optimal performance does not arise from maximising built-in potential alone. Instead, this work highlights the importance of fully characterising interfacial material systems to select self-assembled molecules that enable optimal device performance.

In Chapter 6, ionic redistribution was again used as a probe of interfacial physics, this time to examine the consequences of modifying direct hole injection through Spiro-based self-assembled molecules. Conventional device design often assumes that maximising electronic coupling and built-in potential will enhance charge extraction and, consequently, device performance. However, the results presented here demonstrate that this assumption does not hold universally in mixed ionic–electronic systems. Stabilise and Pulse measurements showed that a molecule engineered to promote direct injection exhibited a larger built-in potential yet a lower steady-state open-circuit voltage than a derivative designed to inhibit this injection pathway. Time-resolved photoluminescence, interpreted in conjunction with

Stabilise and Pulse J–V gradient analysis, further indicated that modifying interfacial coupling shifts the balance between bulk and surface recombination pathways. In this way, ionic motion exposed how interfacial energy barriers, dipole strength, and recombination dynamics must be balanced to achieve optimal performance, rather than maximising injection efficiency alone.

Taken together, these results show that the presence of mobile ions shifts recombination regimes, modifies internal fields, and couples interfacial energetics to carrier accumulation. Extracting meaning from ion migration, therefore, enables a more complete understanding of how voltage and efficiency emerge from the interplay between electrostatics and recombination in mixed ionic–electronic photovoltaics.

Building on these findings, several clear directions for future investigation emerge. The Stabilise and Pulse technique has been shown here to provide access to flat-band conditions and to distinguish between bulk- and interface-limited operation. However, its full diagnostic potential remains unexplored. In particular, further integration of SaP measurements with complementary techniques could provide deeper insight into how ionic redistribution modifies recombination pathways under operational bias. In this thesis, initial time-resolved photoluminescence comparisons suggest that SaP is sensitive to the balance between interfacial and bulk recombination. Extending this approach to TRPL measurements under controlled applied bias, where ionic motion is deliberately manipulated, would enable a more direct link between electrostatic redistribution and recombination dynamics. Such combined measurements would move beyond static characterisation and enable real-time probing of the interplay among ionic motion, charge accumulation, and recombination.

In addition, performing Stabilise and Pulse measurements under controlled temperature conditions would provide a further degree of control over ionic motion, enabling the kinetics of ionic redistribution to be systematically tuned. Such temperature-dependent SaP measurements could offer direct insight into the activation energies and time scales of different mobile defect species, providing a route to explicitly link ionic transport to changes in band bending and recombination pathways within operating devices.

The diagnostic capability of the Stabilise and Pulse technique may also prove valuable in more complex photovoltaic architectures, such as tandem solar cells. In conventional two-terminal tandem configurations, the subcells are electrically connected in series, meaning that the measured current and voltage reflect the combined response of both absorbers. As a result, recombination losses within the perovskite subcell cannot be easily isolated using standard electrical measurements. In contrast, three-terminal tandem architectures provide an additional electrical contact, allowing the perovskite subcell to be biased independently of the lower-band gap cell. Implementing Stabilise and Pulse measurements within such configurations would enable controlled manipulation of the ionic distribution within the perovskite absorber while directly monitoring the resulting electronic response. This could provide a practical route to isolating ion-mediated recombination processes within the perovskite layer of tandem devices, offering a new diagnostic tool for identifying performance limitations in next-generation perovskite-based tandem photovoltaics.

A further strength of the Stabilise and Pulse technique is that it removes the ambiguity behind reports of “hysteresis-free” perovskite solar cells based solely on conventional J–V measurements acquired at different scan rates. In highly efficient p–i–n devices in particular, apparent suppression of hysteresis does not necessarily imply the absence of ionic effects. By separating ionic history from the electronic response, SaP provides a more rigorous method for determining whether mobile ions continue to influence device operation. Because this measurement can be performed with standard laboratory equipment, it offers a practical route to a more reliable assessment of ionic effects across a wide range of perovskite device systems.

Overall, the work presented in this thesis demonstrates that mobile ions in perovskite solar cells should not be regarded solely as a complication to be minimised, but as a source of physical information. Rather than treating ion migration purely as a parasitic effect, the results presented here show that controlled manipulation of ionic distributions can reveal how interfacial energetics, recombination pathways, and charge accumulation shape device performance. The presence of mobile ions does not obscure device physics; when properly interrogated, it exposes it. Recognising this opens a route to more deliberate, physically informed interface design in mixed ionic–electronic photovoltaics.

References

(1) NREL, Best Research-Cell Efficiency Chart, `https://www.nrel.gov/pv/cell-efficiency`.

(2) Walsh, A.; Scanlon, D. O.; Chen, S.; Gong, X. G.; Wei, S.-H. *Angewandte Chemie International Edition* **2015**, *54*, 1791–1794.

(3) Yang, D.; Ming, W.; Shi, H.; Zhang, L.; Du, M.-H. *Chemistry of Materials* **2016**, *28*, 4349–4357.

(4) Snaith, H. J.; Abate, A.; Ball, J. M.; Eperon, G. E.; Leijtens, T.; Noel, N. K.; Stranks, S. D.; Wang, J. T.-W.; Wojciechowski, K.; Zhang, W. *The Journal of Physical Chemistry Letters* **2014**, *5*, 1511–1515.

(5) Thiesbrummel, J. et al. *Nature Energy* **2024**, *9*, 664–676.